University of Cyprus

DEPARTMENT OF ELECTRICAL AND COMPUTER ENGINEERING

INVESTIGATION OF PHYSIOLOGICAL VARIABILITY EFFECTS ON fMRI DYNAMIC FUNCTIONAL CONNECTIVITY

DOCTOR OF PHILOSOPHY DISSERTATION

FOIVIA N. NIKOLAOU

JANUARY 2018

University of Cyprus

DEPARTMENT OF ELECTRICAL AND COMPUTER ENGINEERING

INVESTIGATION OF PHYSIOLOGICAL VARIABILITY EFFECTS ON FMRI DYNAMIC FUNCTIONAL CONNECTIVITY

FOIVIA N. NIKOLAOU

A Dissertation Submitted in Partial Fulfillment of the Requirements for the Degree of Doctor of Philosophy at the University of Cyprus

January, 2018

VALIDATION PAGE

Doctoral Candidate: Foivia N. Nikolaou

Doctoral Thesis Title: Investigation of Physiological Variability Effects on fMRI Dynamic Functional Connectivity

The present Doctoral Dissertation was submitted in partial fulfillment of the requirements for the Degree of Doctor of Philosophy at the Department of Electrical and Computer Engineering, and was approved on the January 15, 2018 by the members of the Examination Committee.

Examination Committee:

Committee Chair _____

Dr. Theocharis Theocharides

Research Supervisor _____

Dr. Georgios D. Mitsis

Research Co-Supervisor _____

Dr. Christina Orphanidou

Committee Member _____

Dr. Constantinos Pitris

Committee Member _____

Dr. Constantinos Pattichis

Committee Member _____

Dr. Fragkiskos Papadopoulos

DECLARATION OF DOCTORAL CANDIDATE

The present doctoral dissertation was submitted in partial fulfillment of the requirements for the degree of Doctor of Philosophy of the University of Cyprus. It is a product of original work of my own, unless otherwise mentioned through references, notes, or any other statements.

……..

Foivia Nikolaou
Department of Electrical and Computer Engineering
University of Cyprus
January 2018

ΠΕΡΙΛΗΨΗ

Η λειτουργική μαγνητική νευροαπεικόνιση σε κατάσταση ηρεμίας (rs-fMRI) είναι μια ισχυρή και σύγχρονη μέθοδος λειτουργικής απεικόνισης του εγκεφάλου που μπορεί να χρησιμοποιηθεί για την αξιολόγηση των αλληλεπιδράσεων που συμβαίνουν όταν ένας εθελοντής βρίσκεται σε κατάσταση ηρεμίας (δεν καλείται να εκτελέσει μια σειρά από εντολές). Αυτή η εγκεφαλική δραστηριότητα ηρεμίας μπορεί να εκτιμηθεί μέσω των αλλαγών στην τοπική ροή του περιφερειακού αίματος στον εγκέφαλο. Αυτές οι αλλαγές δημιουργούν συνακόλουθα αλλαγές στο τοπικό επίπεδο της οξυγόνωσης του αίματος που τροφοδοτεί την ενεργοποιημένη περιοχή και παράγουν ένα σήμα με το ακρωνύμιο BOLD (Blood Oxygen Level Dependent) που μπορεί να μετρηθεί με το fMRI.

Ωστόσο, είναι πολύ γνωστό πλέον ότι το σήμα BOLD σήμα επηρεάζεται επίσης - εκτός από την νευρωνική δραστηριότητα – από τις διακυμάνσεις των φυσιολογικών σημάτων, συμπεριλαμβανομένων του αρτηριακού CO2, της αναπνοής και της μεταβλητότητας του καρδιακού ρυθμού (HR / HRV). Αυτές οι διακυμάνσεις έχουν σαν αποτέλεσμα να προκαλούν μεταβολές στα χαρακτηριστικά της τοπικής αιματικής ροής, είτε μέσω αλλαγών οξυγόνωσης ή μεταβολών του όγκου αίματος και μπορεί κατά συνέπεια να προκαλούν μεταβολές στο σήμα BOLD, εκτός των αλλαγών που προκαλούνται από τις νευρωνικές ενεργοποιήσεις. Ακόμη, πολλές μελέτες έχουν επιβεβαιώσει ότι ακόμη και οι αυθόρμητες διακυμάνσεις των προαναφερθέντων φυσιολογικών σημάτων επηρεάζουν το σήμα BOLD fMRI. Σχετικά με αυτό, οι εκτιμήσεις της λειτουργικής συνδεσιμότητας μεταξύ των διαφόρων περιοχών του εγκεφάλου που εκτελούνται όταν το υποκείμενο είναι σε ηρεμία μπορεί να συγχέονται από τις επιδράσεις των διακυμάνσεων του φυσιολογικού σήματος. Επιπλέον, έχει αποδειχθεί ότι η λειτουργική συνδεσιμότητα σε κατάσταση ηρεμίας αλλάζει μέσα σε ένα σύντομο χρονικό διάστημα (δυναμική λειτουργική συνδεσιμότητα - DFC), με τις πηγές αυτής της διακύμανσης να μην έχουν διευκρινιστεί πλήρως. Η εκτίμηση της DFC έχει προταθεί ως μια ακριβέστερη απεικόνιση των λειτουργικών δικτύων του εγκεφάλου.

Λαμβάνοντας υπόψη όλα τα παραπάνω, ο κύριος στόχος της παρούσας διπλωματικής εργασίας είναι η διερεύνηση και καλύτερη κατανόηση της σχέσης μεταξύ των προτύπων της DFC και των χρονικά μεταβαλλόμενων ιδιοτήτων ταυτόχρονα καταγεγραμμένων φυσιολογικών σημάτων (end-tidal CO2, respiration volume per time - RVT και HR/HRV) χρησιμοποιώντας μεθόδους από τα πεδία της επεξεργασίας σήματος, της μηχανικής μάθησης (Ανάλυση Ανεξάρτητων Συνιστωσών – ICA) καθώς και εργαλεία από την θεωρία των γράφων πάνω σε μετρήσεις fMRI που πάρθηκαν σε κατάσταση ηρεμίας από 12 υγιείς εθελοντές.

Προκειμένου να γίνει αυτό, αξιολογήθηκαν το DFC και ο βαθμός (degree) των δικτύων ηρεμίας για διάφορα ευρέως χρησιμοποιούμενα δίκτυα καταστάσεως ηρεμίας (default mode network – DMN, οπτικό και σωματοκινητικό) και προσδιορίστηκε ποσοτικά η σχέση τους με τη χρονική μεταβολή της φυσιολογικής ισχύος του σήματος. Όπως αναφέρθηκε ήδη, τα δίκτυα καταστάσεως ηρεμίας περιλαμβάνουν ανατομικά απομονωμένες, εντούτοις λειτουργικά συνδεδεμένες, περιοχές που εμφανίζουν υψηλή συσχέτιση όσον αφορά στην δραστηριότητα του σήματος BOLD.

Τα αποτελέσματά μας αποκαλύπτουν ένα ρυθμιστικό αποτέλεσμα των προαναφερθέντων φυσιολογικών σημάτων στα δυναμικά μοντέλα λειτουργικής συνδεσιμότητας για ένα πλήθος δικτύων καταστάσεων ηρεμίας (DMN, οπτικο, σωματοκινητικό) που εξήχθησαν με διάφορες μεθόδους όπως mask-based, seed-based και ICA. Με την χρήση της διακριτής αποσύνθεσης κυματιδίων (wavelets), δείχνουμε επίσης ότι αυτά τα φαινόμενα διαμόρφωσης είναι πιο έντονα σε συγκεκριμένες ζώνες συχνοτήτων. Επιπλέον, χρησιμοποιώντας ένα μοντέλο πολλαπλής γραμμικής παλινδρόμησης, αξιολογήθηκε πιο λεπτομερώς η συγκριτική συνεισφορά των εν λόγω φυσιολογικών σημάτων στα δυναμικά χαρακτηριστικά των RSNs. Επιπλέον, χρησιμοποιώντας τον μετασχηματισμό Hilbert, εξήγαμε την στιγμιαία ισχύ του σήματος HR στις χαμηλές (LF) και υψηλές (HF) συχνότητες και διερευνήσαμε τον τρόπο με τον οποίο η ισχύς στις συγκεκριμένες συχνοτικές ζώνες, οι οποίες συνδέονται με την επίδραση του συμπαθητικού και παρασυμπαθητικού νευρικού συστήματος, επηρεάζουν τα RSNs. Τέλος, δείχνουμε ότι οι παρατηρούμενες επιδράσεις διαμόρφωσης ήταν πιο ευδιάκριτες όταν η επεξεργασία έγινε στο λειτουργικό απεικονιστικό χώρο του κάθε ατόμου ξεχωριστά, παρά στον τυπικό (MNI) χώρο.

ABSTRACT

Resting state functional magnetic resonance imaging (RS-fMRI) is a relatively recent, very promising method of functional brain imaging that can be used for the evaluation of regional interactions that occur when a volunteer is at rest (i.e., not performing an explicit task). This resting brain activity may be assessed through fluctuations in regional blood flow in the brain, which generate the blood-oxygen-level dependent (BOLD) signal that is measured by fMRI.

However, it is well established that the BOLD signal is also influenced – in addition to neuronal activity - by fluctuations in physiological signals, including arterial CO2, respiration and heart rate/ heart rate variability (HR/HRV). These fluctuations cause changes in local blood susceptibility, either through oxygenation changes or blood volume changes and may consequently induce BOLD signal variations, in addition to changes induced by neuronal activations of interest. Numerous studies have confirmed that even spontaneous fluctuations of the previously mentioned physiological signals influence the BOLD fMRI signal in a regionally-specific manner. Related to this, estimates of functional connectivity between different brain regions, performed when the volunteer is at rest may be also confounded by the effects of physiological signal fluctuations. In addition, resting functional connectivity has been demonstrated to change over different time scales (dynamic functional connectivity - DFC), with the sources of this variation not fully. Investigating DFC has been proposed as a more precise portrayal of functional brain networks.

Taking into consideration all the above, the main goal of the present thesis was to investigate the relation between DFC patterns and the time-varying properties of simultaneously recorded physiological signals (end-tidal CO2, respiration volume per time; RVT and HR/HRV) using signal processing, machine learning (independent component analysis – ICA) and graph theoretical tools, as well as resting-state fMRI measurements from 12 healthy volunteers. In order to do so, DFC and its corresponding network degree for three different important resting state networks (RSNs), namely the default mode network (DMN), as well as the visual and somatosensory networks, were assessed and the relation between the dynamic RSN characteristics and the time-varying physiological signal power was quantified. As already reported, these RSNs comprise of anatomically isolated, however functionally connected regions showing a high degree of correlated BOLD signal activity. These networks are observed to be generally reliable over various studies, regardless of differences in the data acquisition and analysis methods. However, the sources of DFC are far from being elucidated.

Our results reveal a modulatory effect of the aforementioned physiological signals on the resting DFC patterns for a number of RSNs (DMN, somatosensory, visual) that were extracted by using different analysis methods, including mask-based, seed-based and ICA analysis. By using discrete wavelet decomposition, we also show that these modulation effects are more pronounced in specific frequency bands. In addition, by using a multiple regression model, we separately quantify the effect of each physiological signal on RSN DFC. Moreover, by using the Hilbert transform, we extracted the instantaneous LF and HF power of the instantaneous HR signal, which are important markers of sympathetic and parasympathetic autonomic nervous system activity and investigated how the activity of these two components affects RSN DFC. Finally, we show that the observed modulation effects are considerably clearer when processing was done in the individual functional imaging space, compared to when it was done in standard (MNI) space.

ACKNOWLEDGEMENTS

Firstly, I would like to express my sincere gratitude to my advisor Prof. Georgios Mitsis and my co-advisor Dr. Christina Orphanidou for the continuous support of my Ph.D. study and related research, for their patience, motivation, and immense knowledge. Their guidance helped me in all the time of research and writing of this thesis. I could not have imagined having a better advisor and co-advisor for my Ph.D. study.

Besides my advisor and co-advisor, I would like to thank the rest members of my thesis committee: Dr. Theocharides, Dr. Pitris, Dr. Pattichis and Dr. Papadopoulos for their insightful comments and encouragement, but also for the hard questions which incented me to widen my research from various perspectives.

I would like to thank my friends for their continued support and encouragement. I would specifically like to recognize Savvas Meliniotis and Nicoletta Polycarpou. You have been there for me when the challenges of graduate school seemed too great to overcome.

Finally, I would like to express the deepest gratitude to my family. Mom, Dad, Anna and Andria you have all provided support, encouragement and interest in my thesis work. Thanks for listening to my problems and providing perspective. Last but not least, my deepest love, respect and gratitude goes to my husband Pavlos and my daughter Elina. Elina your birth gave a new meaning to my life. I cannot wait to see you next to me at my Ph.D. graduation ceremony. Pavlos, you have been continually supportive of my graduate education. You have been patient with me when I was frustrated, you celebrate with me when even the littlest things go right, and you are there whenever I need you to just listen.

DEDICATION

This thesis work is dedicated to my little angle, Elina and to me grandfather, Phivos.

TABLE OF CONTENTS

TABLE OF FIGURES

TABLE OF TABLES

TABLE OF ABBREVIATIONS AND ACRONYMS

2D	2 Dimensional
3D	3 Dimensional
QRS	A pattern seen in an electrocardiogram that indicates the pulses in a heartbeat and their duration.
ACC	Anterior Cingulate Cortex
ANS	Autonomous Nervous System
BOLD	Blood Oxygen Level-Dependent
BET	Brain Extraction Tool
CO2	Carbon Dioxide
CUBRIC	Cardiff University Brain Imaging Centre
CBF	Cerebral Blood Flow
CSF	Cerebrospinal Fluid
CWT	Continuous Wavelet Transform
DMN	Default Mode Network
DWT	Discrete Wavelet Transform
DFC	Dynamic Functional Connectivity
TE	Echo Time: Time from the center of the (radio frequency) RF-pulse to the center of the echo.
EPI	Echo-Planar Imaging
ECG	Electrocardiography
EEG	Electroencephalography
FSGPR	Fast Spoiled Gradient-Echo
FOV	Field of View
FSL	FMRIB Software Library
FLIRT	FMRIB's Linear Image Registration Tool
FC	Functional Connectivity
fMRI	Functional Magnetic Resonance Imaging
FMRIB	Functional Magnetic Resonance Imaging of the Brain: A software library containing image analysis and statistical tools for functional, structural and diffusion MRI brain imaging data.
GLM	General Linear Model

HR	Heart Rate
HRV	Heart Rate Variability
HRF	Hemodynamic Response Function
HD	High Dimensionality
HF	High Frequency
IC	Independent Component
ICA	Independent Component Analysis
IPL	Inferior Parietal Lobule
HFiA	Instantaneous Amplitude of The High Frequency Band
LFiA	Instantaneous Amplitude of The Low Frequency Band
LD	Low Dimensionality
LF	Low Frequency
MRI	Magnetic Resonance Imaging
MEG	Magnetoencephalography
MATLAB	Matrix Laboratory: A multi-paradigm numerical computing environment
MLR	Multiple Linear Regression
MSE	Mean Squared Error
mPFC	Medial Prefrontal Cortex
MELODIC	Model-free FMRI analysis using Probabilistic Independent Component Analysis
MNI	Montreal Neurological Institute
PNS	Parasympathetic Nervous Systems
PaCO2	Partial Pressure of Arterial Carbon Dioxide
PETCO2	Partial Pressure of End-Tidal Carbon Dioxide: a measure of the amount of carbon dioxide present in the exhaled air
PR	Perfect Reconstruction
PET	Positron Emission Tomography
PCC	Posterior Cingulate Cortex
PCA	Principle Component Analysis
pICA	Probabilistic Independent Component Analysis
ROI	Region of Interest
ROIs	Region of Interests
rCBF	Regional Cerebral Blood Flow

TR	Repetition Time: The length of time between corresponding consecutive points on a repeating series of pulses and echoes.
RVT	Respiration Volume Per Time
RS	Resting State
RS-fMRI	Resting State Fmri
RSN	Resting State Network
RSNs	Resting State Networks
RETROICOR	Retrospective Image Correction
SMN	sensory motor network
SQI	Signal Quality Index
SPECT	Single Photon Emission Computed Tomography
SNS	Sympathetic Nervous Systems
VLF	Very Low Frequency
WTC	Wavelet Transform Coherence
WM	White Matter

1. Introduction

1.1 Motivation

The number of functional magnetic resonance imaging (fMRI) studies that are inspecting not only the task-related increases in the fMRI signal within specific brain areas, but also the correlation between time series fluctuations corresponding to different brain regions (functional connectivity) has increased rapidly in the last few years. The catalyst for these investigations is the observation that low frequency (<0.1 Hz) fluctuations in the fMRI signal intensity time series, which can take place either as a result of task-induced signal modulations or in the absence of an external stimulus or explicit task (resting state), are frequently correlated between functionally related areas. The general assumption is that these correlated fluctuations reveal synchronized variations in the neuronal activity of a network of regions. fMRI can, therefore, provide a window into the interaction, or connection, among brain areas. The exploration of these networks by analyzing coherent signal fluctuations has consequently come forth as *functional* or *effective connectivity* analysis (Rogers et al., 2007; Friston, 2011), whereby the term effective connectivity implies that causal interactions are searched for (Friston, 2011).

Specifically, the recent discovery that spontaneous brain activity is not random noise, but is particularly organized in resting state networks (RSNs) has created significant interest, as RSNs provide a way to probe brain function without needing explicit tasks to drive brain activity (Fox and Raichle, 2007). Consistent correlations among low frequency fluctuations between the fMRI time series corresponding to different areas at rest were initially revealed by Biswal et al, 1995. The default mode network (DMN) –a set of brain areas that regularly de-activate through a wide range of cognitive tasks– is one of the first RSNs to be identified (Greicius et al., 2003). Subsequent studies identified numerous consistent and distinct RSNs, including the motor, auditory, visual, and attention networks (Damoiseaux et al., 2006; De Luca et al., 2006). The presence of RSNs was also confirmed using additional modalities (electroencephalography – EEG and magnetoencephalography – MEG) (Smith et al., 2008; De Pasquale et al., 2010). Overall, these observations support the view that the brain at rest comprises several periodically active and synchronized networks.

Notwithstanding, the volunteer test-retest reliability of RSN connectivity is lower than what might have been expected if patterns were anatomically determined (Honey et al., 2009).

This is partly due to the reconfiguration of functional networks, but could also reflect the effect of non-neuronal sources or time-variability. To investigate the latter, RSN non-stationarities are being increasingly considered, mainly using sliding-window techniques combined with seed voxel/region analysis and independent component analysis (ICA) (De Pasquale et al., 2010; Chang and Glover, 2010; Hutchison et al., 2013; Chang et al., 2013; Kiviniemi et al., 2011). Several recent studies have focused on dynamic fMRI-based RSN functional connectivity (Chang and Glover, 2010; Chang et al., 2013; Zalesky et al., 2014).

Furthermore, the blood-oxygen level dependent (BOLD) signal measured by fMRI is only indirectly related to the underlying neuronal activity, as determined by neurovascular coupling mechanisms and quantified by the hemodynamic response function (HRF) (Buxton, 2012). The impact of non-neuronal physiological variability (e.g. heart rate, arterial CO_2, respiration) on fMRI measurements and connectivity has been established (Wise et al., 2004; Napadow et al., 2008). The cerebral vasculature is exquisitely sensitive to arterial CO_2 fluctuations; it has been demonstrated that spontaneous arterial CO_2 fluctuations affect both cerebral blood flow in the middle cerebral artery (Mitsis et al., 2004) and the fMRI BOLD signal regionally (Wise et al., 2004; Pattinson et al., 2009). Moreover, slow changes in respiration depth and rate were found to significantly affect resting-state functional connectivity of the DMN (Birn et al., 2006) and heart rate variability (HRV), as well as its low frequency (LF) and high frequency (HF) power components, have been shown to be correlated with regional BOLD signal variations (Napadow et al., 2008). Additionally, a significant component of BOLD fMRI physiological noise is caused by variations in the depth and rate of respiration. It has previously been demonstrated that a breath-to-breath metric of respiratory variation (respiratory volume per time; RVT), computed from pneumatic belt measurements of chest expansion, has a strong linear relationship with resting-state BOLD signals across the brain (Birn et al., 2006). RVT is believed to capture breathing-induced changes in arterial CO_2, which is a cerebral vasodilator; indeed, separate studies have found that spontaneous fluctuations in end-tidal CO_2 ($PETCO_2$) are correlated with BOLD signal time series (Wise et al., 2004). Overall, these works concluded that RSN studies are particularly susceptible to physiological noise (Murphy et al., 2013; Birn et al., 2012).

1.2 Aim and Objectives

The aim of this Ph.D. thesis is to investigate the dynamic association between fMRI-based functional connectivity and physiological signals in the resting state. While the effects of cardiovascular and respiratory processes on the blood oxygen level dependent (BOLD) signal measured by fMRI have been established, the effect of physiological factors on *dynamic* (time-varying) resting-state functional connectivity has, to our knowledge, not been studied in the past. Understanding the effect of physiological factors on resting-state functional connectivity is a very important topic since physiological noise and neuronal signals may overlap in time, be anatomically co-localized, and can have (or alias into) common temporal frequencies. Separating the underlying neuronal activity from the physiological noise will lead to improved reliability of functional connectivity studies.

The primary objectives of this thesis are:

- To investigate the dynamic variations in resting-state functional connectivity patterns (dynamic functional connectivity) using different analysis techniques. The vast majority of fMRI connectivity research has been performed under the assumption of stationarity. Stationarity in general suggests that some statistic or model parameter of interest is relatively constant (in a statistical sense), and in the context of functional connectivity, it implies that some measure of connectivity (e.g., correlation coefficient between two regions) is not changing significantly over time. Using different data quality and analysis techniques (including mask-based and seed-based analysis and ICA), we explored non-stationarities in order to quantify the dynamics of resting-state correlations of different RSNs.
- To examine whether dynamic resting functional connectivity is modulated by the time-varying properties of simultaneously recorded physiological signals. This was done using end-tidal CO_2 ($PETCO_2$), HRV (a widely-used marker of autonomic activity) and RVT measurements obtained during scanning. To investigate this modulation in a quantitative manner, DFC and its corresponding network degree for the DMN, visual and somatosensory RSNs was assessed and their relation to time-varying physiological signal power was quantified. The network degree was calculated using seed voxel/region analysis and independent component analysis (ICA). In line with this, the examination of the stability of the DMN in both the spatial and temporal domains by using the ICA analysis is also investigated.

Secondary objectives include:

- To identify the frequency band(s) where the modulatory effect of the physiological signals on the fMRI signal is more pronounced. Since different physiological signals may exhibit spectral power that is overlapping, identifying the frequency band with the strongest correlation to the fMRI signal may help elucidating the physiological source of the modulation. We investigated this, for the first time, using discrete wavelet analysis, which allows us to decompose the fMRI and physiological signals in the frequency domain, while preserving temporal information. In addition, application of the wavelet transform allows us to search for modulatory effects within different frequency sub-bands, while still taking the entire signal into consideration.
- To investigate the impact of the cardiac sympathetic and parasympathetic activity, extracted from the HRV signal, on DFC. The finding of a significant correlation between DFC and the cardiac sympathetic and parasympathetic activities may illuminate potential factors underlying dynamic changes in resting-state connectivity. In turn, delineating the brain regions exhibiting such connectivity modulations may yield further insight into neural mechanisms underlying autonomic control mechanisms. The effects of the two different components of the autonomic nervous system was disentangled by obtaining estimates of instantaneous HF and LF power from the HRV signal, using the Hilbert transformation and calculating correlations with the fMRI signals. The HF component of the HRV signal, is attributed to respiration-induced heart rate modulation and is mediated primarily by parasympathetic outflow. The LF component of HRV, while not fully understood, is believed to reflect a mixture of sympathetic and parasympathetic activities.

Additional objectives are:

- To determine the effect of the selected analysis space for the implemented RS-fMRI investigations (MNI vs individual functional spaces). Our analysis was performed both in the MNI and functional spaces and results were compared.
- To quantify the relative modulatory contribution of different physiological signals on the RS-DFC. This will facilitate an understanding of how each physiological signal affects dynamic RSN patterns. We explored this by applying multiple linear regression (MLP) to quantify the relative contribution of different physiological signals.

1.3 Novel Contributions

The original research contributions presented in this thesis are as follows:

- We rigorously investigated the characteristics of fMRI-based DFC patterns using different algorithms, including mask based analysis, seed voxel/region analysis and independent component analysis (ICA) combined with graph-theoretic measures and wavelet analysis. In the ICA analysis, in addition to the standard analysis, a spatial sliding window ICA was performed, which constitutes a novel approach. According to this approach, we split the original 3D dataset of the brain into volumes and then created spatial windows by merging the desired volume in each window. A low dimensionality ICA was then performed in each window.
- We demonstrated, for the first time, that the characteristics of different RSNs over time are clearly modulated by physiological signals (PETCO2, RVT, HR). In addition, we identified the specific frequency sub-bands within which these effects are more pronounced for each physiological signal, by using discrete wavelet decomposition.
- We demonstrated that the imaging space (individual functional vs. standard MNI space) in which the analysis is carried out has a pronounced effect in the context of assessing DFC and its relation to physiological signals. In many studies it is typical that fMRI time-series are registered to the MNI space in similar analyses. We showed that the observed physiological signal modulatory effects were much clearer when processing was done in the individual functional space, compared to when it was done in standard (MNI) space, suggesting that registration to the latter may considerably blur the observed DFC patterns.
- We investigated the impact of the cardiac sympathetic and cardiac parasympathetic neural activity on resting-state DFC for the first time. The effects of these two components was disentangled by obtaining estimates of instantaneous HF and LF HRV power by using the Hilbert transformation. The HF component of HRV is attributed to respiration-induced heart rate modulation and is mediated primarily by parasympathetic outflow. The LF component of HRV is not fully understood but believed to rather reflect a mixture of sympathetic and parasympathetic activities. Both instantaneous HF and LF HRV power were found to affect RS-DFC considerably.
- We applied multiple general linear and linear regression models to quantify the relative modulatory contribution of different physiological signals on RS-DFC. The general linear models for instantaneous HF and LF HRV power yielded very similar results. As

mentioned before, these two had a similar modulatory effect on RS-DFC. Multiple linear regression models were applied for $PETCO_2$, RVT and HR. From these models, the strong relationship between $PETCO_2$ and RVT was shown as the calculated estimated coefficients for these two dependent variables yielded similar values.

1.4 Outline of the thesis

The material in this thesis is organized as follows:

Chapter 2 describes the physiological principles of FMRI. The nature and interpretation of the BOLD (blood oxygen level dependent) signal, and the spatial and temporal resolution of the signal are discussed. Chapter 3 describes in a comprehensive manner the experimental data, pre-processing and processing steps used and applied in this research. Chapter 4 presents the results we have obtained so far using the methods described in the Chapter 3. Chapter 5 presents a summary of the previous chapters and results, and discusses the contributions of this thesis. Chapter 6, in its first section, provides some concluding remarks and also the advantages and limitation of our implementations. In the second section of this Chapter, we present some possible directions for future work.

2. Functional Neuroimaging: Fundamental Principles and Key terms

In this chapter, the fundamental principles of functional neuroimaging and related basic terms and definitions will be provided. In more detail, this chapter stipulates the scientific and clinical background of neuroimaging methods for the study of brain dynamic functional connectivity, aiming to assist the reader to thoroughly understand general key terms that will be used in the following chapters. Initially, the key concepts of "fMRI", "Functional Connectivity" and "Dynamic Functional Connectivity" will be presented. Later on, in the chapter, the theoretical background behind the interaction between physiological signals and the fMRI BOLD signals will be extensively analyzed.

2.1 fMRI

The emergence of modern functional neuroimaging techniques such as brain positron emission tomography (PET), brain single photon emission computed tomography (SPECT), functional magnetic resonance imaging (fMRI), high resolution EEG, and magnetoencephalography (MEG) have brought forth excellent opportunities for researching the human brain *in vivo* and, consequently, have opened a new era in the study of brain function.

Despite the existence of a variety of functional neuroimaging techniques, in the last two decades, fMRI has developed into the most popular method used for functional brain imaging (Bandettini, 2012; Howseman and Bowtell, 1999). fMRI is a non-invasive technique that uses the physical phenomenon of nuclear magnetic resonance and the associated technology of magnetic resonance imaging to map human brain function. This is achieved by indirectly measuring neural activity via the use of blood oxygen level-dependent (BOLD) contrast. This contrast relies on two basic principles: i) hemoglobin has different magnetic properties according to its level of oxygenation: it is diamagnetic when oxygenated but paramagnetic when deoxygenated (Ogawa et al., 1990; Kim and Ogawa 2012); ii) regional blood oxygenation varies according to the levels of neural activity: when neuronal activity increases there is an increased demand for oxygen and the local response is an increase in blood flow in regions of increased neural activity. This is indirectly sensed, since arterial blood accelerates the hemodynamic mean transit time in the district, thus pushing away a portion of de-oxygenated blood in the venous capillaries. As deoxyhemoglobin is paramagnetic, it increases the local

microscopic magnetic field inhomogeneity ΔB thus shortening the T_2* relaxation time which in turn results in accelerated signal fading. All the steps are outlined in the Figure 2.1. Because of this, changes in the BOLD signal can be used to identify areas of decreased or increased neuronal activity.

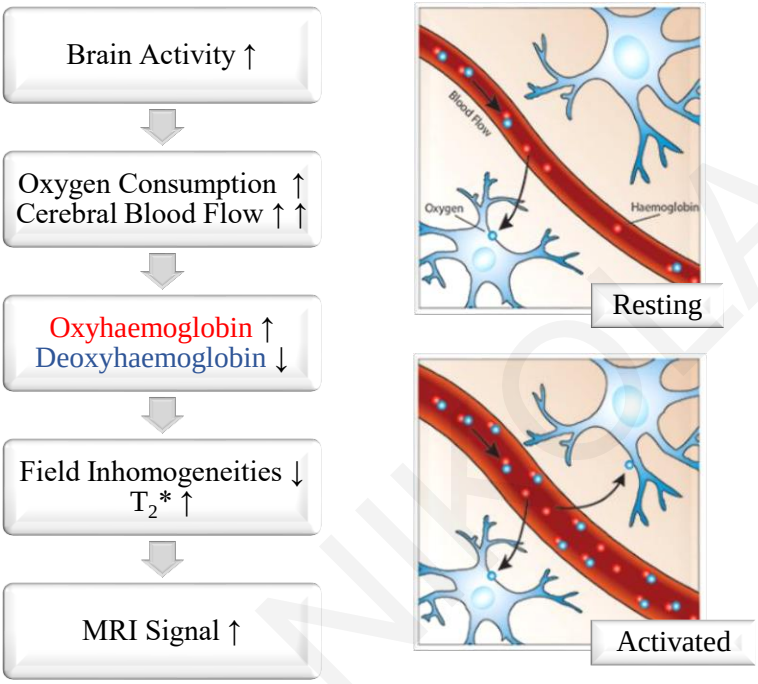

Figure 2.1. Brain activity and BOLD signal principles.

This property of fMRI has made it a very useful tool in studying and understanding brain function both related to tasks and at rest. fMRI studies can, thus, be divided in two areas: task-related and resting state.

2.1.1 Task-Related fMRI

The first fMRI studies used the task-related approach to measure human brain activity. In this approach, individuals perform a variety of different tasks designed to activate and identify the brain areas related to these tasks. Such tasks include the processing of various kinds of information (e.g., words, pictures, sounds, letters, images), using different types of thinking skills (e.g., memory, decision-making, language generation) and responding to stimuli in different ways (e.g., button presses, speaking aloud). In a typical task-related fMRI experiment, a volunteer alternates between periods of performing a task and resting (e.g., looking at a visual stimulus for 30 seconds and then closing their eyes for 30 seconds as a control state as can be

seen in Figure 2.2). The fMRI data can then be analyzed to identify which brain areas show a matching pattern of changes, and these areas are considered to be activated by the stimulus. Task-related fMRI analysis has, therefore, helped us identify and characterize functionally distinct nodes in the human brain. This understanding has, in turn, created the grounds for validating, and interpreting the results of the connectivity analysis obtained using resting state fMRI, explained next.

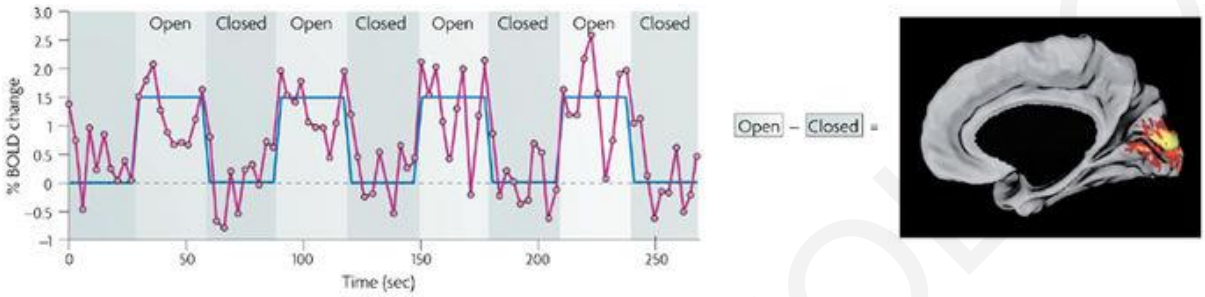

Figure 2.2. Traditional fMRI analysis and BOLD noise: Unaveraged BOLD time course (magenta) from a region in the primary visual cortex during a simple task paradigm that requires volunteers to open and close their eyes. The paradigm is shown in blue (delayed to account for the haemodynamic response) (Fox and Raichle, 2007).

2.1.2 Resting State fMRI

The study of human brain function in the absence of a particular mental task, termed resting state fMRI (RS-fMRI) involves asking individuals to lie at rest while brain images are acquired. The aim of this approach is to further our understanding of human brain function by detecting significant activity which is related only to the mutual dependency of the ongoing activity in different areas.

As mentioned earlier, a strong link with task related activity has been recognized and has had a primary role in the discovery and classification of Resting State (RS) networks (see below). In fact, the brain regions similarly modulated (i.e., either activated or inhibited) by stimuli or tasks, rather than being idle during rest, display instead vigorous and persistent functional activity (Buckner et al., 2008) detected as spontaneous low-frequency (< 0.08 Hz) BOLD signal fluctuations. These low frequency BOLD fluctuations are presumed to be related to "spontaneous" neural activity. For instance, by cross-correlating the time series of a particular brain region (seed region – Figure 2.3) with all other voxels, one can determine which voxels are "functionally connected" with that region.

RS studies are of interest for several reasons. Firstly, some researchers consider them to be associated to anatomical connectivity. Secondly, the reliance of functional connectivity MRI on RS data eliminates the difficulties of task-related fMRI such as experimental design, volunteer compliance, and training demands, making it attractive for studies in all kinds of developmental and clinical groups.

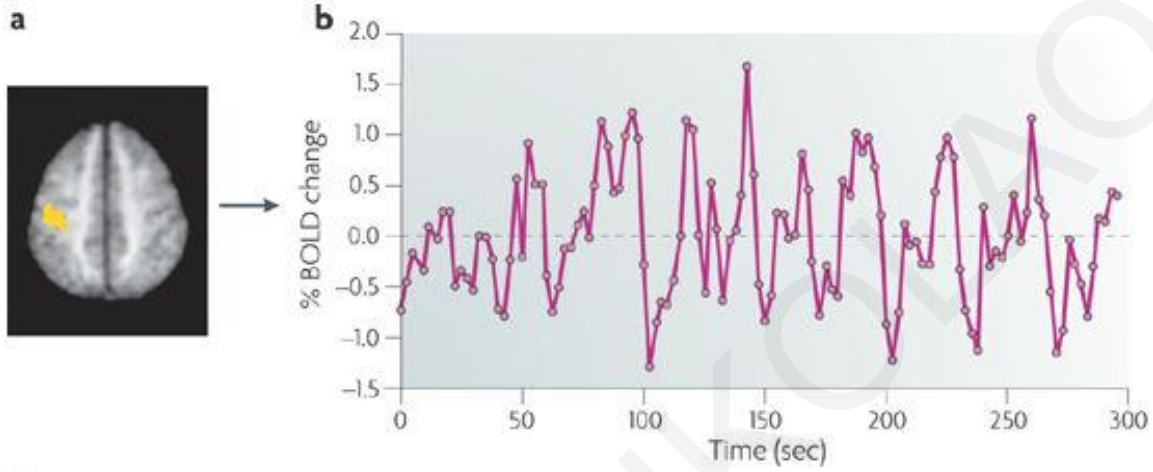

Figure 2.3. Generation of resting-state correlation map: a) Seed region in the left sensory-motor cortex is shown in yellow. b) Time course of spontaneous BOLD activity recorded during resting fixation and extracted from the seed region. (Fox and Raichle, 2007)

2.2 Functional Connectivity

Functional connectivity (FC) is generally characterized as the temporal dependency between spatially remote neurophysiological events (Friston, 2011). In the field of functional neuroimaging, FC is proposed to describe the regional interactions of anatomically separated brain regions, thus reflecting which of these regions are "functionally connected" (Figure 2.4). As mentioned earlier, these regional interactions can be captured in the BOLD signal during RS-fMRI acquisitions. According to the first RS-fMRI study (Biswal et al., 1995), by cross-correlating the time series of a seed region of interest (ROI) in the motor area with all other voxels, it was determined that during rest, the left and right hemispheric regions of the primary motor network are not silent but show a high correlation between their fMRI BOLD time series. This suggests ongoing information processing and ongoing functional connectivity between these regions during rest.

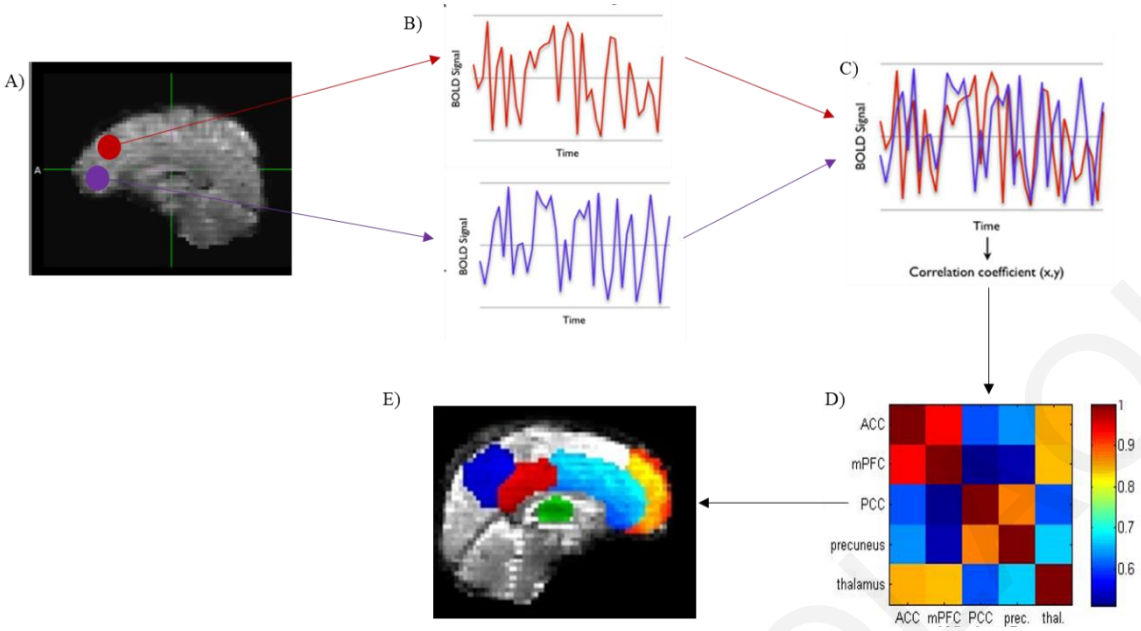

Figure 2.4. Functional connectivity analysis. Consecutive steps of the functional connectivity analysis. A) Select a seed voxel (red) to correlate with other voxel (purple), (B) Presentation of their timeseries, (C) Calculation of correlation coefficients of ROIs, (D) Computation of weighted correlation for all ROIs and (E) Functional Connectivity of ROIs.

Several researchers replicated the results from this RS-fMRI first study, showing a high level of FC between other regions as well. In fact, when fMRI studies started to examine the possibility of measuring FC between brain regions as a reflection of the level of co-activation of spontaneous fMRI time series recorded during rest (Biswal et al., 1997; Cordes et al., 2000; Greicius et al., 2003), it was observed that, at rest, the brain is organized into networks, called Resting State Networks (RSNs), consistent across volunteers and highly similar to networks of task-induced activations and deactivations (Beckmann et al., 2005; Damoiseaux et al., 2006; De Luca et al., 2006; Veer et al., 2010; Smith et al., 2009). RSNs are believed to belong to distinct networks serving different functions such as vision, language, etc. Today the most studied RSNs are: the default mode network (DMN), the sensory motor network (SMN), the right and the left lateral networks, the salience network, the ventral stream network, the task positive network, the primary, the medial and lateral visual networks as well as the visual and auditory networks (see Figure 2.5).

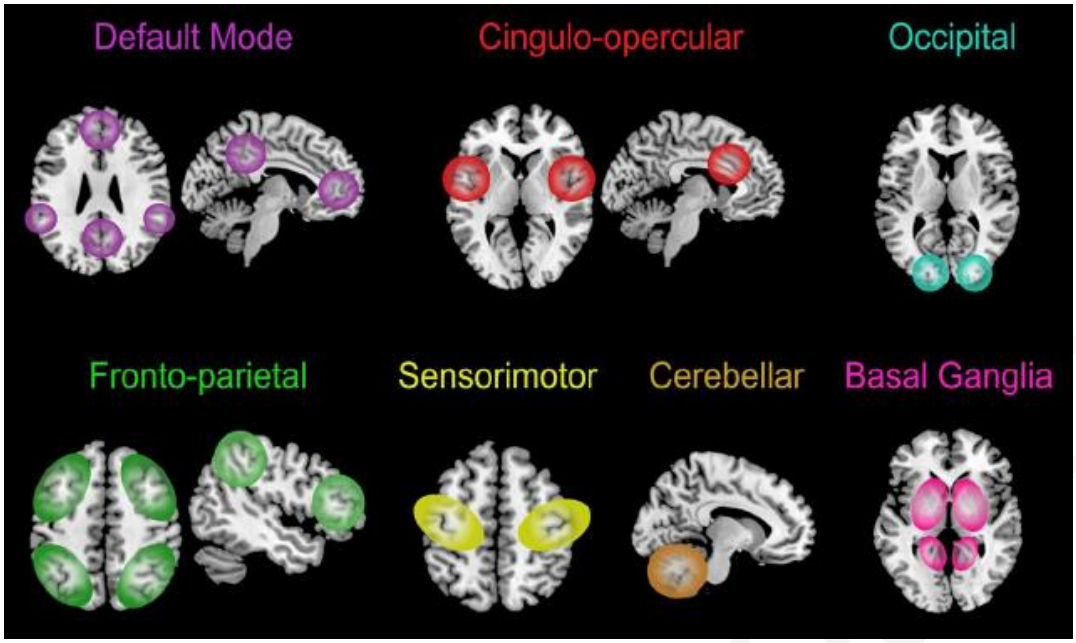

Figure 2.5. The principal, more widely investigated resting-state networks (Sedeno et al., 2014).

In particular, the first-discovered and most studied RSN is the DMN, which was identified from PET data by Raichle et al., 2001. It includes the posterior and anterior cingulate cortex (PCC and ACC), the thalamus, the medial prefrontal cortex (mPFC) and the precuneus, regions that are known to show a high level of neuronal activity during rest and a deactivation in physiological conditions during the execution of cognitive tasks. This suggests that activity in this network reflects a default state of neuronal activity of the human brain (Gusnard et al., 2001; Raichle et al., 2001; Raichle and Snyder, 2007).

2.2.1 Functional connectivity analysis methods

The lack of an *a priori* hypothesis about the brain activation (no specific task during acquisition) makes the RS-fMRI data analysis more challenging than task-based fMRI. In the next sub-section, the most widely used methods for analyzing RS-fMRI FC will be described.

2.2.1.1 Seed-based Analysis

One of the most widely used method for the analysis of the FC in RS-fMRI is called either seed-based or voxel-based analysis (hereinafter called seed-based). This approach, introduced by Biswal et al., 1995, has been widely used by many researchers (Raichle et al., 2001; Fox et al., 2005; Cordes et al., 2000; Taylor et al., 2009; Di Martino et al., 2008;

Andrews-Hanna et al., 2007). Standard seed-based analysis is performed by first selecting one seed voxel or region for the primary ROI. Then this selected voxel/region is correlated with the other voxels of the brain in order to evaluate the similarity of its average time course with each other area or single voxel in the brain. The result is a map of brain voxels significantly correlated with the chosen seed ROI (Golestani and Goodyear, 2011) (see Figure 2.6).

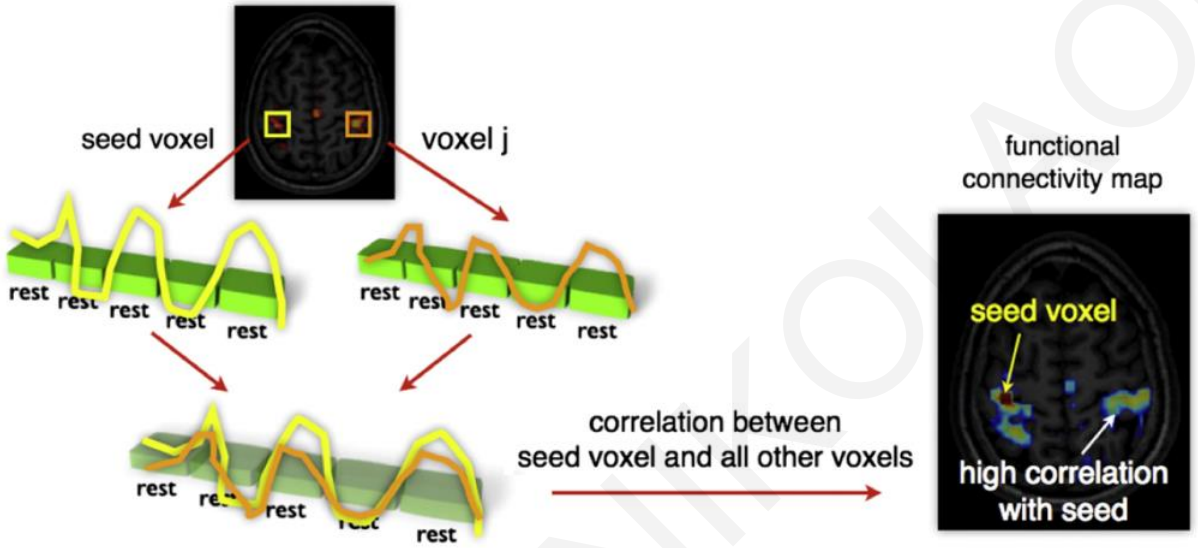

Figure 2.6. Seed-based FC: To examine the level of functional connectivity between the selected seed voxel and a second brain region j, the RS time series of the seed voxel is correlated with the RS time series of region j. A significant correlation between the time series of ROI and voxel j reflects a significant level of FC between these regions. Furthermore, to map out all functional connections of the selected seed region, the time series of the seed voxel can be correlated with the time series of all other voxels in the brain, resulting in a functional connectivity map that reflects the regions that show a high level of functional connectivity with the selected seed region (Van Den Heuvel and Hulshoff Pol, 2010).

Seed-based correlation has developed into a powerful, easily interpretable, and effective tool in identifying and characterizing the brain areas that show activity during RS. Nevertheless, the networks obtained from the seed-based method highly depend on the way the seed regions are initially defined (Cole et al., 2010). Typically, seeds are chosen based on *a priori* knowledge about the location of brain activity during a task (Biswal et al., 1995; Xiong et al., 1999), using anatomical images as a guide (Di Martino et al., 2008; Taylor et al., 2009), or based on standardized coordinates (Maldjian et al., 2003). However, the anatomical volume of known regions may vary between subjects, in the presence of a neurological disease, or may change with aging, and functional boundaries of brain regions may not be well-defined. Hence,

using this approach may result in the inclusion of undesired voxels, or the exclusion of functionally relevant ones. Moreover, the seed-based method only evaluates the relationship between the brain and the seed and considers one seed at a time, while, in absence of an a priori hypothesis, it might be more informative to simultaneously detect and characterize various RSNs from a single RS-fMRI acquisition.

2.2.1.2 Principal Component Analysis (PCA)

Principal Component Analysis (PCA) is a classic technique for data reduction, feature extraction and statistical data analysis. PCA works by finding an orthogonal basis for its given data. The first eigenvector, which is taken as the first principal component, gives the direction of maximum variance in the data. Given a set of multivariate measurements, the purpose is to find a smaller set of variables with less redundancy (the redundancy is measured by correlations between data elements) that would give the best representation possible. This solution, discarding a subset of the components, provides a reduction of the data size and eliminates most of the random noise prior to analysis (Friston et al., 1995; Strother et al, 1997; Laconte et al., 2003). The most important goal of PCA is to reduce the dimensionality of the original dataset. Therefore, PCA is often used as a pre-processing step for other data-driven analysis methods such as clustering and ICA. A pioneering work in functional connectivity using PCA was done by Friston et al., 1994. They defined time-series functional connectivity as temporal correlations between spatially remote neurophysiological events. They modeled a connected brain system as a pattern of activity in terms of correlations or covariance and used PCA analysis to assess functional connectivity during a verbal test.

2.2.1.3 Independent Component Analysis (ICA)

Independent component analysis (ICA) (Beckmann et al., 2005; De Luca et al., 2006; Smith et al., 2009) is another powerful and popular approach in the field of functional neuroimaging for investigating general connectivity patterns across brain regions. ICA aims to discover the underlying structure of the data rather than impose an *a priori* knowledge on the model, with a blind separation of meaningful sources. Unlike the seed-based approach, only a few *a priori* assumptions are required.

ICA was firstly introduced by McKeown (McKeown et al., 1998) as an fMRI analysis method able to use decomposition into spatially independent components (see Figure 2.7) to

distinguish between non-task-related signal components, movements and other artefacts, as well as task-related activations. From a clinical perspective, it was established that psychomotor functions are performed in localized brain areas and these can be inferred from specific deficits in patients. This led to the assumption that brain areas that respond to a psychomotor task are independently distributed from brain areas affected by other sources of variability. This does not require these areas to be completely non-overlapping, but only that other sources of signal change are not distributed in the same way as the task-related areas, i.e. that knowledge about the spatial distribution of one does not provide any information on the spatial distribution of the other (Beckmann, 2012).

Next, the general formulation of ICA will be introduced in the context of its application to RS-fMRI analysis.

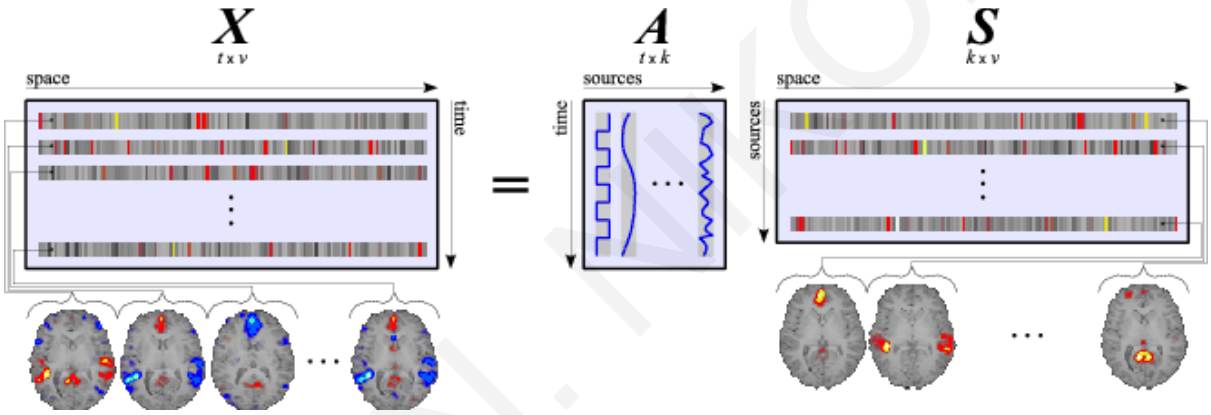

Figure 2.7. Spatial ICA of fMRI data: The rows of the data matrix X and sources matrix S are vectorized volumes. The corresponding columns of the mixing matrix A are the time-courses. Note, that the statistical independence applies to the volumes (Calhoun et al., 2003).

2.2.1.3.1 ICA Formulation

The ICA model can be expressed as:

$$\boldsymbol{X} = \boldsymbol{AS} \tag{2.1}$$

where the data that were obtained from fMRI, are represented by the $\boldsymbol{t} \times \boldsymbol{v}$ matrix $\boldsymbol{X}$ (where $\boldsymbol{v}$ is the number of voxels belonging to the volume analyzed at $\boldsymbol{t}$ different time points), the matrix $\boldsymbol{S}$ contains statistically independent spatial maps in its rows (which are the spatial areas in the brain, each with an internally consistent temporal dynamic) (Beckmann, 2012), and $\boldsymbol{A}$ is the mixing matrix which contains in its columns the time courses associated to the maps. The sources $\boldsymbol{S}$ are estimated by iteratively optimizing the unmixing matrix $\boldsymbol{W} = \boldsymbol{A}^{-1}$, so that

$\boldsymbol{S = WX}$ contains mutually independent rows, using the information-maximization (Infomax) algorithm (Bell and Sejnowski, 1995).

An extension of the Independent Component Analysis is the probabilistic ICA (pICA) model, which assumes that the t-dimensional vectors of observations (time series) are generated from a set of $q < t$ (i.e., there are fewer source processes than observations in time) statistically independent non-Gaussian sources (spatial maps) via a linear and instantaneous "mixing" process corrupted by additive Gaussian noise, $\eta(t)$:

$$\boldsymbol{x_i = As_i + \mu + \eta_i} \quad \textbf{(2.2)}$$

where x_i denotes the individual measurements at voxel location *i*, s_i denotes the non-Gaussian source signals contained in the data and η_i denoted Gaussian noise $\eta_i \sim N(0, \sigma^2 \Sigma_i)$. The vector μ defines the mean of the observations x_i and the matrix A $t \times q$ is assumed to be non-degenerate, i.e. of rank q. Solving the blind separation problem requires finding a linear transformation matrix $\boldsymbol{W}$ such that $\hat{\boldsymbol{s}} = \boldsymbol{Wx}$ is a good approximation to the true source signals $\boldsymbol{s}$ (Beckmann, 2012). The detailed steps involved in estimating the pICA model, described by Beckmann and Smith (2004), implemented in the FSL's tool MELODIC (www.fmrib.ox.ac.uk/fsl/, University of Oxford), and used in this thesis, are schematically illustrated in figure 2.8.

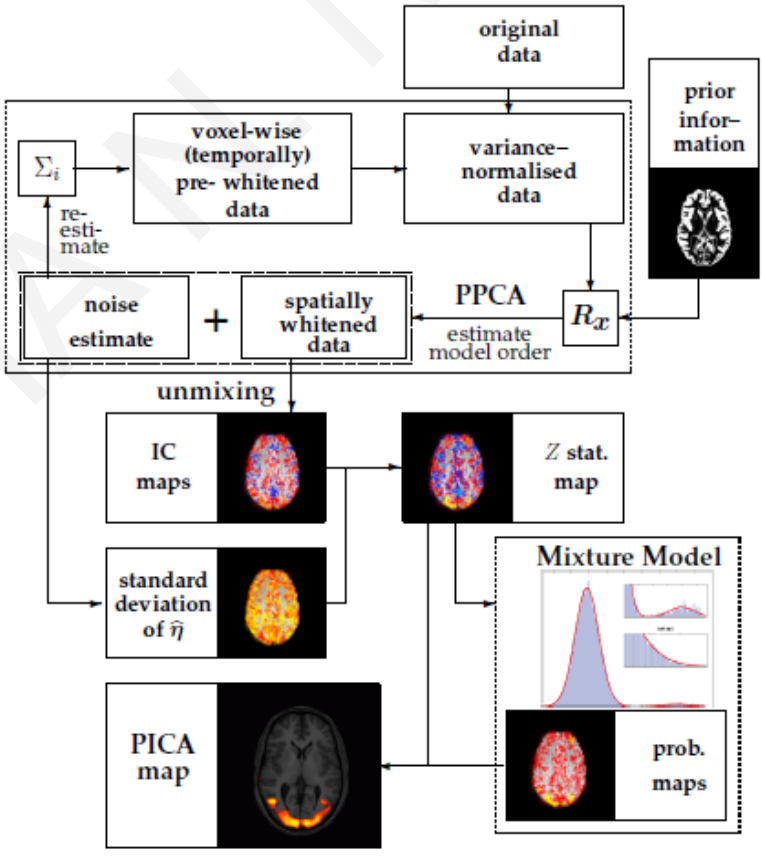

Figure 2.8. Schematic view of the probabilistic ICA model (Beckmann and Smith, 2004).

As mentioned earlier, compared with seed-based methods, ICA has the advantage of requiring few *a priori* assumptions but does require the user to manually select the important components and distinguish noise from physiological signals. Despite the differences in the two approaches, the overall results obtained using seed-based analysis and ICA were found to be similar in a group of healthy volunteers.

2.2.1.4 Network analysis

A complementary method to seed-based and model-free (such as ICA) analyses for investigating functional connectivity of the brain using RS-fMRI is network analysis. In particular, one area of rapidly increasing interest is the mapping of functional networks. This kind of mapping starts by identifying a set of functional "nodes", and then attempts to estimate the set of connections or "edges" between these nodes based on the analysis of the fMRI time series associated with the nodes (Smith et al., 2011; Smith, 2012; Rubinov and Sporns, 2010).

There are several methods for defining network nodes using fMRI. Some of these methods define the nodes according to the spatial regions of interest, as obtained from task-fMRI activation or from brain atlases. Alternatively, parcellation via a data-driven clustering of the fMRI data itself (e.g., hierarchical clustering or ICA) can be run in order to define clusters or components (spatial maps with associated timecourses), which can be considered network nodes.

Once the nodes are defined, each has its own associated timecourse (e.g., the average time series from all voxels within the node). These are then used to estimate the connections (edges) between nodes: in general, the more similar the timecourses are between any given pair of nodes, the more likely it is that there is a functional connection between those nodes. The simplest measure for estimating the connection between nodes is cross-correlation, which, however, neither implies causality (in itself it tells one nothing about the direction of information flow), nor determines whether the functional connection between two nodes is direct (there may be a third node "in-between" the two under consideration, or a third node may be feeding into the two, without a direct, or even causally-indirect, connection existing between them).

While the interest in this field is growing and the approaches are many, the scope of network-related research almost falls onto a one-dimensional continuum that starts with neural-level simulations at one end, passes through network modelling methods that are applied to

real fMRI data, and ends with the most abstract of the graph-theoretic summaries of a network matrix (Figure 2.9). The various dissimilarity between the different sections relate to many of the respective advantages and weaknesses of different analyses, and also inform some thoughts about valuable future directions (Smith, 2012).

To summarize, complementing the widely used RS-fMRI analytic methods (e.g. seed-based functional connectivity and ICA), the graph based network analyses allow us not only to visualize the overall connectivity pattern among all the elements of the brain (e.g., brain regions) but also to quantitatively characterize the global organization using a set of summative measures such as network degree and clustering coefficient (Rubinov and Sporns, 2010).

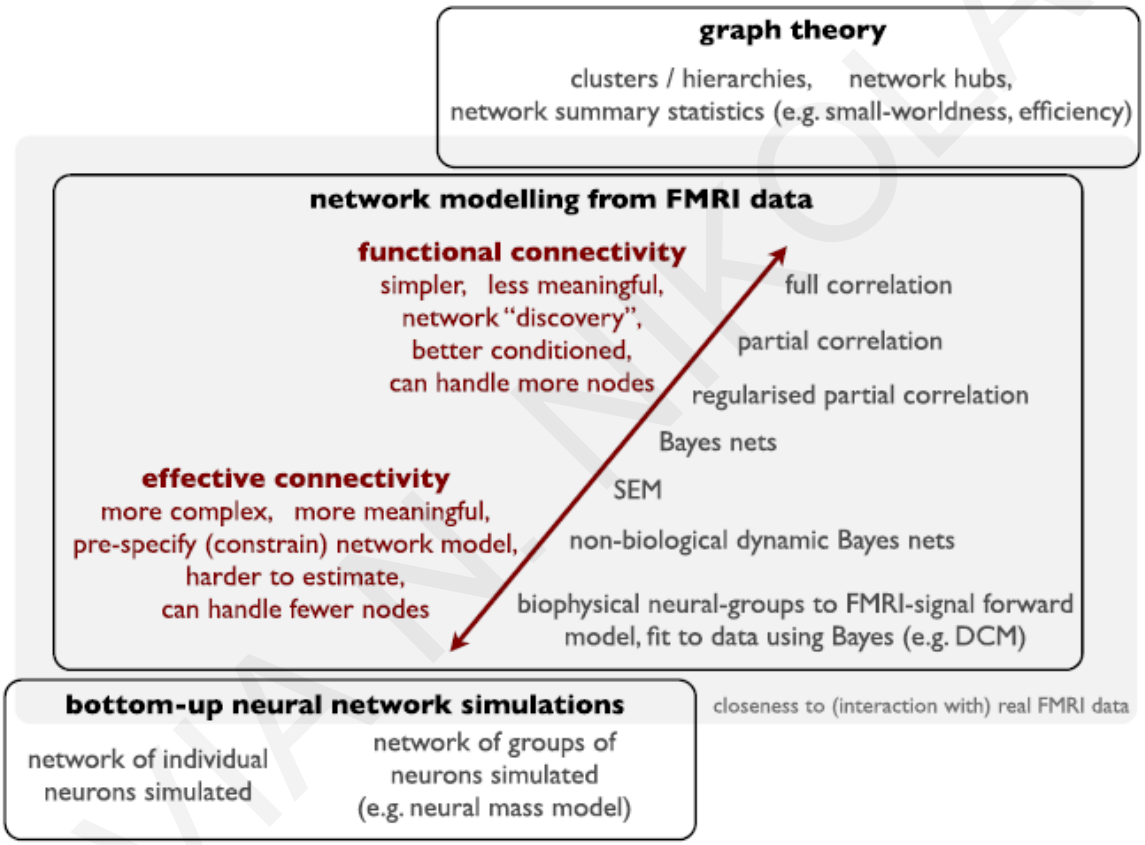

Figure 2.9. Oversimplified schematic of relationships between various network modelling analyses for/from fMRI (Smith, 2012).

2.2.2 Assessment of Functional Connectivity

Correlation is a statistical measure that indicates the strength of association between two variables and the direction of the relationship. In terms of the strength of the relationship, the value of the correlation coefficient varies between +1 and -1. When the value of the correlation coefficient lies around ± 1, then it is said to reflect a perfect degree of linear

association between the two variables. As the correlation coefficient value goes towards 0, the relationship between the two variables will be weaker. The direction of the relationship is simply the sign of the correlation; with "+" indicating a positive relationship between the variables (when one variable increases the other variable increases) and with "-" indicating a negative relationship between the variables (when one variable increases the other variable decreases). The three most common correlation indices used in the literature are: Pearson correlation, Kendall rank correlation and Spearman correlation, explained next.

2.2.2.1 Pearson Correlation

Pearson's $\boldsymbol{r}$ correlation is the most widely used correlation statistic to measure the degree of the relationship between linearly related variables. For example, if we want to measure how two fMRI series are related to each other, Pearson's $\boldsymbol{r}$ correlation is used to measure the degree of relationship between the two. The following formula is used to calculate the Pearson $\boldsymbol{r}$ correlation:

$$\boldsymbol{r} = \frac{\sum_{i=1}^{n}(\boldsymbol{x_i} - \overline{\boldsymbol{x}})(\boldsymbol{y_i} - \overline{\boldsymbol{y}})}{\sqrt{\sum_{i=1}^{n}(\boldsymbol{x_i} - \overline{\boldsymbol{x}})^2 \sum_{i=1}^{n}(\boldsymbol{y_i} - \overline{\boldsymbol{y}})^2}} \quad \textbf{(2.3)}$$

where $\boldsymbol{r}$ is the Pearson $\boldsymbol{r}$ correlation coefficient, *N* is the number of observations in each data set, $\overline{\boldsymbol{x}}$ denotes the mean value of **x** timeseries and $\overline{\boldsymbol{y}}$ denotes the mean values of **y** timeseries.

For the Pearson $\boldsymbol{r}$ correlation, both variables should be normally distributed. Other assumptions include linearity and homoscedasticity. Linearity assumes a straight-line relationship between each of the variables in the analysis and homoscedasticity assumes that data is normally distributed about the regression line (Kelley, 2007).

2.2.2.2 Kendall rank Correlation

Kendall rank correlation is a non-parametric measure that quantifies the strength of dependence between two variables. If we consider two samples, **x** and **y**, where each sample size is *n*, we know that the total number of pairings with **x** and **y** is ½*n*(*n*-1). The following formula is used to calculate the value of Kendall rank correlation:

$$\boldsymbol{\tau} = \frac{\boldsymbol{n_c} - \boldsymbol{n_d}}{\frac{\mathbf{1}}{\mathbf{2}}\boldsymbol{n}(\boldsymbol{n} - \mathbf{1})} \quad \textbf{(2.4)}$$

where $\boldsymbol{n_c}$ is the number of concordant (ordered in the same way) and $\boldsymbol{n_d}$ is the Number of discordant (ordered differently) (Kelley, 2007).

Specifically, let $(\boldsymbol{x_1}, \boldsymbol{y_1})$, $(\boldsymbol{x_2}, \boldsymbol{y_2})$, …, $(\boldsymbol{x_n}, \boldsymbol{y_n})$ be a set of observations from the two data samples **x** and **y**, such that all the values of $(\boldsymbol{x_i})$ and $(\boldsymbol{y_i})$ are unique. Any pair of observations $(\boldsymbol{x_i}, \boldsymbol{y_i})$ and $(\boldsymbol{x_j}, \boldsymbol{y_j})$, where $i \neq j$, are said to be concordant, if both $\boldsymbol{x_i} < \boldsymbol{x_j}$ and $\boldsymbol{y_i} < \boldsymbol{y_j}$ or if both $\boldsymbol{x_i} > \boldsymbol{x_j}$ and $\boldsymbol{y_i} > \boldsymbol{y_j}$. They are said to be discordant, if $\boldsymbol{x_i} < \boldsymbol{x_j}$ and $\boldsymbol{y_i} > \boldsymbol{y_j}$; or $\boldsymbol{x_i} > \boldsymbol{x_j}$ and $\boldsymbol{y_i} < \boldsymbol{y_j}$. If $\boldsymbol{x_i} = \boldsymbol{x_j}$ and $\boldsymbol{y_i} = \boldsymbol{y_j}$, the pair is neither concordant nor discordant.

2.2.2.3 Spearman rank Correlation

Spearman rank correlation is also a non-parametric measure that is used to quantify the degree of association between two variables. Spearman rank correlation is not based on any assumptions about the distribution of the data and is the appropriate correlation analysis when the variables are measured on a scale that is at least ordinal.

The following formula is used to calculate the Spearman rank correlation:

$$\boldsymbol{\rho = 1 - \frac{6 \sum d_i^2}{n(n^2 - 1)}} \qquad \textbf{(2.5)}$$

where $\boldsymbol{\rho}$ is the Spearman rank correlation, $\boldsymbol{d_i}$ is the difference between the ranks of corresponding values $\boldsymbol{X_i}$ and $\boldsymbol{Y_i}$ and $\boldsymbol{n}$ is the number of value in each dataset (Kelley, 2007). Ranking is achieved by assigning the ranking '1' to the biggest number in a timeseries, '2' to the second biggest value and so on. The smallest value in the timeseries will get the lowest ranking. This should be done for both sets of measurements.

In practice, a general rule for non-parametric tests is to use Spearman's correlation for n<30 if there are no expected differences in ranks or outliers; otherwise, Kendall's correlation is preferred. For n>30, either Spearman's or Kendall's correlation is acceptable, however, Spearman's coefficient may perform better that Kendall for a large n and is easier to calculate (Kelley, 2007).

2.3 Dynamic Functional Connectivity

Resting functional connectivity has been demonstrated to change over a short time (Chang and Glover, 2010), implying that measures assuming stationarity over a full RS scan

may be too simplistic to capture the full extent of RS activity. Dynamic functional connectivity (DFC) is an extension of conventional functional connectivity analysis, which assumes that functional networks are not stationary in time. The most straightforward strategy to investigate DFC is to segment the timeseries from ROIs into a set of temporal windows, inside which their pairwise connectivity is assessed (Figure 2.10). As a consequence, by gathering FC descriptive measures over subsequent windows, fluctuations in connectivity can be captured.

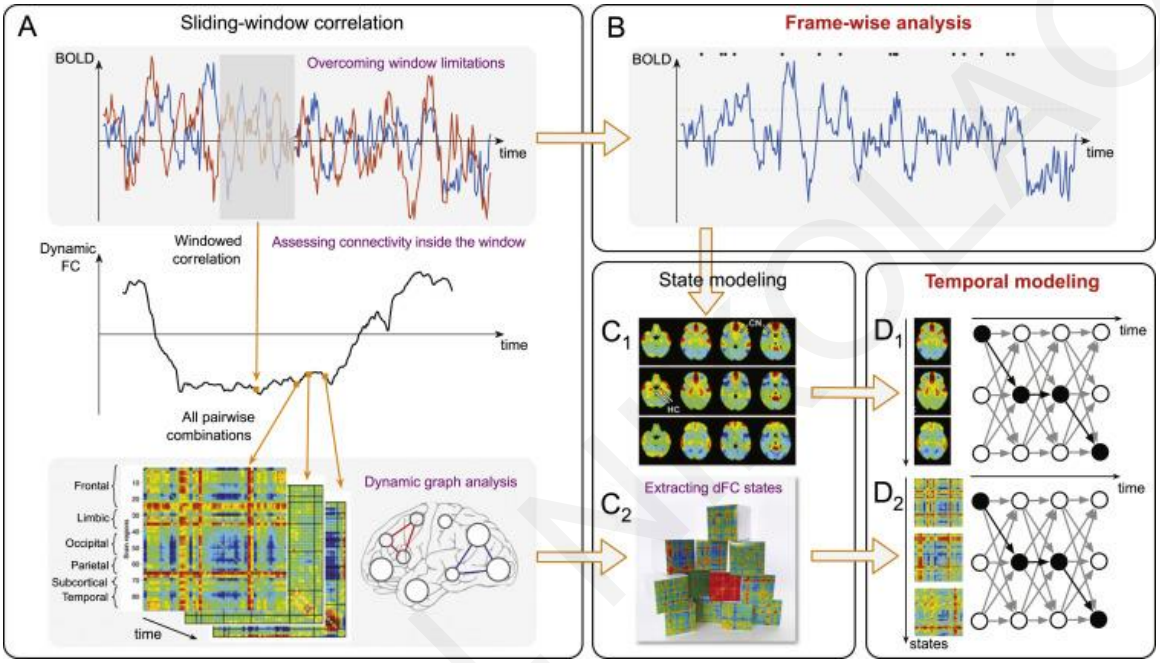

Figure 2.10. Summary figure of existing DFC analytical strategies. (A) Sliding-window correlation, where the connectivity between brain regions is computed as correlation coefficients. This computation is repeated iteratively, shifting the window by a specific step every time, to generate a connectivity timeseries (middle panel). Performing this procedure for all connections yields one connectivity matrix per window, i.e. a dynamic characterization of whole-brain connectivity (lower left panel). (B) Frame-wise description of timecourses, where only moments when the BOLD signal exceeds a threshold are retained for the analysis. These frames can be used for the generation of voxel wise brain states (C_1), the co-activation patterns (CAPs). Alternatively, the connectivity matrices obtained from (A) can be used to retrieve DFC states (C_2). Through temporal modeling, parameters describing CAPs (D_1) or connectivity states (D_2) and their relationship can be inferred. (Preti et al., 2016)

2.3.1 Dynamic Connectivity Analysis Methods

2.3.1.1 Sliding window analysis

Sliding window analysis is currently the most popular technique for examining dynamics in resting state FC (Chang and Glover, 2010; Handwerker et al., 2012; Jones et al.,

2012; Kiviniemi et al., 2011; Sakoglu et al., 2010; Hutchison et al., 2013; Karahanoglu and van De Ville, 2017). In this technique, a time window of a specific length is chosen, and data points of the first time-series within that window are correlated with the data points of another time-series in the same window in order to calculate the FC metric of interest. The window is then shifted in time by a fixed number of data points, and the process is repeated for the entire scan length. This technique (see Figure 2.11) results in the quantification of the time-varying behavior of the chosen metric over the duration of the scan. When all windows are considered, a set of connectivity matrices—a dynamic functional connectome—recapitulating the temporal evolution of whole-brain functional connectivity- is obtained.

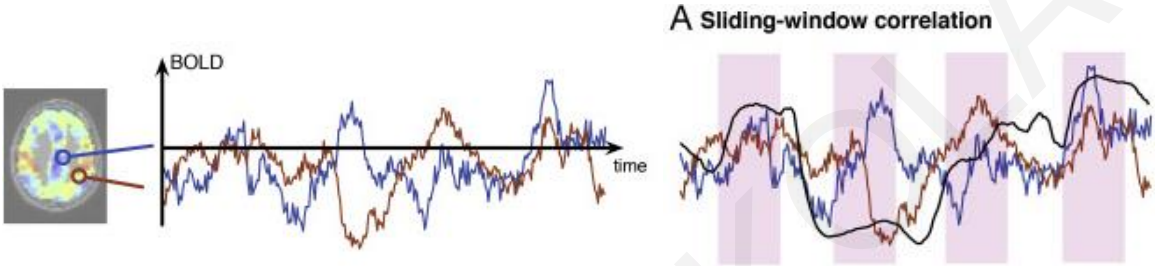

Figure 2.11. Visualization of dynamic functional connectivity (DFC) analysis on two brain regions (Karahanoglu and van De Ville, 2017).

2.3.1.2 Dynamic Graph Analysis

Graph theory is a popular technique to extract information from DFC, where large-scale measures characterizing the architecture and the information flow of the brain functional network are derived (Bullmore and Sporns, 2009). Using this approach, many different quantities can be extracted, each informing on a particular aspect of the network (Rubinov and Sporns, 2010).

Network analysis is applied separately to each generated connectivity matrix in order to make these metrics dynamic, yielding timecourses of graph measures. Note that a dependence use between graph metrics of subsequent windows can also be modeled, for example imposing a specific smoothness over time (Mucha et al., 2010). It turns out that strong fluctuations over time occur across diverse graph metrics (Tagliazucchi et al., 2012), highlighting a continuous functional reorganization of the brain regarding different network features.

The most recent efforts to understand this phenomenon have been relying on three metrics in particular: network degree, which is the most straightforward way to quantify overall

functional connectivity in a network, as it is an overall index of how "connected" the network is, efficiency, which describes the ease with which a signal can travel from one brain region to another, and modularity, which quantifies the extent to which the network is organized into a set of compact communities with few inter-classes connections (Clauset et al., 2004). Zalesky et al. (2014) reported moments of high efficiency that predominantly concerned remote brain regions; at the same time, the most dynamic connections over time were the ones linking different brain networks. Betzel et al. (2016) observed large variations of modularity, which was strong in periods when a large number of strong connections could be detected.

2.3.1.3 Time Frequency Analysis – Wavelet Transform

Wavelet methods are widely used to decompose fMRI signals into time series representing neurophysiological activity in fixed frequency bands. Using these time series, one can estimate frequency-band specific functional connectivity between sensors or regions of interest, and thereby construct functional brain networks that can be examined from a graph theoretic perspective.

Wavelets are scaled and shifted versions of a mother wavelet function, whose properties are discussed below. Wavelet analysis is similar to Fourier analysis (Xu and Chan 2002) in the sense that it decomposes a signal down into its basic constituent components. Whereas the Fourier transform represents the signal as a series of sine waves of different frequencies, the wavelet transform represents signals as linear combinations of wavelets. There are differences between the trigonometric and wavelet base signal representations. In comparison to the smooth and infinitely periodic sine wave decomposition, the wavelet representation is irregular (often fractal) in shape and uses compactly supported base functions. These properties of irregularity in shape and compact supportedness make wavelets a useful tool for analyzing non-stationary signals. Their irregular shape lends them to analyzing signals with discontinuities or sharp changes, while their compactly supported nature enables temporal localization of signal features (Daubechies, 1992).

2.3.1.3.1 Continuous Wavelet Transform

Mathematically, the continuous wavelet transform (CWT) computes the inner products of a continuous signal with a set of continuous wavelets according to the following equation:

$$\boldsymbol{WT_{u,a} = \langle s, \Psi_{u,a} \rangle = \int_{-\infty}^{+\infty} s(t)\, \Psi^{*}_{u,a}(t) dt} \quad \textbf{(2.6)}$$

and

$$\boldsymbol{\Psi_{u,a}(t) = \frac{1}{\sqrt{a}} \Psi \left(\frac{t-u}{a} \right)} \quad \textbf{(2.7)}$$

where $\boldsymbol{WT_{u,a}}$ are the resulting wavelet coefficients. $\boldsymbol{\Psi_{u,a}}$ denotes a continuous wavelet, where *u* is the shift factor and *a* is the scale factor of the wavelet. $\boldsymbol{\Psi^{*}_{u,a}}$ is the complex conjugate of $\boldsymbol{\Psi_{u,a}}$. For the continuous-time signal $\boldsymbol{s(t)}$, the scale factor must be a positive real number, whereas the shift factor can be any real number. If the continuous wavelet $\boldsymbol{\Psi_{u,a}}$ meets the admissibility condition ($\boldsymbol{0 = \Psi(0) = \int \psi(x) dx}$), the computed wavelet coefficients can be used to reconstruct the original signal $\boldsymbol{s(t)}$.

2.3.1.3.2 Discrete Wavelet Transform

The discrete wavelet transform (DWT) is not exactly a discrete version of the continuous wavelet transform (CWT). Instead, the DWT is functionally different from the CWT. To implement the DWT, discrete filter banks are used to compute discrete wavelet coefficients. Two-channel perfect reconstruction (PR) filter banks are a common and efficient way to implement the DWT.

The signal ***X(z)*** first is filtered by a filter bank consisting of $\boldsymbol{G_0(z)}$ (lowpass filter) and $\boldsymbol{G_1(z)}$ (high-pass filter) (Fig. 2.12). The outputs of $\boldsymbol{G_0(z)}$ and $\boldsymbol{G_1(z)}$ then are down sampled by a factor of ***2***. After some processing, the modified signals are up sampled by a factor of ***2*** and filtered by another filter bank consisting of $\boldsymbol{H_0(z)}$ (lowpass filter) and $\boldsymbol{H_1(z)}$ (high-pass filter) (Fig. 2.12). If no processing takes place between the two filter banks, the sum of outputs of $\boldsymbol{H_0(z)}$ and $\boldsymbol{H_1(z)}$ is identical to the original signal ***X(z)***, except for the time delay. This system is a two-channel PR filter bank, where $\boldsymbol{G_0(z)}$ and $\boldsymbol{G_1(z)}$ form an analysis filter bank, and $\boldsymbol{H_0(z)}$ and $\boldsymbol{H_1(z)}$ form a synthesis filter bank.

As mentioned above, traditionally, $\boldsymbol{G_0(z)}$ and $\boldsymbol{H_0(z)}$ are lowpass filters, and $\boldsymbol{G_1(z)}$ and $\boldsymbol{H_1(z)}$ are high-pass filters. Therefore, the subscripts 0 and 1 represent lowpass and high-pass filters respectively. The operation $\boldsymbol{\downarrow 2}$ denotes a decimation of the signal by a factor of two. Applying decimation factors to the signal ensures that the number of output samples of the two lowpass filters equal the number of original input samples $\boldsymbol{X(z)}$. Therefore, no redundant

information is added during the decomposition. The two-channel PR filter bank system can be used to consecutively decompose the outputs of the lowpass filters, as shown in the following figure.

Lowpass filters remove high-frequency fluctuations from the signal and preserve slow trends. The outputs of lowpass filters provide an approximation of the signal. High-pass filters remove the slow trends from the signal and preserve high-frequency fluctuations. The outputs of high-pass filters provide detail information about the signal. The outputs of lowpass filters and high-pass filters define the approximation coefficients and detail coefficients, respectively. The symbols ***A*** and ***D*** in Figure 2.12 denote approximation and detail respectively. The detail coefficients are also termed *wavelet coefficients* because they approximate the inner products of the signal and the corresponding wavelets.

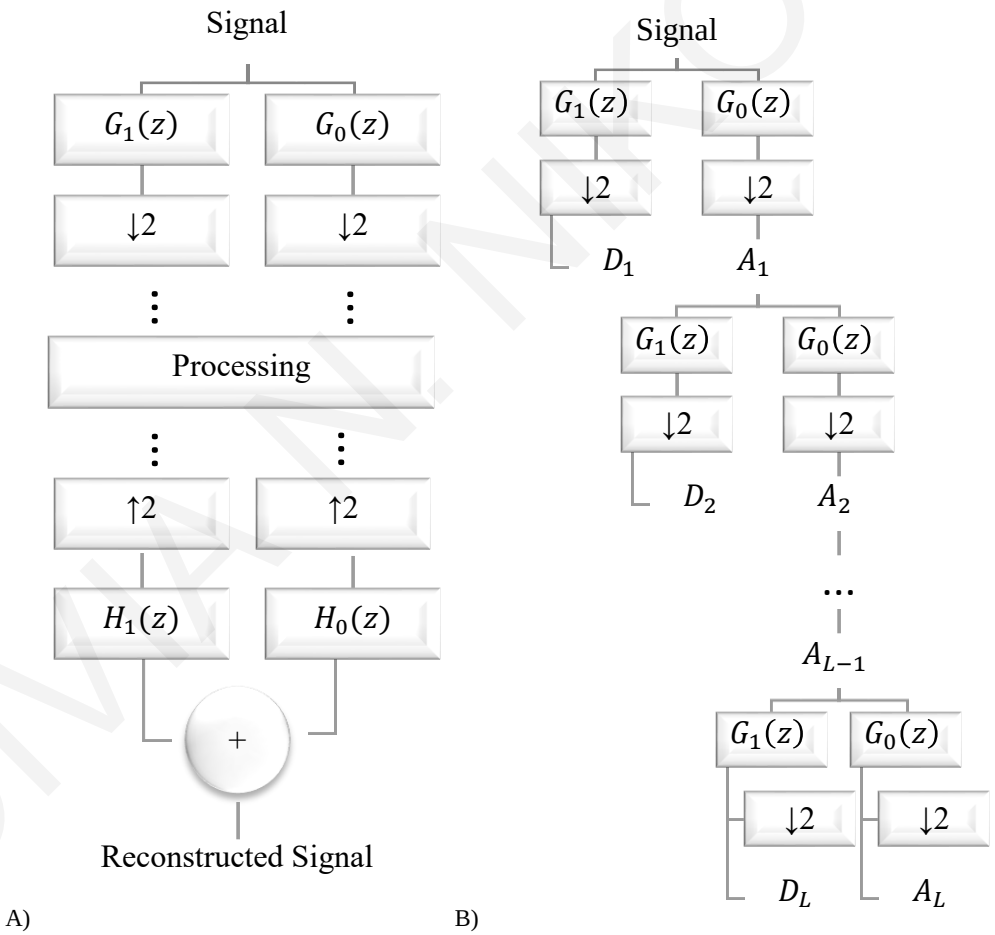

Figure 2.12. Discrete Wavelet Transform: A) Typical two-channel PR filter bank system to implement DWT. B) Decompose the output of low pass filter for redundant information suppression.

2.4 Effects of Physiological Signals on BOLD fMRI

In this section, the theoretical and physiological background of the effects of the physiological signals related to cardiovascular and respiratory processes on the fMRI BOLD signal in specific RSNs are discussed.

As previously mentioned, while fMRI is widely employed to study spatial and temporal patterns of neural activity (Bandettini et al., 1992; Kwong et al., 1992; Ogawa et al.,1992), the blood-oxygen level dependent (BOLD) signal measured by fMRI is also influenced by the effects of cardiovascular and respiratory processes (Biswal et al., 1993; Dagli et al., 1999; Jezzard et al., 1993; Weisskoff et al., 1993). The physiological signals resulting from such processes can obscure neuronal signals because the physiological noise and neuronal signals can overlap in time, be anatomically co-localized, and have (or alias into) common temporal frequencies. It is therefore important to understand how physiological processes – which may be unrelated to neural activation – influence fMRI time series.

The respiratory process introduces noise into fMRI time series in several ways. Firstly, respiration causes modulation of the static magnetic field due to thoracic and abdominal movement, which, if uncorrected, results in distortion, blurring, or displacement of the image, depending on the k-space trajectory. Secondly, natural fluctuations in the depth and rate of breathing over the course of an fMRI scan may cause substantial BOLD signal fluctuations by directly modulating deoxyhemoglobin concentrations. The *respiration volume per time* (RVT), which quantifies respiratory variations using a pneumatic belt to measure breathing-related chest expansion, was demonstrated to have significant time-lagged correlations with fMRI time series (Birn et al., 2006). Importantly, the mapping between RVT and BOLD signal changes is significant across widespread regions of gray matter, thus impeding the detection of neural activation in response to many tasks, as well as altering correlations between brain regions (functional connectivity).

It is assumed that respiration modulates the BOLD signal primarily by inducing changes in levels of carbon dioxide (CO2), a potent vasodilator (Birn et al., 2006). This assumption is supported on several grounds: (1) the partial pressure of arterial CO2 (PaCO2) is a function of ventilation, which is defined as the product of the depth and rate of respiration (Berne and Levy, 1993); (2) inhaling elevated concentrations of CO2, as well as holding one's breath, initiates cerebral vasodilation leading to increased cerebral blood flow (CBF) and corresponding BOLD signal changes (Bandettini and Wong, 1997; Kastrup et al., 1999; Kwong et al., 1995; Li et al., 1999; Nakada et al., 2001; Rostrup et al., 2000; Stillman et al., 1995;

Vesely et al., 2001; Wise et al., 2007) (Figure 2.13); (3) spontaneous fluctuations in end-tidal CO2 (PETCO2) have been observed to correlate significantly with resting-state fMRI time series (Wise et al., 2004); (4) brain regions that correlated with PETCO2 in (Wise et al., 2004) appeared to be similar to those correlating with RVT in (Birn et al., 2006).

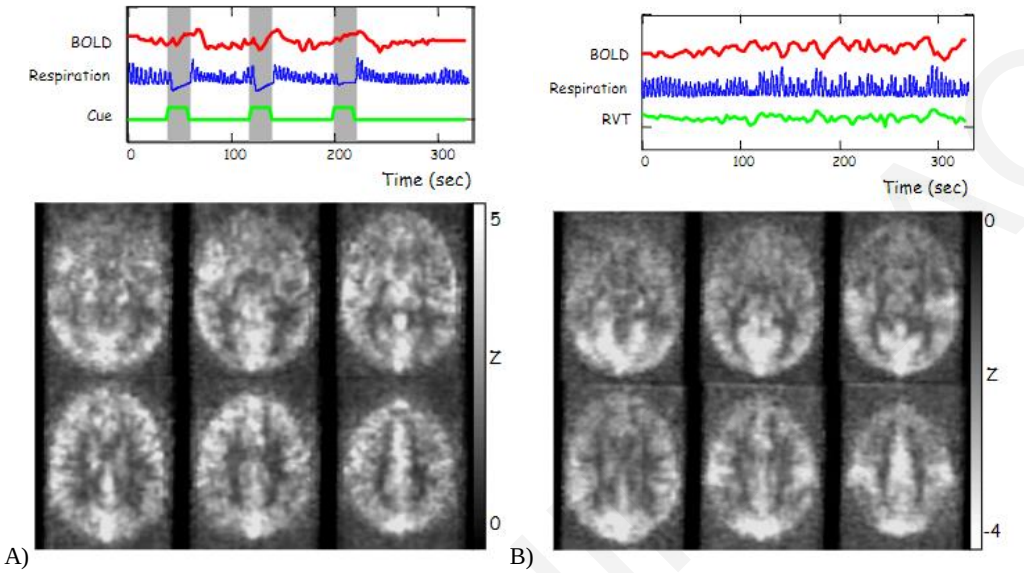

Figure 2.13. Respiration induces fMRI Signal Changes. A) Breath-Holding and B) Resting-State fMRI. (Birn et al., 2006)

Heart rate variability (HRV), defined as changes in the beat-to-beat interval or in the instantaneous heart rate, is a widely-used marker of autonomic activity (Task Force, 1996). HRV results from the interaction between parasympathetic (vagal) and sympathetic nervous system influences on the sinoatrial node (reviewed by (Berntson et al., 1997)). The high frequency (HF) component of HRV, spanning approximately the range 0.15–0.4 Hz, is attributed to respiration-induced heart rate modulation and is mediated primarily by parasympathetic outflow. A lower-frequency (LF) component of HRV, typically defined as 0.05–0.15 Hz, is not fully understood but believed to rather reflect a mixture of sympathetic and parasympathetic activities. The relative balance of parasympathetic and sympathetic influences can be modulated by breathing, physical activity (Bernardi et al., 1990), arousal, drug intake (Elghozi and Julien, 2007; Elghozi et al., 2001; Penttila et al., 2005) and more stable states such as mood or diseases involving the autonomous nervous system (ANS), such as cardiac ischemia (reviewed in Montano et al., 2009). These components of the HRV signal along with the fMRI signal can be seen in Figure 2.14. HRV is an important predictor of mortality (Huikuri et al., 2009), and decreased HRV is also one well-described symptom of

ANS dysregulation in depression (Kemp et al., 2010; Licht et al., 2008). States of different HRV levels can be readily connected to distinct states of ANS activity; e.g., HRV is modulated by emotionally salient contexts, with subsequent changes in sympathetic tone (Jonsson and SonnbyBorgstrom, 2003; Wallentin et al., 2011).

Finally, previous fMRI studies have also examined the neural basis of heart rate variability (HRV) changes, as well as its low frequency and high frequency power components, by measuring BOLD activity (Critchley et al., 2003; Napadow et al., 2008) and regional cerebral blood flow (rCBF; Gianaros et al., 2004; Lane et al., 2009) in relation to task induced emotional, physical, and cognitive changes in HRV. Results of a task-based study relating HRV to brain activation might be affected by the specific task, causing a coincidence of brain activation and changes in HRV.

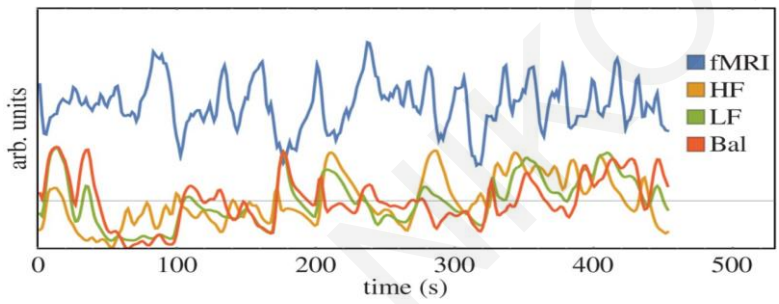

Figure 2.14. Example of the fMRI BOLD signal (blue solid line) and HRV regressors HF (parasympathetic – yellow solid line), LF ((sympathetic + parasympathetic) – green solid line) and Bal (sympathovagal balance – red solid line) for one healthy volunteer. (Duggento et al., 2016)

2.5 Hilbert Transform for extracting instantaneous LF and HF from HRV

As mentioned above, it is generally accepted that the activities of the autonomic nervous system (ANS), which consists of the sympathetic (SNS) and parasympathetic nervous systems (PNS), are reflected in the low- (LF) and high-frequency (HF) bands in HRV (Figure 2.15) - while the ratio of the powers in those frequency bands, the so called LF-HF ratio (LF/HF), has been used to quantify the degree of sympathovagal balance (Von Rosenberg et al., 2017).

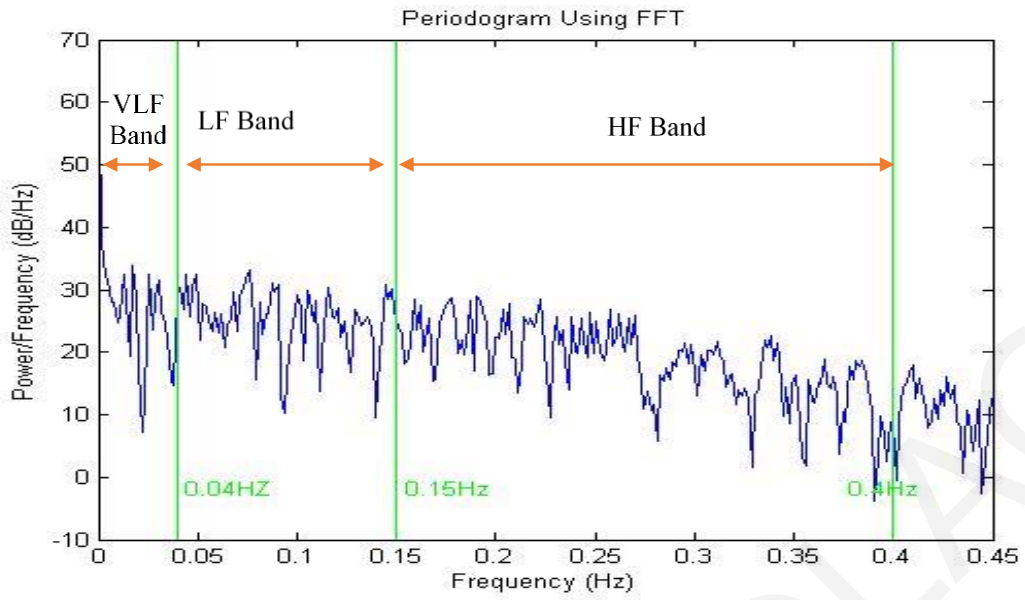

Figure 2.15. Spectral components of HRV: Power in different frequency bands corresponds to the function of the ANS. VLF-Very Low Frequency; LF-Low Frequency; HF-High Frequency.

The first step in order to extract the aforementioned frequency bands is to apply a bandpass filter to the HRV signal within the low (0.04-0.15Hz) and high (0.15-0.4Hz) frequency bands. Consequently the Hilbert transform can be applied to both the resulting time series in order to generate the corresponding complex analytic signals, which exhibit time varying amplitudes (Mandic et al., 2013; Looney et al., 2014; Hemakom et al., 2016), the so called instantaneous amplitude of the low frequency band (LFiA) and the instantaneous amplitude of the high frequency band (HFiA).

The Hilbert transform of a function $f(x)$ is defined by:

$$\boldsymbol{F(t) = \frac{1}{\pi}\int_{-\infty}^{+\infty}\frac{f(x)}{t-x}dx} \quad \textbf{(2.10)}$$

Theoretically, the integral is evaluated as a Cauchy principal value. Computationally one can write the Hilbert transform as the convolution:

$$\boldsymbol{F(t) = \frac{1}{\pi}f(t)} \quad \textbf{(2.11)}$$

which by the convolution theorem of Fourier transforms, may be evaluated as the product of the transform of $f(x)$ with $-i * sgn(x)$, where:

$$sgx(x) = \begin{cases} -1 & x < 0 \\ 0 & x = 0 \\ 1 & x > 0 \end{cases} \quad \textbf{(2.12)}$$

The Hilbert transform can be considered to be a filter which simply shifts phases of all frequency components of its input by -π/2 radians. An "analytic" (complex time) signal $\boldsymbol{Y(t)}$ can be constructed from a real-valued input signal $\boldsymbol{y(t)}$:

$$\boldsymbol{Y(t) = y(t) + jh(t)} \quad \textbf{(2.13)}$$

where $\boldsymbol{Y(t)}$ is the analytic signal constructed from $\boldsymbol{y(t)}$ and its Hilbert transform, $\boldsymbol{y(t)}$ is the input signal and $\boldsymbol{h(t)}$ is the Hilbert Transform of the input signal.

The real and imaginary parts can be expressed in polar coordinates as:

$$\boldsymbol{Y(t) = A(t)e^{j\psi(t)}} \quad \textbf{(2.14)}$$

where $\boldsymbol{A(t)}$ is the "envelope" or amplitude of the analytic signal and ψ is the phase of the analytic signal (the derivative of ψ is called the "instantaneous frequency"). Note that the Hilbert transform of a constant is zero. If the Hilbert transform is computed in more than one dimension and one of the dimensions does not vary (is a constant), the transform will be zero (or at least numerically close to zero).

2.6 General Linear Model

The general linear model (GLM) or multivariate regression model is a statistical linear model. It may be written as

$$\boldsymbol{Y = XB + U} \quad \textbf{(2.8)}$$

where $\boldsymbol{Y}$ is a matrix with series of multivariate measurements (each column being a set of measurements on one of the dependent variables), $\boldsymbol{X}$ is a matrix of observations on independent variables that might be a design matrix (each column being a set of observations on one of the independent variables), $\boldsymbol{B}$ is a matrix containing parameters that are usually estimated and $\boldsymbol{U}$ is a matrix containing errors (noise). The errors are usually assumed to be uncorrelated across measurements, and to follow a multivariate normal distribution. If the errors do not follow a multivariate normal distribution, generalized linear models may be used to relax assumptions about $\boldsymbol{Y}$ and $\boldsymbol{U}$.

The GLM is a generalization of multiple linear regression model to the case of more than one dependent variable. If $\boldsymbol{Y}$, $\boldsymbol{B}$, and $\boldsymbol{U}$ were column vectors, the matrix equation above would represent multiple linear regressions.

In the fMRI literature, the term "General Linear Model" refers to its univariate version. The term "univariate" does in this context not refer to the number of independent variables, but to the number of dependent variables. In its general form, the GLM has been defined for multiple dependent variables.

2.6.1 Multiple Linear Regression

Multiple linear regression is a generalization of linear regression by considering more than one independent variable, and a special case of general linear models formed by restricting the number of dependent variables to one. The basic model for linear regression is:

$$\boldsymbol{Y_i = \beta_0 + \beta_1 X_{i1} + \beta_2 X_{i2} + \cdots + \beta_p X_{ip} + \varepsilon_i} \quad \textbf{(2.9)}$$

In the formula above we consider n observations of one dependent variable and p independent variables. Thus, $\boldsymbol{Y_i}$ is the i^{th} observation of the dependent variable, $\boldsymbol{X_{ij}}$ is the i^{th} observation of the j^{th} independent variable where $j = 1,2,...,p$. The values $\boldsymbol{\beta_j}$ represent parameters to be estimated, and $\boldsymbol{\varepsilon_i}$ is the i^{th} independent identically distributed normal error.

3. Experimental Data and Processing Methods

In this chapter, all materials, pre-processing and processing steps used and applied in this research will be explained and analyzed in a comprehensive manner.

3.1 Experimental Data

The experimental data were collected at the Cardiff University Brain Imaging Centre (CUBRIC) for the purpose of investigating the resting state networks of the human brain. Twelve healthy volunteers (s03-s14) participated in these experiments, of which 5 were women and 7 were men with an average age of 29.2 ± 4.6. The experiments were approved by the Cardiff University School of Phycology Ethics and all volunteers yielded their written consent.

A 3T scanner (General Electric) was used to perform the imaging. During the resting-state scan, the volunteers were instructed to keep their eyes closed and not to fall asleep. Moreover, head movement was minimized with a bite bar.

For each volunteer, a T1-weighted FSGPR structural scan (91x109x91 voxels of 2x2x2mm) (Figure 3.1) was acquired and used to assist in placing individual volunteers' data into a common stereotactic space. In addition, for each volunteer, a functional scan (256x256x172 voxels of 1x1x1mm) (Figure 3.2) was acquired. The duration of the experiment was 630sec, corresponding to 210 timepoints (gradient echo EPI sequence, TR=3sec, TE=35ms, FOV/slice=20.5cm/3.2mm, flip=90º, 53 slices with 91x109x91 voxels of 3.2x3.2x3.2 mm).

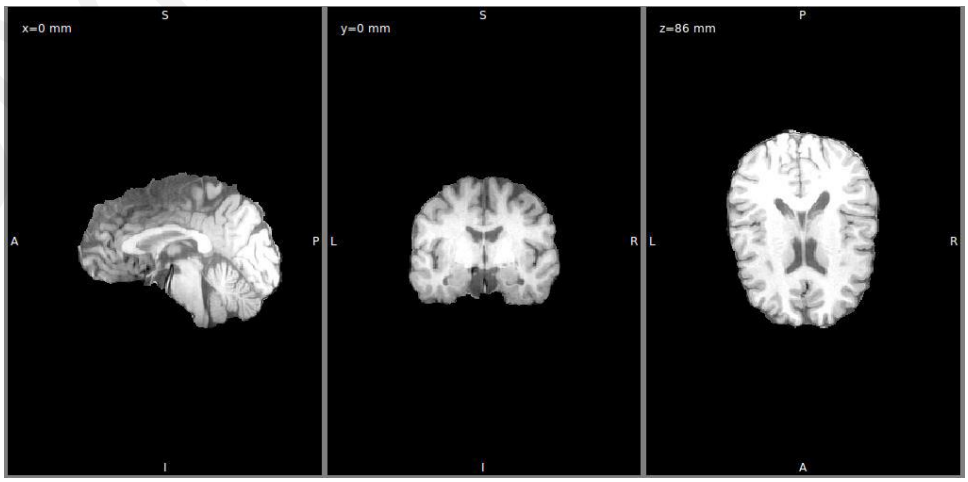

Figure 3.1. Anatomical Image (MRI) from one volunteer

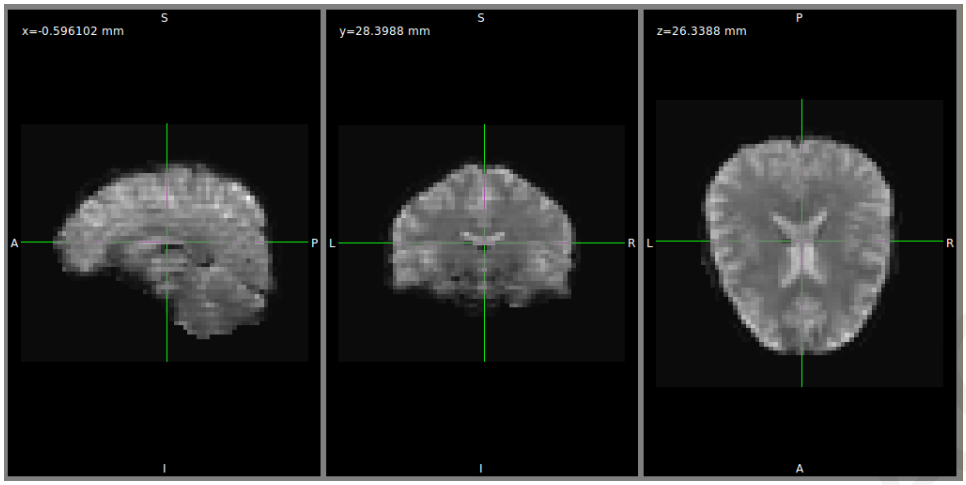

Figure 3.2. Functional Image (fMRI) from one volunteer

Physiological Signals

$PETCO_2$ and ECG signals were recorded in parallel to the scanning experiment (Figure 3.3). $PETCO_2$ was recorded using a nasal cannula attached to a gas analyser (AEI Technologies). ECG waveforms obtained during the scan were used to extract the HR and HRV signals (Figure 3.3). Specifically, before initiating the computation of these signals, the raw signal quality was checked by using a Signal Quality Index (SQI) which labels every ten seconds of data as "reliable" or "unreliable", based on a set of physiologically-relevant checks, followed by QRS template matching (Orphanidou et al., 2015). For the subsequent computation and analysis, only time series which were labeled as "reliable" for more than 80% of the time were used. Subsequently, QRS detection was performed using the Hamilton and Tompkins algorithm (Hamilton and Tompkins, 2015). The HRV signal at each beat was defined as the periods between consecutive R-peaks, while the HR signal was defined as the inverse of these periods multiplied by 60 – in units of beats/min. Spline interpolation at a frequency of 4 Hz (to account for the subsequent extraction of HF frequencies) was applied to obtain the final HR and HRV signals and subsequently filtering with a median filter in order to remove spurious spike artefacts. During the experiment, the volunteers during the fMRI duration wore 3 respiration belts in order to compare the position of different belts. For this study, only the inverted respiration signal was used.

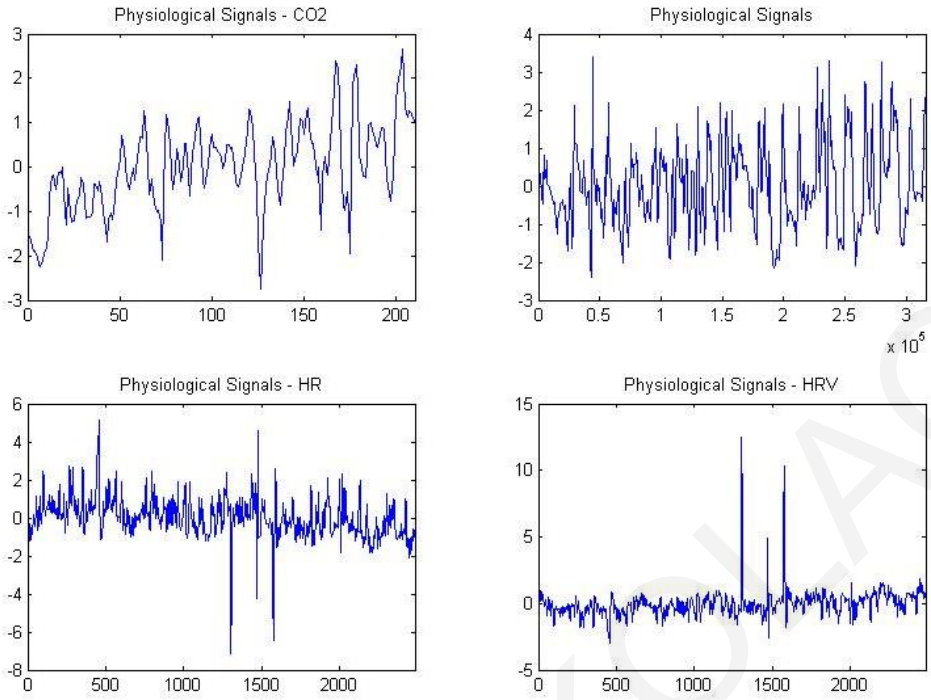

Figure 3.3. Physiological signals extracted from the fMRI data. Clockwise from top left CO2, RVT, HR and HRV.

3.2 Pre-Processing Steps

A processing pipeline was applied which was developed using FSL (Smith et al., 2004) and in-house-developed MATLAB scripts. The pre-processing of the experimental data consisted of various steps such as: rigid body motion correction and skull removal for functional images using the BET function. For each of the volunteers, motion parameters were calculated to reflect head motion in six directions with respect to the mean image. The last pre-processing step was that the resting-state functional images were normalized into MNI standard space using linear registration implemented using FSL-FLIRT (Smith et al., 2004). Specifically, the fist sub-step in the last pre-processing step was to spit our raw data in separate brain slices. Then, on each slide of the brain, the FSL-FLIRT function was used for registration to the MNI space. After that, the FSL-MERGE function was used in order to connect the registered slides on the brain. Finally, masks of each region of interest was created and the average timeseries of each mask was calculated by using the FSLMATHS function.

3.2.1 Brain Extraction

The raw data from an fMRI image may contain voxels that corresponds to the skull or other anatomical regions of the head (Figure 3.4). In this study, only the voxels that correspond to the brain tissues are of interest. Therefore, the voxels that correspond to non-brain tissues were removed from the experimental images. In order to extract the voxels of interest, the FSL's Brain Extraction Tool (BET), which removes non-brain tissues, was used (Figure 3.5). BET deletes non-brain tissue from an image of the whole head. It can also estimate the external skull surface. For this procedure the default values of the program parameters were used.

In more detail, the value of 0.5 was used for the fractional intensity threshold, since smaller values of threshold may give a larger brain contour and as a consequence may give voxels that correspond to skull. On the other hand, higher values of this threshold will give fewer brain contours and may result in the loss of voxels of interest. The presence of a small number of skull voxels does not particularly affect the subsequent analysis processes. The standard value of zero was used for the second parameter, which is the vertical gradient fraction. For this parameter, the choice of a positive value gives a larger brain contour at the bottom and lower at the top.

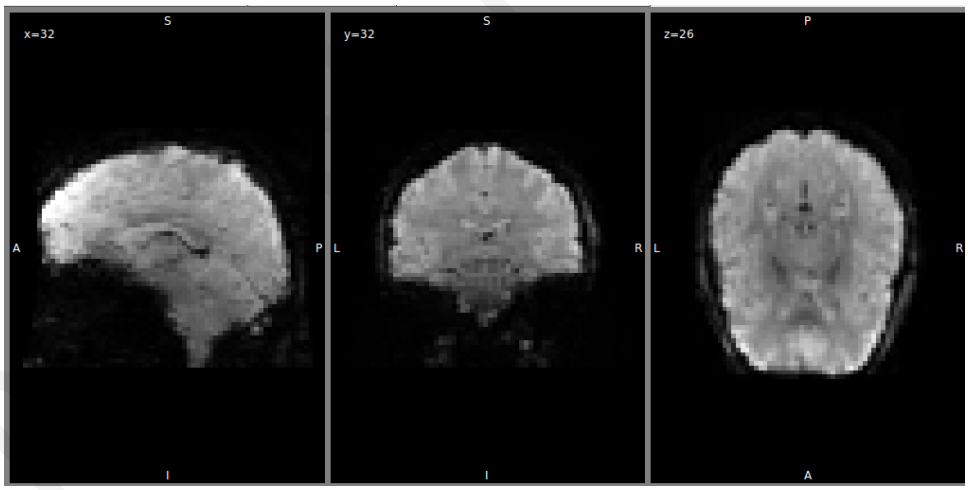

Figure 3.4. Raw fMRI image in the three planes of section (Sagittal, Coronal and Horizontal).

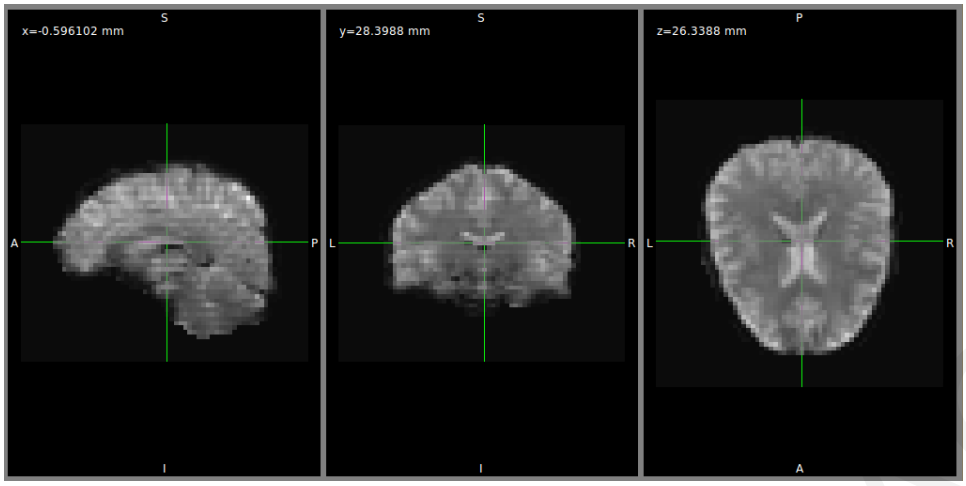

Figure 3.5. No-brain Tissues Extraction using BET in the three planes of section (Sagittal, Coronal and Horizontal).

3.2.2 Linear Image Registration

The second pre-processing step was to apply linear registration using FMRIB's Linear Image Registration Tool (FLIRT). FLIRT is a fully automated robust and accurate tool for linear (affine) intra- and inter-modal brain image registration. The linear image mapping of the functional image was first performed with respect to the corresponding individual structural image (Figure 3.6) and then with the image of the standard MN152_T1_2mm brain (Figure 3.7). FLIRT was considered necessary for correcting artefacts caused by head movements or other external factors, which may be due to the MR scanner, to ensure all voxels were matched with the appropriate anatomic regions regardless of their location. For best results, all images were properly mapped to each other so that each voxel is well defined at all times. As a good reference picture, the typical brain GNU152_T1_2mm, which is the average of 152 brains, was used.

The parameters used in FLIRT were the default ones. For bounded areas, 12 degrees of freedom (3 degrees of rotation, 3 shifts, 3 scaling, 3 Skews / Shears) were used. More degrees of freedom do not give a better result especially between images from the same person. The most common cost function for fMRI data registration is the cross ratio and this function was also applied in our data. The cost function is used to measure how well matches are made, and thus determines the transformation that achieves the minimum cost value.

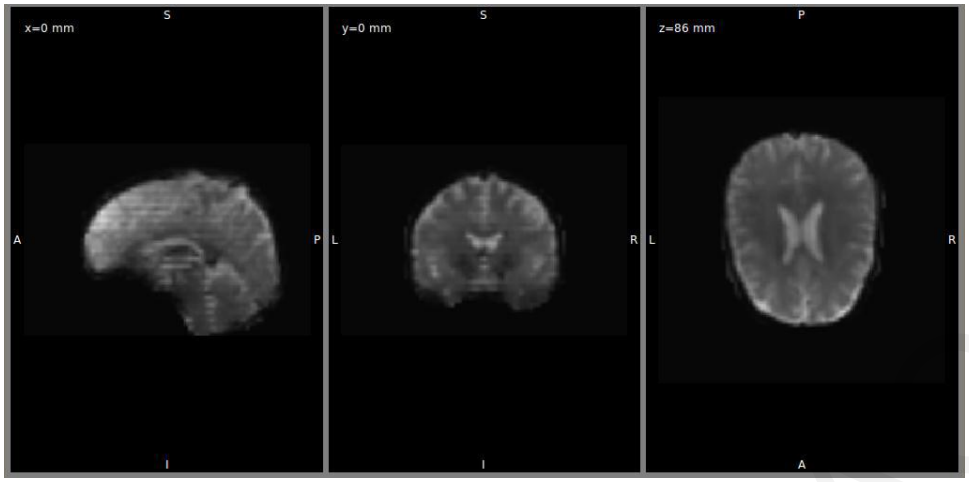

Figure 3.6. Registered image on its own anatomical image in the three planes of section (Sagittal (left), Coronal (middle) and Horizontal (right)).

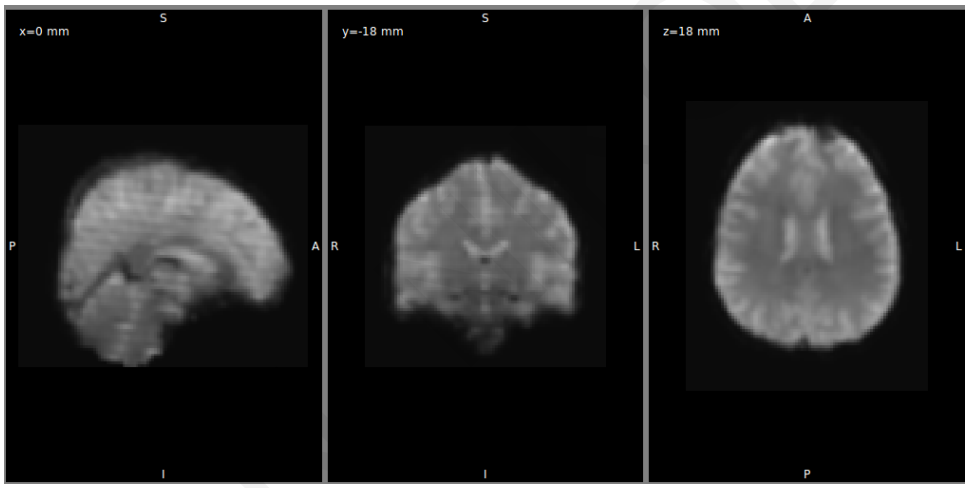

Figure 3.7. Registered image on MNI152_T1_2mm anatomical image in the three planes of section (Sagittal (left), Coronal(middle) and Horizontal(right)).

3.3 Resting-state Dynamic Functional Connectivity Analysis

After the pre-processing steps, various methods and analyses which were theoretically provided in chapter 2, were applied in practice. The techniques we implemented in order to extract the RSNs and investigate their relationship with the physiological signals will be as will be below rigorously presented and explained next.

3.3.1 Mask-based Analysis

Two different versions of seed-based resting-state analysis were implemented. In the first version, mask-based analysis was applied as outlined in Figure 3.8. In this method,

anatomical masks defined in the MNI space (using the Harvard Oxford cortical - Figure 3.9, the Harvard Oxford subcortical - Figure 3.10 and the Juelich FSL atlases - Figure 3.11) were used in order to define regions of interest (ROIs). Specifically, the following grey matter ROIs were defined (which consist the DMN): medial prefrontal cortex (mPFC), posterior cingulate cortex (PCC), anterior cingulate cortex (ACC), thalamus and precuneus.

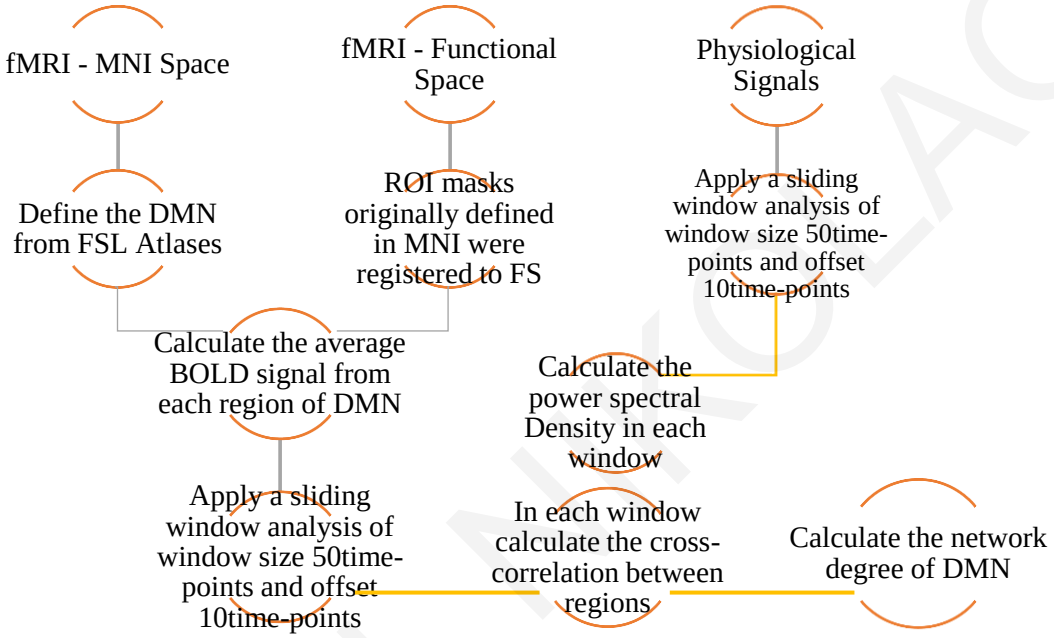

Figure 3.8. Processing Steps of Mask-based Analysis Algorithm.

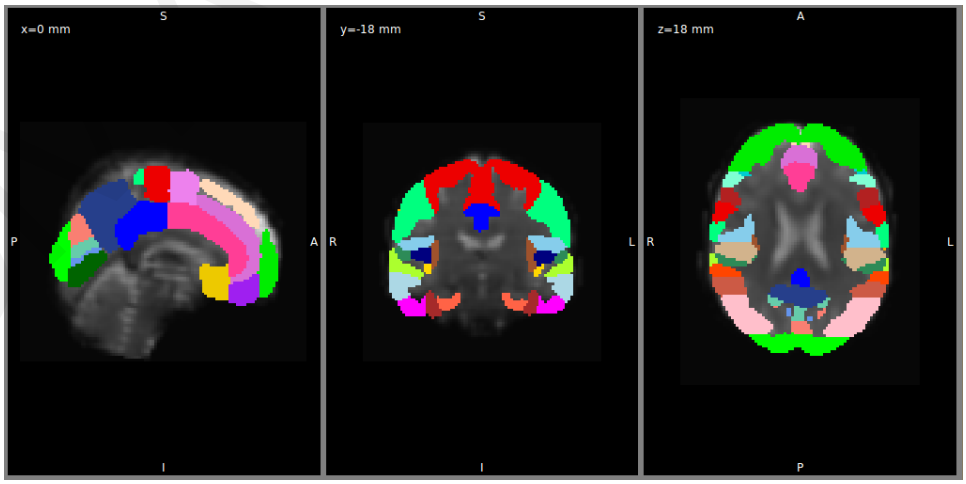

Figure 3.9. Applying areas from Harvard Oxford cortical atlas in one Functional Image.

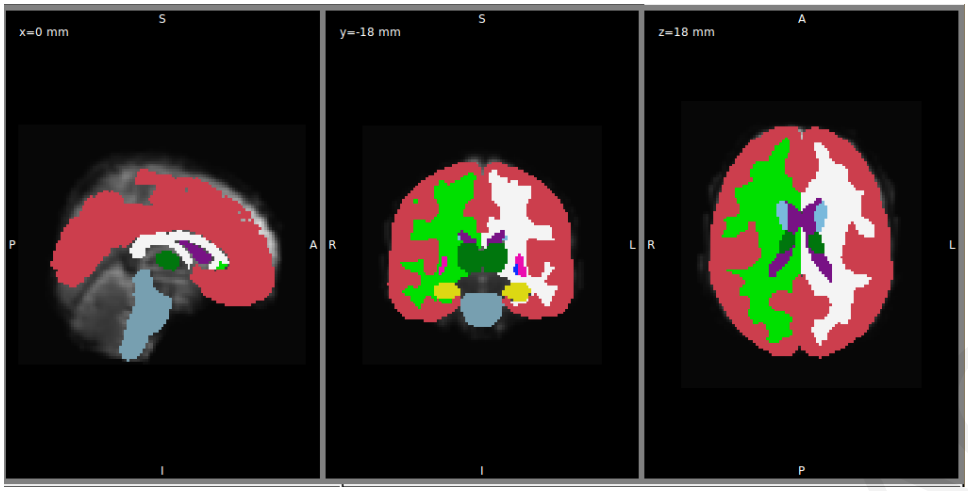

Figure 3.10. Applying areas from Harvard Oxford sub cortical atlas in one Functional Image.

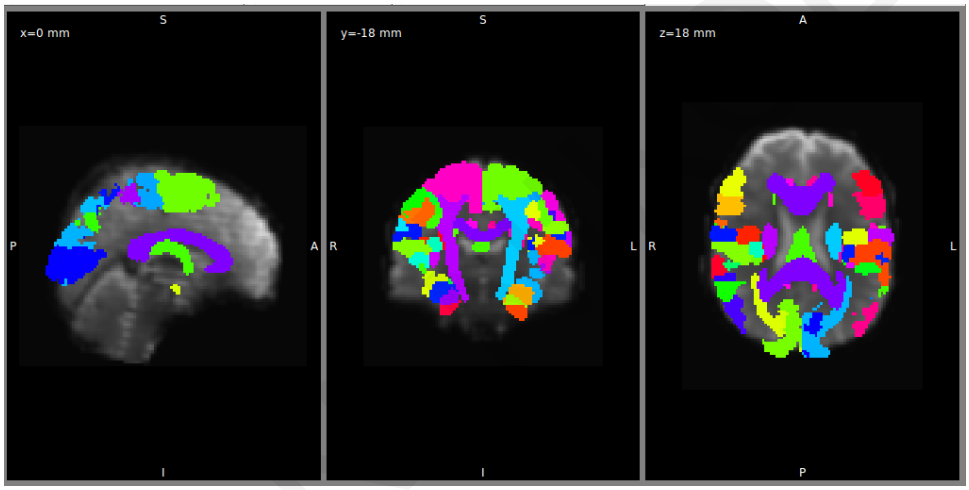

Figure 3.11. Applying areas from Juelich atlas in one Functional Image.

The average BOLD fMRI time series in each region were then extracted and correlated with each other in order to obtain a functional connectivity matrix in sliding windows of 150 seconds duration (50 time lags), overlapped by 30 seconds (10 time lags). To select the optimal window length, correlation matrices for different window lengths were calculated (Figure 3.12). Specifically, the cross-correlation between two time-series is estimated from finite data samples using the following sum:

$$\widehat{\boldsymbol{\Phi}}_{\boldsymbol{xy}}(\boldsymbol{m}) = \frac{\mathbf{1}}{\boldsymbol{N} - |\boldsymbol{m}|} \sum_{\boldsymbol{n}=\mathbf{0}}^{\boldsymbol{N}-|\boldsymbol{m}|-\mathbf{1}} \boldsymbol{y}(\boldsymbol{n}+\boldsymbol{m})\boldsymbol{x}(\boldsymbol{n}) \qquad \textbf{(3.1)}$$

where x, y are the two time series (in our case, fMRI time series corresponding to different regions), *N* is data length and *m* is cross-correlation lag. For stationary time series,

this estimate tends to the true underlying cross-correlation sequence as N tends to infinity (consistent estimate), while it worsens for smaller N, particularly for large values of m. A window length of 50 was eventually selected, as it achieved a good balance between being able to track time-varying functional connectivity while providing reliable estimates (i.e. closer to their values for longer time windows) of the cross-correlation function.

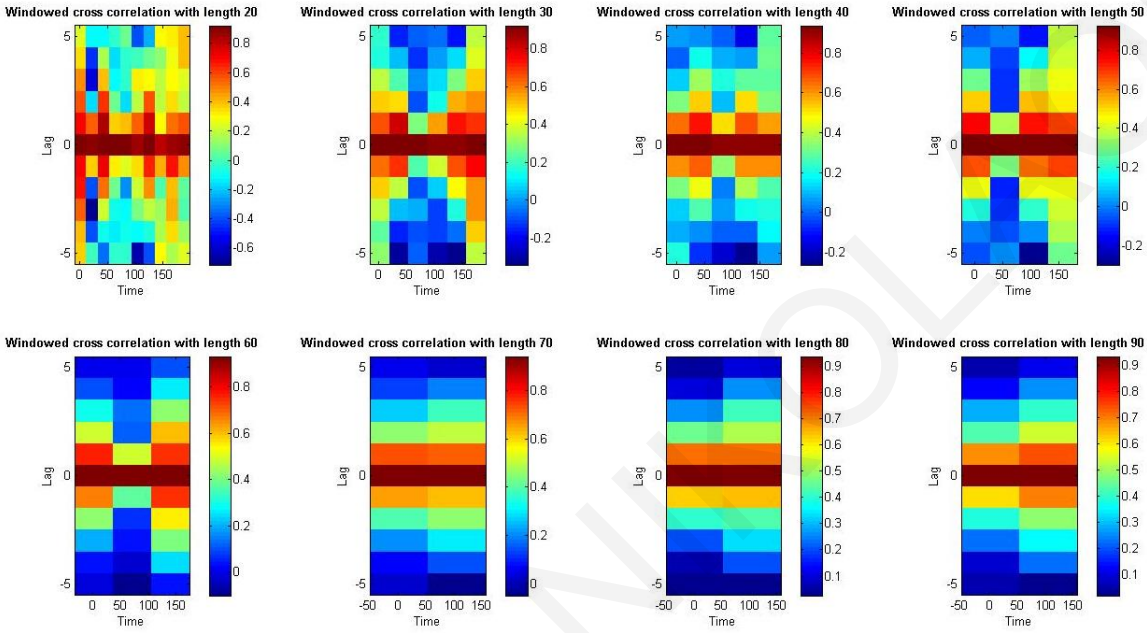

Figure 3.12. Correlation matrices for different window lengths were calculated in order to select the optimal window length.

The power spectral density of the $PETCO_2$ and HR signals was calculated using the same sliding windows by applying the Welch method (Oppenheim and Schafer, 2009). Welch's method for estimating power spectral density is carried out by dividing the time signal into successive blocks, forming the periodogram for each block, and averaging:

$$\hat{S}_x^W(\omega_k) = \frac{1}{K}\sum_{m=0}^{K-1} P_{x_m,M}(\omega_k) \qquad \textbf{(3.2)}$$

where K denotes the number of available frames and m denotes the window. In other words, it is an average of periodograms across time.

To quantify correlation between different ROIs, both the absolute maximum and the absolute average cross-correlation values between 0 and ±5 time lags were calculated. In addition to performing these calculations in standard MNI space, the procedure was repeated in the functional space of each volunteer or the purpose of examining the effects of registration

(of the BOLD time series to the MNI space) on the results. To achieve this, the ROI masks originally defined in MNI space were registered to the functional space of each volunteer (FLIRT). Specifically, the masks that were obtained from the registration in the MNI space, were first split to separate slices. Then, each slice of masks was registered to the functional space and the FSL-MERGE function combined these slices into a single volume.

After obtaining cross-correlation values between all areas in the examined RSNs, the overall time-varying connectivity of the network was quantified by computing the graded network degree, as it is an overall index of how "connected" the network is (i.e. brain networks were not converted to binary graphs as done in many connectivity studies, because this method discards information about the exact correlation values) (Rubinov and Sporns, 2010) for all 150 s windows.

Specifically, the graded degree is defined as:

$$k_i^W = \sum_{j \in N} W_{ij} \qquad \textbf{(3.3)}$$

where N is the number of brain regions in the network and W_{ij} are the absolute maximum (or average) correlation values (within ±5lags) between the network nodes *i* and *j*. The values of the graded network degree in each window were subsequently correlated to the time-varying power spectral density of the examined physiological signals.

3.3.2 Seed-based Analysis

Standard seed-based analysis was performed (as outlined in Figure 3.13) by first selecting a seed voxel, correlating all voxels of the brain to this voxel and applying a threshold in order to define the spatial pattern of the corresponding RSN. Subsequently, different threshold values were examined, and it was found that an appropriate threshold value for the presentation of the results was 0.65, as it yielded spatial RSN patterns relatively similar to the mask-based analysis, whereby similarity is defined as spatial overlap between the regions defined by mask-based and seed-based analysis (i.e. number of overlapping voxels over number of voxels of the smaller mask which in this case was yielded by the seed-based analysis). It should be noted that the precise threshold value was not found to affect the overall results. This is further discussed below. For the DMN, the seed voxel was selected within the PCC, whereas for the visual and somatosensory networks the seed voxels were selected in the

occipital cortex and postcentral gyrus respectively. The time-varying RSN graded degree for all networks was computed as described above.

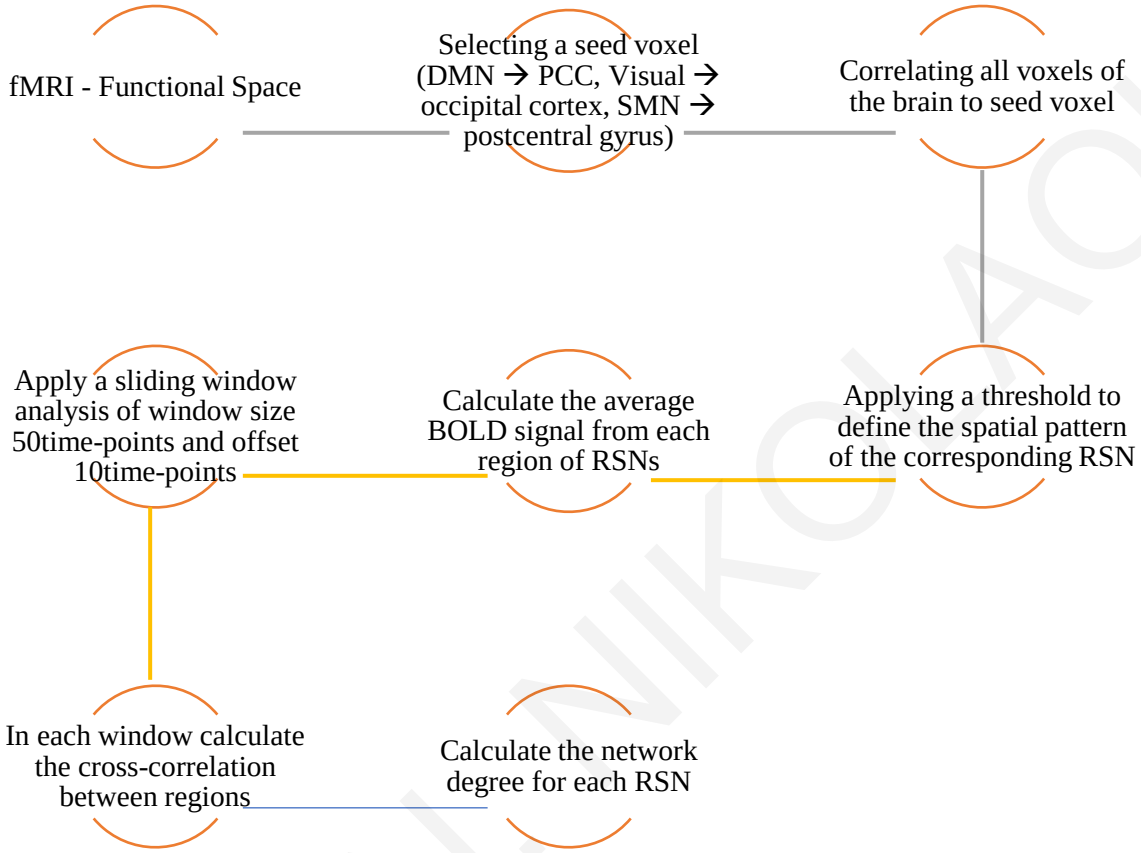

Figure 3.13. Processing Steps of Seed-based Analysis Algorithm.

3.3.3 Independent Component Analysis

ICA analysis was carried out using FSL 5.0.9 MELODIC, whereby the three first volumes were regressed out from the analysis. The single-subject ICA was performed in two ways: 1) conventionally, using the entire timeseries consisting of all 210 brain volumes imaged (Dipasquale et al., 2015) and 2) using a sliding time window approach with the spatial domain–independent component analysis (Spatial-Sliding-ICA).

In the first ICA approach, a time-sliding window was applied in the same way as mentioned previously and subsequent analyses were focused on the previously mentioned RSNs of interest: the DMN, as well as the visual and somatosensory networks. In addition, a new sliding window was performed for these methods where the window offset has changed to one time-point instead of 10 time-points in order to capture the changes across the windows

with an improved time resolution. Spatial maps and temporal (amplitude and network) analyses on these ICs of interest, both at low and high dimensionality were performed. For the high dimensionality ICA, the resting state networks (RSNs) are decomposed in sub-networks to obtain more detailed and informative network analyses with respect to the more common low dimensional approach. The components yielded by the high-dimensionality ICA could be the result of a differential functionality of sub-networks forming the larger networks obtained with the low dimensional analysis (Smith et al., 2009; Abou Elseoud et al., 2010). The time-varying RSN graded degree for all networks was computed as described before and the power spectral density of the PETCO2 and HR signals was calculated in the same sliding windows by applying the Welch method (Oppenheim and Schafer, 2009), as explained previously. Additionally, for this method the power spectral density of the RVT was calculated, using the same procedure. Moreover, the Instantaneous power of LF and LH of HRV was also used, extracted using the methodology described in section 3.3.5.

Low Dimensionality ICA:

The procedure for the low-dimensionality ICA is outlined in Figure 3.14. For the low-dimensionality ICA, a model order of 25 ICs was chosen, in line with previous studies and guidelines. In general, using model orders < or =20 provides a general picture of large scale brain networks. However, detection of some components (i.e., S(1), S(2), and striatum) requires higher model order estimation. Model orders 30-40 showed spatial overlapping of some IC sources (Abou Elseoud et al., 2010). These components were first manually classified as RSNs or motion-related ICA components. To do this, the spatial map, time course and power spectrum of the time course for each component were used. Spatial characteristics of typical structured noise components are: ringing around the head (motion), and primarily being in the ventricles or in the brain stem (physiological noise). In terms of temporal characteristics, noise components often have sudden spikes in the time course and/or a lot of high frequency content (Figure 3.15). Signal components, on the other hand, are typically characterized by predominantly low frequency power and 'blob-like' spatial maps primarily covering grey matter. It is normal that a large number of the components are labelled as noise. Subsequently, ICA-AROMA, which is a robust ICA-based strategy for removing motion artifacts from fMRI data was used. (Mi, 2014)

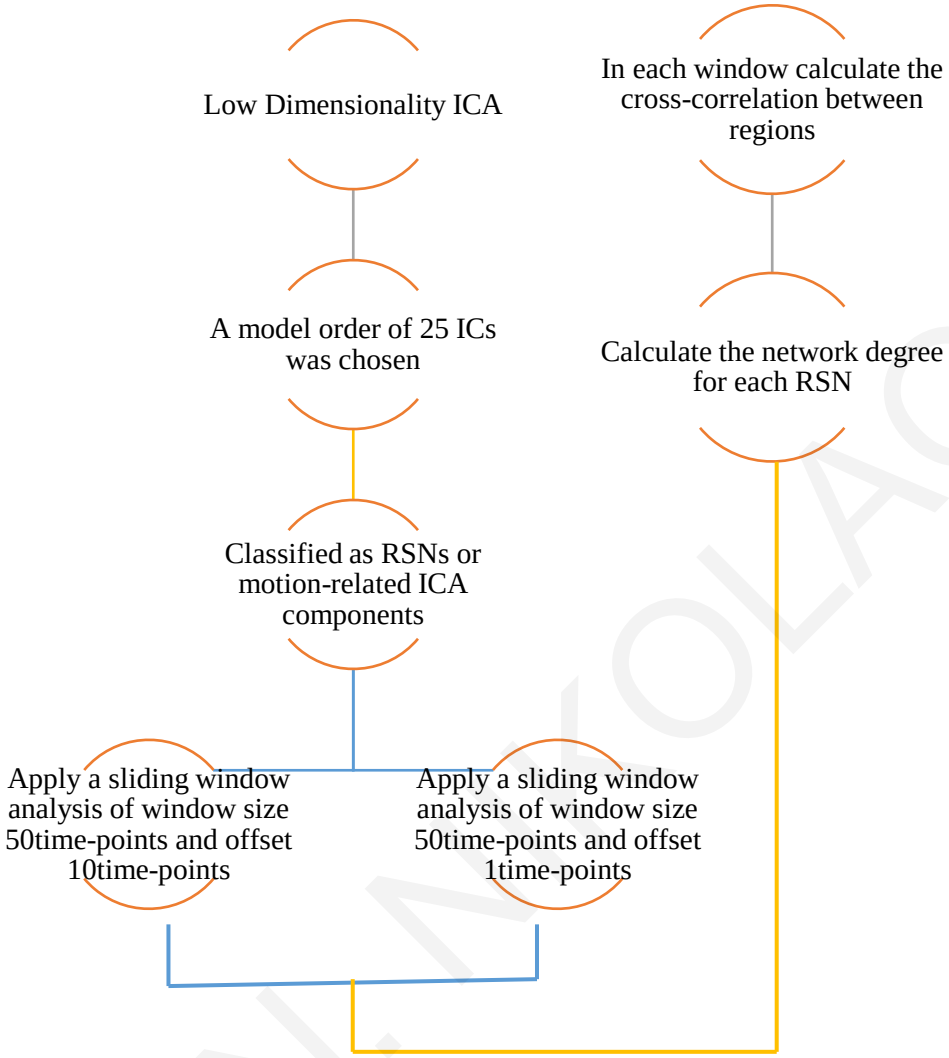

Figure 3.14. Processing Steps for the Low Dimensionality ICA Algorithm.

A)

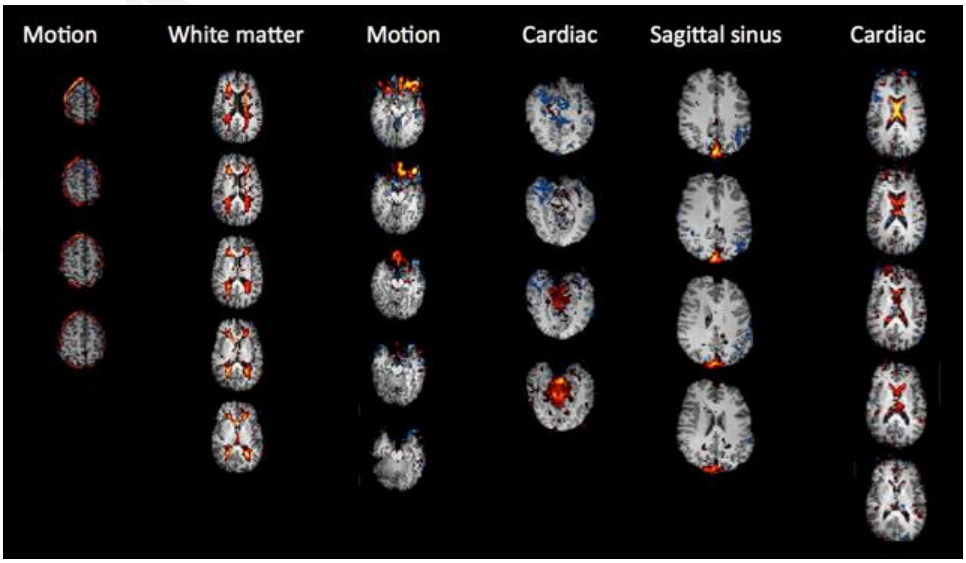

B) 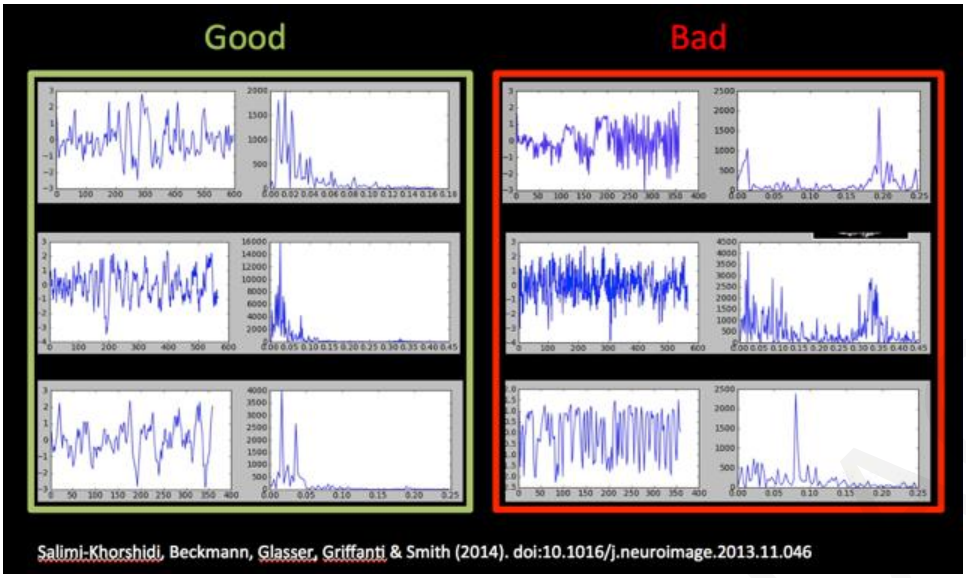

Figure 3.15. Classified noise components by using (A) the spatial maps for each component and (B) the time course and power spectrum of the time course for each component. Spatial characteristics of typical structured noise components are: ringing around the head (motion), and primarily being in the ventricles or in the brain stem (physiological noise). In terms of temporal characteristics, noise components often have sudden spikes in the time course and/or a lot of high frequency content. Signal components, on the other hand, are typically characterized by predominantly low frequency power and 'blob-like' spatial maps primarily covering grey matter.

High Dimensionality ICA:

The procedure for the high-dimensionality ICA is outlined in Figure 3.16. For the high-dimensionality ICA, a dimensionality of 70 ICs was selected. This number was chosen because previous work (Abou Elseoud et al., 2010) showed that ICA analyses results are affected by model order selection. In addition, another study demonstrated that, in patients with seasonal affected disorder, the between-group differences measured with ICA increase with model order (reaching a maximum around 70 components) (Abou Elseoud et al., 2011). These components were subsequently classified by taking the low-dimensional RSNs as reference templates and using a spatio-temporal labeling criterion: the high dimensional component *i* was labeled as part of the low-dimensional component *j* with which it had the highest spatial overlap (using the fslcc function) and the highest temporal correlation (calculated with Spearman's correlation among single-subject time series) (Kiviniemi et al., 2011). A component was classified as residual noise if all spatial overlap and temporal correlations were below a threshold empirically determined during the algorithm development by evaluating different values against manual classification (0.4 for spatial overlap and 0.4 for temporal correlation). Both

the residual noise and the components form other networks or areas of the brain except the DMN, visual and somatosensory networks were ignored in subsequent analyses.

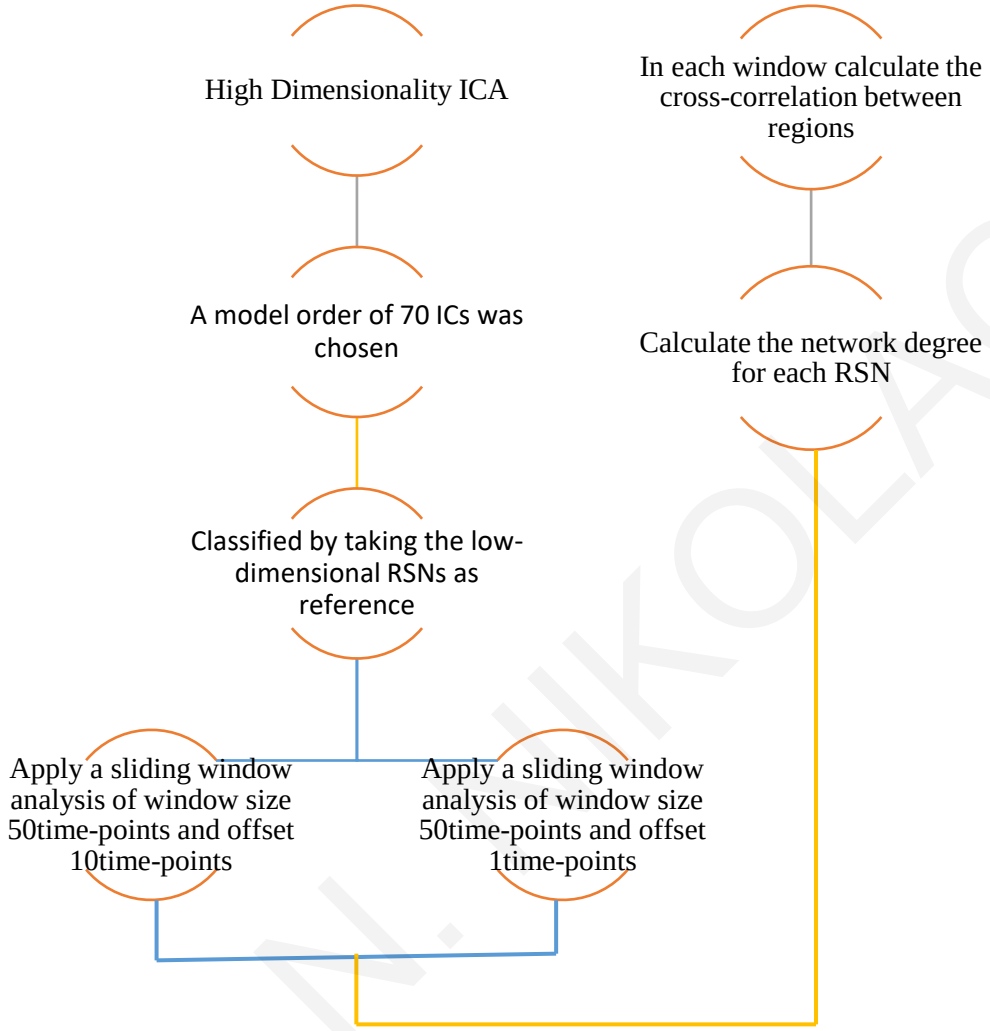

Figure 3.16. Processing Steps of High Dimensionality ICA Algorithm.

Spatial Sliding Window ICA:

In the second ICA approach, Spatial-Sliding-ICA was performed (as outlined in Figure 3.17) by cropping the original 210 time-point BOLD fMRI data set into time windows of 50 time-points and sliding the 50-volumes time window 10 volumes at a time: 10-60, 20-70… 150-200. In this way, the same 15 time windows that were used in the mask-based and seed-based analysis were obtained. Subsequently, low dimensionality ICA was applied in each window. Then, both time and spatial analysis was performed as follows: for the time analysis, the network degree for the selected components that were associated to the DMN was extracted for each window and compared against the power of the physiological signals of interest in the same time window. The spatial stability of the DMN was analyzed by measuring the spatial correlation of the detected DMN Spatial-Sliding-ICA sources using an FSL routine (fslcc),

which computes cross-correlations between the volume in two different 4D data sets for investigating similarities in ICA outputs. The stability measures were obtained by comparing a commonly used DMN template from every individual.

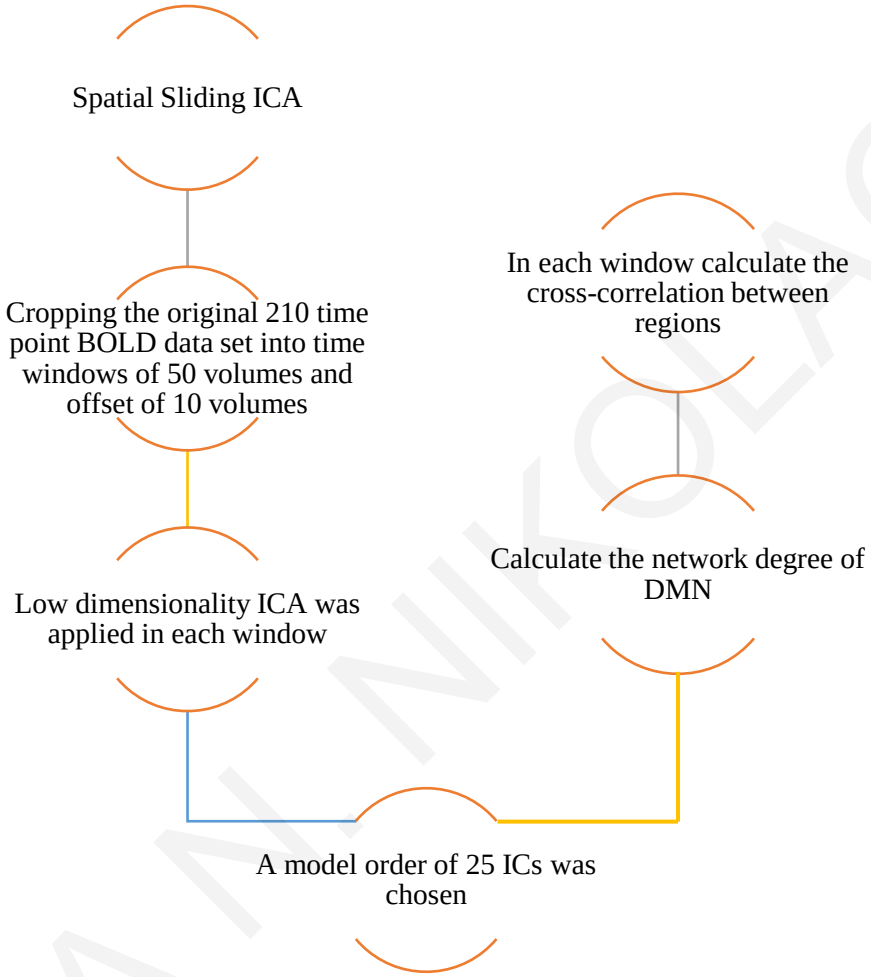

Figure 3.17. Processing Steps of Spatial Sliding Window ICA Algorithm.

3.3.4 Wavelet Transformation

Wavelet transforms are multi-resolution decompositions that can be used to analyze signals and images offering good time- and scale-resolution (Ville et al., 2006), (Daubechies, 1992). In the case of one-dimensional signal, the discrete wavelet transform (DWT) is essentially a decomposition into a sum of basic functions. These basic functions are shifted and dilated versions of a (bandpass) wavelet function and shifted versions of a (lowpass) scaling function. This decomposition, which is achieved via a fast filter bank algorithm and includes a digital filtering and dyadic subsampling step at each level, results in a set of wavelet and scaling coefficients. The signal can subsequently be reconstructed via the inverse scheme (Ville et al.,

2006). By decomposing the fMRI and physiological signals via the discrete wavelet decomposition and reconstructing them using the coefficients of a single decomposition level at each time, the signal was basically decomposed into its different frequency sub-bands which then makes it possible to determine whether the effect of the physiological signals on the fMRI signal is more pronounced within a specific frequency sub-band. An advantage of this approach compared to other frequency-based analysis approaches is that the temporal information of the signal is preserved. In addition, application of the wavelet filter bank allows us to search for modulatory effects at different frequency sub-bands, while still taking the entire signal into consideration. Using the techniques described in section 2.3.1.3 and using the wavelet toolbox in MATLAB, a 5-level wavelet decomposition was applied to the $PETCO_2$, RVT and HR signals, and the corresponding frequency decompositions were obtained. The Spearman correlations coefficients for each decomposition levels with the corresponding time-varying RSN degree at all the resulting frequency sub-bands were then calculated. Since the frequency sub-bands resulting from a wavelet decomposition are the result of digital filtering and dyadic subsampling, their frequency sub-band depends on the initial sampling rate of the signal analyzed. They were, therefore, different for PETCO2/RVT and HR because they were sampled at 1/3Hz and 4Hz respectively, as shown in figure 3.18. In the case of ICA case though, we interpolated all the signals at 4Hz in order to apply them later on MLR models and a 7-level wavelet decomposition was applied to the physiological signals. Lastly, it is worth mentioning that the choice of wavelet basis function did not make a significant difference in our analysis. The results presented were obtained by using the Coiflets wavelet basis (Daubechies, 1992).

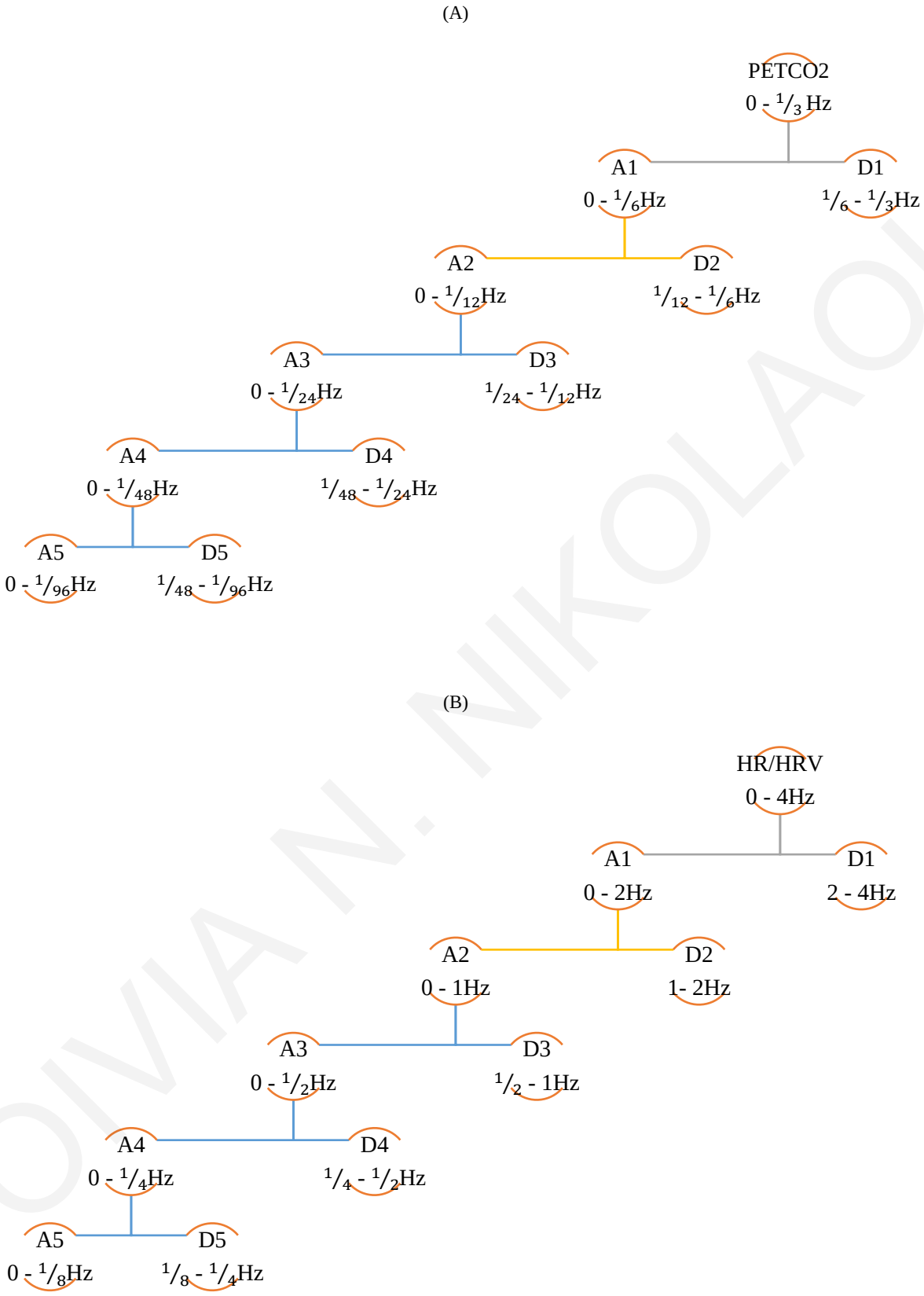

Figure 3.18. A 5-level wavelet decomposition was applied to (A) PETCO2 and (B) HR/HRV signals.

3.3.5 Extraction of instantaneous power of HRV LF and HF bands through Hilbert Transform

In order to extract the desired information from the LF and HF frequency bands, we implemented the following algorithm (outlined in Table 3-1), whereby after bandpass filtering (Figure 3.19) the HRV signal within the low- and high-frequency bands, the Hilbert transform was applied to both resulting time series in order to generate the corresponding complex analytic signals which exhibit time varying amplitudes (Mandic et al., 2013; Looney et al., 2014; Hemakom et al., 2016), the so called instantaneous Amplitude (iA) concept (Looney et al., 2008). The so-obtained signals were processed using the same time windows as those used for the sliding window analysis, typically 50 time-points long sliding windows with an overlap of 10 time-points and one time-point respectively. The 20% largest and smallest signal values in every time window under consideration were removed and the mean amplitude values were calculated. This removed the outliers, while at the same time retaining the essential information: the average amplitude of a large proportion of the time window for both frequency bands, the instantaneous amplitude of the low frequency band (LFiA) and the instantaneous amplitude of the high frequency band (HFiA).

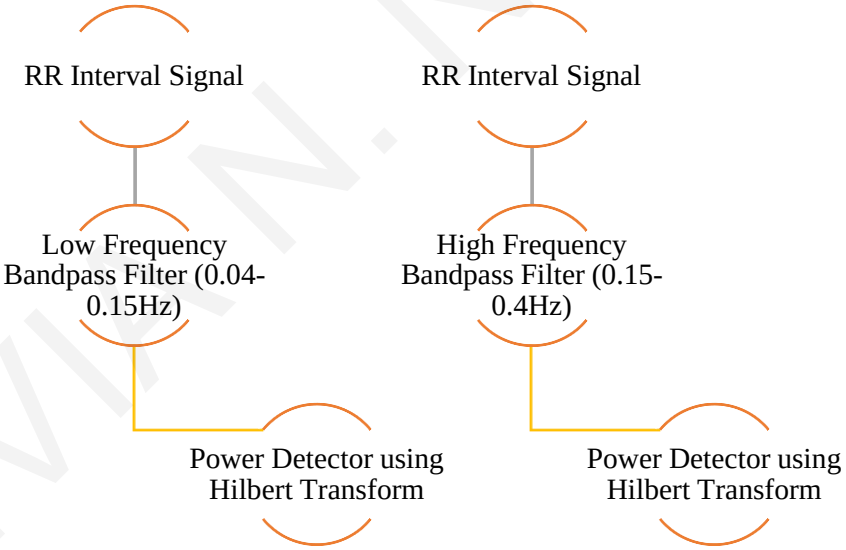

Figure 3.19. HRV Bandpass Filtering within the LF and HF bands

1. Bandpass-filter HRV within two bands, LF and HF
2. Apply the Hilbert transform to LF (0.04-0.15Hz) and HF (0.15-0.4Hz) to generate analytical signals
3. From the complex-valued analytic signals, obtain the amplitude at every point in time
4. Divide signals into time windows, typically sliding windows with a length of 50 time-points and offset of 10 or 1 time-point respectively
5. In every time window, exclude the 20% largest and smallest values, to remove outliers
6. Calculate the mean for every time window

Table 3-1. Extraction of instantaneous power of HRV LF and HF bands through Hilbert Transform

3.3.6 General Linear Model and Multiple Linear Regression

Both General Linear Model and Multiple linear regression were applied in order to investigate further the relationship between the DFC patterns and the physiological signals. In the following equation of Multiple Linear Regression (as can be seen from Figure 3.20):

$$\boldsymbol{Y = \beta_1 X_{i1} + \beta_2 X_{i2} + \cdots + \beta_p X_{ip}} \quad \textbf{(3.1)}$$

the Y variable corresponds RSN degree and the $\boldsymbol{X_{ij}}$ variables are the power of the physiological signals.

Initially, multiple univariate linear regression models (as can be seen from Table 3-2) were applied in order to separately assess the effect of each physiological signal on the examined RSNs. Additionally, the *p*-values for the estimated coefficients were calculated to assess whether these values were significant, with the significance level set at 0.05. Subsequently, multiple linear regression models were applied to assess the relative contribution of different physiological signals as well as the statistical significance of the corresponding coefficients. The same was done for the LF and HF power of the HRV signal. Regarding the MLR models 4-6, it was found that the instantaneous power of LF and HF of HRV were highly correlated to each other.

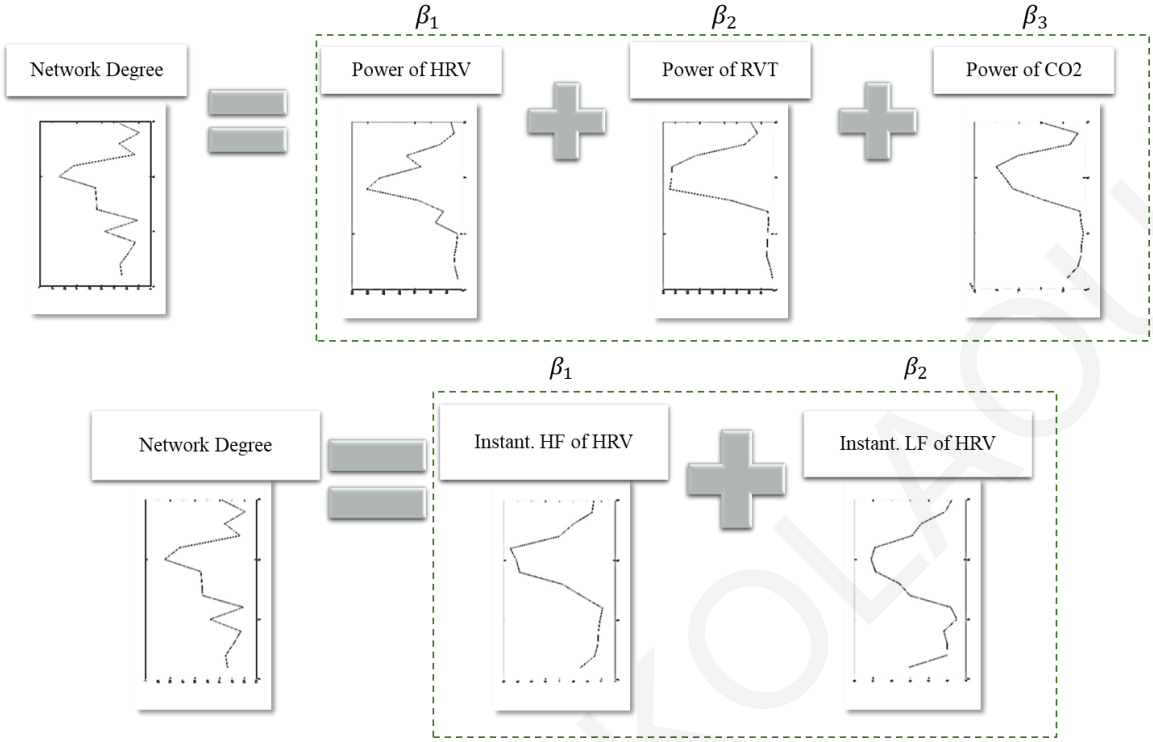

Figure 3.20. Multiple Linear Regression models for examining the effect of physiological signals on fMRI-based RS-DFC.

GLMs and MLRs						
		Physiological Signals				
		PETCO2	RVT	HR	LF OF HRV	HF OF HRV
RSNs	DMN	GLM1	GLM2	GLM3	GLM4	GLM5
		MLR1			MLR4	
	SMN	GLM6	GLM7	GLM8	GLM9	GLM10
		MLR2			MLR5	
	VISUAL	GLM11	GLM12	GLM13	GLM14	GLM15
		MLR3			MLR6	

Table 3-2. Different combinations used for General Linear Models and Multiple Regression Models. The independent variables in the models were the physiological signals.

3.3.7 Correlation Coefficients

In all the cases, the modulating effect of time-varying physiological signal power for PETCO2, RVT and HR on the time-varying RSN degree was quantified by calculating the Spearman rank correlation coefficient, which is suitable in our case due to the fact that our results are paired with respect to time (network degree versus time-varying physiological signal

power). The analysis was performed on all 12 volunteers (11 for HR analysis, as one volunteer did not satisfy the SQI mentioned above) and then the mean and standard deviation of the resulting correlation coefficients over all volunteers was calculated. This was done for the mask-based analysis (functional and MNI space), seed-based analysis, ICA analyses and also for different wavelet sub-bands. Finally, statistical significance for the computed correlation coefficients was assessed by calculating *p*-values for all volunteers, accounting for multiple comparisons by using Hommel's correction method (Hommel, 1988).

4. Mask-based and Seed Based Analyses

In this chapter, the results from the investigation of the mask-based and seed-based DFC analyses and the effect of physiological signals are discussed. The preliminary results of this study have been reported in one full conference paper (Nikolaou et al., EMBS 2015), while the final work has been reported in an abstract proceeding and in a full journal paper (Nikolaou et al., 2016; Nikolaou et al., OHBM 2016).

4.1 Physiological signals and fMRI time-series

As explained previously, the ECG data obtained from one subject were deemed unreliable, based on the quality assessment performed. The results presented here are consequently based on the analysis of 11 out of the 12 volunteers. Representative global BOLD time series, along with the corresponding $PETCO_2$ time series is shown in Figure 4.1. Note that in functional space the correlations between spontaneous $PETCO_2$ fluctuations and the BOLD signal (Fig. 4.1 – A) are clearer compared to the MNI space (Fig 4.1 – B), due to the blurring effect of registering the BOLD time series to the MNI space.

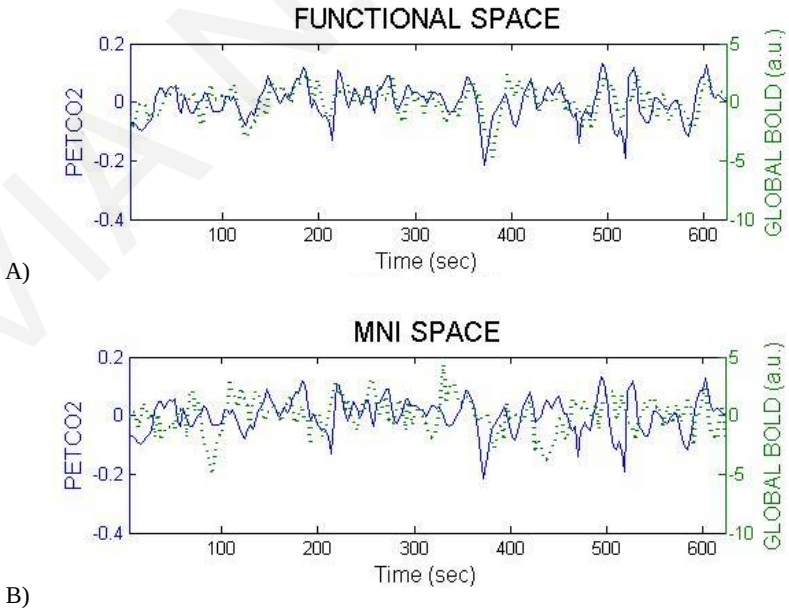

Figure 4.1. Representative global BOLD fMRI (dashed line): (A) functional and B) MNI space) and PETCO2 time series (solid line). The $PETCO_2$ signal is shown after linear detrending to illustrate that the correlations between the $PETCO_2$ and global BOLD signals are more evident in the individual functional space compared to MNI space.

4.2 Time-varying connectivity patterns and signal properties

The time-varying DMN resting functional connectivity matrices for one representative volunteer are shown in Figure 4.2-A for successive windows of 50 sec length, where considerable variability can be observed. The results shown in the Figure were obtained using mask-based analysis in the individual functional space. As shown in the corresponding color maps, the correlation values between DMN areas are overall high. In Figure 4.2-B the power spectral density of the $PETCO_2$ and HR signals in the same successive 50 s windows are presented and the existence of the time variations in the spectral content of the signals can be seen.

A)

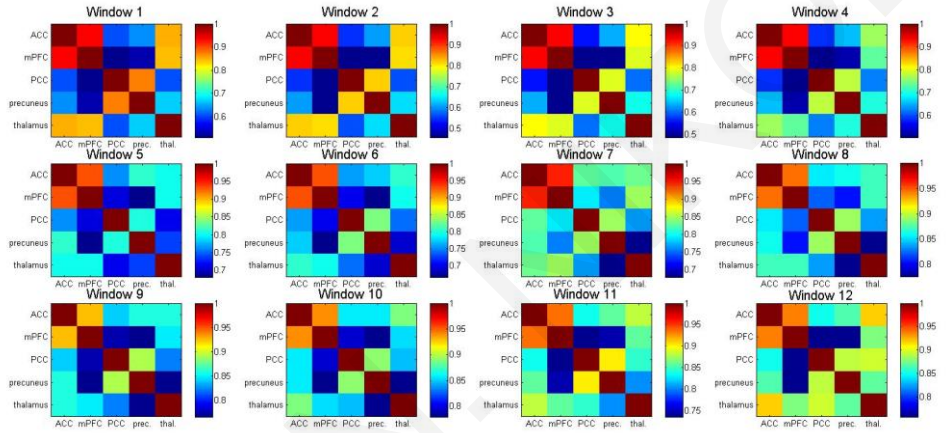

B)

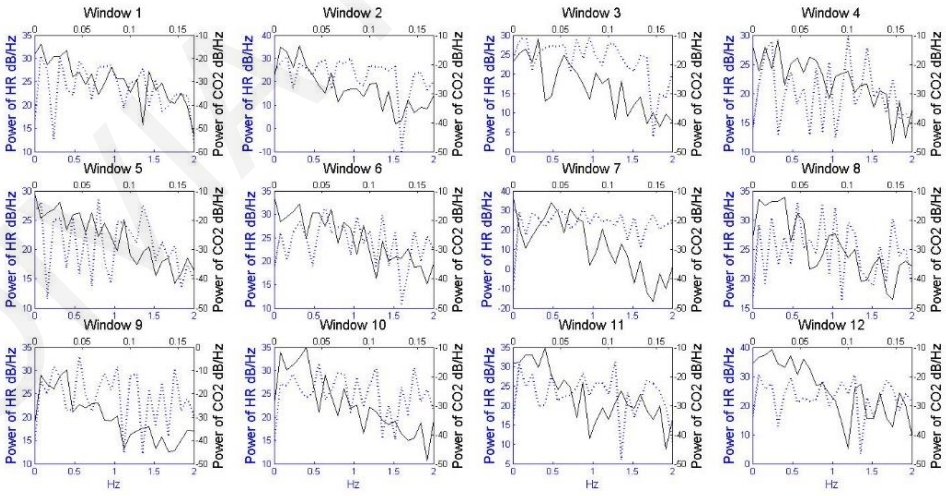

Figure 4.2. Time-varying connectivity patterns: A) Dynamic resting DMN functional connectivity matrices obtained using the maximum absolute correlation value in the individual functional space (mask-based analysis) of one representative volunteer for twelve successive time windows. B) Time-varying power spectral density of the HR (dashed line) and $PETCO_2$ (solid line) signals in the same windows. Each

successive window has a length of 50 sec and the overlap between successive windows is 30 s. Despite the large overlap between successive windows, variations in the spectral content are evident. In addition, this variability is more pronounced for the HR signal.

4.3 Resting-state Dynamic Functional Connectivity Analysis

4.3.1 Mask-based Analysis

4.3.1.1 Default Mode Network

The DMN is shown in both standard MNI space and functional space in Figure 4.3. Specifically, Figure 4.3-A shows the DMN in the standard MNI space and the Figure 4.3B illustrates the DMN in a representative functional space. In the MNI space the areas are smaller than in the functional space as can be seen from the Figure 4.3A and B.

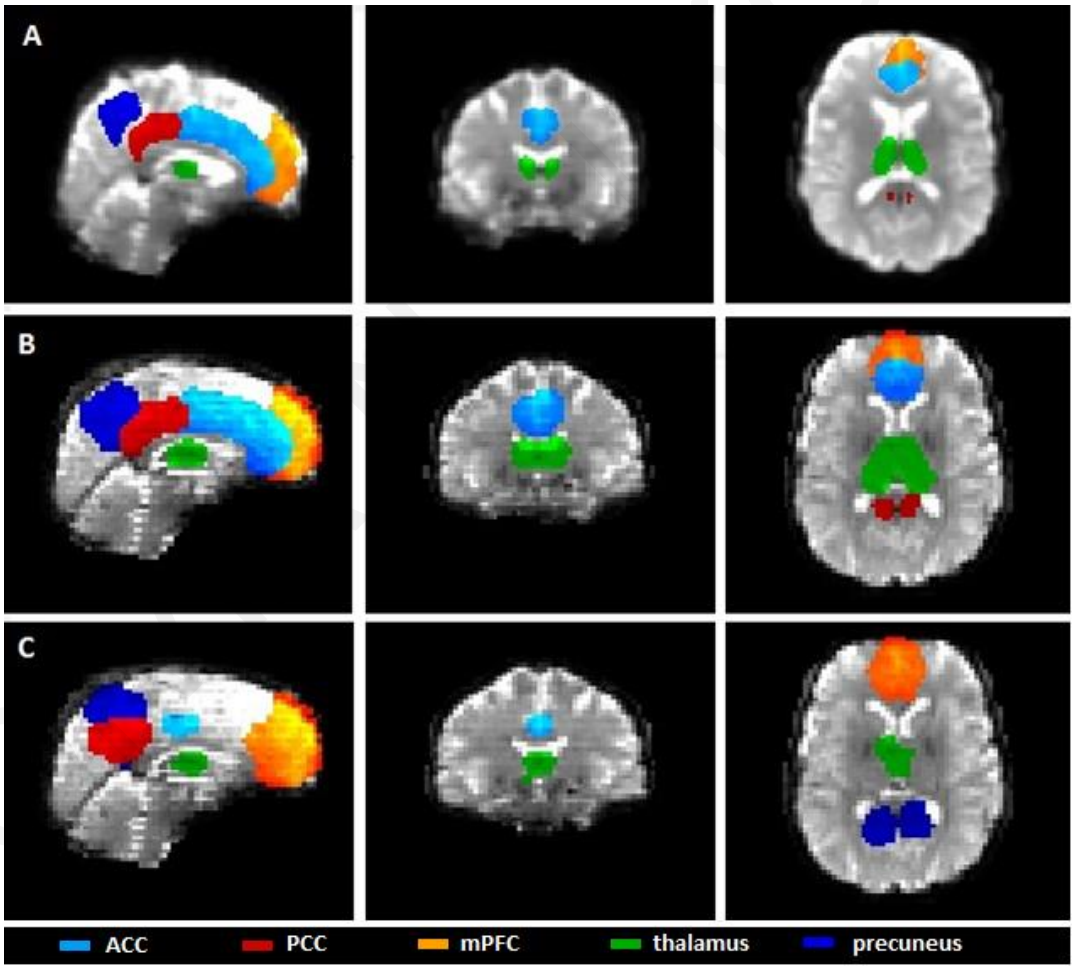

Figure 4.3. DMN in both standard MNI space and functional space: A) The default mode network (DMN) as defined in the MNI space using mask analysis, containing the following anatomical areas: posterior cingulate cortex, anterior cingulate cortex, precuneus, thalamus and medial prefrontal cortex B) The DMN

as defined in the functional space of a representative volunteer using mask analysis and C) The DMN as defined in the individual functional space using seed based analysis.

The time-varying network degree, the time-varying $PETCO_2$ and HR signal power for a representative volunteer in the case of mask-based analysis in the individual functional and MNI spaces are illustrated in Figure 4.4. In the case presented here, the degree was computed for the case in which correlations between areas were quantified using the average absolute cross-correlation value between 0 and ±5 time lags (similar results were obtained when the absolute maximum cross-correlation value was used). As explained in chapter 3, window size did not significantly affect the results, however a window length of 50 s was selected since it achieved a good balance between time resolution and reliable cross-correlation function estimation. Considerable differences can be seen between the results in the functional and MNI spaces. Specifically, in Figures 4.4-A, 4.4-B, 4.4-E and 4.4-F we can see that the time-varying DMN degree follows both the time-varying HR and $PETCO_2$ power closely. On the other hand, in Figures 4.4-C, 4.4-D, 4.4-G and 4.4-H the same relation is not so apparent, which also reflects on the obtained correlation coefficients (see Table 4-1 below).

In the same figure, results obtained when using the wavelet transform, for the frequency sub-bands with maximum correlation between time-varying network degree and band-limited signal power are presented. The A4 level (0-0.25Hz (see Figure 3.18)) yielded the highest correlations for the HR signal in both functional and MNI spaces, while for the $PETCO_2$ signal, the A2 level (0-0.08Hz) yielded the highest correlations in the functional space, as resting $PETCO_2$ fluctuations exhibit most of their power below 0.05 Hz (Liang et al., 1996). In the MNI space, level A4 (0-0.02Hz) yielded the stronger correlations for the $PETCO_2$ signal, possibly because registration of the BOLD time series to the MNI space essentially results in low pass filtering. Overall, the correlations between time-varying degree and signal power were found to be stronger for the time-varying band-limited power (after the wavelet decomposition) compared to total signal power. This can be clearly seen in tables 4-1 and 4-2.

CO2-FS		***CO2-FS-A2***		***CO2-MNI***		***CO2-MNI-A4***	
MEAN	**STD**	**MEAN**	**STD**	**MEAN**	**STD**	**MEAN**	**STD**
0.6	0.32	0.75	0.2	0.17	0.42	0.22	0.28
HR-FS		***HR-FS-A4***		***HR-MNI***		***HR-MNI-A4***	
MEAN	**STD**	**MEAN**	**STD**	**MEAN**	**STD**	**MEAN**	**STD**
0.67	0.1	0.77	0.1	0.2	0.07	0.47	0.22

Table 4-1. Spearman correlation coefficients between time-varying DMN network degree and total and band-limited time-varying $PETCO_2$ and HR power using masked-based analysis. The FS space yielded higher values than the MNI space. FS: functional space, CO_2-FS-A2: functional space, wavelet level A2 (0-0.08 Hz), HR-FS-A4: functional space, wavelet level A4 (0-0.25 Hz). MNI: MNI space, CO_2-MNI-A2: MNI space, wavelet level A4 (0-0.02 Hz), HR-MNI-A4: functional space, wavelet level A4 (0-0.25 Hz).

Volunteers	1	2	3	4	5	6	7	8	9	10	11	12
CO2-FS	0.0570	0.2749	**0.0071**	**1.94E-05**	**0.0153**	0.2749	**0.0380**	**0.0135**	**3.23E-06**	**0.0077**	**0.0008**	0.0570
CO2-FS-A2	**0.0342**	0.1706	**0.0055**	**0.0002**	**0.0228**	0.1706	**0.0342**	**0.0190**	**4.12E-05**	**0.0097**	**0.0034**	**0.0342**
CO2-MNI	0.2069	0.2943	0.1226	0.4899	**0.0007**	0.4899	0.4899	0.4899	0.4899	0.4899	0.4899	0.2069
CO2-MNI-A4	0.3788	0.4950	0.3135	0.1614	0.4950	0.4950	0.3041	0.4950	0.4321	0.4950	0.3041	0.3788
HR-FS	**0.0105**	**0.0104**	**0.0092**	**0.0107**	-	**0.0013**	**0.0087**	**0.0116**	**0.0092**	**0.0105**	**0.0105**	**0.0104**
HR-FS-A4	**0.0013**	**0.0011**	**0.0014**	**0.0012**	-	**0.0014**	**0.0014**	**0.0014**	**0.0012**	**0.0014**	**0.0013**	**0.0011**
HR-MNI	0.3058	0.3058	0.3058	0.2579	-	0.3058	0.3058	0.3058	0.3058	0.3058	0.3058	0.3058
HR-MNI-A4	0.0887	0.0887	0.0887	0.0887	-	0.0887	0.0887	0.0887	0.0887	0.0887	0.0887	0.0887

Table 4-2. Spearman correlation coefficient p-values obtained after using Hommel's method for all volunteers in the case of masked-based analysis. The FS shows consistent significance. FS: functional space, CO2-FS-A2: functional space, wavelet level A2 (0-0.08 Hz), HR-FS-A4: functional space, wavelet level A4 (0-0.25 Hz). MNI: MNI space, CO2-MNI-A2: MNI space, wavelet level A4 (0-0.02 Hz), HR-MNI-A4: functional space, wavelet level A4 (0-0.25 Hz). Values in bold black are significant and values in blue are non-significant.

The results for $PETCO_2$ and HR are given in Table 4-1 with respect to the correlation coefficient values between time-varying DMN degree and the total/band-limited power of the $PETCO_2$ for all volunteers (mean ± standard deviation). These suggest the presence of temporal correlations between network degree and signal power. Correlations were found to be much higher in the functional space compared to the MNI space. The correlation coefficients for the band-limited power are given for the wavelet sub-bands that yielded the highest correlation values (A4 (0-0.25 Hz) for HR in both spaces, A2 (0-0.08 Hz) and A4 (0-0.02 Hz) for $PETCO_2$ in the functional and MNI spaces respectively). In both cases, using the band-limited time-varying signal power yielded higher mean correlations. For instance, the correlation coefficients for $PETCO_2$ increased from around 0.6 (total signal power) to almost 0.8 (A2 level) in functional space. The values obtained in functional space are also considerably higher, suggesting that registration to the MNI space blurs the modulatory effect of $PETCO_2$ on time-varying network degree.

Table 4-2 shows the obtained *p*-values for the Spearman correlation coefficients for all volunteers in each space/sub-band. In agreement to the above observations, statistical significance ($p<0.05$) was observed for most volunteers in the individual functional space when total signal power was used and for almost all volunteers (10 out of 12 for $PETCO_2$, 11 out of 11 for HR) when the corresponding optimal sub-band was used. On the other hand, statistical significance was not achieved for most volunteers in the MNI space, even when the optimal frequency sub-band was used.

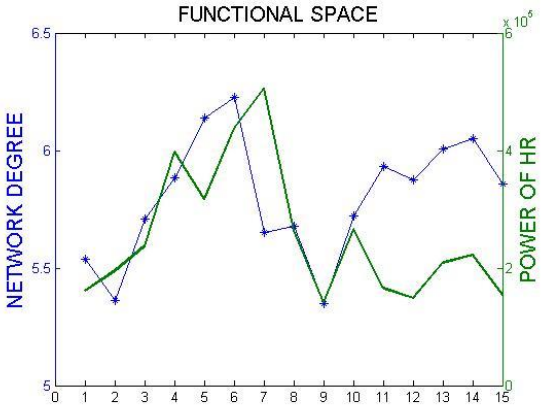

A)

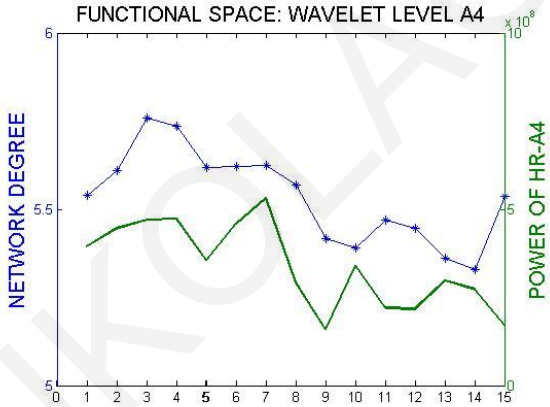

B)

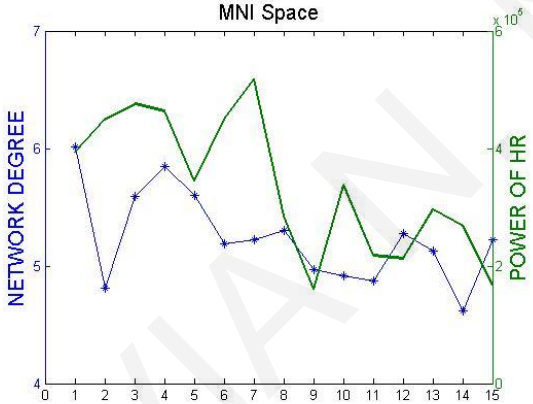

C)

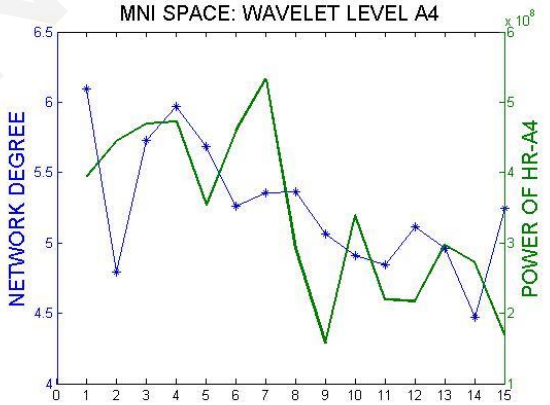

D)

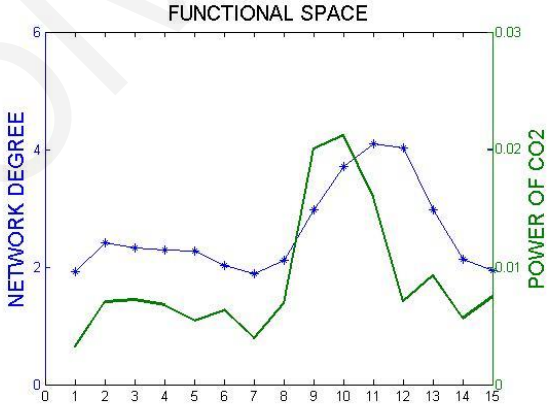

E)

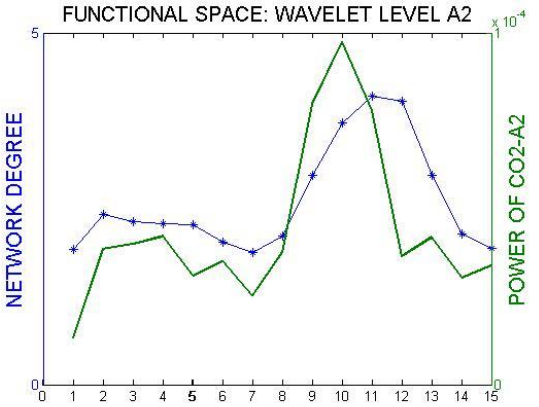

F)

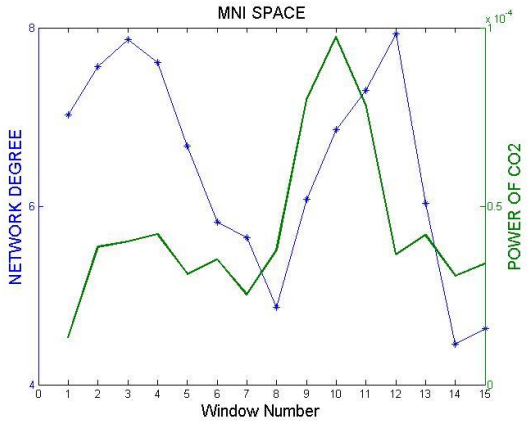

G)

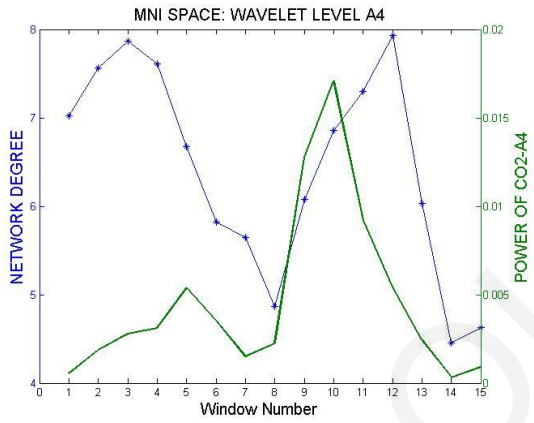

H)

Figure 4.4. DMN degree and power of HR (top four panels) and PETCO2 (bottom four panels) signals as a function of time for two representative volunteers obtained from mask-based analysis in (A) functional space, (B) functional space, wavelet level A4 (0-0.25 Hz), (C) MNI space, (D) MNI space, wavelet level A4 (0-0.25 Hz), (E) functional space, (F) functional space, wavelet level A2 (0-0.08 Hz), (G) MNI space and (H) MNI space, wavelet level A4 (0-0.02 Hz).

4.3.2 Seed based Analysis

4.3.2.1 Default Mode Network

Results presented in this section were obtained from the individual functional space of each volunteer (Figure 4.5). That is because the results from the seed-based analysis indicated clearly that registration to the MNI space (and the resulting blurring of the corresponding BOLD time series) considerably affects the results. The spatial overlap between mask-based and seed-based analysis for the DMN areas was 94.82% for the ACC, 44.65% for the PCC, 76.33% for the thalamus, 83.15% for the precuneus and 92.85% for the medial prefrontal cortex ROIs. The Spearman correlation coefficients between time-varying DMN degree and band-limited PETCO2/HR power are given in Table 4-3 for all volunteers (mean ± standard deviation). These suggest the presence of temporal correlations between network degree and the PETCO2/HR power, as in the case of mask-based analysis (somewhat lower values – not shown - were obtained for total power, as above). As before, correlations were found to be much higher in the wavelet sub-band A2 for PETCO2 (0-0.08 Hz) and in the wavelet sub-band A4 for HR (0-0.25 Hz). As before, presents the *p* values for the obtained Spearman correlation coefficients for all volunteers in each space/sub-band are presented (Table 4-4). Overall, the results from the seed-based analysis are similar to the mask-based analysis, with statistical significance attained in most volunteers (9 out of 12 for PETCO2, 9 out of 11 for HR).

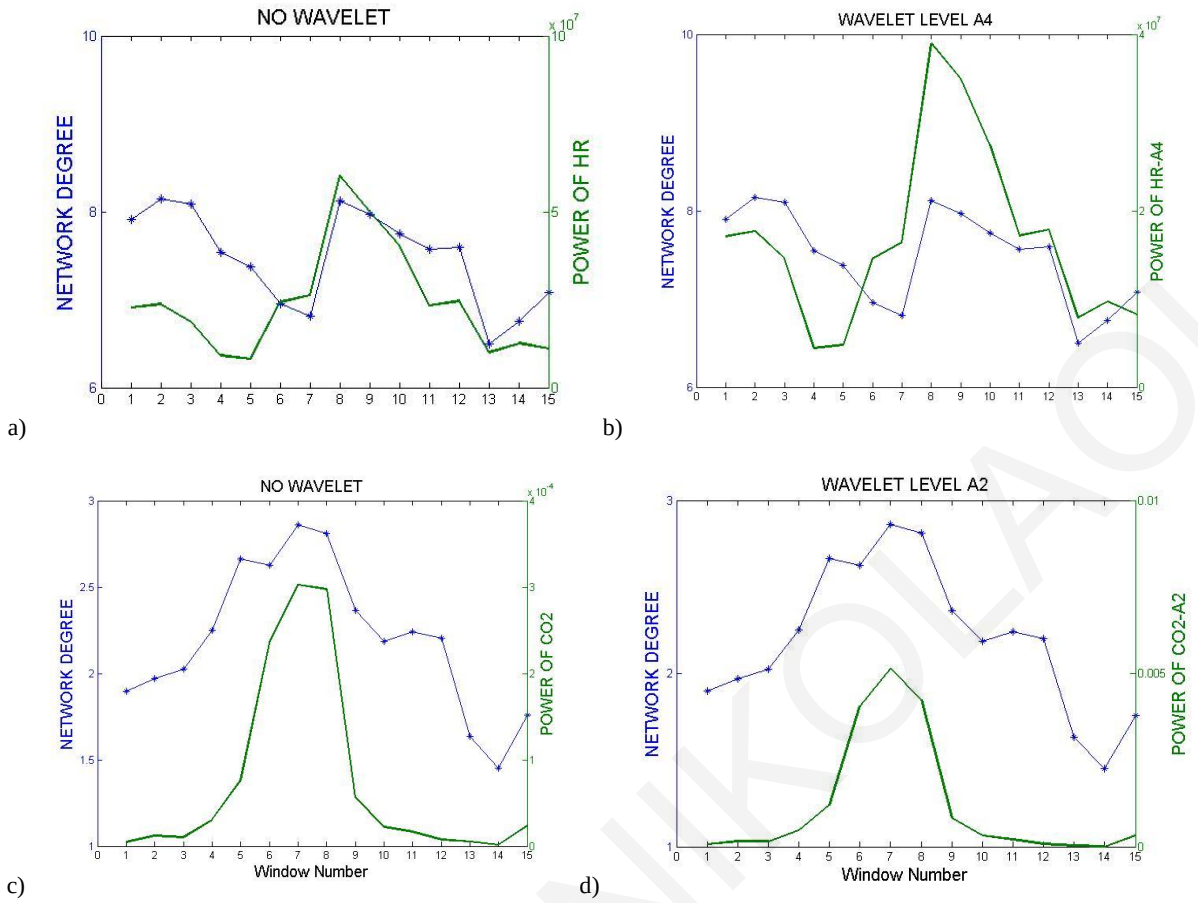

Figure 4.5. DMN degree and power of HR (top two panels) and PETCO2 (bottom two panels) signals as a function of time for two representative volunteers obtained from seed-based analysis in a) FS, power of CO2 vs network Degree, b) FS, power of CO2 at wavelet level A2(0-0.08 Hz) vs network Degree, c) FS, power of HR vs network Degree and d) FS, power of HR at wavelet level A4(0-0.25 Hz) vs network Degree. All correlations were quantified using the average cross-correlation absolute value between 0±5time lags.

CO2-FS		*CO2-FS-A2*		*HR-FS*		*HR-FS-A4*	
MEAN	**STD**	**MEAN**	**STD**	**MEAN**	**STD**	**MEAN**	**STD**
0.57	0.22	0.65	0.1	0.67	0.28	0.75	0.18

Table 4-3. Spearman correlation coefficients between time-varying DMN network degree and band-limited PETCO2 and HR power using seed-based analysis. FS: functional space, CO2-FS-A2: functional space, wavelet level A2 (0-0.08 Hz), HR-FS-A4: functional space, wavelet level A4 (0-0.25 Hz)

Volunteers	**1**	**2**	**3**	**4**	**5**	**6**	**7**	**8**	**9**	**10**	**11**	**12**
CO2-FS-A2	**0.0357**	0.0590	**0.0130**	0.0570	0.0956	**0.0246**	0.0786	**0.0128**	**0.0006**	**0.0002**	**0.0233**	**0.0357**
HR-FS-A4	**0.0092**	**0.0007**	**0.0174**	0.0711	-	0.1357	**0.0533**	**0.0017**	**3.75E-05**	**0.0004**	**0.0004**	**0.0092**

Table 4-4. Spearman correlation coefficient p-values obtained after using Hommel's method for all volunteers in the case of seed-based analysis. FS: Functional space, CO2-FS-A2: Functional space, wavelet level A2 (0-0.08 Hz), HR-FS-A4: Functional space, wavelet level A4 (0-0.25 Hz). Values in bold black are significant and values in blue are non-significant.

4.3.2.2 Visual and Somatosensory Networks

The procedure described above was applied to two additional RSNs, the Visual and Somatosensory networks (see Figure 4.6). The results were overall similar to those obtained for the DMN and revealed a modulatory effect for both PETCO2 and HR on the time-varying degree for both networks. The wavelet-based analysis yielded higher correlations than those achieved for the total signal power for the same frequency sub-bands as above (Tables 4-5 and 4-6). Statistically significant correlations between the time-varying visual and somatosensory RSN degree and band-limited HR and PETCO2 power were obtained for all volunteers in the case of the visual cortex, while interestingly for the somatosensory cortex significance was obtained for all volunteers in the case of HR but for only 2 out of 12 volunteers for PETCO2 - even though results were marginally significant for all the remaining volunteers (Table 4-6).

V-HR-A4		***SM-HR-A4***		***V-CO2-A4***		***SM-CO2-A2***	
MEAN	**STD**	**MEAN**	**STD**	**MEAN**	**STD**	**MEAN**	**STD**
0.60	0.12	0.70	0.18	0.52	0.11	0.7	0.06

Table 4-5. Spearman correlation coefficients between time-varying visual (V) and somatosensory (SM) network degree and time-varying HR and PETCO2 band-limited signal power. V-HR-A4: wavelet level A4 (0-0.25 Hz), SM-HR-A4: wavelet level A4 (0-0.25 Hz). V-CO2-A4: visual, wavelet level A4 (0-0.02 Hz), SM-CO2-A2: wavelet level A2 (0-0.08 Hz).

Volunteer	**1**	**2**	**3**	**4**	**5**	**6**	**7**	**8**	**9**	**10**	**11**	**12**
V-HR-A4	**0.0206**	**0.0232**	**0.0239**	**0.0299**	**-**	**0.0206**	**0.0299**	**0.0179**	**0.0194**	**0.0232**	**0.0206**	**0.0206**
SM-HR-A4	**0.0062**	**0.0123**	**0.0042**	**0.0050**	**-**	**0.0127**	**0.0130**	**0.0130**	**0.0123**	**0.0036**	**0.0018**	**0.0062**
V-CO2-A4	**0.0052**	**0.0090**	**0.0018**	**0.0052**	**0.0028**	**0.0094**	**0.0070**	**0.0002**	**0.0052**	**0.0218**	**0.0062**	**0.0052**
SM-CO2-A2	0.0668	0.0548	0.0596	0.0664	**0.0497**	0.0668	0.0528	0.0530	0.0548	0.0596	**0.0254**	0.0668

Table 4-6. Spearman correlation coefficient p-values obtained after using Hommel's method for all volunteers. V-HR-A4: visual, wavelet level A4 (0-0.25 Hz), SM-HR-A4: somatosensory wavelet level A4 (0-0.25 Hz), V-CO2-A4: visual, wavelet level A4 (0-0.02 Hz), SM-CO2-A2: somatosensory wavelet level A2 (0-0.08 Hz). Values in bold black are significant and values in blue are non-significant.

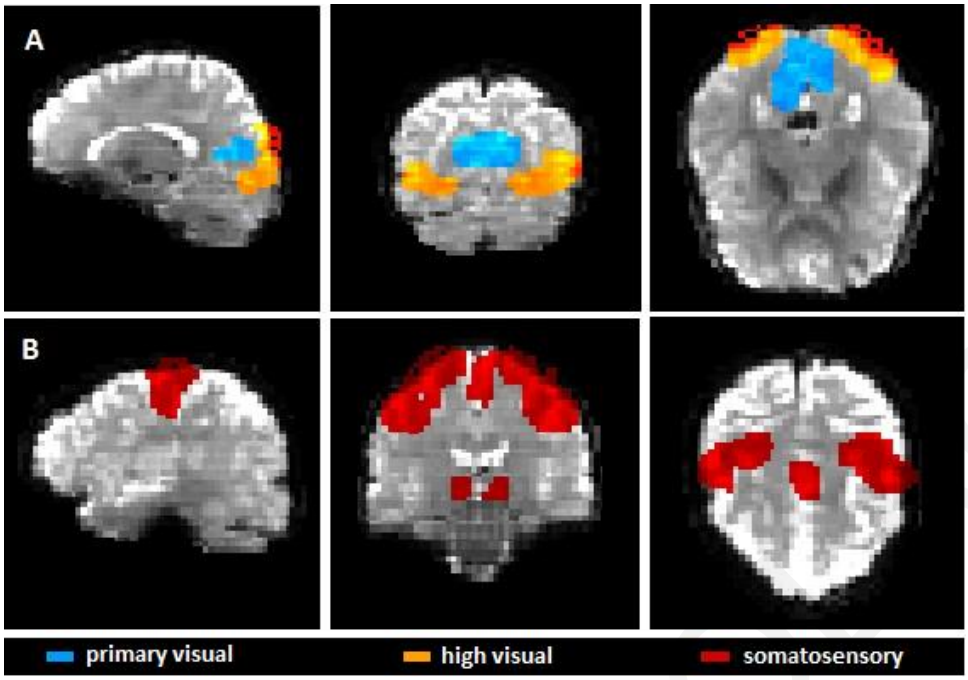

Figure 4.6. A) Resting-state visual network (high visual: orange and primary visual: cyan) and B) resting-state somatosensory network as obtained from seed-based analysis

5. Independent Component Analysis

In this chapter, the results from the investigation of DFC using various forms of independent component analysis and the effect of physiological signals are displayed. The preliminary results of this study are reported in an abstract proceeding (Nikolaou et al., ISMRM 2018) while the final work is reported in a conference proceeding (Nikolaou et al., EMBS 2018).

5.1 Resting-state Dynamic Functional Connectivity Analysis Using ICA

5.1.1 Low Dimensionality ICA

For the low dimensionality analysis, out of the 25 independent components, 9 RSNs were identified. Our analysis was then focused on the following ones:

1) DMN. For the DMN the posterior portion and anterior part of the DMN was identified. The first part is composed by the posterior cingulate cortex (PCC), the inferior parietal lobule and part of the frontal lobe. The second part is composed mainly by the medial prefrontal cortex (mPFC)
2) the somatosensory network (SMN)
3) the visual network (see Figure 5.1).

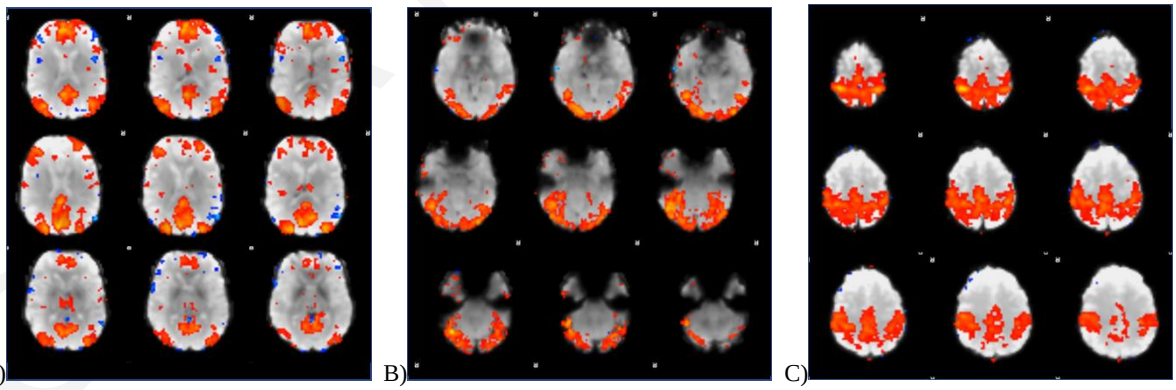

Figure 5.1. Low dimensional components relative to the networks of interest selected for this study : A) the DMN, B) the Visual Network and C) the SMN.

For these three RSNs, results from the functional space of each subject were obtained. As outlined in chapter 3, for the low dimensionality analysis, a new sliding-windows approach was applied with an increment of one time-point, to compare it with the results from the 10

time-point increment (the one volume increment was used to assess DFC with a better time resolution). Results obtained using RVT were also extracted. The Spearman correlation coefficients between time-varying DMN/SMN/Visual network degree and band-limited $PETCO_2$/RVT/HR/HRV power for the 10 time-point and for 1 time-point increments are given in Table 5-1 for the sub-bands of maximum correlation.

		LOW DIMENSIONALITY			
		10 TIME-POINT INCREMENT		1 TIME-POINT INCREMENT	
		MEAN	**STD**	**MEAN**	**STD**
DMN	**CO2-A6**	0.5321	0.1	0.5844	0.13
	RVT-A6	0.5607	0.05	0.6032	0.083
	HR-A4	0.6179	0.08	0.6755	0.11
	HRV-A4	0.5821	0.079	0.6655	0.11
SMN	**CO2-A7**	0.5357	0.15	0.5571	0.18
	RVT-A7	0.5214	0.09	0.5571	0.12
	HR-A5	0.6143	0.075	0.6092	0.10
	HRV-A5	0.575	0.072	0.5999	0.11
VISUAL	**CO2-A8**	0.5679	0.13	0.5231	0.16
	RVT-A8	0.6532	0.12	0.6532	0.15
	HR-A6	0.7286	0.077	0.8118	0.10
	HRV-A6	0.7932	0.089	0.7964	0.12

Table 5-1. Spearman correlation coefficients between time-varying DMN/SMN/Visual network degree and time-varying PETCO2/RVT/HR/HRV band-limited signal power for 10 time-point and 1 time-point increments. CO2-A6: wavelet level A6 (0-0.063Hz), RVT-A6: wavelet level A6(0-0.063Hz), HR-A4: wavelet level A4 (0-0.25 Hz), HRV-A4: wavelet level A4 (0-0.25 Hz).

These suggest the presence of temporal correlations between network degree and the band-limited power of the physiological signals. In more detail, the wavelet level A6 yielded higher values for the $PETCO_2$ and RVT signals, whereas the wavelet level A4 yielded higher values for HR and HRV. The values obtained for HR and HRV were, as expected, very similar. Figures 5.2-5.4 demonstrate these temporal similarities very clearly. The sliding window approach using one time-point increment yielded slightly higher values compared to the 10 time-point increment. In the following figures (Figures 5.2-5.4), results from the above tables are shown for some representative volunteers.

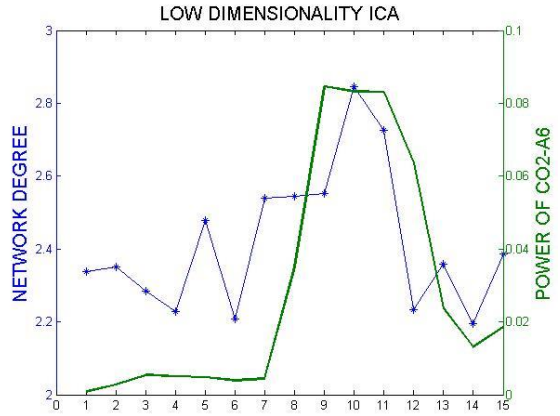

A)

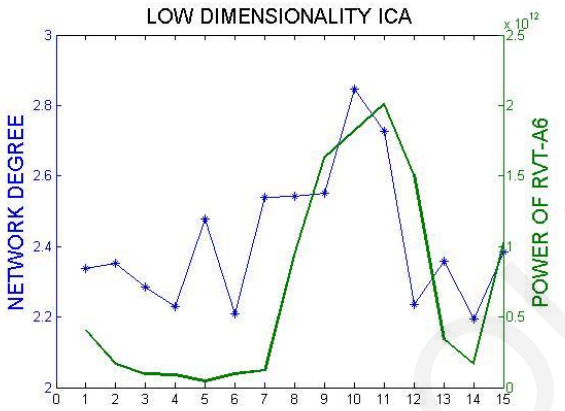

B)

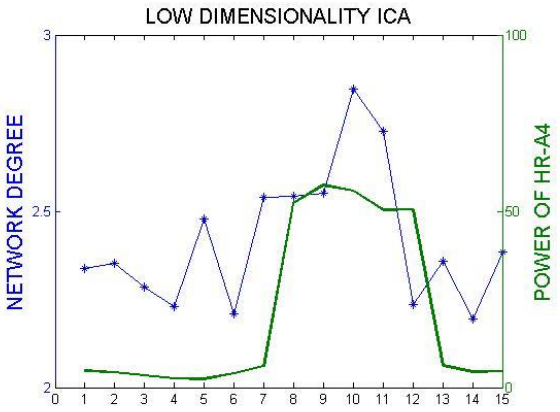

C)

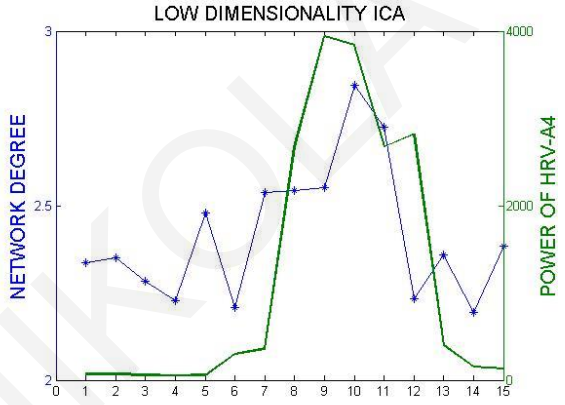

D)

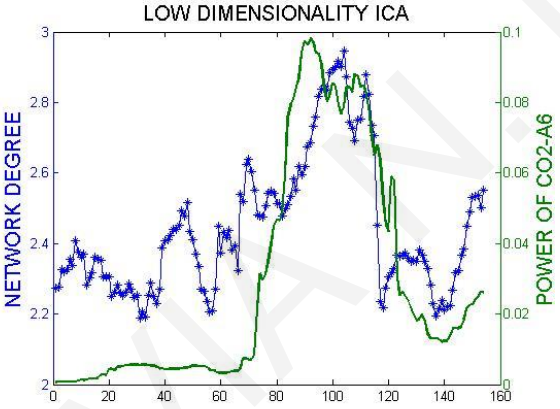

E)

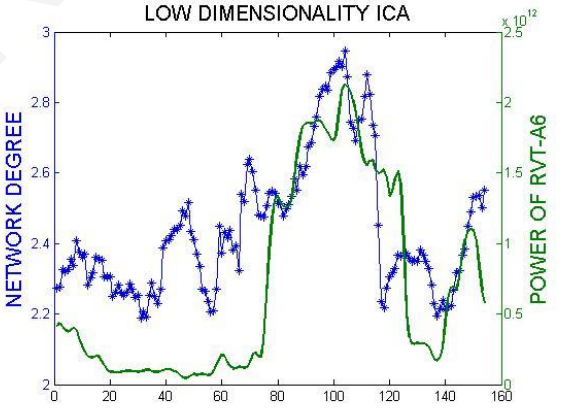

F)

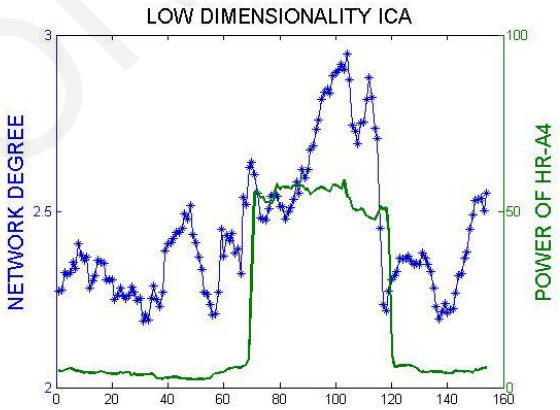

G)

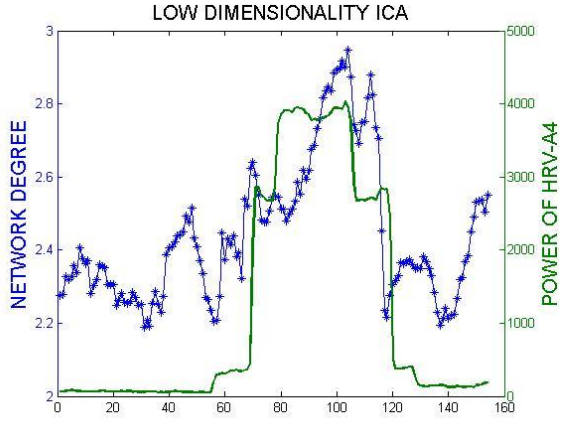

H)

Figure 5.2. DMN degree and band-limited power of CO2/RVT/HR/HRV signals as a function of time for one representative volunteer obtained from low dimensionality ICA A) power of CO2 at wavelet level A6 (0-0.0625Hz) vs network Degree for a 10 time-point increment, B) power of RVT at wavelet level A6 (0-0.0625Hz) vs network Degree for a 10 time-point increment, C) power of HR at wavelet level A4 (0-0.25Hz) vs network Degree for a 10 time-point increment, D) power of HRV at wavelet level A4 (0-0.25Hz) vs network Degree for a 10 time-point increment, E) power of CO2 at wavelet level A6 (0-0.0625Hz) vs network Degree for a 1 time-point increment, F) power of RVT at wavelet level A6 (0-0.0625Hz) vs network Degree for a 1 time-point increment, G) power of HR at wavelet level A4 (0-0.25Hz) vs network Degree for a 1 time-point increment and H) power of HRV at wavelet level A4 (0-0.25Hz) vs network Degree for a 1 time-point increment. All correlations were quantified using the average cross-correlation absolute value between 0±5time lags.

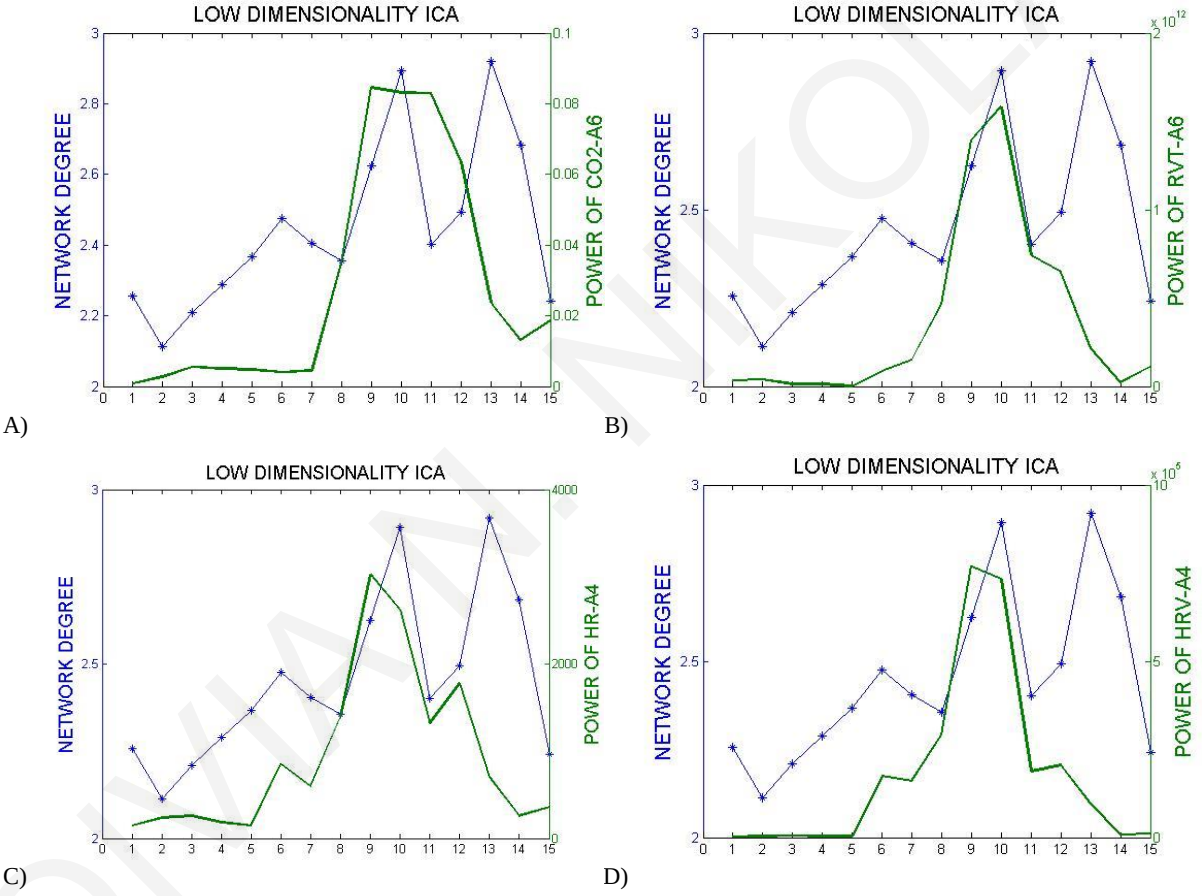

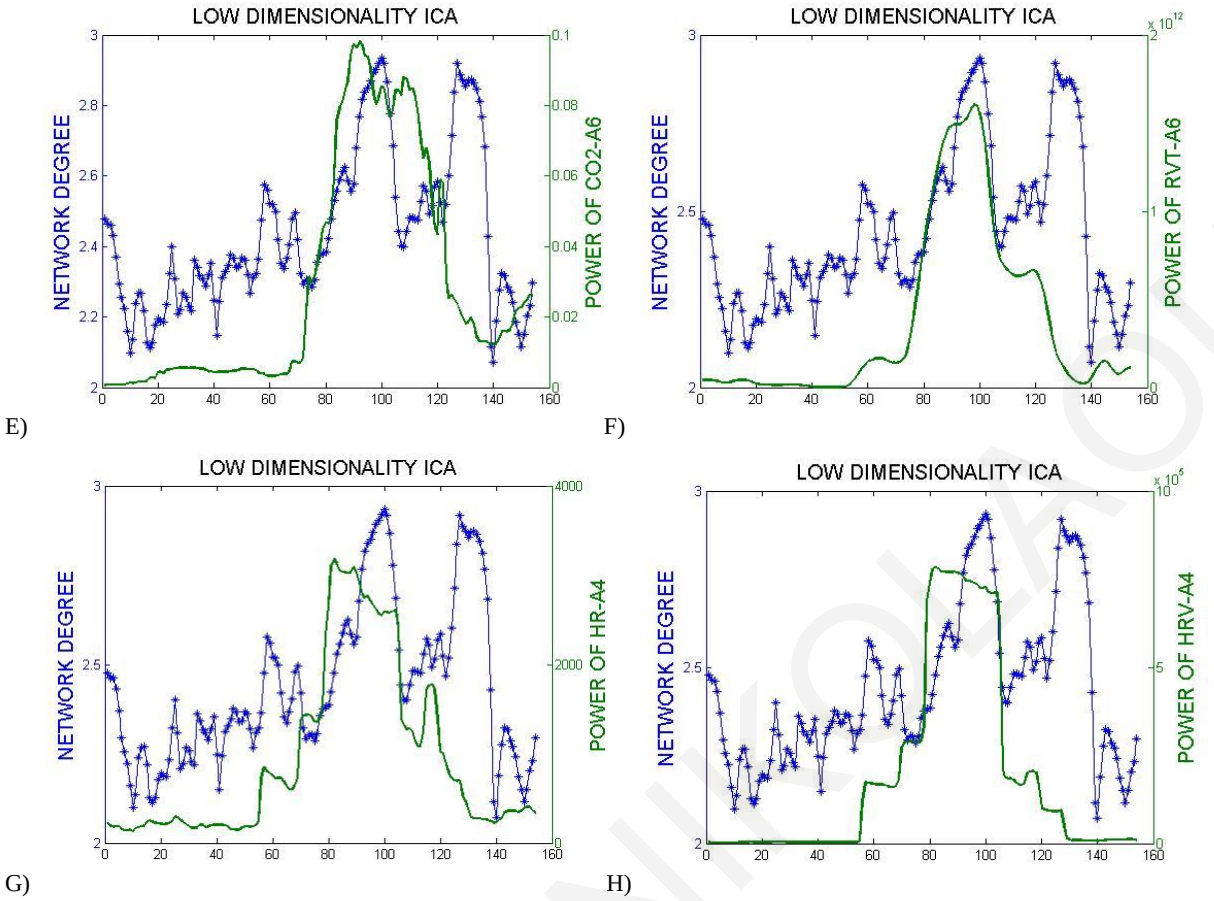

Figure 5.3. SMN degree and band-limited power of CO2/RVT/HR/HRV signals as a function of time for one representative volunteer obtained from low dimensionality ICA in A) power of CO2 at wavelet level A6 (0-0.0625Hz) vs network Degree for a 10 time-point increment, B) power of RVT at wavelet level A6 (0-0.0625Hz) vs network Degree for a 10 time-point increment, C) power of HR at wavelet level A4 (0-0.25Hz) vs network Degree for a 10 time-point increment, D) power of HRV at wavelet level A4 (0-0.25Hz) vs network Degree for a 10 time-point increment, E) power of CO2 at wavelet level A6 (0-0.0625Hz) vs network Degree for a 1 time-point increment, F) power of RVT at wavelet level A6 (0-0.0625Hz) vs network Degree for a 1 time-point increment, G) power of HR at wavelet level A4 (0-0.25Hz) vs network Degree for a 1 time-point increment and H) power of HRV at wavelet level A4 (0-0.25Hz) vs network Degree for a 1 time-point increment. All correlations were quantified using the average cross-correlation absolute value between 0±5time lags.

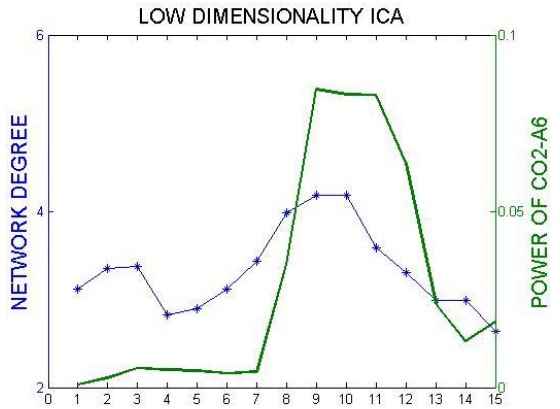

A)

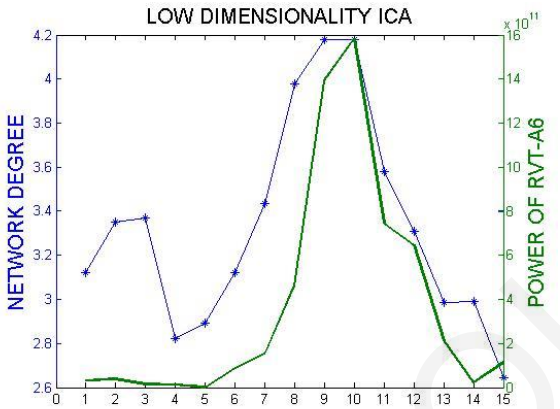

B)

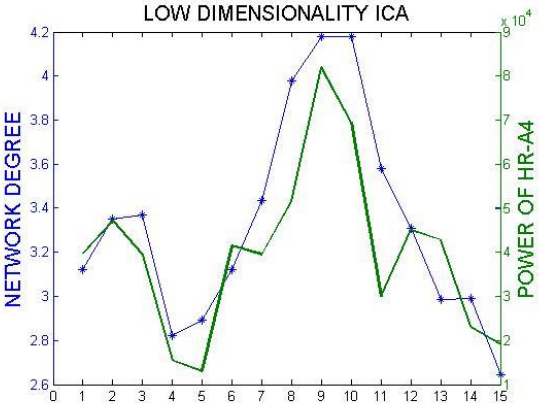

C)

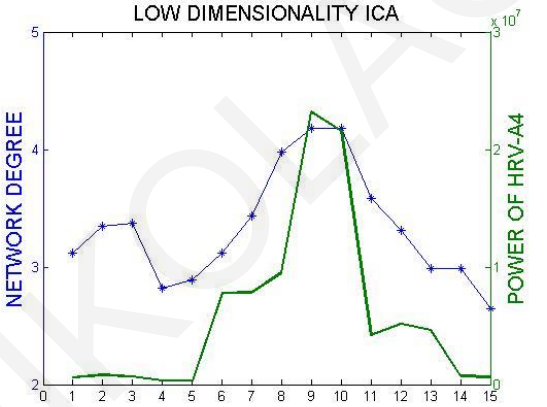

D)

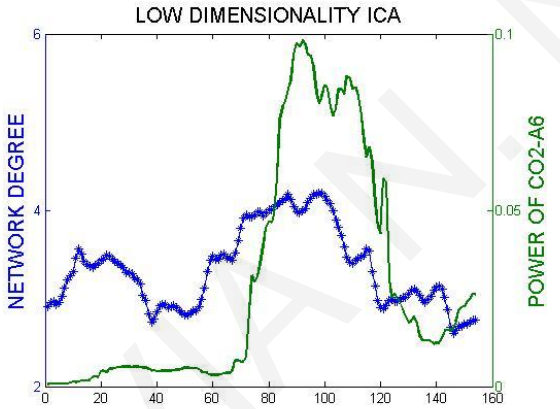

E)

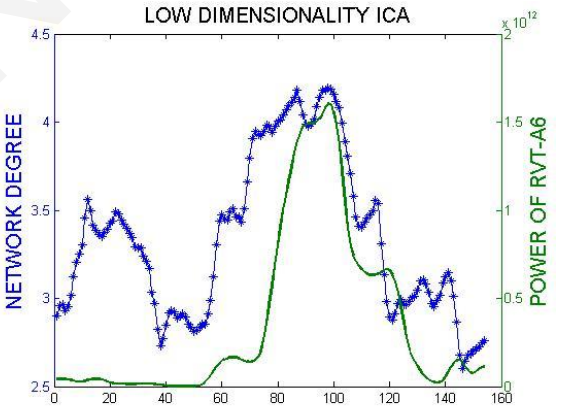

F)

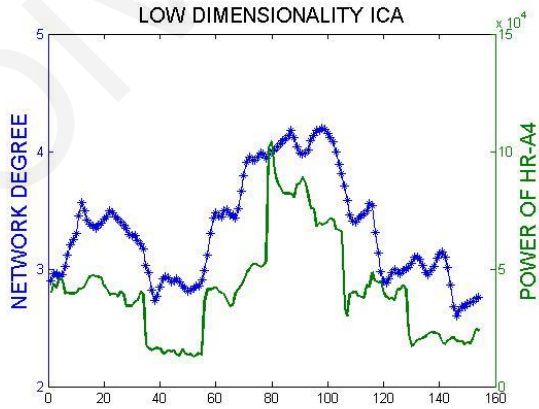

G)

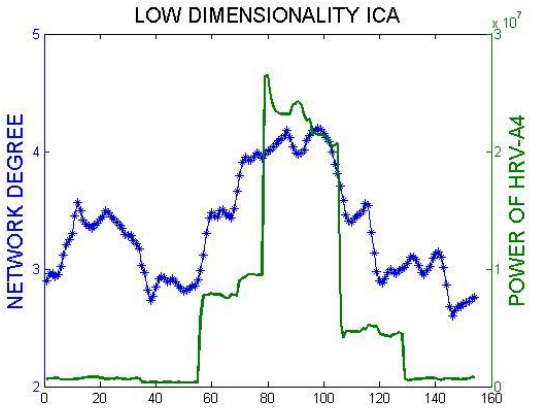

H)

Figure 5.4. Visual network degree and band-limited power of CO2/RVT/HR/HRV signals as a function of time for one representative volunteer obtained from low dimensionality ICA in A) power of CO2 at wavelet level A6 (0-0.0625Hz) vs network Degree for a 10 time-point increment, B) power of RVT at wavelet level A6 (0-0.0625Hz) vs network Degree for a 10 time-point increment, C) power of HR at wavelet level A4 (0-0.25Hz) vs network Degree for a 10 time-point increment, D) power of HRV at wavelet level A4 (0-0.25Hz) vs network Degree for a 10 time-point increment, E) power of CO2 at wavelet level A6 (0-0.0625Hz) vs network Degree for a 1 time-point increment, F) power of RVT at wavelet level A6 (0-0.0625Hz) vs network Degree for a 1 time-point increment, G) power of HR at wavelet level A4 (0-0.25Hz) vs network Degree for a 1 time-point increment and H) power of HRV at wavelet level A4 (0-0.25Hz) vs network Degree for a 1 time-point increment. All correlations were quantified using the average cross-correlation absolute value between 0±5time lags.

General Linear Models and Multiple Linear Regression

As explained in the previous chapters, to investigate further the relationship between the time-varying RSN degree and the band-limited power of CO_2/RVT/HR, general linear models were created for both sliding window analysis increments (1 and 10 time lags). In the following figures (Figures 5.5-5.7), the values of the RSN degree versus the values of the band-limited power of CO_2/RVT/HR can be seen (in blue crosses). The underlying relationship between the dependent variable (RSNs degree) and independent variable (band-limited power of CO_2/RVT/HR) as extracted by the GLM models obtained can be seen in red. (The term "linear" in linear regression means that the regression function is linear in the coefficients α and β_j. It is not required that the independent variables X_i appear as linear terms in the regression function.)

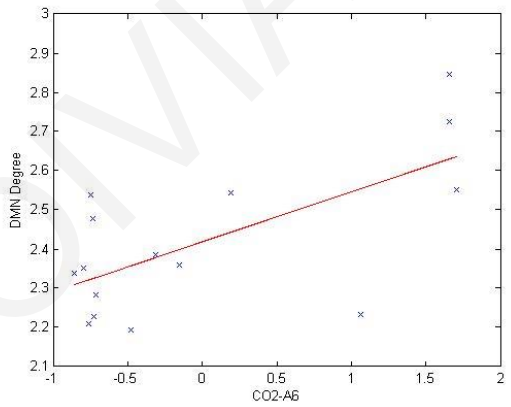

A)

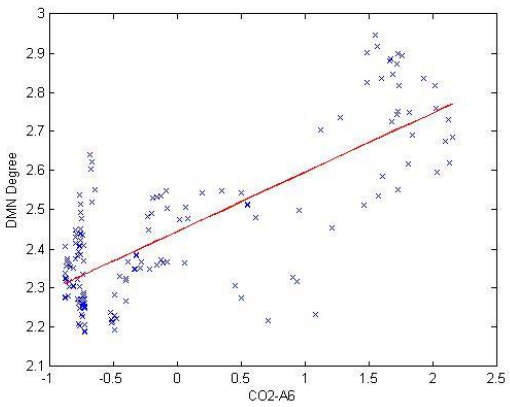

B)

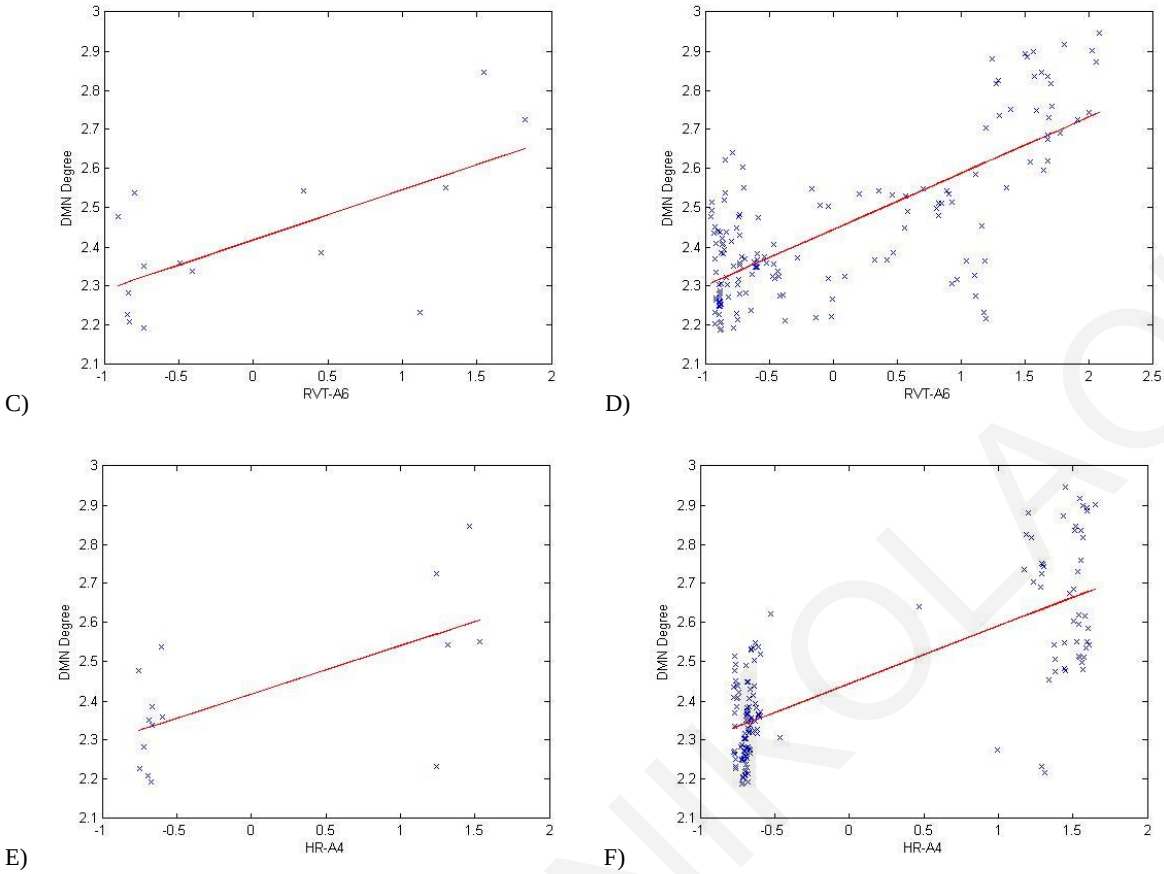

Figure 5.5. DMN degree versus band-limited power of CO2/RVT/HR/HRV signals for one representative volunteer obtained from low dimensionality ICA in A) network degree vs power of CO2 at wavelet level A6 (0-0.0625Hz) for a 10 time-point increment, B) network degree vs power of CO2 at wavelet level A6 (0-0.0625Hz) for a 1 time-point increment, C) network degree vs power of RVT at wavelet level A6 (0-0.0625Hz) for a 10 time-point increment, D) network degree vs power of RVT at wavelet level A6 (0-0.0625Hz) for a 1 time-point increment, E) network degree vs power of HR at wavelet level A4 (0-0.25Hz) for a 10 time-point increment and F) network degree vs power of HR at wavelet level A4 (0-0.25Hz) for a 1 time-point increment.

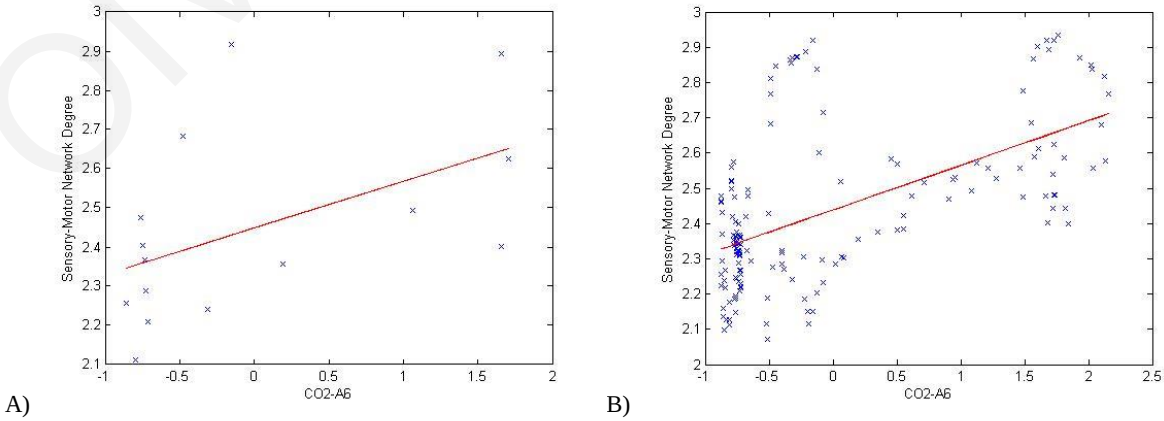

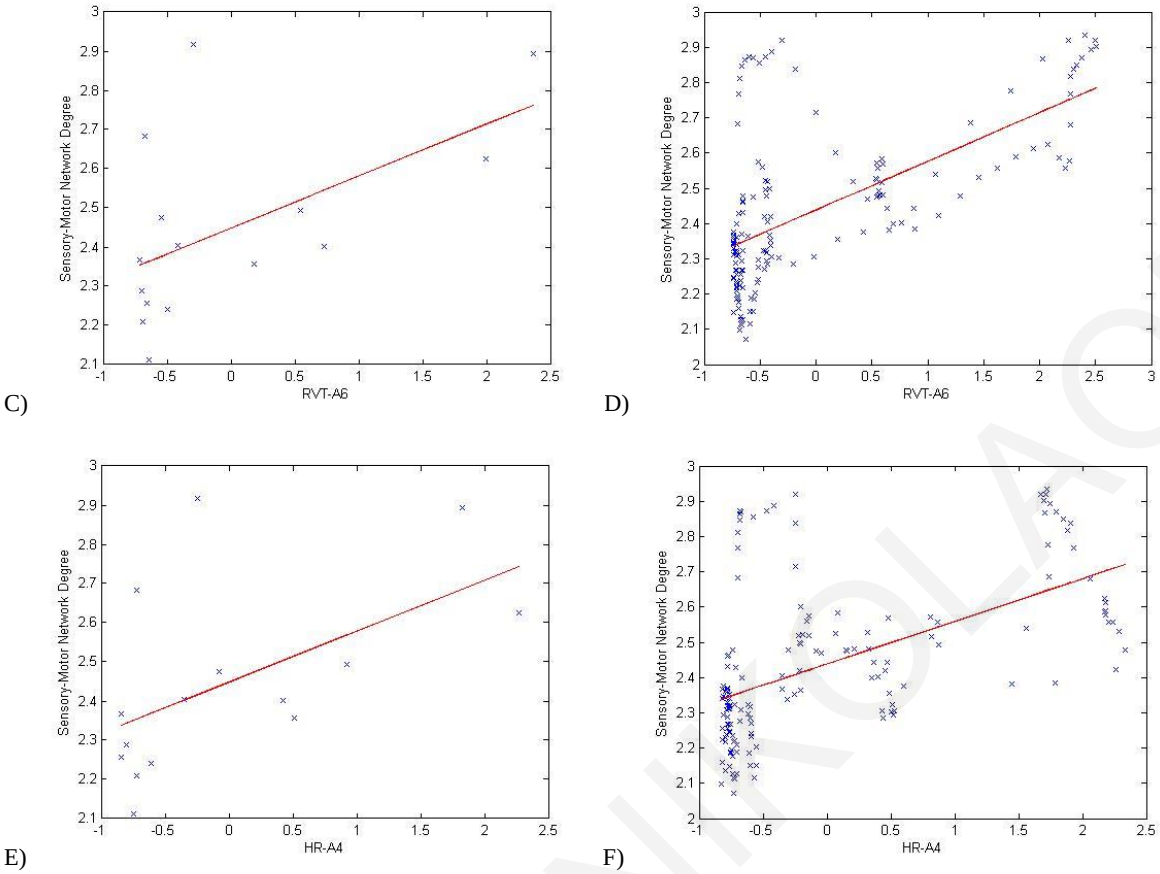

Figure 5.6. Sensory-Motor network degree versus band-limited power of CO2/RVT/HR/HRV signals for one representative volunteer obtained from low dimensionality ICA in A) network degree vs power of CO2 at wavelet level A6 (0-0.0625Hz) for a 10 time-point increment, B) network degree vs power of CO2 at wavelet level A6 (0-0.0625Hz) for a 1 time-point increment, C) network degree vs power of RVT at wavelet level A6 (0-0.0625Hz) for a 10 time-point increment, D) network degree vs power of RVT at wavelet level A6 (0-0.0625Hz) for a 1 time-point increment, E) network degree vs power of HR at wavelet level A4 (0-0.25Hz) for a 10 time-point increment and F) network degree vs power of HR at wavelet level A4 (0-0.25Hz) for a 1 time-point increment.

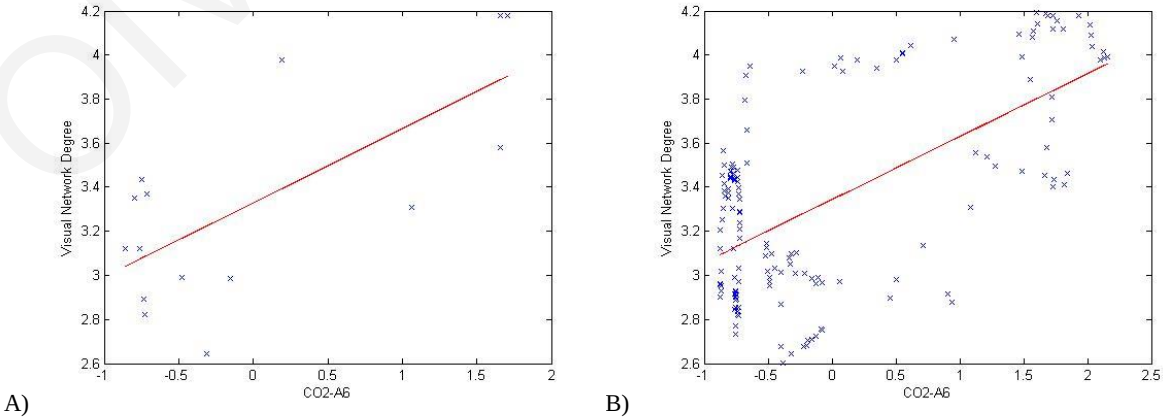

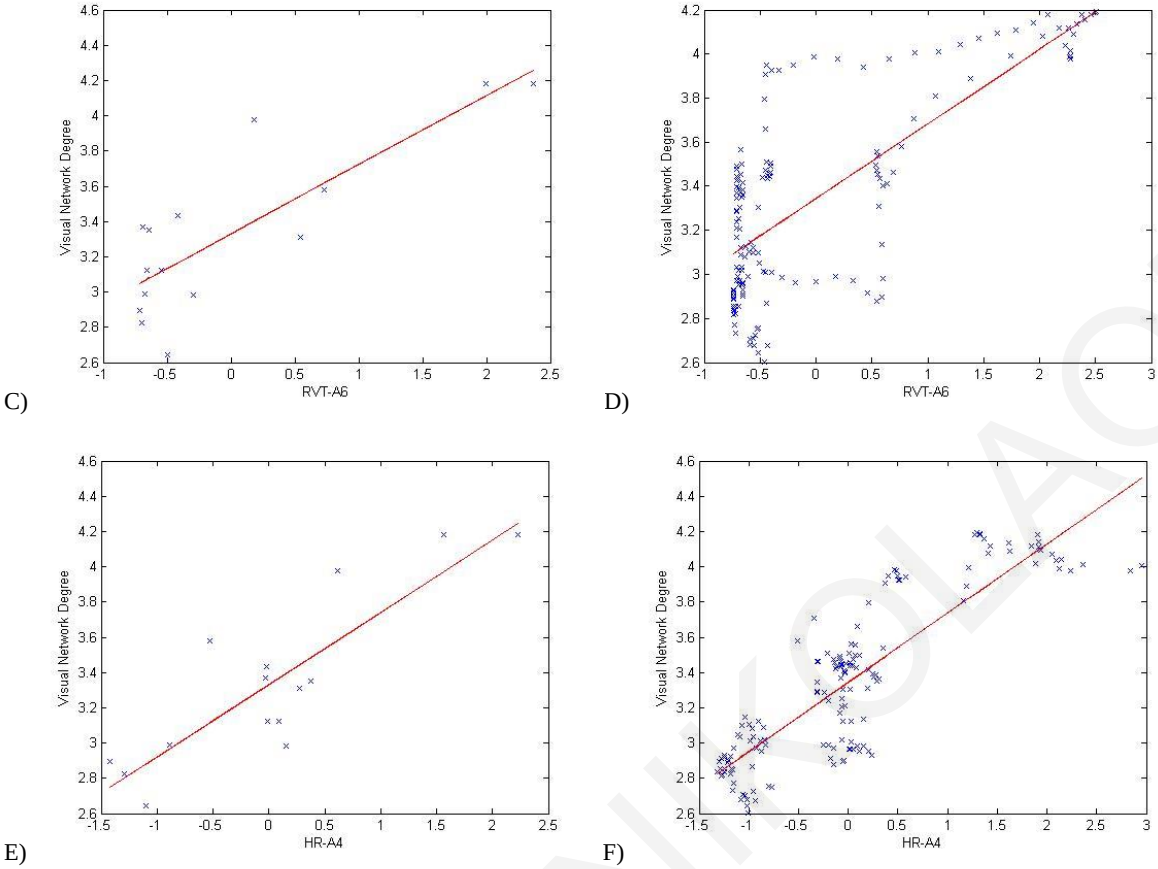

Figure 5.7. Visual network degree versus band-limited power of CO2/RVT/HR/HRV signals for one representative volunteer obtained from low dimensionality ICA in A) network degree vs power of CO2 at wavelet level A6 (0-0.0625Hz) for a 10 time-point increment, B) network degree vs power of CO2 at wavelet level A6 (0-0.0625Hz) for a 1 time-point increment, C) network degree vs power of RVT at wavelet level A6 (0-0.0625Hz) for a 10 time-point increment, D) network degree vs power of RVT at wavelet level A6 (0-0.0625Hz) for a 1 time-point increment, E) network degree vs power of HR at wavelet level A4 (0-0.25Hz) for a 10 time-point increment and F) network degree vs power of HR at wavelet level A4 (0-0.25Hz) for a 1 time-point increment.

For the low dimensionality ICA analysis and sliding window analysis with a 1 time-point increment (it is generally accepted that in this model, a large amount of data is acquired), all the limited bands of the power of the physiological signals were used as the independent variables in the GLMs that were fitted for each RSN.

- For the DMN, separate GLMs for the band limited power of CO_2, RVT and HR were applied as can be seen in Figures 5.8 A and B. Subsequently a multiple linear model incorporating all signals was applied (Figure 5.8-C). In the case of GLM, CO_2 yielded a higher value for the estimated regression coefficient b1 compared to RVT and HR. In

the case of MLR, CO_2 yielded the higher coefficient value and both CO_2 and HR yielded *p*-values lower than 0.05.

- The same procedure was applied for the Sensory-Motor network as can be seen in Figure 5.9. In the case of univariate GLMs, CO_2 and RVT yielded larger values for the estimated coefficient b1 compared to HR. In the case of MLR, RVT yielded the larger coefficient value and was the only signal which yielded *p*-values lower than 0.05.
- For the Visual network the results can be seen in Figure 5.10. In the case of univariate GLMs, HR yielded a larger value for the regression coefficient b1 compared to RVT and CO_2. In the case of the MLR model, HR yielded the highest coefficient and was the only signal which yielded *p*-values lower than 0.05.
- Larger values for an estimated regression coefficient suggest that the corresponding physiological signal has a more pronounced effect on the independent variable y, which is the time-varying degree of each RSN. As can be seen, for different RSNs, different signals seem to be more important. HR seems to be more important for the visual network. Some possible reasons for this is that there is a strong relationship between HRV and vision. For example, red color makes the heart beat faster.

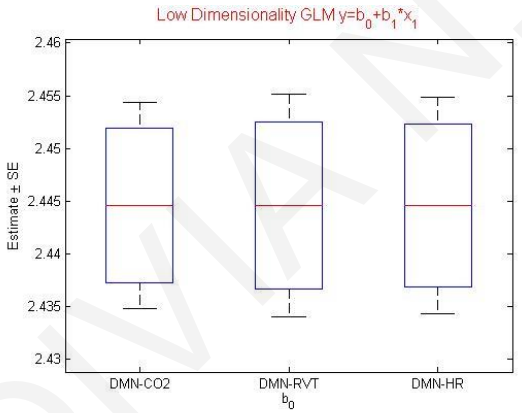

A)

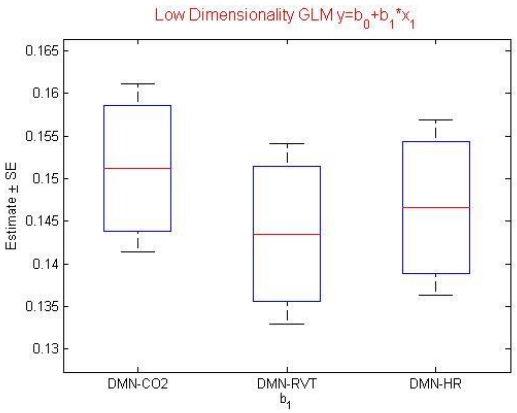

B)

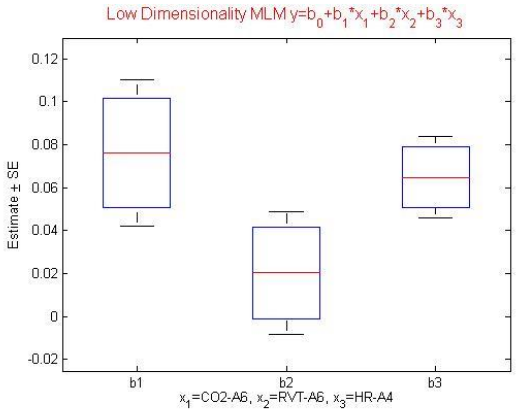

C)

Figure 5.8. A) Estimated values of b0 and B) b1 for the three univariate GLMs between DMN degree and band-limited power of CO2/RVT/HR obtained from low dimensionality ICA for a 1 time-point increment, C) Estimated values of b1, b2 and b3 for the MLR model between DMN degree and band-limited power of CO2/RVT/HR obtained from low dimensionality ICA for a 1 time-point increment.

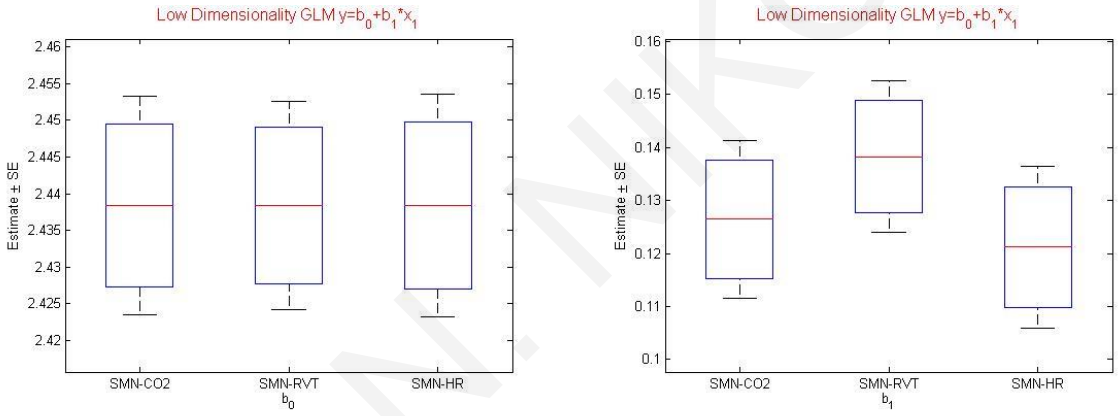

A) B)

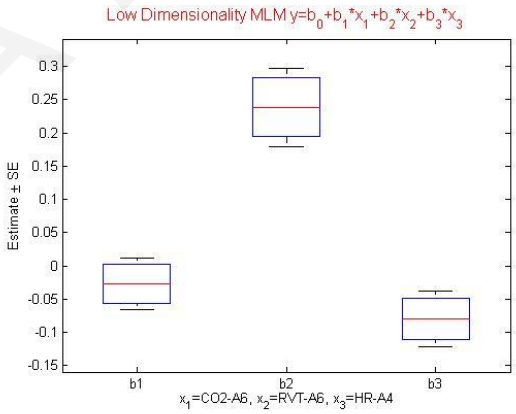

C)

Figure 5.9. A) Estimated values of b0 and B) b1 for the three univariate GLMs between SMN degree and band-limited power of CO2/RVT/HR obtained from low dimensionality ICA for a 1 time-point increment, C) Estimated values of b1, b2 and b3 for the MLR model between SMN degree and band-limited power of CO2/RVT/HR obtained from low dimensionality ICA for a 1 time-point increment.

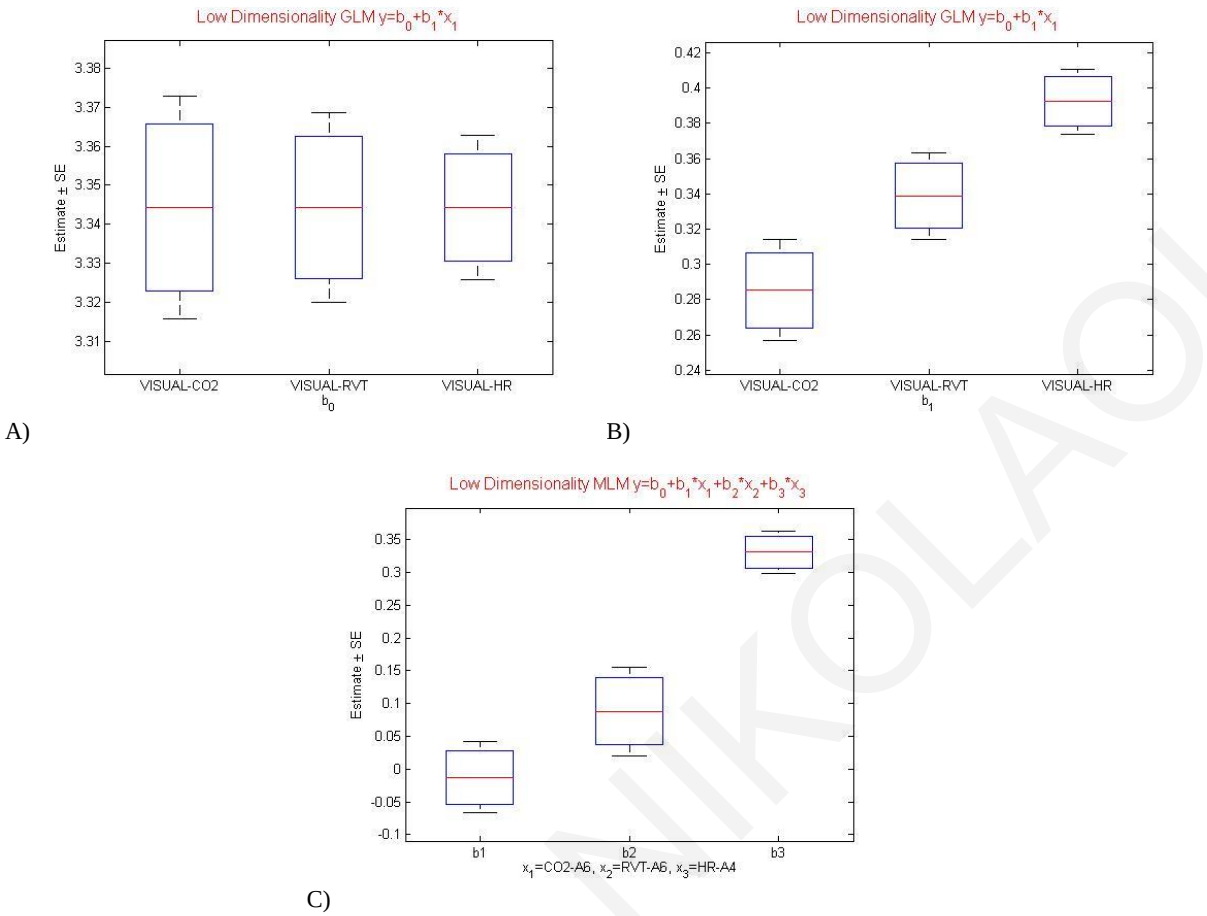

Figure 5.10. A) Estimated values of b0 and B) b1 for the three univariate GLMs between Visual Network degree and band-limited power of CO2/RVT/HR obtained from low dimensionality ICA for a 1 time-point increment, C) Estimated values of b1, b2 and b3 for the MLR model between Visual Network degree and band-limited power of CO2/RVT/HR obtained from low dimensionality ICA for a 1 time-point increment.

5.1.2 High Dimensionality ICA

Components of interest, related to the DMN, Visual network and SMN (see Figure 5.11) were apparent in several subcomponents when high dimensionality ICA was performed. Out of the 70 independent components, we identified 47 sub-networks of RSNs and detected 22 RSNs in total such DMN, SMN, Visual, Auditory and Basal Ganglia. Both the total number of RSNs and the number of sub-networks of RSNs increased as a function of ICA model order. Specifically, in the low dimensionality ICA only 9 RSNs were identified.

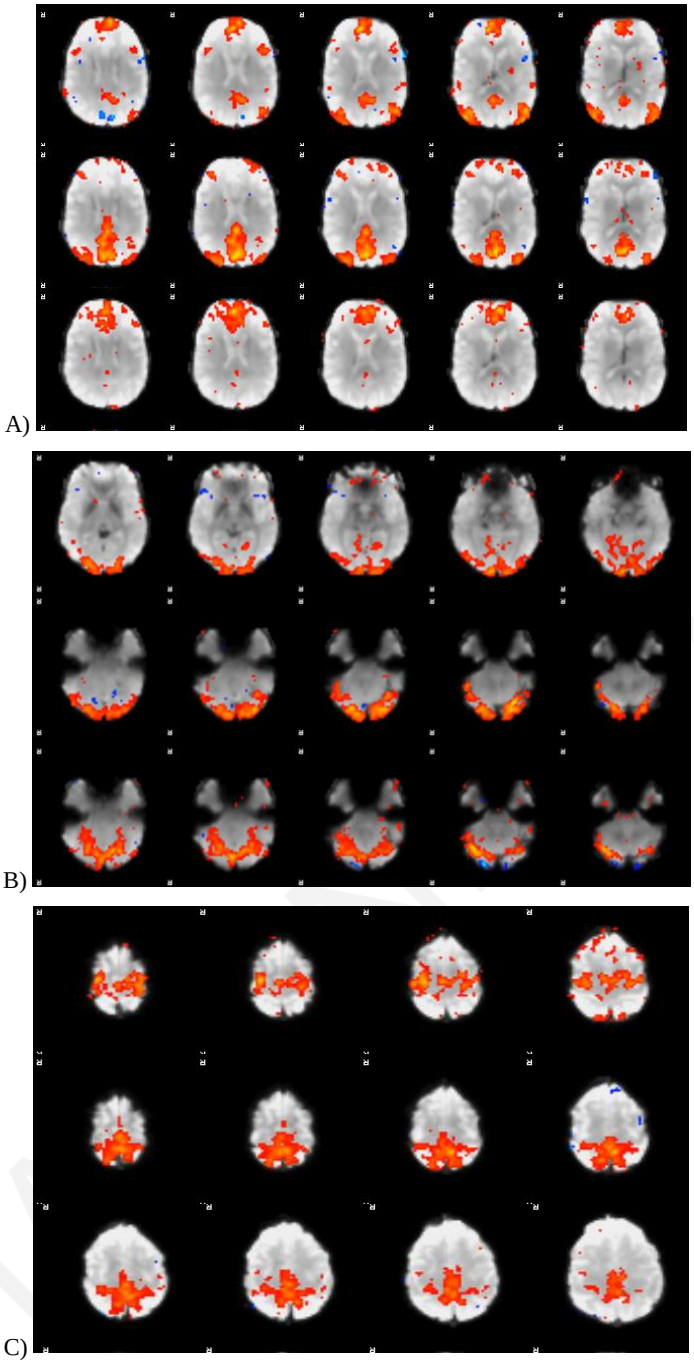

Figure 5.11. High dimensional components relative to the networks of interest selected for this study : A) the DMN, B) the Visual Network and C) the SMN.

The same procedure used for the low dimensionality ICA for the three mentioned RSNs (DMN, Visual network and SMN) was applied for the high dimensionality ICA. Specifically, the new sliding windows approach was applied with an increment on one time-point, to compare it with the results from the 10 time-point increment. The band-limited power of all physiological signals ($PETCO_2$, RVT, HR, HRV) was used to obtain our results. The Spearman correlation coefficients for the high dimensionality ICA between time-varying

DMN/SMN/Visual network degree and band-limited $PETCO_2$/RVT/HR/HRV power for the 10 time-point increment and for 1 time-point increment are given in Table 5-2. In the band-limited case, sub-bands of maximum correlation are presented. The correlations coefficients are averaged over all subjects (mean ± standard deviation).

		HIGH DIMENSIONALITY			
		10 TIME-POINT INCREMENT		1 TIME-POINT INCREMENT	
		MEAN	**STD**	**MEAN**	**STD**
DMN	**CO2-A6**	0.6505	0.20	0.6571	0.22
	RVT-A6	0.6705	0.15	0.6771	0.17
	HR-A4	0.8	0.18	0.8179	0.20
	HRV-A4	0.7829	0.18	0.8144	0.20
SMN	**CO2-A7**	0.5821	0.25	0.5839	0.27
	RVT-A7	0.5929	0.19	0.6486	0.21
	HR-A5	0.6429	0.17	0.641	0.19
	HRV-A5	0.6286	0.17	0.6497	0.19
VISUAL	**CO2-A8**	0.5964	0.23	0.6214	0.25
	RVT-A8	0.6946	0.22	0.7071	0.25
	HR-A6	0.7794	0.18	0.8179	0.20
	HRV-A6	0.8286	0.19	0.8476	0.21

Table 5-2. Spearman correlation coefficients between time-varying DMN/SMN/Visual network degree and time-varying PETCO2/RVT/HR/HRV band-limited signal power for 10 time-point and 1 time-point increments. CO2-A6: wavelet level A6 (0-0.063Hz), RVT-A6: wavelet level A6(0-0.063Hz), HR-A4: wavelet level A4 (0-0.25 Hz), HRV-A4: wavelet level A4 (0-0.25 Hz).

As can be seen from the above tables, results were consistent with the alternative analysis techniques used. Specifically, our results suggest the presence of temporal correlations between network degree and the band-limited power of the physiological signals. As before, the wavelet level A6 (0-0.063Hz) yielded the highest values for the $PETCO_2$ and RVT signals, whereas the wavelet level A4 (0-0.25Hz) yielded higher values for the HR and HRV as can be seen from the following figures. The sliding window using one time-point offset yielded slightly higher values against the 10 time-points offset. In the following figures (Figures 5.12-5.14) results corresponding to the above tables are shown for some representative volunteers.

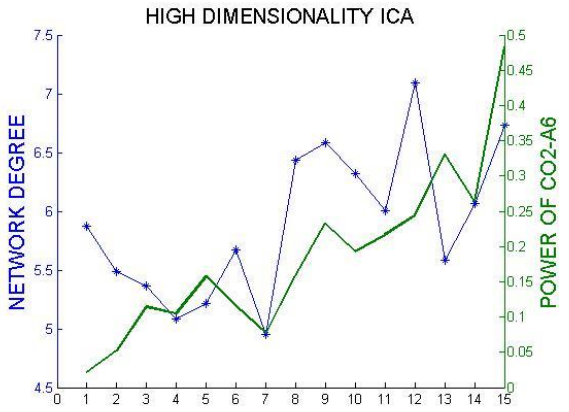

A)

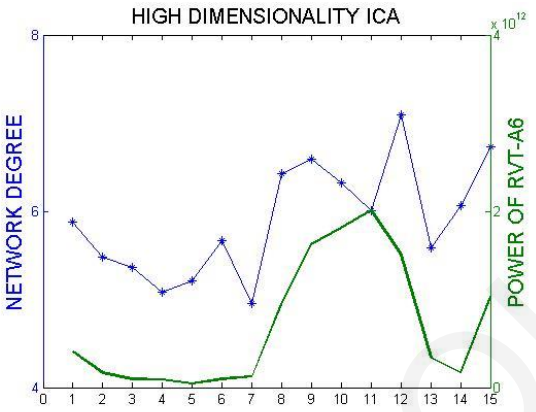

B)

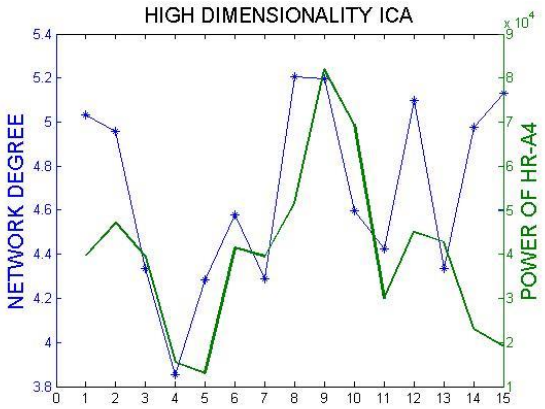

C)

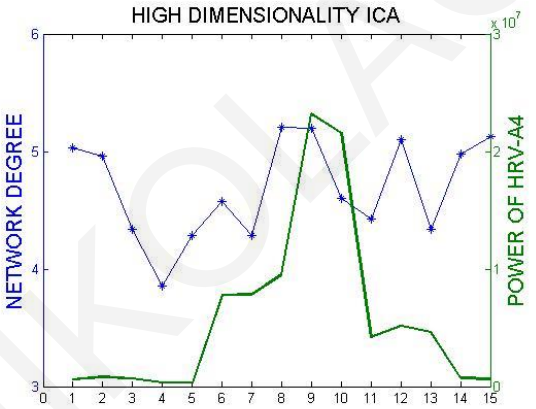

D)

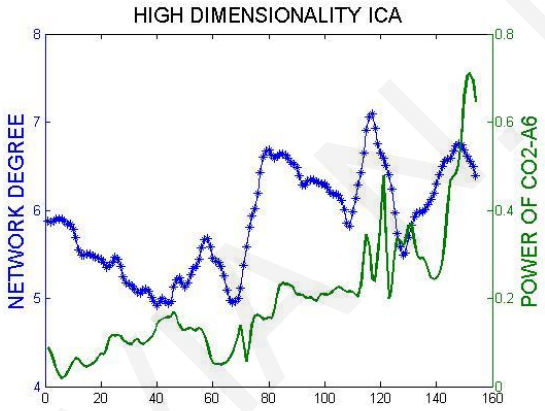

E)

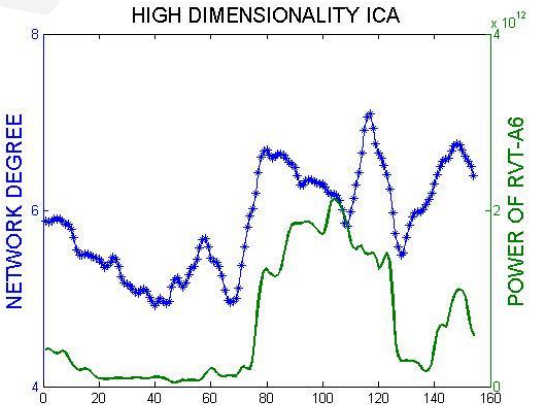

F)

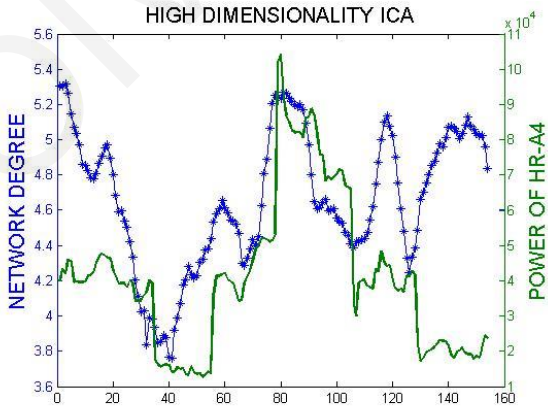

G)

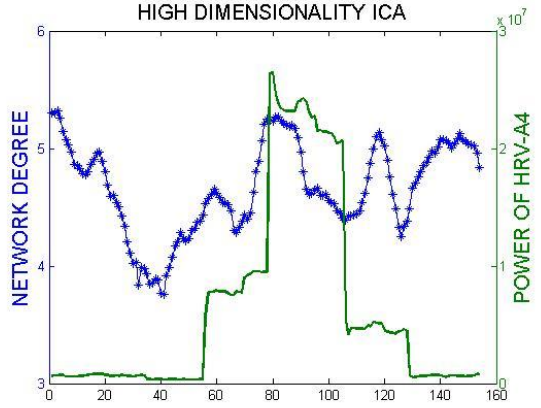

H)

Figure 5.12. DMN degree and band-limited power of CO2/RVT/HR/HRV signals as a function of time for one representative volunteer obtained from high dimensionality ICA. A) power of CO2 at wavelet level A6 (0-0.0625Hz) vs network Degree for a 10 time-point increment, B) power of RVT at wavelet level A6 (0-0.0625Hz) vs network Degree for a 10 time-point increment, C) power of HR at wavelet level A4 (0-0.25Hz) vs network Degree for a 10 time-point increment, D) power of HRV at wavelet level A4 (0-0.25Hz) vs network Degree for a 10 time-point increment, E) power of CO2 at wavelet level A6 (0-0.0625Hz) vs network Degree for a 1 time-point increment, F) power of RVT at wavelet level A6 (0-0.0625Hz) vs network Degree for a 1 time-point increment, G) power of HR at wavelet level A4 (0-0.25Hz) vs network Degree for a 1 time-point increment and H) power of HRV at wavelet level A4 (0-0.25Hz) vs network Degree for a 1 time-point increment. All correlations were quantified using the average cross-correlation absolute value between 0±5time lags.

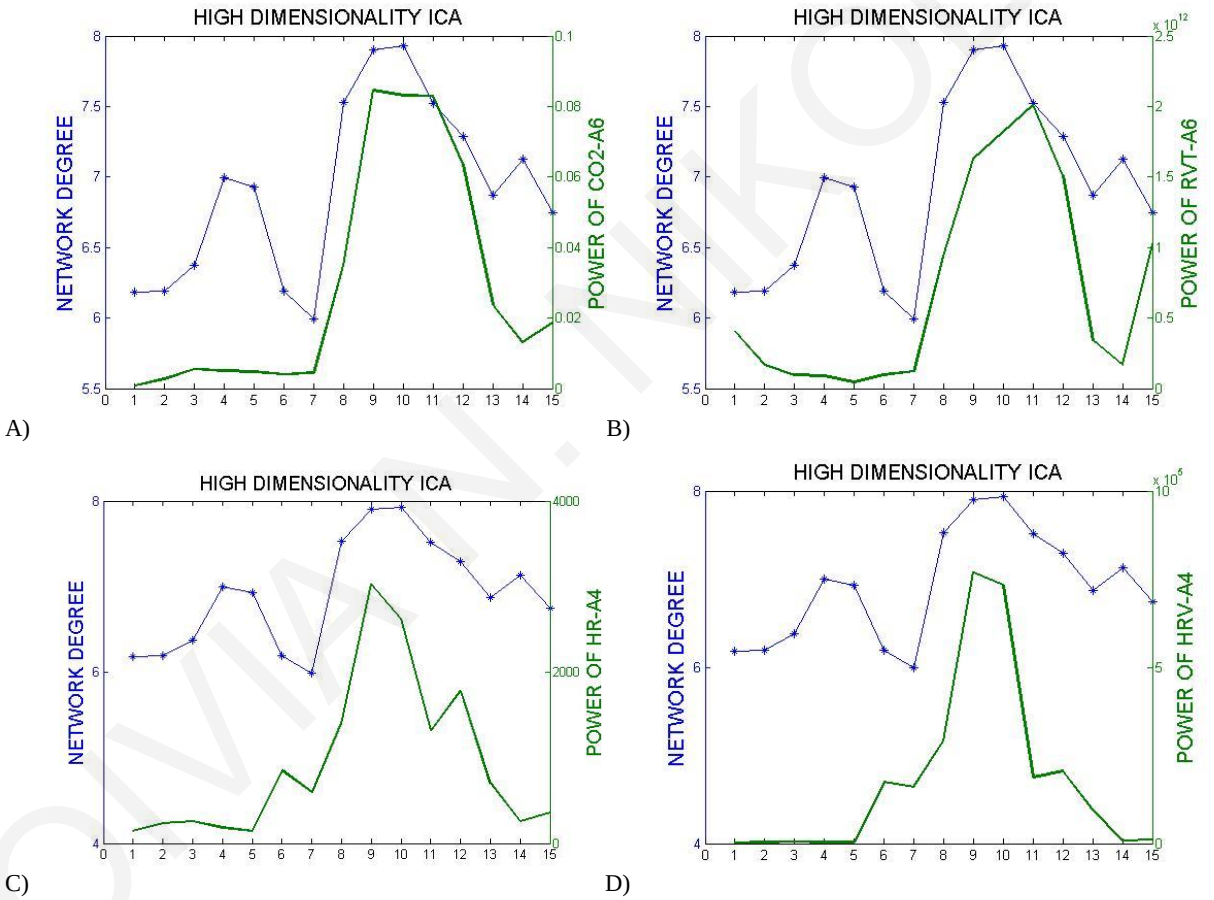

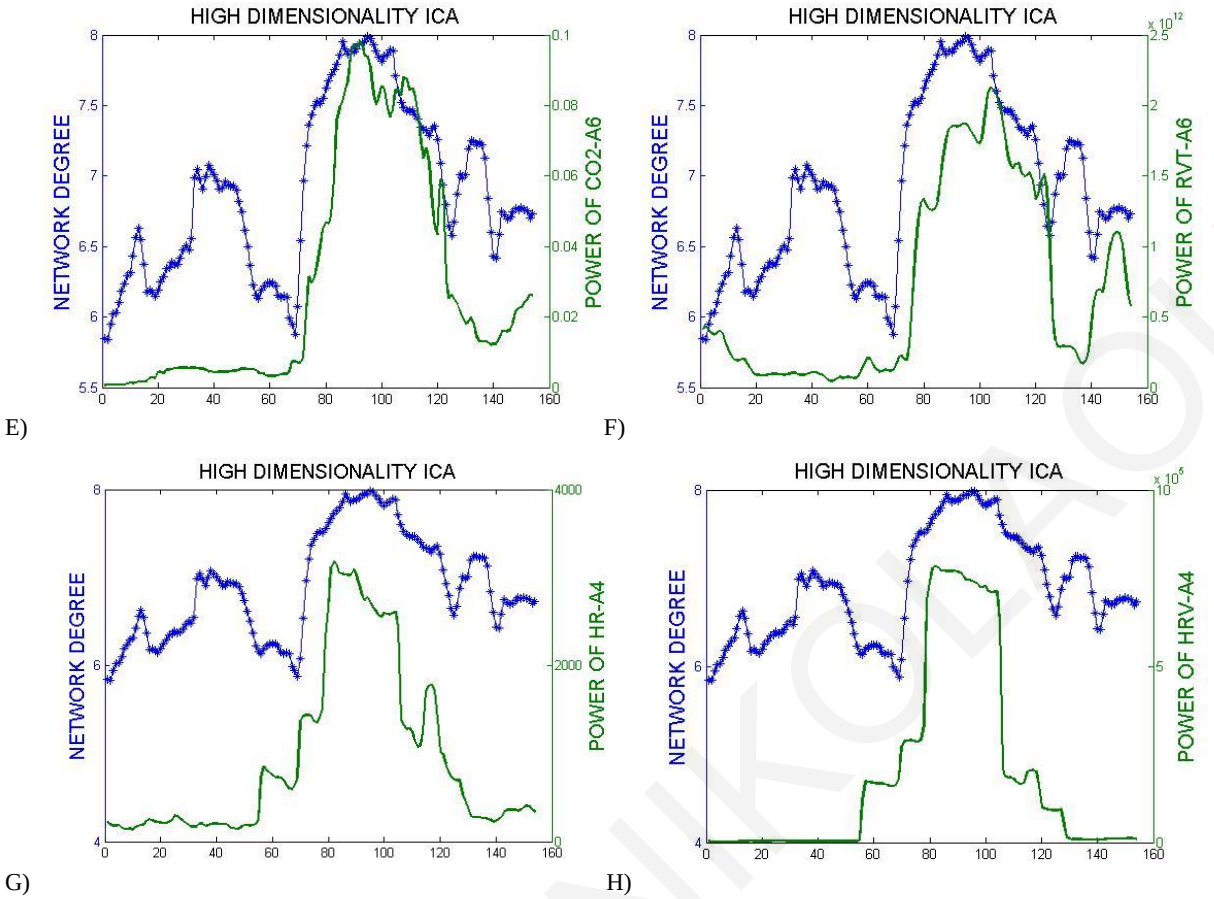

Figure 5.13. SMN degree and band-limited power of CO2/RVT/HR/HRV signals as a function of time for one representative volunteer obtained from high dimensionality ICA. A) power of CO2 at wavelet level A6 (0-0.0625Hz) vs network Degree for a 10 time-point increment, B) power of RVT at wavelet level A6 (0-0.0625Hz) vs network Degree for a 10 time-point increment, C) power of HR at wavelet level A4 (0-0.25Hz) vs network Degree for a 10 time-point increment, D) power of HRV at wavelet level A4 (0-0.25Hz) vs network Degree for a 10 time-point increment, E) power of CO2 at wavelet level A6 (0-0.0625Hz) vs network Degree for a 1 time-point increment, F) power of RVT at wavelet level A6 (0-0.0625Hz) vs network Degree for a 1 time-point increment, G) power of HR at wavelet level A4 (0-0.25Hz) vs network Degree for a 1 time-point increment and H) power of HRV at wavelet level A4 (0-0.25Hz) vs network Degree for a 1 time-point increment. All correlations were quantified using the average cross-correlation absolute value between 0±5time lags.

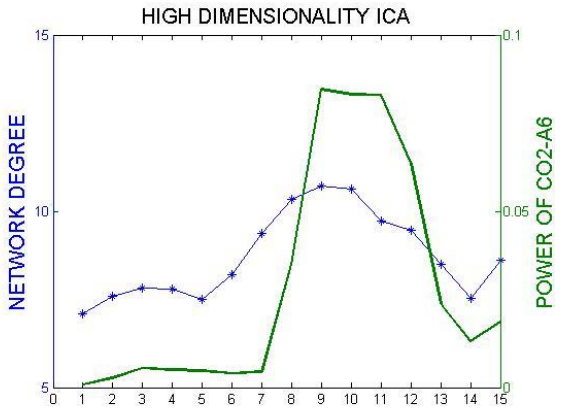

A)

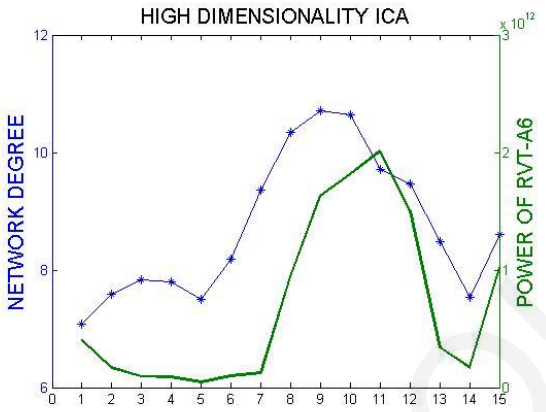

B)

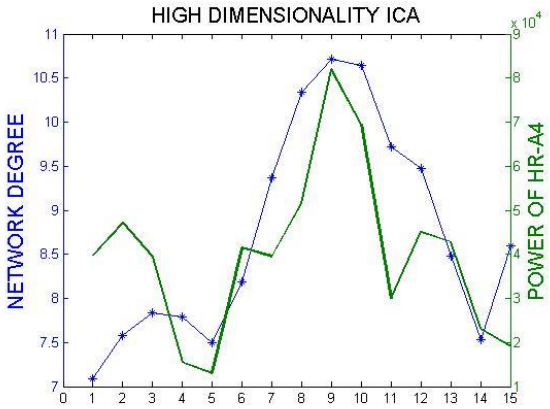

C)

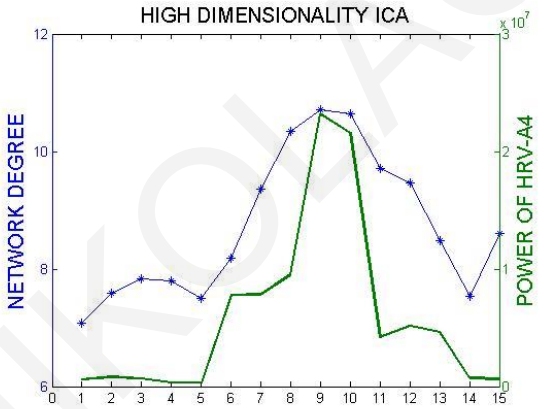

D)

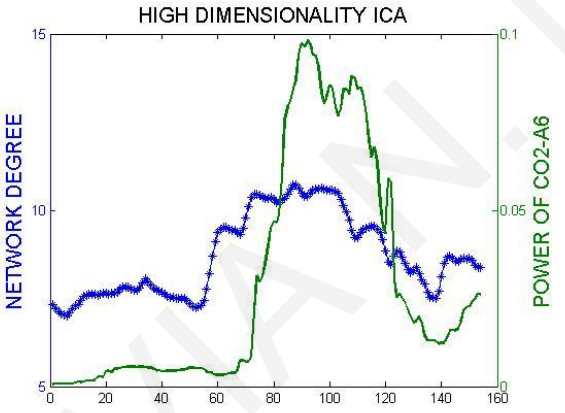

E)

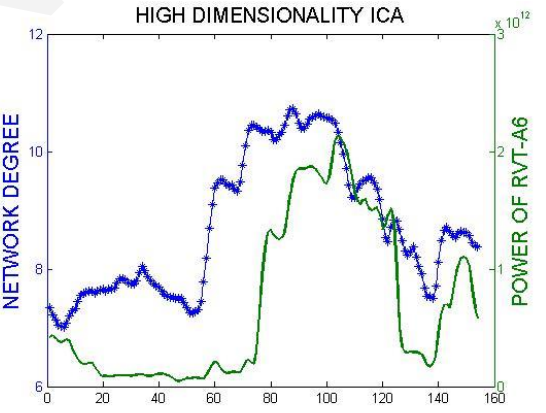

F)

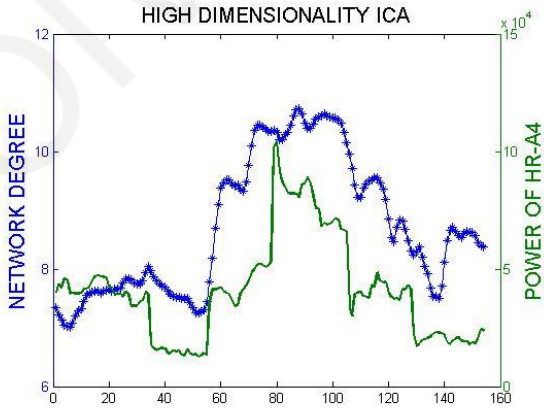

G)

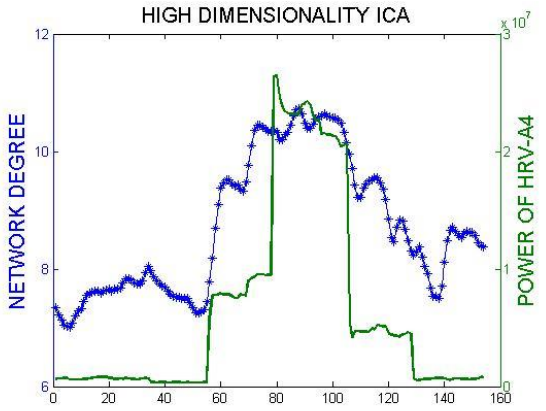

H)

Figure 5.14. Visual network degree and band-limited power of CO2/RVT/HR/HRV signals as a function of time for one representative volunteer obtained from high dimensionality ICA. A) power of CO2 at wavelet level A6 (0-0.0625Hz) vs network Degree for a 10 time-point increment, B) power of RVT at wavelet level A6 (0-0.0625Hz) vs network Degree for a 10 time-point increment, C) power of HR at wavelet level A4 (0-0.25Hz) vs network Degree for a 10 time-point increment, D) power of HRV at wavelet level A4 (0-0.25Hz) vs network Degree for a 10 time-point increment, E) power of CO2 at wavelet level A6 (0-0.0625Hz) vs network Degree for a 1 time-point increment, F) power of RVT at wavelet level A6 (0-0.0625Hz) vs network Degree for a 1 time-point increment, G) power of HR at wavelet level A4 (0-0.25Hz) vs network Degree for a 1 time-point increment and H) power of HRV at wavelet level A4 (0-0.25Hz) vs network Degree for a 1 time-point increment. All correlations were quantified using the average cross-correlation absolute value between 0±5time lags.

General Linear Models and Multiple Linear Regressions

The same steps as in the section of the low dimensionality analysis were applied. Specifically, various GLMs were applied in order to investigate a bit further the relationship between the RSNs degree and the band-limited power of CO_2/RVT/HR. General linear models created for both sliding window analysis offsets. In the following figures, the values of the RSN degree versus the values of the band-limited power of CO_2/RVT/HR are shown in blue color. The underlying best linear fit between the dependent variable (RSN degree) and independent variable (band-limited power of CO_2/RVT/HR) is shown in red color (Figures 5.15-5.17). Again, the term "linear" in linear regression means that the regression function is linear in the coefficients α and β_j. It is not required that the independent variables X_i appear as linear terms in the regression function.

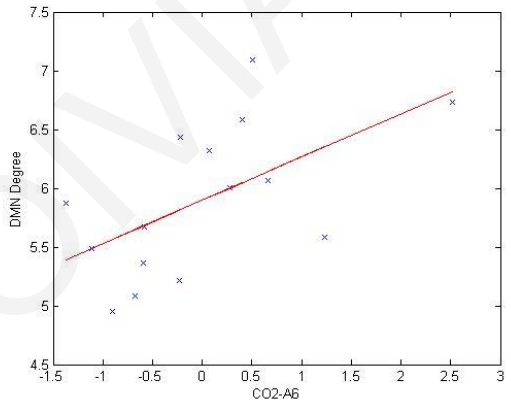

A)

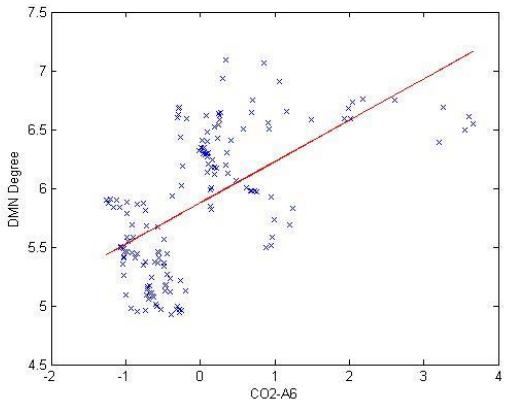

B)

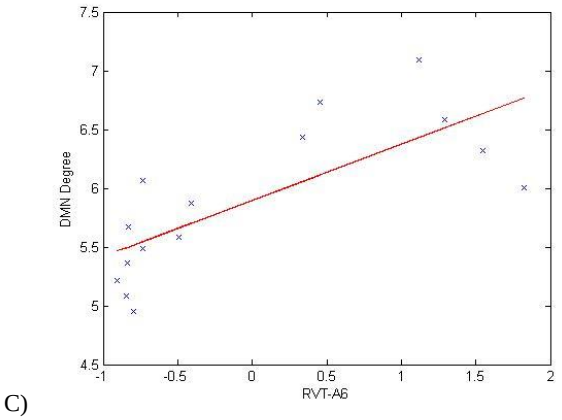

C)

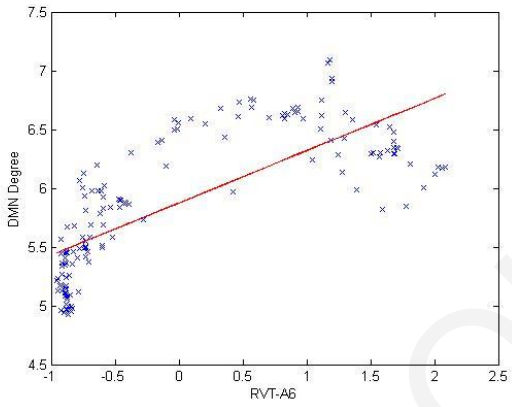

D)

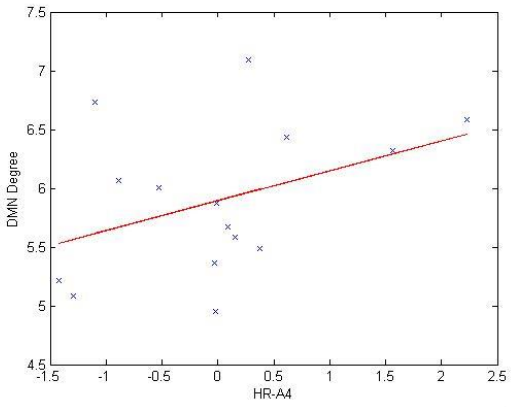

E)

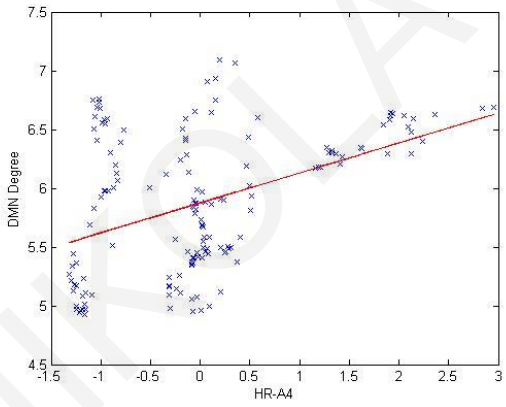

F)

Figure 5.15. DMN degree versus band-limited power of CO2/RVT/HR/HRV signals for one representative volunteer obtained from high dimensionality ICA in A) network degree vs power of CO2 at wavelet level A6 (0-0.0625Hz) for a 10 time-point increment, B) network degree vs power of CO2 at wavelet level A6 (0-0.0625Hz) for a 1 time-point increment, C) network degree vs power of RVT at wavelet level A6 (0-0.0625Hz) for a 10 time-point increment, D) network degree vs power of RVT at wavelet level A6 (0-0.0625Hz) for a 1 time-point increment, E) network degree vs power of HR at wavelet level A4 (0-0.25Hz) for a 10 time-point increment and F) network degree vs power of HR at wavelet level A4 (0-0.25Hz) for a 1 time-point increment.

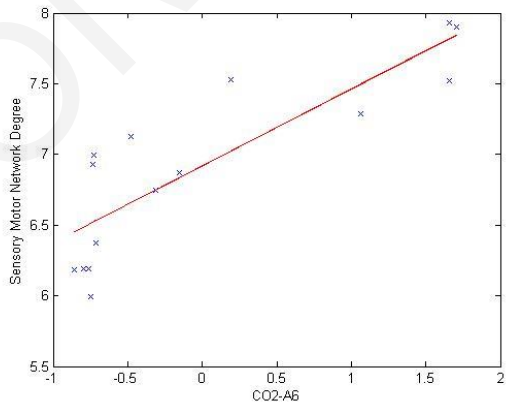

A)

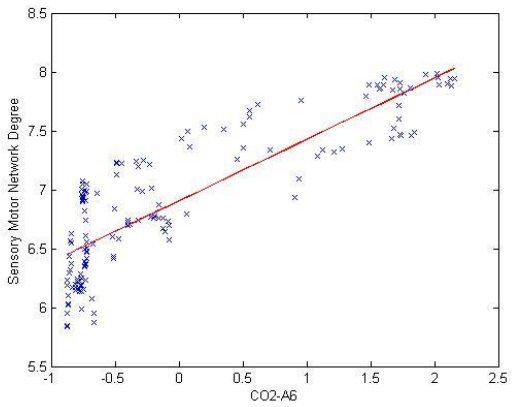

B)

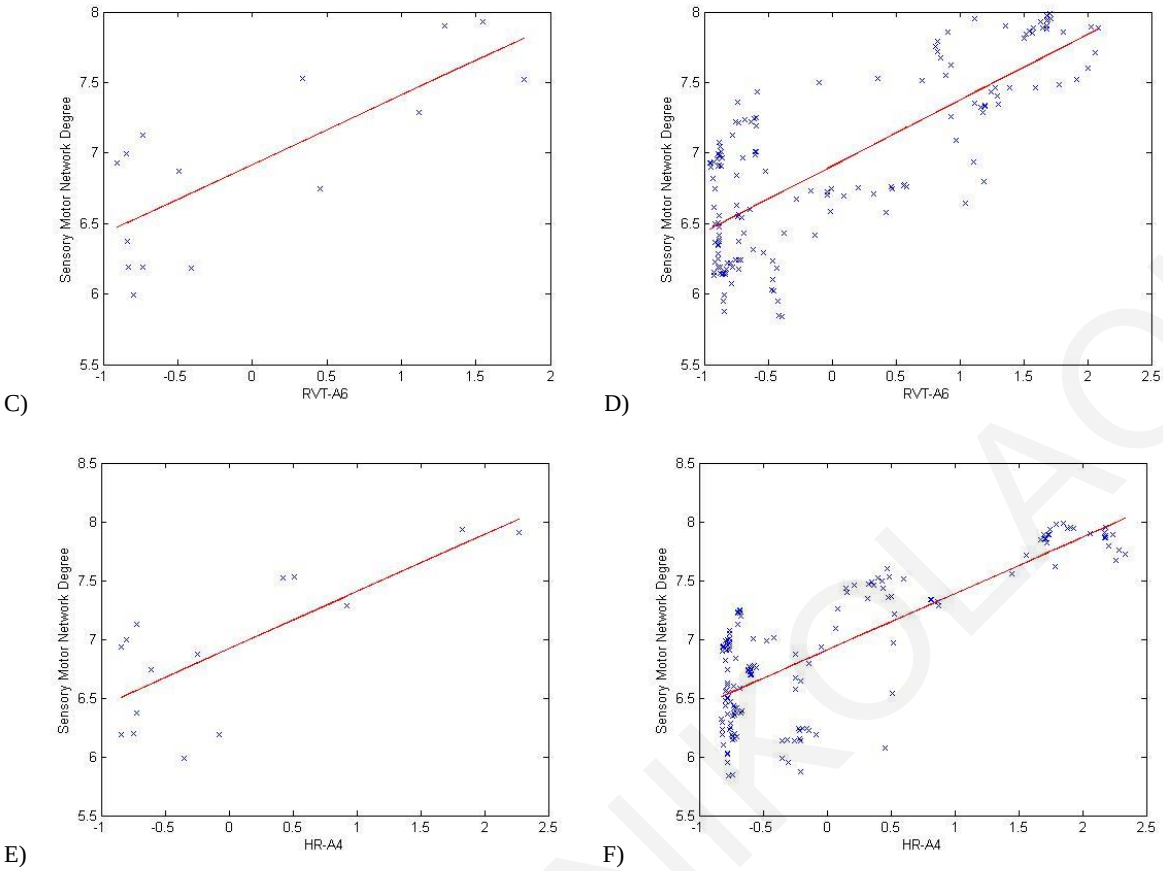

Figure 5.16. SMN degree versus band-limited power of CO2/RVT/HR/HRV signals for one representative volunteer obtained from high dimensionality ICA in A) network degree vs power of CO2 at wavelet level A6 (0-0.0625Hz) for a 10 time-point increment, B) network degree vs power of CO2 at wavelet level A6 (0-0.0625Hz) for a 1 time-point increment, C) network degree vs power of RVT at wavelet level A6 (0-0.0625Hz) for a 10 time-point increment, D) network degree vs power of RVT at wavelet level A6 (0-0.0625Hz) for a 1 time-point increment, E) network degree vs power of HR at wavelet level A4 (0-0.25Hz) for a 10 time-point increment and F) network degree vs power of HR at wavelet level A4 (0-0.25Hz) for a 1 time-point increment.

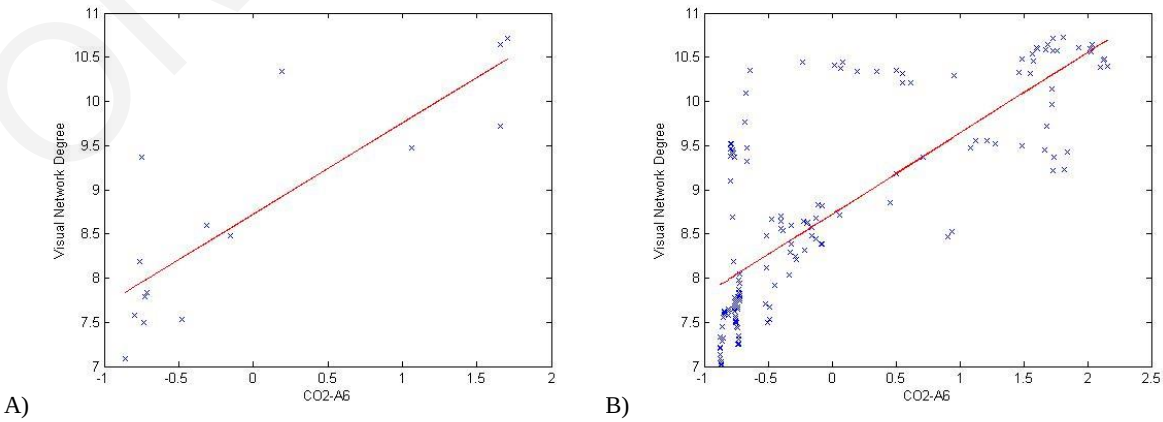

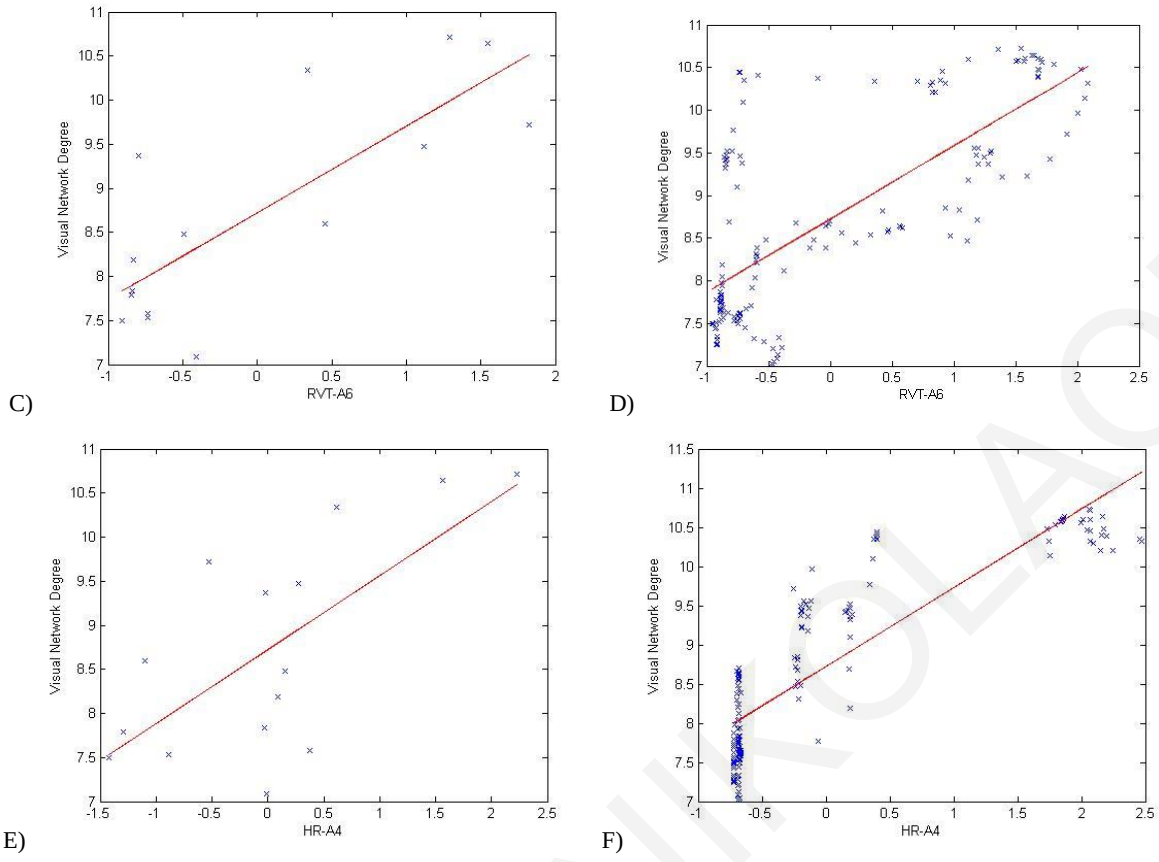

Figure 5.17. Visual network degree versus band-limited power of CO2/RVT/HR/HRV signals for one representative volunteer obtained from high dimensionality ICA in A) network degree vs power of CO2 at wavelet level A6 (0-0.0625Hz) for a 10 time-point increment, B) network degree vs power of CO2 at wavelet level A6 (0-0.0625Hz) for a 1 time-point increment, C) network degree vs power of RVT at wavelet level A6 (0-0.0625Hz) for a 10 time-point increment, D) network degree vs power of RVT at wavelet level A6 (0-0.0625Hz) for a 1 time-point increment, E) network degree vs power of HR at wavelet level A4 (0-0.25Hz) for a 10 time-point increment and F) network degree vs power of HR at wavelet level A4 (0-0.25Hz) for a 1 time-point increment.

For the high dimensionality ICA analysis and sliding window analysis with a 1 time-point increment, all the limited bands of the power of the physiological signals were used as the independent variables in the GLMs that were fitted for each RSN.

- For the DMN, separate GLMs for the band limited power of CO_2, RVT and HR were applied as can be seen in Figures 5.18 A and B. Subsequently a multiple linear model incorporating all signals was applied (Figure 5.18-C). In the case of GLM, RVT yielded a higher value for the estimated regression coefficient b1 compared to CO_2 and HR. In the case of MLR, CO_2 yielded the higher coefficient value and both CO_2 and HR yielded *p*-values lower than 0.05.

- The same procedure was applied for the Sensory-Motor network as can be seen in Figure 5.19. In the case of univariate GLMs, CO_2 yielded larger values for the estimated coefficient b1 compared to RVT and HR. In the case of MLR, CO_2 yielded the larger coefficient value. CO_2 and HR yielded *p*-values lower than 0.05.
- For the Visual network the results can be seen in Figure 5.20. In the case of univariate GLMs, HR yielded a larger value for the regression coefficient b1 compared to RVT and CO_2. In the case of the MLR model, HR yielded the highest coefficient and was the only signal which yielded *p*-values lower than 0.05.
- Larger values for an estimated regression coefficient suggest that the corresponding physiological signal has a more pronounced effect on the independent variable y, which is the time-varying degree of each RSN. As can be seen for the mentioned results, for different RSNs, different signals seem to be more important. HR seems to be more important for the visual network.
- The results yielded by the low and high dimensionality ICA were very similar.

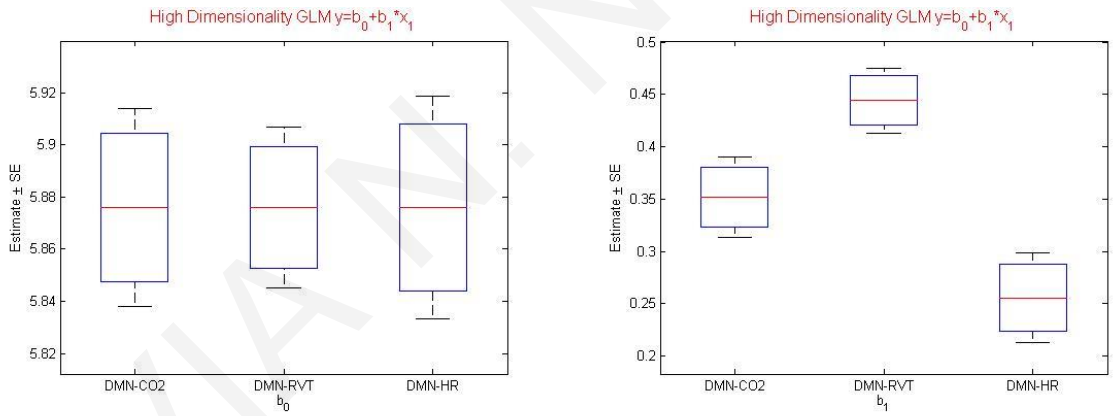

A) B)

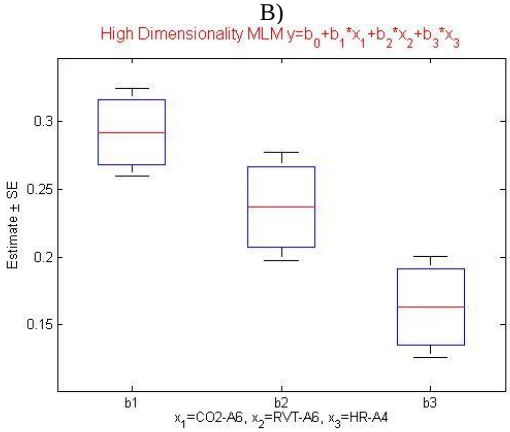

C)

Figure 5.18. A) Estimated values of b0 and B) b1 for the three univariate GLMs between DMN degree and band-limited power of CO2/RVT/HR obtained from low dimensionality ICA for a 1 time-point increment, C) Estimated values of b1, b2 and b3 for the MLR model between DMN degree and band-limited power of CO2/RVT/HR obtained from low dimensionality ICA for a 1 time-point increment.

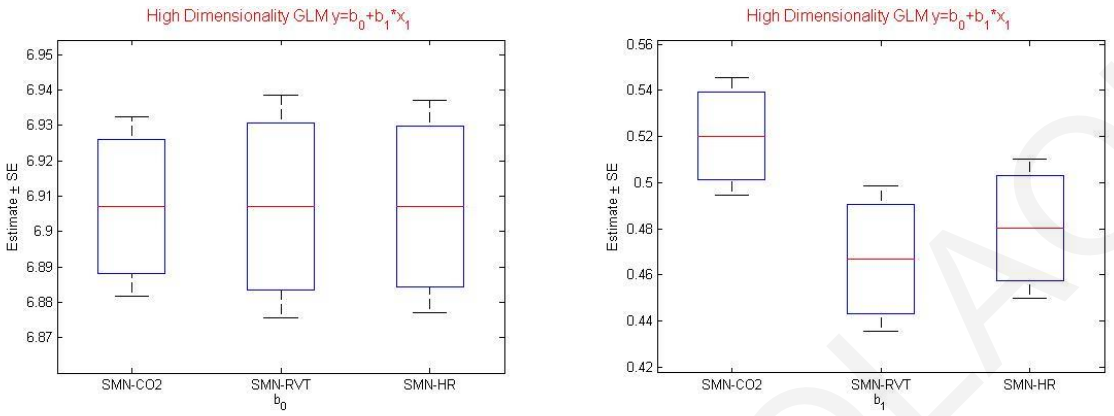

A) B)

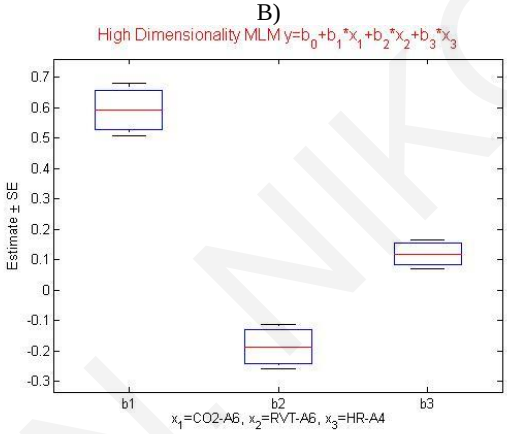

C)

Figure 5.19. A) Estimated values of b0 and B) b1 for the three univariate GLMs between SMN degree and band-limited power of CO2/RVT/HR obtained from low dimensionality ICA for a 1 time-point increment, C) Estimated values of b1, b2 and b3 for the MLR model between SMN degree and band-limited power of CO2/RVT/HR obtained from low dimensionality ICA for a 1 time-point increment.

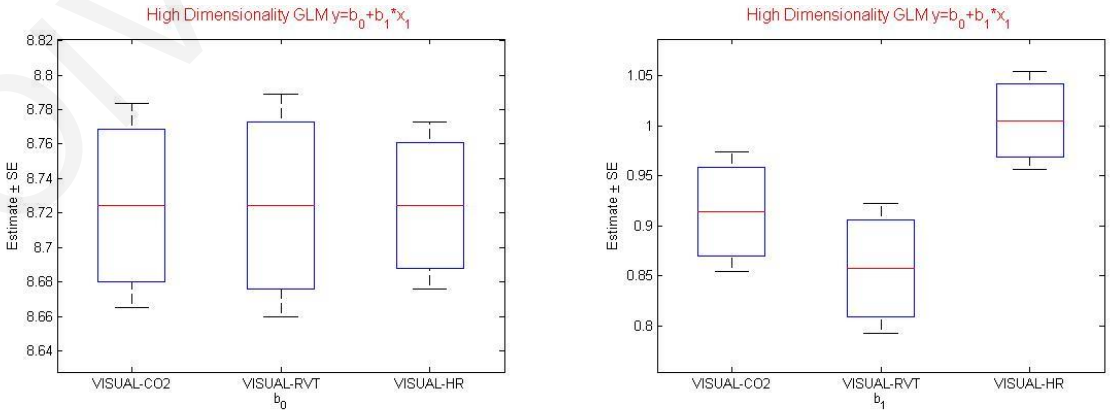

A) B)

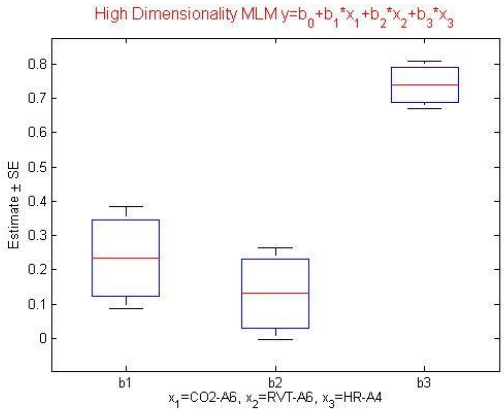

C)

Figure 5.20. A) Estimated values of b0 and B) b1 for the three univariate GLMs between Visual Network degree and band-limited power of CO2/RVT/HR obtained from low dimensionality ICA for a 1 time-point increment, C) Estimated values of b1, b2 and b3 for the MLR model between Visual Network degree and band-limited power of CO2/RVT/HR obtained from low dimensionality ICA for a 1 time-point increment.

5.1.3 Spatial Sliding Window ICA

For the second ICA approach, the "Spatial-Sliding-ICA", our results were obtained from the individual functional space of each subject, since as mentioned before it was found that registration to the MNI space and the resulting blurring of the corresponding BOLD time series considerably affects the results. The Spearman correlation coefficients between time-varying DMN degree and band-limited PETCO2/HR power are given in Table 5-3 for all subjects (mean ± standard deviation). These suggest the presence of temporal correlations between network degree and the PETCO2/HR power (somewhat lower values – not shown - were obtained for total power, as above). As before, correlations were found to be much higher in the wavelet sub-band A2 for PETCO2 (0-0.08 Hz) and for the HR, this approach yielded better results in the wavelet sub-band A2 (0-1 Hz). Additionally, for this approach the stability of the DMN network was calculated and most of the windows yielded a correlation value above 0.5 using a commonly used DMN template (Figure 5.21). This suggest that the components indeed show an activation of the DMN. Furthermore, this activation is not stable across all windows. In some windows the activation of the DMN has a greater spatial extent compared to other windows. Furthermore, only the selected DMN independent components yielded us high correlation values with the DMN template, which confirms that the selection of the DMN components was correct. In Figure 5.22, the results for one representative volunteer are shown for spatial sliding window ICA.

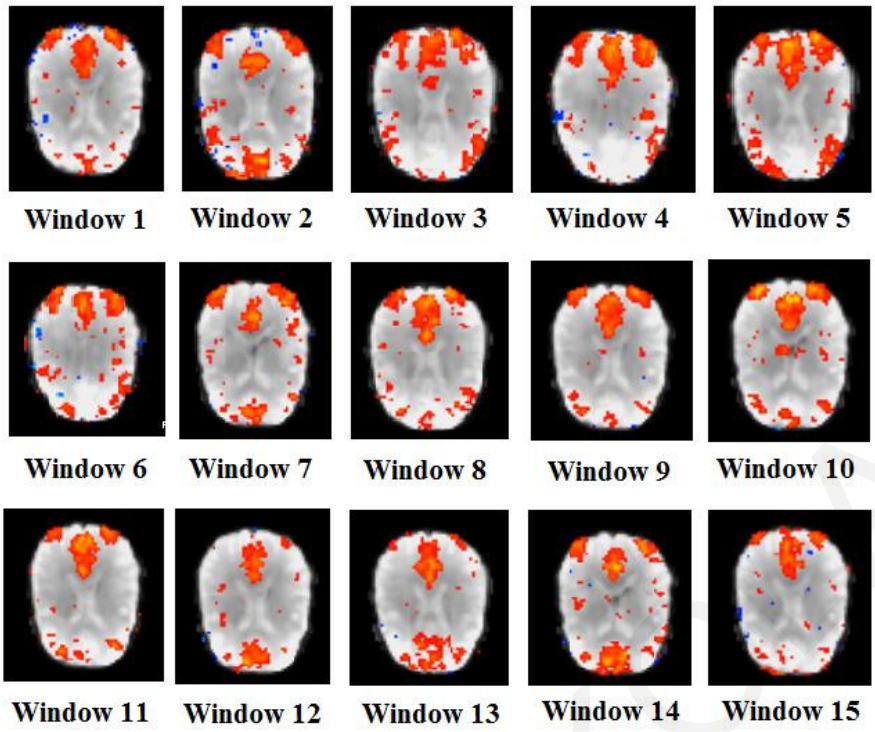

Figure 5.21. DMN network in each Spatial Sliding Window using the ICA analysis.

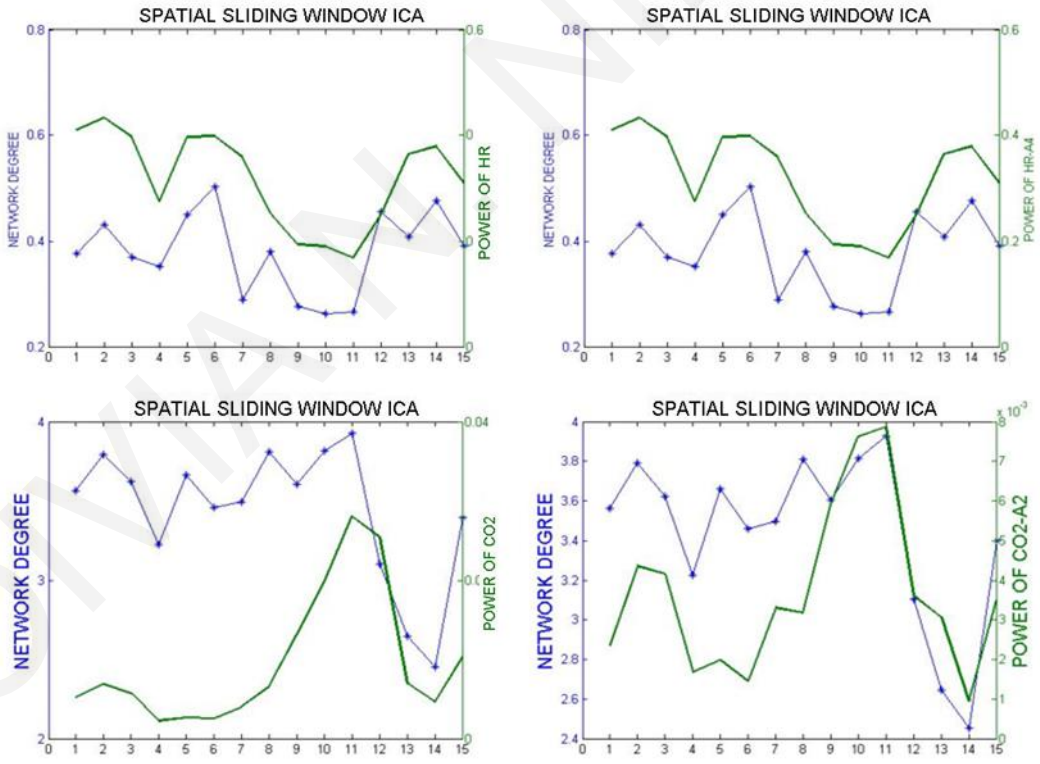

Figure 5.22. DMN degree and power of HR (top two panels) and PETCO2 (bottom two panels) signals as a function of time for representative subjects obtained from spatial sliding window ICA without and with wavelet analysis in A) FS, power of HR vs DMN network Degree, B) FS, power of HR at wavelet level A4 (0-1 Hz) vs DMN network Degree, C) FS, power of CO2 vs DMN network Degree and D) FS, power of CO2

at wavelet level A2 (0-0.08 Hz) vs DMN Degree. All correlations were quantified using the average cross-correlation absolute value between 0 and ±5 time lags.

	CO2-FS		*CO2-FS-A2*		*HR-FS*		*HR-FS-A4*	
	MEAN	**STD**	**MEAN**	**STD**	**MEAN**	**STD**	**MEAN**	**STD**
Spatial-Sliding-ICA	0.32	0.33	0.59	0.11	0.39	0.36	0.73	0.23

Table 5-3. Spearman correlation coefficients between time-varying DMN network degree and band-limited PETCO2 and HR power using spatial sliding window ICA. FS: functional space, CO2-FS-A2: functional space, wavelet level A2 (0-0.08 Hz), HR-FS-A4: functional space, wavelet level A2 (0-1 Hz)

6. Effects of Cardiac Sympathetic and Parasympathetic Activity on DFC

In this chapter, the results from the investigation of the impact of the cardiac sympathetic and parasympathetic activity on DFC using ICA are presented.

6.1 Resting-state Functional Connectivity Analysis Using ICA

6.1.1 Low Dimensionality ICA

For the three RSNs of interest (DMN, SMN and Visual Network), results from the functional space of each subject were obtained. As outlined in Chapter 3, for the low dimensionality analysis, a new sliding-windows approach was applied with an increment of one time-point, to compare it with the results from the 10 time-point increment (the one volume increment was used to assess DFC with a better time resolution). Results obtained using Instantaneous LF power and HF power extracted from the HRV were extracted. The Spearman correlation coefficients between time-varying DMN/SMN/Visual network degree and the instantaneous power of LH/HF of HRV for the 10 time-point increment and for 1 time-point increment are given in Table 6-1. The correlation coefficients are averaged over all the subjects (mean ± standard deviation).

		LOW DIMENSIONALITY			
		10 TIME-POINT INCREMENT		1 TIME-POINT INCREMENT	
		MEAN	STD	MEAN	STD
DMN	THF	0.65535	0.028	0.65065	0.029
	TLF	0.59645	0.01	0.61255	0.019
SMN	THF	0.5268	0.015	0.6509	0.018
	TLF	0.5	0.018	0.6363	0.018
VISUAL	THF	0.7	0.014	0.7279	0.016
	TLF	0.6464	0.07	0.5528	0.089

Table 6-1. Spearman correlation coefficients between time-varying DMN/SMN/Visual network degree and time-varying instantaneous power of HF/LF of HRV (THF and TLF, respectively) for 10 time-point and 1 time-point increments. HF: high frequency band of HRV (0.15-0.4Hz), LF: low frequency band of HRV (0.04-0.15 Hz).

These suggest the presence of temporal correlations between network degree and the instantaneous LF and HF power of HRV. In more detail, the sliding window approach using a one time-point increment yielded slightly higher values compared to the 10 time-point increment. Additionally, the instantaneous power of HF yielded slightly higher values than the instantaneous power of LF. Finally, the ratio LF/HF yielded negative correlation values. As can be seen from the Figures 6.1-6.3, the instantaneous power of HF band of HRV has similar waveform with the instantaneous power of LF band of HRV and in addition the waveform of the instantaneous power of HF band of HRV had bigger values compared to the waveform of the instantaneous power of LF band of HRV. Moreover, these two-mentioned waveforms have similar waveform with the RSN degree. As a consequence, the ratio of LF/HF yielded negative correlation values. In the following figures (Figures 6.1-6.3) results from the above tables are shown for some representative volunteers.

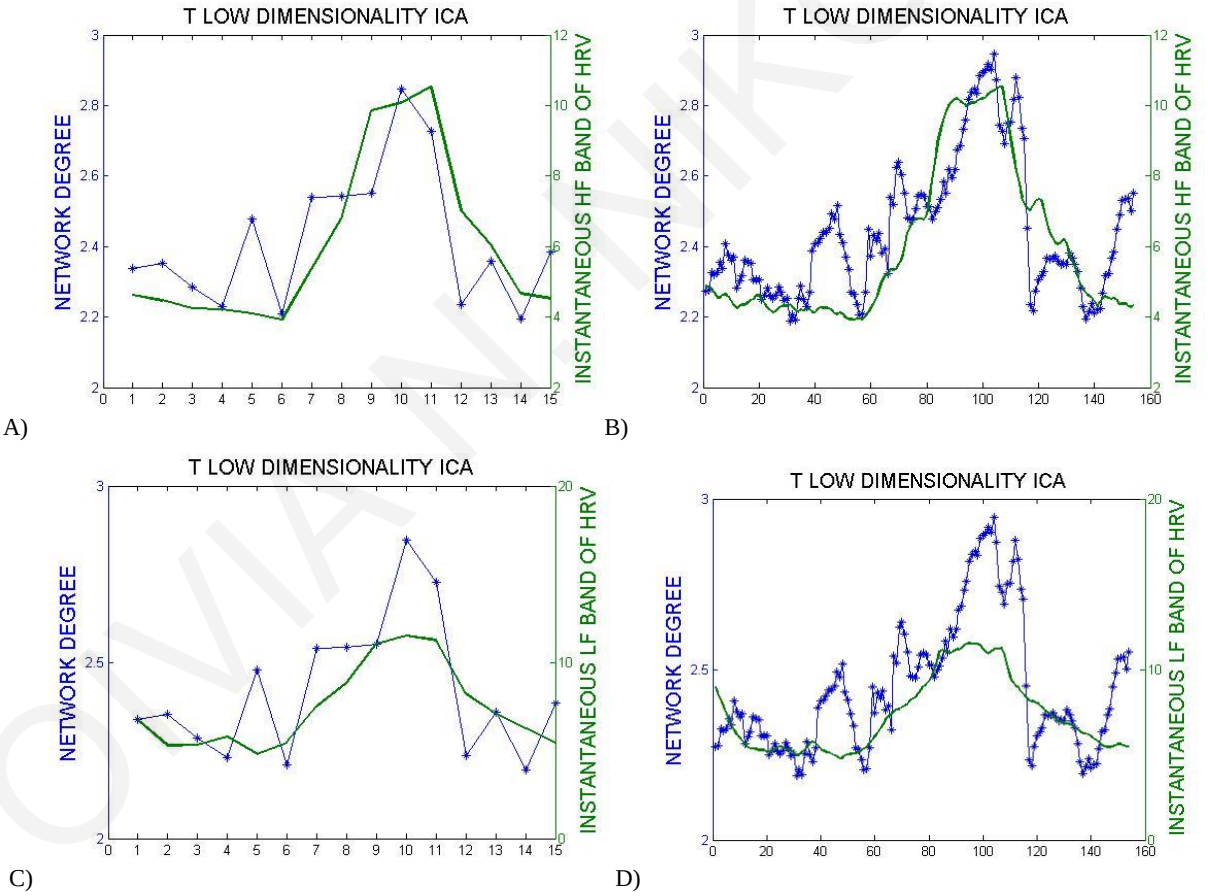

Figure 6.1. DMN degree and instantaneous power of HF/LF of HRV signals as a function of time for one representative volunteer obtained from low dimensionality ICA. A) instantaneous power of HF (0.15-0.4Hz) vs network Degree for a 10 time-point increment, B) instantaneous power of HF (0.15-0.4Hz) vs network Degree for a 1 time-point increment, C) instantaneous power of LF (0.04-0.15Hz) vs network Degree for a 10 time-point increment and D) instantaneous power of LF (0.04-0.15Hz) vs network Degree

for a 1 time-point increment. All correlations were quantified using the average cross-correlation absolute value between 0±5time lags.

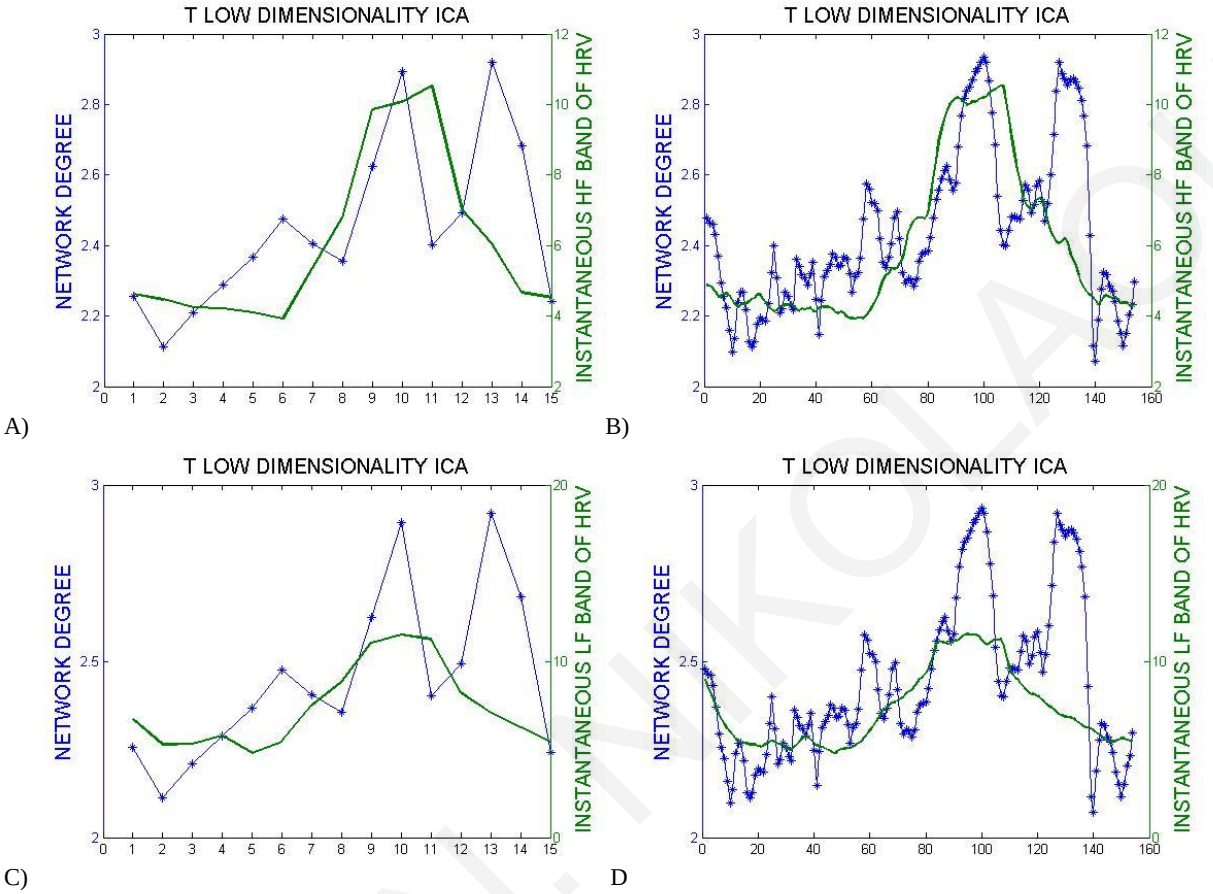

Figure 6.2. SMN degree and instantaneous power of HF/LF of HRV signals as a function of time for one representative volunteer obtained from low dimensionality ICA. A) instantaneous power of HF (0.15-0.4Hz) vs network Degree for a 10 time-point increment, B) instantaneous power of HF (0.15-0.4Hz) vs network Degree for a 1 time-point increment, C) instantaneous power of LF (0.04-0.15Hz) vs network Degree for a 10 time-point increment and D) instantaneous power of LF (0.04-0.15Hz) vs network Degree for a 1 time-point increment. All correlations were quantified using the average cross-correlation absolute value between 0±5time lags.

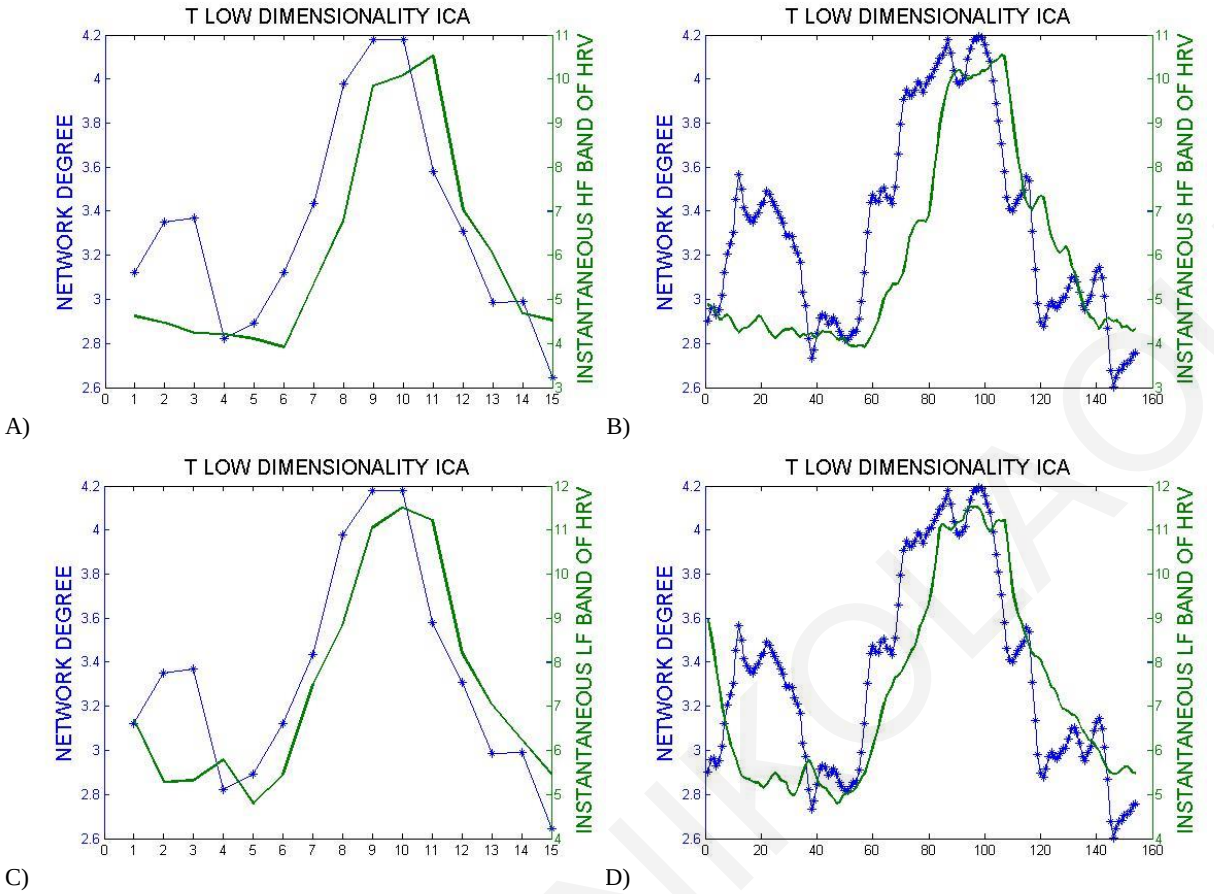

Figure 6.3. Visual network degree and instantaneous power of HF/LF of HRV signals as a function of time for one representative volunteer obtained from low dimensionality ICA. A) instantaneous power of HF (0.15-0.4Hz) vs network Degree for a 10 time-point increment, B) instantaneous power of HF (0.15-0.4Hz) vs network Degree for a 1 time-point increment, C) instantaneous power of LF (0.04-0.15Hz) vs network Degree for a 10 time-point increment and D) instantaneous power of LF (0.04-0.15Hz) vs network Degree for a 1 time-point increment. All correlations were quantified using the average cross-correlation absolute value between 0±5time lags.

General Linear Models and Multiple Linear Regression

As explained in the previous chapters, to investigate further the relationship between the RSN degree and the instantaneous power of LF/HF of HRV, general linear models were created for both sliding window analysis increments (1 and 10 time lags). In the following figures (Figures 6.4-6.6), the values of the RSN degree versus the values of the instantaneous power of LF/HF of HRV can be seen (in blue crosses). The best linear fit between the dependent variable (RSN degree) and independent variable (instantaneous power of LF/HF of HRV) as extracted by the GLM models obtained can be seen in red. (As before, the term "linear" in linear regression means that the regression function is linear in the coefficients α and β_j. It is not required that the X_i appear as linear terms in the regression function.)

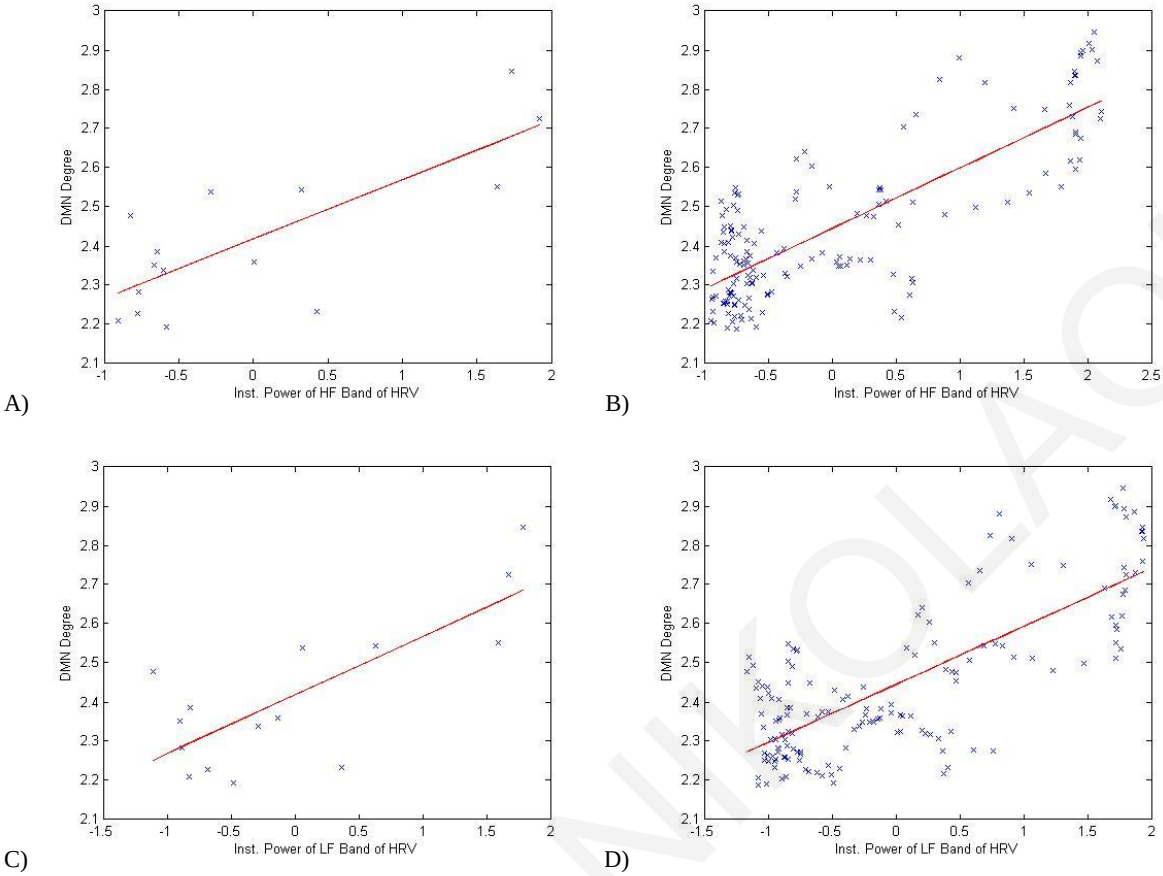

Figure 6.4. DMN degree versus instantaneous power of LF/HF of HRV for one representative volunteer obtained from low dimensionality ICA. A) network degree vs instantaneous power of HF for a 10 time-point increment, B) network degree vs instantaneous power of HF for a 1 time-point increment, C) network degree vs instantaneous power of LF for a 10 time-point increment and D) network degree vs instantaneous power of LF for a 1 time-point increment.

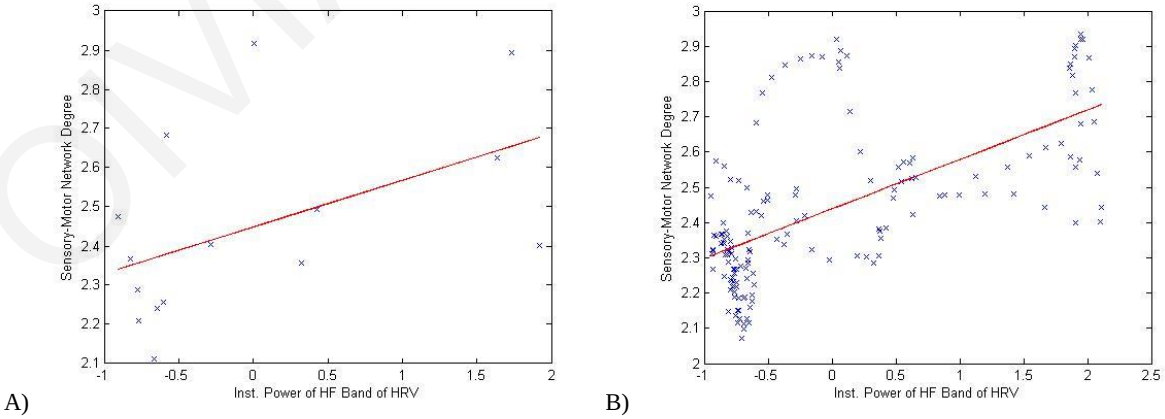

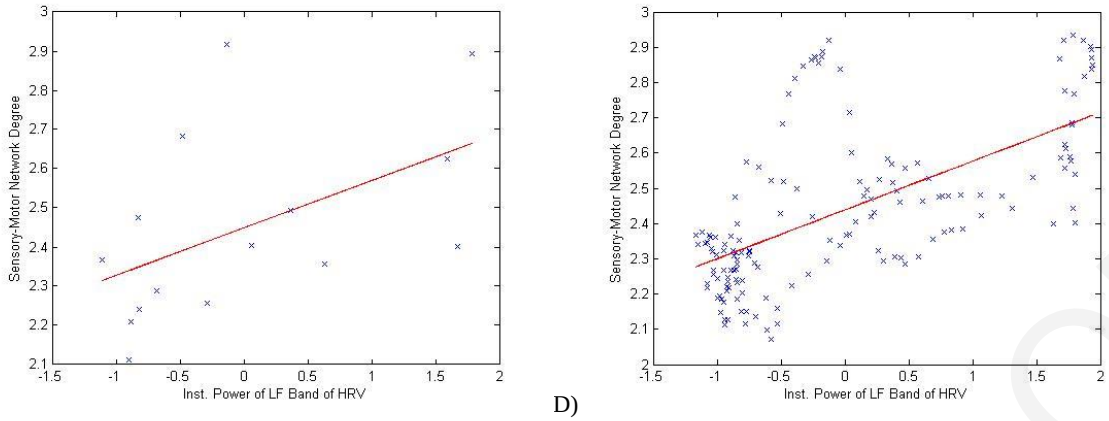

C) D)

Figure 6.5. Sensory-Motor network degree versus instantaneous power of LF/HF of HRV for one representative volunteer obtained from low dimensionality ICA. A) network degree vs instantaneous power of HF for a 10 time-point increment, B) network degree vs instantaneous power of HF for a 1 time-point increment, C) network degree vs instantaneous power of LF for a 10 time-point increment and D) network degree vs instantaneous power of LF for a 1 time-point increment.

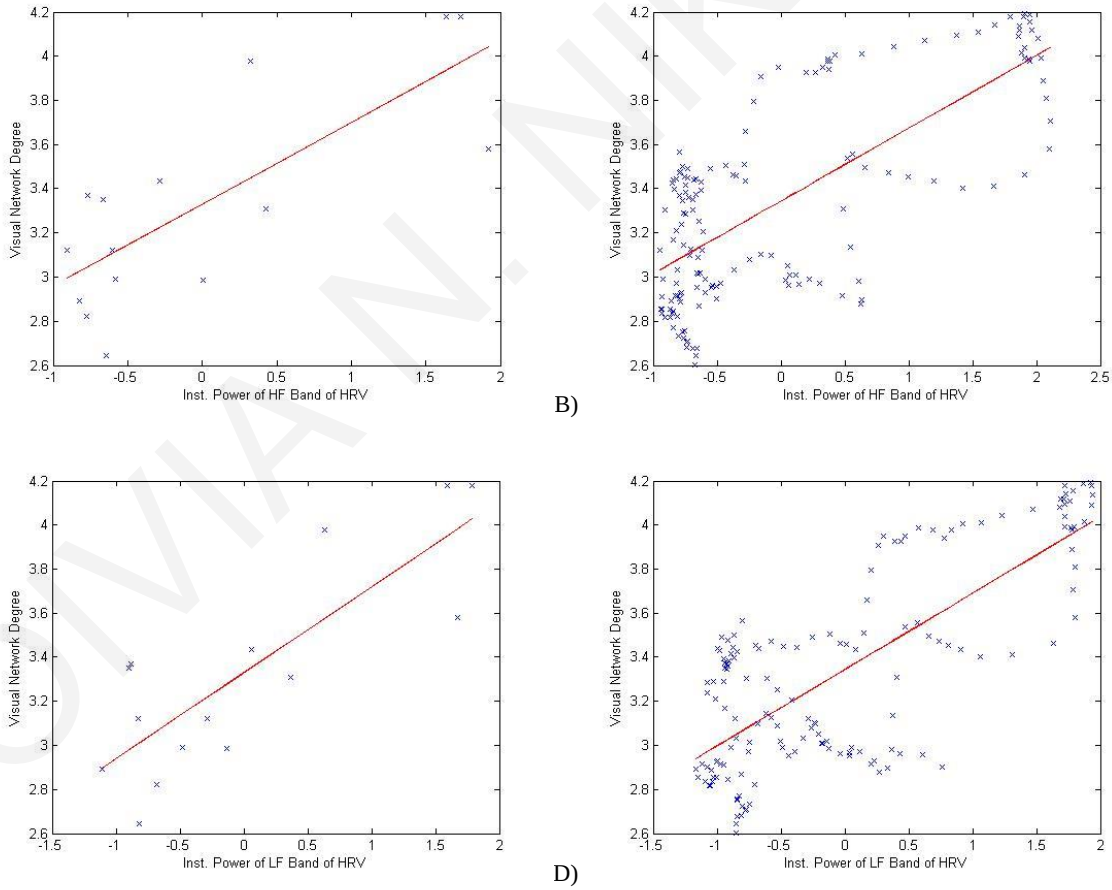

A) B)

C) D)

Figure 6.6. Visual network degree versus instantaneous power of LF/HF of HRV for one representative volunteer obtained from low dimensionality ICA. A) network degree vs instantaneous power of HF for a 10 time-point increment, B) network degree vs instantaneous power of HF for a 1 time-point increment, C)

network degree vs instantaneous power of LF for a 10 time-point increment and D) network degree vs instantaneous power of LF for a 1 time-point increment.

For the low dimensionality ICA analysis and sliding window analysis with 1time-point increment, the instantaneous power of LF and HF of HRV were used as the independent variables in the GLMs that were fitted for each RSN.

- For the DMN, two general linear models were applied and as independent variables, we used the instantaneous power of LF and HF of HRV (Figure 6.7- A and B). These two signals affected similarly the Network Degree of DMN. A MLR model was not applied in this case because the signals are highly correlated to each other.
- The same procedure was applied for the Sensory-Motor network as can be seen in Figure 6.8 - A and B. In the case of univariate GLMs, two general linear models were created and as independent variables, we used the instantaneous power of LF and HF of HRV. These two signals affected similarly the Network Degree of Sensory-Motor Network. An MLR was not applied in this case because the signals are highly correlated to each other.
- Finally, for the Visual network the results can be seen in Figures 6.9 - A and B. Two general linear models were created and as independent variables, we used the instantaneous power of LF and HF of HRV. These two signals affected similarly the Network Degree of DMN. An MLR was not applied in this case because the signals are highly correlated with each other.

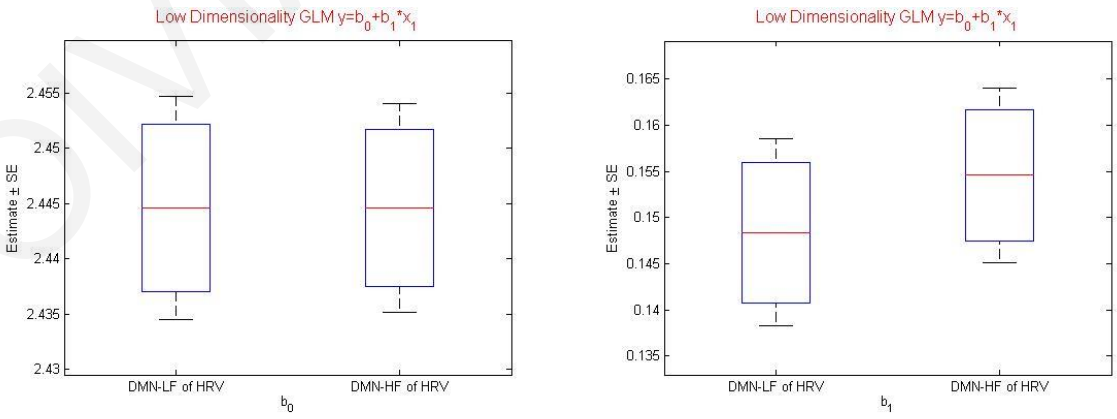

A) B)

Figure 6.7. A) Estimated values of b0 and B) b1 for the three univariate GLMs between DMN degree and instantaneous power of LF/HF of HRV obtained from low dimensionality ICA for a 1 time-point increment.

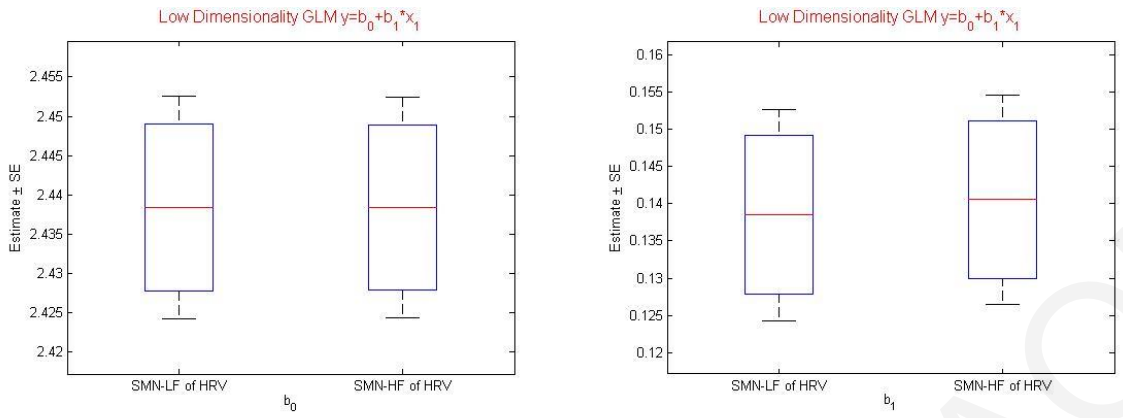

A) B)

Figure 6.8. A) Estimated values of b0 and B) b1 for the three univariate GLMs between SMN degree and instantaneous power of LF/HF of HRV obtained from low dimensionality ICA for a 1 time-point increment.

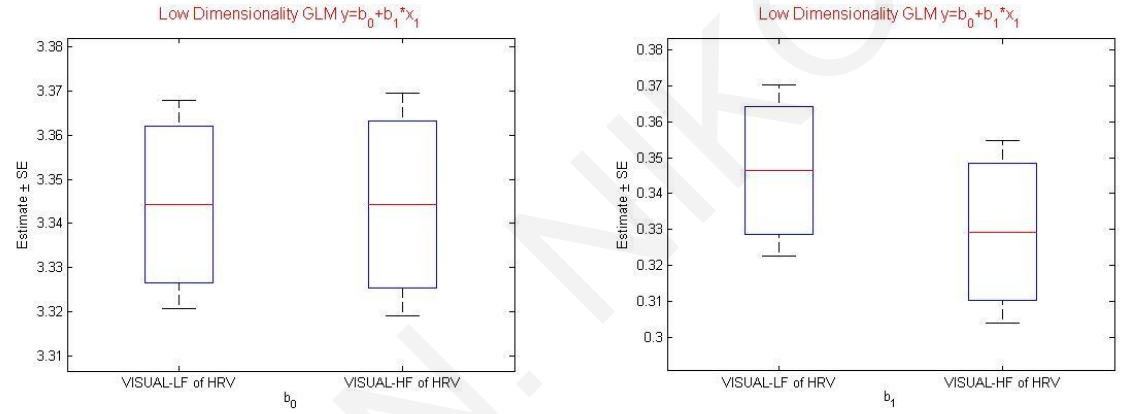

A) B)

Figure 6.9. A) Estimated values of b0 and B) b1 for the three univariate GLMs between Visual Network degree and instantaneous power of LF/HF of HRV obtained from low dimensionality ICA for a 1 time-point increment.

6.1.2 High Dimensionality ICA

The same procedure used for the low dimensionality ICA for the three RSNs of interest (DMN, Visual network and SMN) was applied for the high dimensionality ICA. Specifically, the sliding windows approach was applied with an increment of one time-point, to compare it with the results from the 10 time-point increment. Again, the instantaneous power of LF and HF of HRV were used to investigate the impact of cardiac sympathetic and parasympathetic activity on DFC. The Spearman correlation coefficients for the high dimensionality ICA between time-varying DMN/SMN/Visual network degree and the instantaneous power of LH/HF of HRV for the 10 time-point increment and for 1 time-point increment are given in

Table 6-2. The correlations coefficients are averaged over all subjects (mean ± standard deviation).

		HIGH DIMENSIONALITY			
		10 TIME-POINT INCREMENT		1 TIME-POINT INCREMENT	
		MEAN	**STD**	**MEAN**	**STD**
DMN	**THF**	0.8268	0.003	0.86345	0.028
	TLF	0.7696	0.088	0.81995	0.058
SMN	**THF**	0.65785	0.015	0.6607	0.000778
	TLF	0.5896	0.035	0.6108	0.032
VISUAL	**THF**	0.77145	0.025	0.79836	0.062
	TLF	0.76965	0.033	0.77275	0.002

Table 6-2. Spearman correlation coefficients between time-varying DMN/SMN/Visual network degree and time-varying instantaneous power of HF/LF of HRV for 10 time-points and 1 time-point increments. HF: high frequency band of HRV (0.15-0.4Hz), LF: low frequency band of HRV (0.04-0.15 Hz).

As can be seen from the above tables, results were consistent with the other analysis techniques. Specifically, our results suggest the presence of temporal correlations between network degree and the band-limited power of the instantaneous power of HF/LF of HRV. The sliding window using one time-point offset yielded slightly higher values against the 10 time-points offset. Also, the instantaneous power of HF also yielded slightly higher values than the instantaneous power of LF. Finally, the ratio LF/HF yielded negative values of correlations which was expected because the shape of it is the inverse of the corresponding network degree. In the following figures (Figures 6.10-6.12) results from the above tables are shown for some representative volunteers.

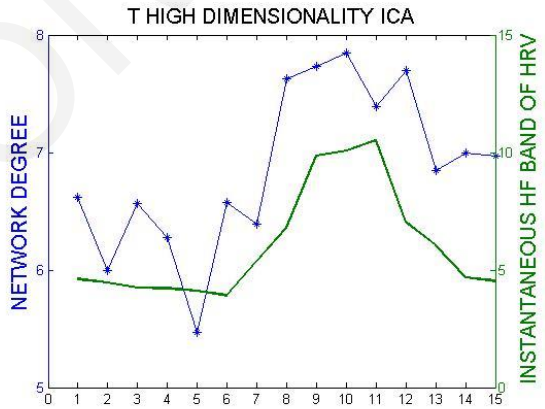

A)

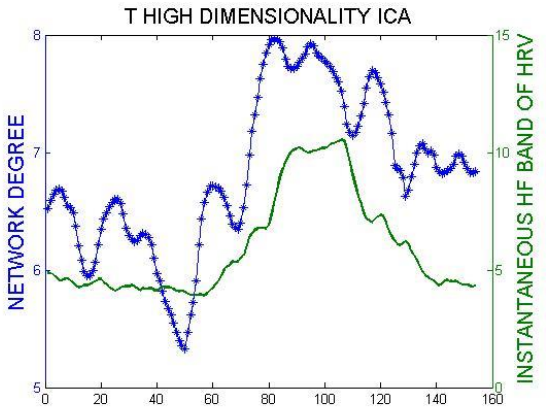

B)

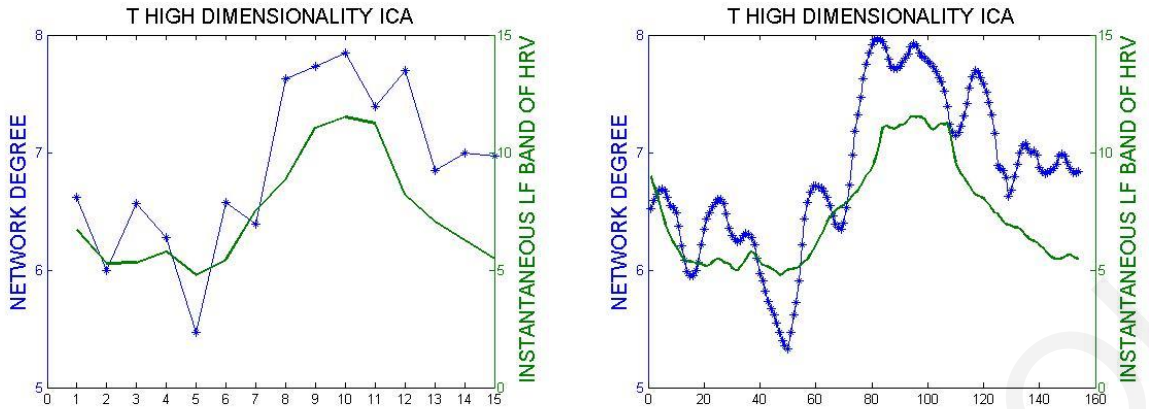

C) D)

Figure 6.10. DMN degree and instantaneous power of HF/LF of HRV signals as a function of time for one representative volunteer obtained from high dimensionality ICA. A) instantaneous power of HF (0.15-0.4Hz) vs network Degree for a 10 time-point increment, B) instantaneous power of HF (0.15-0.4Hz) vs network Degree for a 1 time-point increment, C) instantaneous power of LF (0.04-0.15Hz) vs network Degree for a 10 time-point increment and D) instantaneous power of LF (0.04-0.15Hz) vs network Degree for a 1 time-point increment. All correlations were quantified using the average cross-correlation absolute value between 0±5time lags.

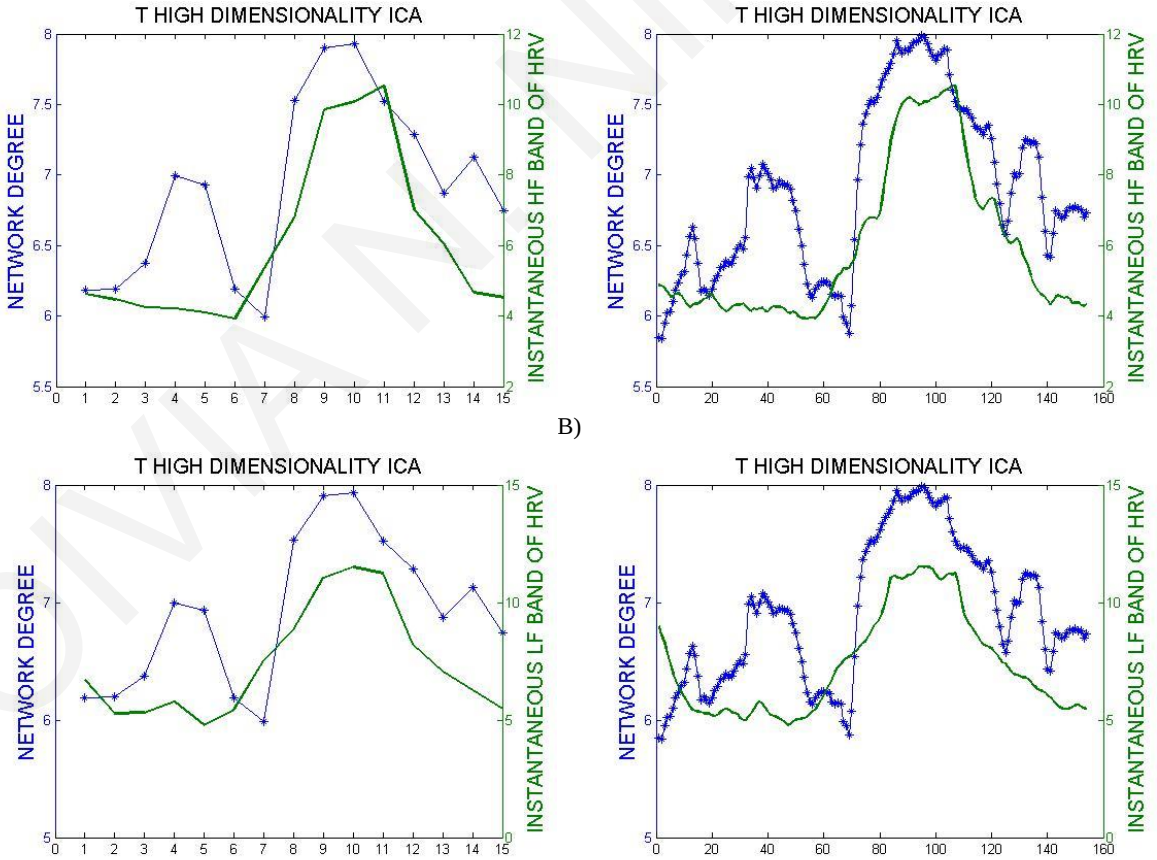

A) B)

C) D)

Figure 6.11. SMN degree and instantaneous power of HF/LF of HRV signals as a function of time for one representative volunteer obtained from high dimensionality ICA. A) instantaneous power of HF (0.15-

0.4Hz) vs network Degree for a 10 time-point increment, B) instantaneous power of HF (0.15-0.4Hz) vs network Degree for a 1 time-point increment, C) instantaneous power of LF (0.04-0.15Hz) vs network Degree for a 10 time-point increment and D) instantaneous power of LF (0.04-0.15Hz) vs network Degree for a 1 time-point increment. All correlations were quantified using the average cross-correlation absolute value between 0±5time lags.

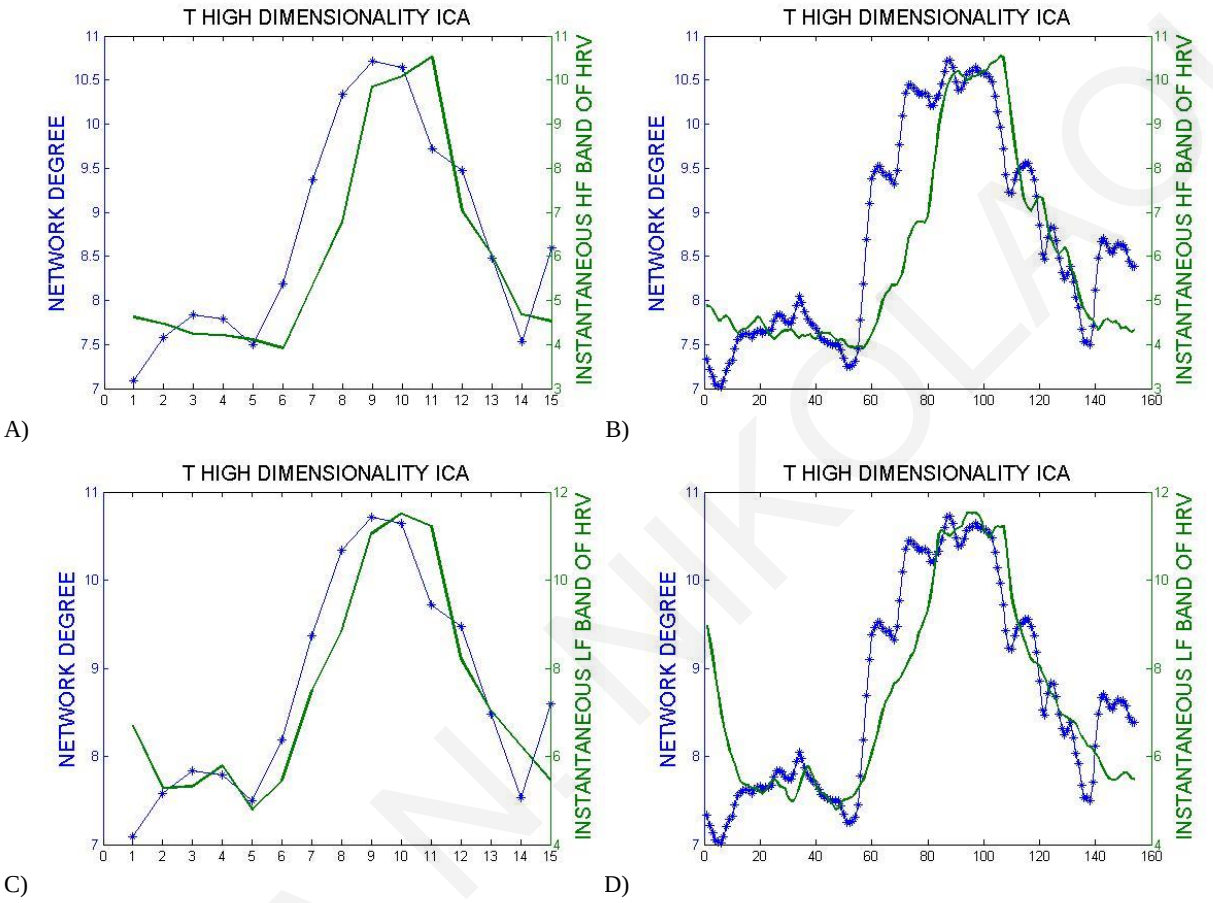

Figure 6.12. Visual network degree and instantaneous power of HF/LF of HRV signals as a function of time for one representative volunteer obtained from high dimensionality ICA. A) instantaneous power of HF (0.15-0.4Hz) vs network Degree for a 10 time-point increment, B) instantaneous power of HF (0.15-0.4Hz) vs network Degree for a 1 time-point increment, C) instantaneous power of LF (0.04-0.15Hz) vs network Degree for a 10 time-point increment and D) instantaneous power of LF (0.04-0.15Hz) vs network Degree for a 1 time-point increment. All correlations were quantified using the average cross-correlation absolute value between 0±5time lag.

General Linear Models and Multiple Linear Regressions

The same steps as in the section of the low dimensionality analysis were applied. Specifically, various GLMs were applied in order to investigate a bit further the relationship between the RSNs degree and the instantaneous power of LF/HF of HRV. General linear models created for both sliding window analysis offsets. In the following figures (Figures 6.13-

6.15), with blue color can be seen the values of the RSNs degree versus the values of the instantaneous power of LF/HF of HRV. With red color is the underlying relationship between the dependent variable (RSNs degree) and independent variable (instantaneous power of LF/HF of HRV). The term "linear" in linear regression means that the regression function is linear in the coefficients α and β_j. It is not required that the X_i appear as linear terms in the regression function.

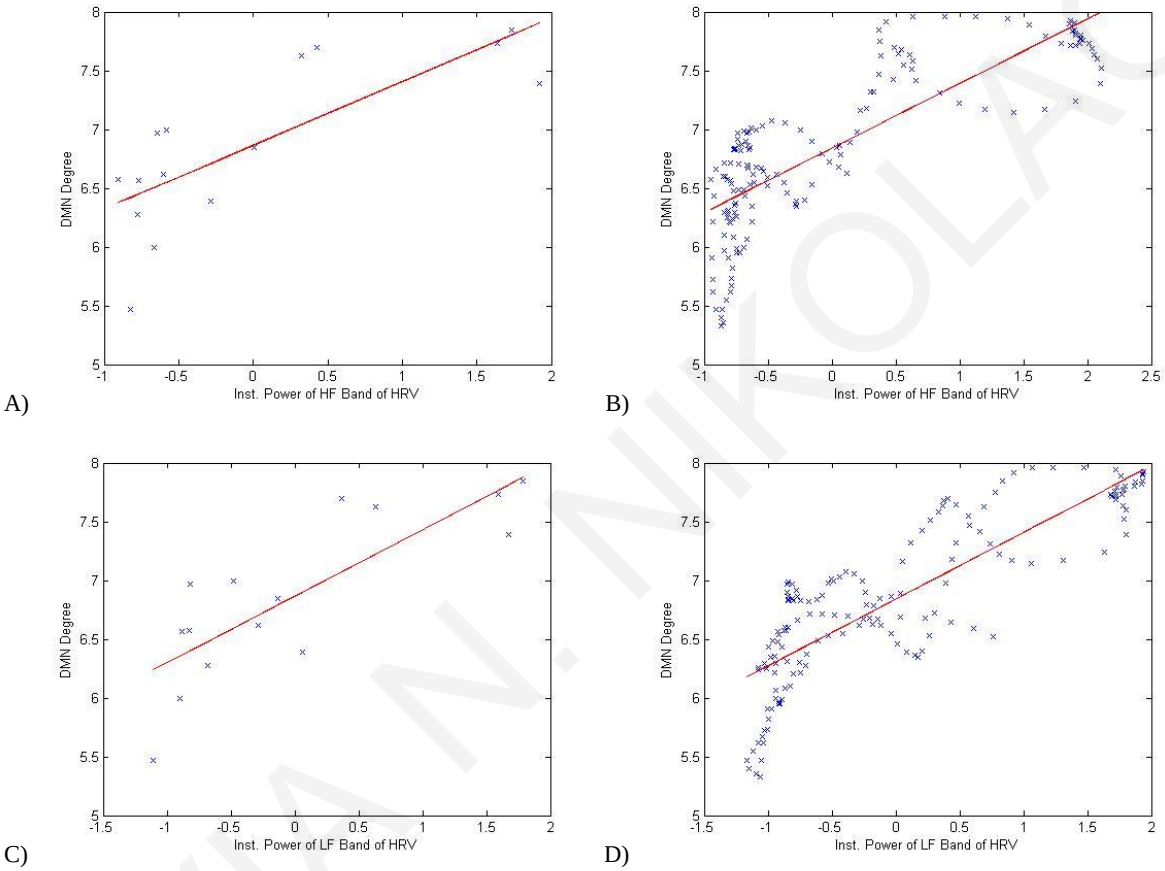

Figure 6.13. DMN network degree versus instantaneous power of LF/HF of HRV for one representative volunteer obtained from high dimensionality ICA. A) network degree vs instantaneous power of HF for a 10 time-point increment, B) network degree vs instantaneous power of HF for a 1 time-point increment, C) network degree vs instantaneous power of LF for a 10 time-point increment and D) network degree vs instantaneous power of LF for a 1 time-point increment.

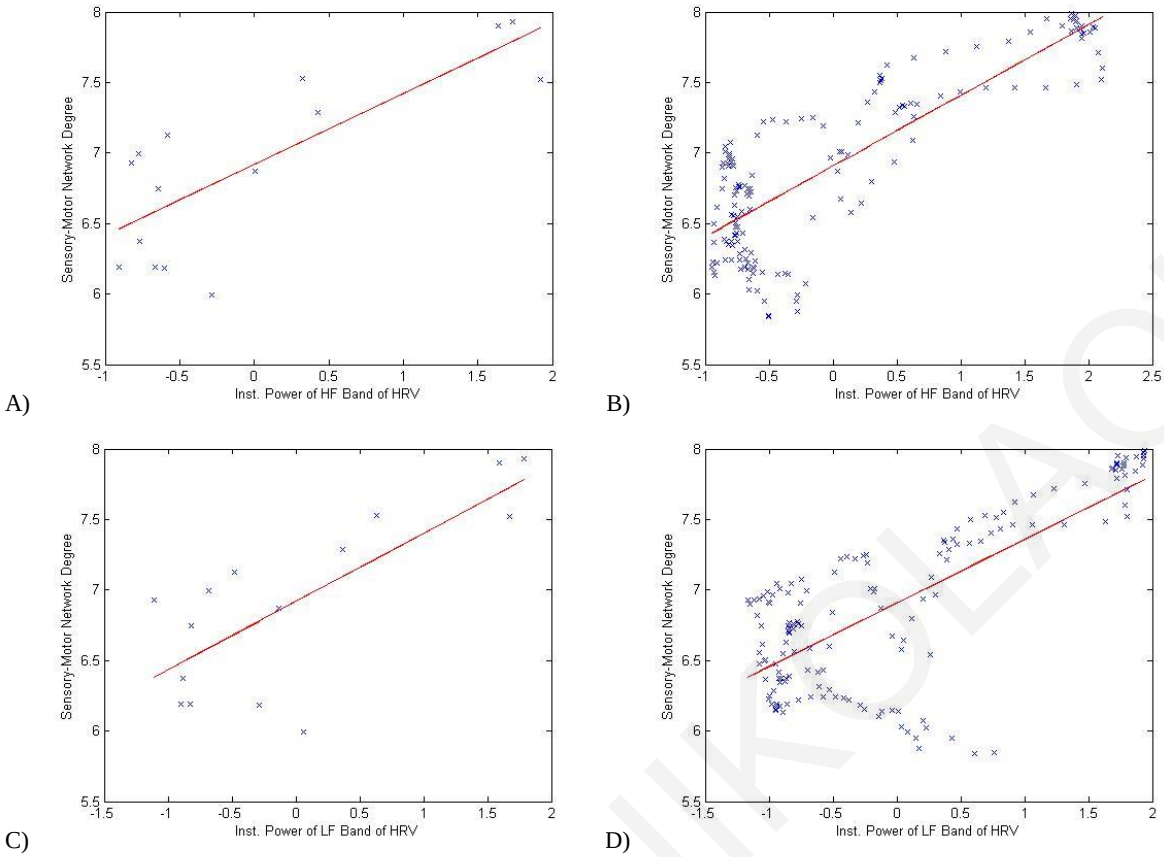

Figure 6.14. Sensory-Motor network degree versus instantaneous power of LF/HF of HRV for one representative volunteer obtained from high dimensionality ICA. A) network degree vs instantaneous power of HF for a 10 time-point increment, B) network degree vs instantaneous power of HF for a 1 time-point increment, C) network degree vs instantaneous power of LF for a 10 time-point increment and D) network degree vs instantaneous power of LF for a 1 time-point increment.

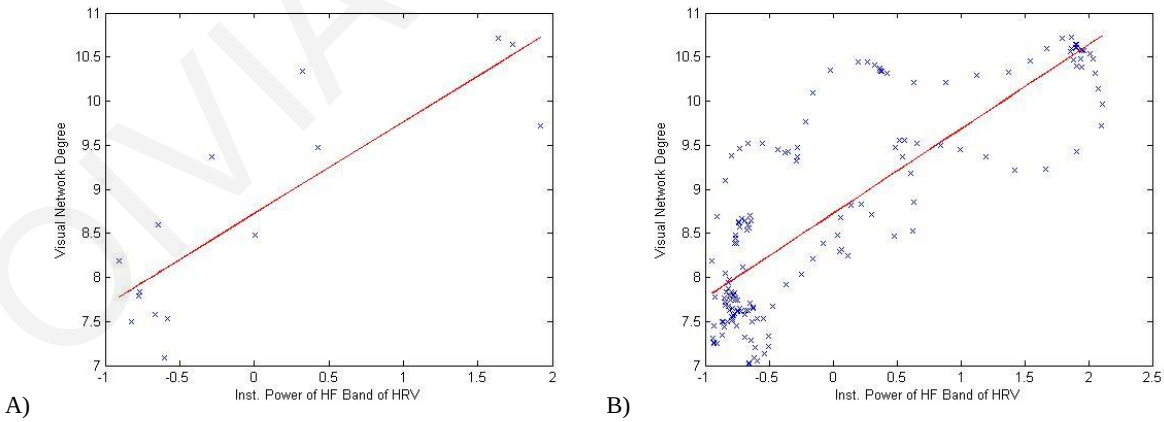

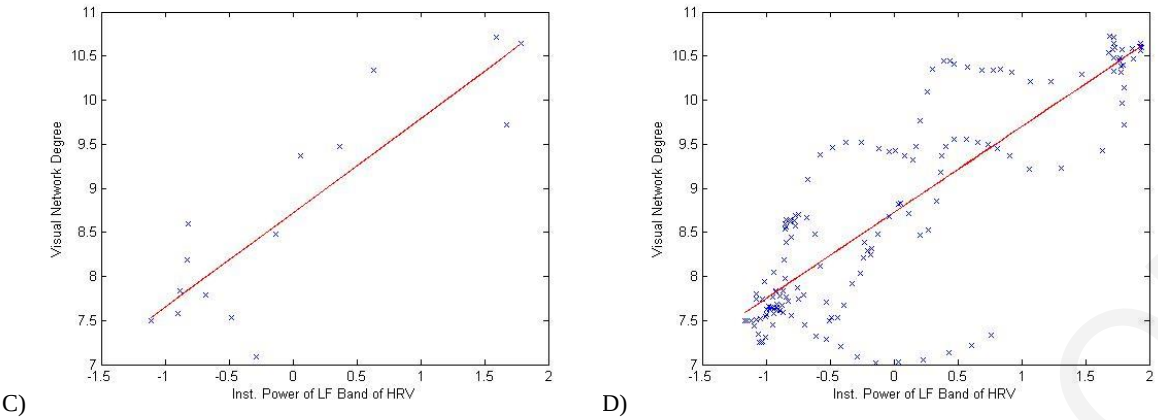

C) D)

Figure 6.15. Visual network degree versus instantaneous power of LF/HF of HRV for one representative volunteer obtained from high dimensionality ICA. A) network degree vs instantaneous power of HF for a 10 time-point increment, B) network degree vs instantaneous power of HF for a 1 time-point increment, C) network degree vs instantaneous power of LF for a 10 time-point increment and D) network degree vs instantaneous power of LF for a 1 time-point increment.

For the high dimensionality ICA analysis, all the limited bands of the instantaneous power of LF and HF of HRV were used as the independent variables in the general linear models that were conducted for each RSN.

- For the DMN, two univariate general linear models were created and as independent variables, we used the instantaneous power of LF and HF of HRV (Figure 6.16 – A and B). These two signals affected similarly the Network Degree of DMN. A MLR was not applied in this case because the signals re highly correlated with each other.
- The same procedure was applied and for the Sensory-Motor network as can be seen from the Figure 6.17 - A and B. In the case of the GLM, two general linear models were created and as independent variables, we used the instantaneous power of LF and HF of HRV. The HF of HRV yielded a slightly higher value that LF. A MLR was not applied in this case because the signals re highly correlated with each other.
- For the Visual network the results can be seen in Figures 6.18 – A and B. The same results were obtained in the case of low dimensionality ICA. In more detail, for the case of the GLM, two general linear models were created and as independent variables, we used the instantaneous power of LF and HF of HRV. These two signals affected similarly the Network Degree of DMN. A MLR was not applied in this case because the signals re highly correlated with each other.

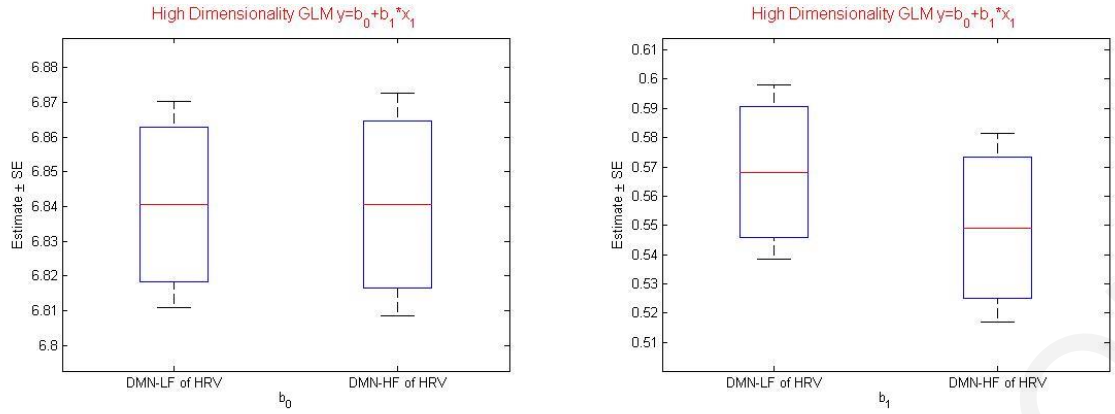

A) B)

Figure 6.16. A) Estimated values of b0 and B) b1 for the three univariate GLMs between DMN degree and instantaneous power of LF/HF of HRV obtained from low dimensionality ICA for a 1 time-point increment.

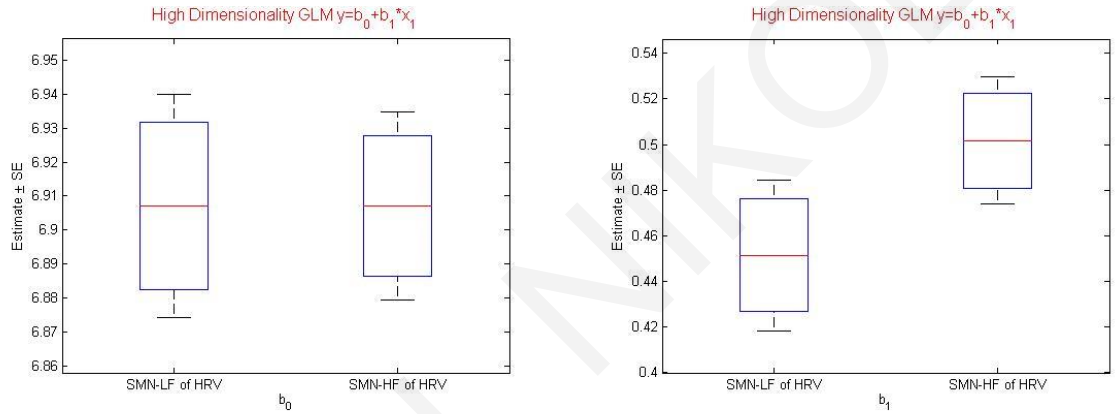

A) B)

Figure 6.17. A) Estimated values of b0 and B) b1 for the three univariate GLMs between SMN degree and instantaneous power of LF/HF of HRV obtained from low dimensionality ICA for a 1 time-point increment.

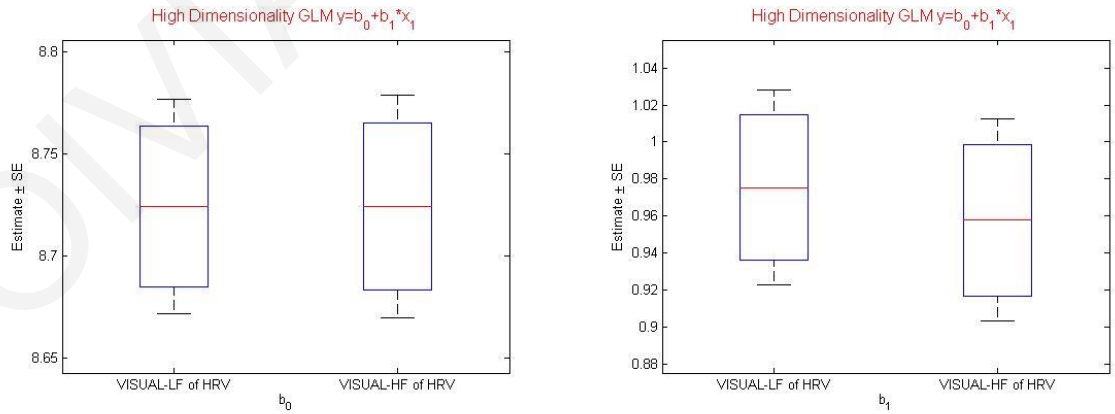

A) B)

Figure 6.18. A) Estimated values of b0 and B) b1 for the three univariate GLMs between Visual Network degree and instantaneous power of LF/HF of HRV obtained from low dimensionality ICA for a 1 time-point increment.

7. Discussion

The present thesis examines the emergence of dynamic, resting-state fMRI-based functional connectivity patterns and its modulation by physiological signal fluctuations using a variety of neuroimaging analysis tools (seed-based analysis, independent component analysis), signal processing methods (wavelets) and graph theory. Since estimates of time-varying connectivity are based on relatively few time points, dynamic analysis is particularly sensitive to noise. Variations in the magnitude of noise levels across the scan, as well as non-neuronal events that generate strong spatially correlated signal fluctuations, can masquerade as dynamics of FC. Sources of noise in fMRI include scanner drift, head motion, and physiological noise. Physiological noise can arise from cardiac pulsation, shifts in the main magnetic field caused by motion of the body during respiration, and variations in the respiratory volume/ rate and cardiac rate that evoke changes in BOLD contrast (Birn et al., 2008; Chang et al., 2009; Dagli et al., 1999; Shmueli et al., 2007). Variations in respiratory volume/rate and cardiac rate are of particular concern for resting-state analysis, as they reside predominantly in the low frequencies (<0.1 Hz) and tend to cause synchronous global modulations of the fMRI time series owing to their influence on arterial CO2 levels and cerebral blood flow (Chang and Glover, 2009; Peng et al., 2013; Wise et al., 2004). Since head motion and certain physiological events (such as a deep breath) are transient in nature, their adverse effects are lessened when resting-state data are analyzed using long time windows (as in conventional static analysis) to calculate FC. However, the impact on a dynamic analysis can be considerable: a slight head movement or a short deep breath will introduce strong signal fluctuations that can manifest as temporary changes in connectivity patterns.

The results of this thesis reveal a clear effect of time-varying signal power for three important physiological signals, the RVT, HR and PETCO2 on the time-varying network degree for three well-described RSNs: the default-mode, visual and somatosensory RSNs, revealing the important and possible confounding role of non-neuronal, physiological fluctuations in the context of fMRI-based RSN connectivity studies. This effect was found to be more pronounced for the fluctuations in the physiological spectral content in specific frequency sub-bands (time-varying band-limited power), as revealed by wavelet analysis. Furthermore, the same results were obtained by comparing the instantaneous power of LF and HF band of the HRV signal against the time-varying network degree for the networks of interest. Furthermore, it was found that the observed modulations were not as clear when the

analysis was performed in the MNI space, using anatomical masks to define the RSNs of interest.

Despite the well-established effect of physiological signals on fMRI connectivity and particular RSN connectivity (Wise et al., 2004; Napadow et al., 2008; Birn et al., 2006; Birn et al., 2012), to our knowledge the present work is the first to demonstrate that the time-varying properties of physiological signals may affect dynamic resting-state functional connectivity. The significance of this is that it suggests that even moderate modulations in the power of these signals can considerably influence RSN analyses and that a significant source of dynamic variations in resting-state connectivity is physiological in nature. Given that resting-state (spontaneous) fluctuations of physiological signals such as RVT, HR, PETCO2, LF and HF of HRV are of small magnitude, they are not expected to significantly effect neuronal activity *per se*; therefore, the observed modulatory effects are likely physiological in origin. In turn, this implies that fMRI studies that are based on DFC should take into account this possibly confounding factor, as these studies are typically interested in the neural source of fMRI-based DFC.

Fluctuations in fMRI-based functional brain networks have been observed in time scales from tens of seconds to several minutes (Chang and Glover, 2010; Hutchison et al., 2013; Zalesky et al., 2014). For instance, recent fMRI studies with high temporal resolution (Zalesky et al., 2014) have demonstrated the presence of time-varying patterns that are related to large-scale topological properties of the brain. It has been speculated that these fluctuations may achieve more efficient information transfer and energy expenditure. An important parameter in the context of DFC analyses employing sliding window analysis, is the window length. We investigated the effect of this choice in detail and based on our results, we concluded that a window length of 50 time lags (150 s) is a good trade-off between time resolution and obtaining a good cross-correlation estimate. There are, however, studies on related to dynamic functional connectivity have used sliding windows of around 50 s (some with lower TR values than 3 s) (Chang and Glover, 2010; Jones et al., 2012), while in (Zalesky et al., 2014) 60s windows were used, albeit with a sub second TR (60 s = 83 time lags). Furthermore, in (Van Dijk et al., 2010) it was suggested that average correlation values within and between RSNs stabilize at approximately 240 s. Given these observations the chosen window length is reasonable and is similar to the window lengths examined in other studies (e.g. (Hutchison et al., 2013)).

In order to obtain an overall measure of dynamic functional RSN connectivity, the time-varying average degree of the brain network defined by the corresponding RSN was computed,

as this graph theoretic measure is a straightforward way to quantify overall connectivity in a brain network and to monitor its variations over time. It should be noted that the *graded* degree (Rubinov and Sporns, 2010) was computed, i.e. the networks were not converted to binary networks, as often done in practice. As the focus was on the precise degree of modulation of dynamic connectivity by physiological fluctuations and not on which network connections, if any, are deemed "significant" (non-zero), which would further complicate matters and importantly would also depend on the method of network binarization (i.e. simple thresholding, surrogate data (Theiler, 1992) etc.). Furthermore, functional connectivity was quantified, not effective connectivity, as the use of the latter has been questioned in the case of fMRI-based connectivity (particularly RSN connectivity), owing to the low-pass filtering introduced by the HRF, which limits the time resolution and the ability to infer causal effects (Smith et al., 2011). However, it is worth noting that methods for estimating the hemodynamic response function (HRF) from resting-state data have been recently proposed (Wu et al., 2013), which could in turn provide more reliable effective connectivity estimates from fMRI RSN data (Smith et al., 2011), (Deshpande et al., 2010). This is an important point that deserves further attention.

Various methods were examined such as mask-based analysis, seed-based analysis and independent component analysis to define the appropriate RSNs as the network node definition procedure has been shown to influence all connectivity analyses (Smith et al., 2011) and statistical comparisons between different conditions (Mitsis et al., 2008) in fMRI studies. Results were not greatly affected. Whereas, registration of the BOLD time series to the MNI atlas was found to blur the modulatory effects of physiological fluctuations to a large extent. This suggests that sensitivity in tracking dynamic functional connectivity changes is lost when working in the MNI space and that possibly the overall connectivity patterns may not be as accurate as in the individual functional space. Overall, our results were found to be similar among all RSNs examined, with HR yielding overall more pronounced modulations of time-varying degree compared to PETCO2 (Tables 4-2, 4-4, 4-6) and in case of ICA analysis HR yielding overall more pronounced modulations of time-varying degree compared to PETCO2 and RVT (Tables 5-1, 5-2 and 5-3). Also, the LF and HF bands of HRV yielded pronounced modulations and especially the HF band of HRV (Tables 6-1 and 6-2). Interestingly, it was found that the somatosensory network yielded marginally significant results for PETCO2 for most volunteers in comparison to other networks (Table 4-6), which could be due to vascular anatomy differences between these networks.

While many pre-processing steps commonly applied to resting-state fMRI data are equally applicable when performing dynamic FC analysis (e.g. spatial filtering, nuisance regression), certain steps require special consideration. For example, censoring or down weighting time points with excessive motion or other known artifacts would affect a dynamic analysis due to its interruption of the temporal structure of the data; in a sliding window analysis, it would result in different effective numbers of time points available within different windows. Regarding temporal filtering, one may apply additional high-pass filtering or similar detrending operations prior to sliding-window analysis if it is desired that changes in FC on the scale of the sliding window reflect only frequencies with periods smaller than the window size.

To further investigate the effect of commonly used noise correction algorithms on the results, two different schemes of physiological correction (RETROICOR (Glover et al., 2000)) to regress out the effects of: (a) HR and respiration and (b) HR, respiration and PETCO2 were implemented in the case of seed-based analysis. A summary of the Spearman correlation coefficients results is presented in Table 7-1 for the broadband signals (i.e. without using wavelets).

Physiological correction type	**CO2**		**HR**	
	MEAN	**STD**	**MEAN**	**STD**
HR, respiration, CO2	0.35	0.15	0.53	0.25
HR, respiration	0.63	0.2	0.59	0.28

Table 7-1. Spearman correlation coefficients between time varying physiological signal power and network degree after performing physiological correction.

The modulatory effects of both signals were found to be reduced but not entirely removed when HR, CO2 and respiration were regressed out. However, the drop in correlation coefficient value is more substantial for CO2 when all the signals are regressed out. Consequently, modulating physiological effects on fMRI DFC do not disappear even after physiological correction – particularly for HR, for which the correlation coefficient remains fairly high (0.53). Likewise, it should be emphasized that whereas in most fMRI studies HR and respiration are regressed out using RETROICOR or other similar techniques, PETCO2 data are typically not recorded and consequently the effects of CO2 are not regressed out. The results suggest that collecting PETCO2 data in resting state studies is important and also that better physiological denoising algorithms for such data are needed. Successful denoising is

extremely important for properly interpreting dynamic FC results and recording respiration and cardiac events with a pneumatic belt and a plethysmograph is highly recommended.

Furthermore, white matter (WM) or cerebrospinal fluid (CSF) regression were not performed, which is a relatively common practice in similar studies, as it is rather difficult to obtain accurate individualized masks for WM and/or CSF and consequently some fraction of the grey matter signal may be regressed from the data, masking out the pure effects of physiological noise, which were the volunteer of interest (Murphy et al., 2013).

Seed-based analysis was repeated for different threshold values to investigate the effect on the threshold value. Our findings show that for values between around the reported value (between 0.55 and 0.75) the resulting areas from seed-based analysis were relatively cohesive and the results were very similar to those reported above. In addition, for larger threshold values, the seed-based areas become more disjointed; however, they can be constrained anatomically to yield the same number of DMN areas (ACC, PCC etc.) and the physiological modulations were found to be overall similar. Moreover, for smaller threshold values, the seed-based areas become more extensive (and possibly overlapping) but the effect of physiological modulations is still present. Finally, it should be noted that extreme threshold values yield either a few voxels or very extensive areas and are not of much practical interest.

With regards to ICA analysis, two different implementations were performed. First, both low and high dimensionality ICA were used. The low dimensionality ICA was used to identify the most commonly observed RSNs and then high dimensionality ICA was used to investigate subnetworks inside each RSN. By definition, high dimensionality ICA yielded more components for each RSN which were used to calculate the network degree compared to the low dimensionality approach. Specifically, ICA model order selection significantly influenced the RSN characteristics. At high ICA model orders, a network may be ‘split’ into a number of sub-networks depending on the number of estimated ICA components. Thus, the choice of ICA model order is a crucial element in the analysis, especially in functional brain connectivity studies. Large-scale networks (i.e. low model order components) are compact and easy to identify and include networks such as the visual, auditory, sensory-motor, etc. At low model orders (e.g. < 25), signal sources tend to aggregate into singular components involving various neuroanatomically and functionally separate units. These units become detectable later as separate components at higher model orders. Our results show that the wavelet decomposition yields considerably stronger correlations between network degree and physiological signal power as in the case of mask and seed-based analysis. Furthermore, the wavelet bands that

were extracted as the best, were overall the same throughout our examinations. When the second approach of the ICA analysis, the "Spatial-Sliding-ICA", was applied, the results were similar to the other methods. This approach required computation time, which was considerably larger compared to the standard ICA implementation. The user has to first create the spatial windows and then run on every window the low dimensionality ICA (again a model order of 25 ICs was chosen). Subsequently, for each window, its components were first manually classified as RSNs or motion-related ICA components. This procedure was applied for all the subjects. For this reason, this procedure was implemented only for the DMN in order to compare the results to the previous methods of analysis.

The frequency sub-bands that yielded the stronger correlations between time-varying degree and band-limited power are related to the spectral characteristics of each signal characteristic and suggest that fluctuations in these bands have a clearer modulatory effect. For PETCO2 modulations in very low frequency power (for mask-based and seed based analysis: 0-0.08Hz in functional space and 0-0.02Hz in MNI space, for low and high dimensionality ICA: 0-0.0625Hz in functional space, for spatial-sliding-ICA: 0.08Hz in functional space) were found to have the clearer effect, which is consistent with the previously described spectral characteristics of PETCO2 fluctuations (Mitsis et al., 2004; Liang et al., 1996). For HR a wider frequency band was identified (0-0.25Hz in all the methods of analysis) reflecting the fact that HR has a richer spectral content than PETCO2. Additionally, the identified frequency band contains the low frequency (LF - around 0.04-0.15Hz) spectral peak and possibly also the high frequency (HF - around 0.15-0.4Hz) spectral peak of the HR signal. While, often, these two spectral peaks are assumed to correspond to cardiac sympathetic and cardiac parasympathetic neural activity, respectively, the relative contributions of each mechanism still remain the subject of controversy and investigation. It is generally accepted that both LF and HF components of the HR signal (or HRV – note that fluctuations in these two signals have the same spectral characteristics) are affected by the complex interactions between both parasympathetic and sympathetic nerve fibers as well as mechanical, and other factors on the pacemaker cells usually located in the sinoatrial node (Billman, 2011). The effects of these two components was disentangled by obtaining estimates of instantaneous HF and LF HR power by using e.g. the Hilbert transform (Von Rosenberg et al., 2017).

Finally, for the low and high dimensionality ICA analysis and sliding window analysis with a 1 time-point increment, all the limited bands of the power of the physiological signals and the instantaneous power of LF and HF of HRV were used as the independent variables in

the general linear models that were implemented for each RSN. In the MLR models, not all the physiological signals yielded *p*-values lower than 0.05. On the other hand, in every GLM all the values yielded *p*-values lower than 0.05. In the GLMs where the independent variables were the instantaneous power of LF and HF of HRV, the results were very similar between these two independent variables with respect to their effect on time-varying RSN degree. Finally, in the low and high dimensionality analysis, the visual network yielded the same results in the MLR and GLM.

8. Conclusion and Future Work

8.1 Conclusion

The dynamic association between functional connectivity and physiological signals in the resting state has been investigated. In order to examine this association, we implemented and developed several methods for assessing dynamic functional connectivity RSNs: the DMN, as well as the visual and somatosensory networks. The DMN, as well as the visual and the somatosensory networks are among the most well established and important RSNs. In addition, the DMN exhibits robust resting-state functional connectivity with other regions related to physiological signals.

Overall, our results up to now are promising and we believe that they will have a significant impact in the field. The finding of a significant correlation between functional connectivity and physiological signals could demonstrate potential factors underlying dynamic changes in resting-state connectivity. Following this, delineating the brain regions exhibiting such connectivity modulation may bring further insight into neural mechanisms underlying autonomic control mechanisms. The results documented here reveal a modulatory effect of the aforementioned physiological signals on the dynamic resting functional connectivity patterns for a number of resting state networks (default mode network, somatosensory, visual). These modulation effects are more pronounced in specific frequency bands as it has been shown with the use of discrete wavelet decomposition. Finally, it has a great interest that the observed modulation effects were considerably clearer when processing was done in the individual functional space, compared to when it was done in standard (MNI) space.

8.2 Future Work

In this thesis, single-subject ICA was performed by using low and high dimensionality ICA. One idea for future work is to apply a group-level ICA. The group-level ICA can be performed again at two dimensionalities, low and high dimensionalities. By using the group-level ICA approach, we will extract independent components that will describe the DMN, SMN and Visual network for all subject in one. This will help us to summarizes our results and see the interaction between the RSNs degree and the band-limited power of physiological signals.

Additionally, a new method for regress out for each RSNs the physiological signals will be very interesting and also regress out the WM with better masks and CSF.

Furthermore, an investigation of how the combination with simultaneous EEG data to figure out electrophysiological (more directly related to neuronal activation) vs physiological signal power (non-neuronal mostly) can be performed to better understand the sources of DFC.

In this thesis, functional connectivity was quantified, not effective connectivity, as the use of the latter has been questioned in the case of fMRI-based connectivity (particularly RSN connectivity), owing to the low-pass filtering introduced by the HRF, which limits the time resolution and the ability to infer causal effects (Smith et al., 2011). However, it is worth noting that methods for estimating the hemodynamic response function (HRF) from resting-state data have been recently proposed (Wu et al., 2013), which could in turn provide more reliable effective connectivity estimates from fMRI RSN data (Smith et al., 2011), (Deshpande et al., 2010). This is an important point that deserves further attention.

The past years have seen many attempts to address what type of DFC abnormalities may occur in different brain disorders. Spontaneous thought, and therefore RS connectivity, is in fact altered in a wide range of clinical conditions, which were divided into two categories: the ones characterized by excessive variability of thought content over time, and the ones marked by its excessive stability (Christoff et al., 2016). Only DFC is able to capture the inner dynamic nature of FC alterations and, therefore, to describe these two conditions standing as causes of altered cognitive functions.

Finally, aside from its potential as a biomarker of various brain disorders, direct therapeutical applications of DFC can also be foreseen. For example, in real time fMRI neurofeedback (Stoeckel et al., 2014), subjects must learn to regulate the activity of a target region (or sometimes, the connectivity within a given network; Koush et al., 2013), so that beneficial cognitive changes are achieved. In this context, tracking brain functional dynamics through DFC methods stands out as an attractive tool. Further, the regulation of dynamic features of activity or connectivity could also turn out to be a fruitful strategy for the treatment of conditions in which brain dynamics is specifically hampered.

Finally, while a number of strategies for analyzing dynamic FC were discussed above, there are many possible extensions and unexplored avenues. Techniques can be adopted from other fields such as electrophysiology (LFP analysis) or computer science (pattern recognition) that offer a wide variety of tools for dynamic data analysis. Visualization is also an important area for development, due to the multi-dimensional nature of the output from a dynamic analysis.

Many authors are now submitting movies as supplementary material, displaying how FC varies over time. There is inherent value in having readers examine dynamics to identify patterns that may exist in the data and not detected by most algorithms. However, there must be a balance between data transparency and overwhelming the reader with information, hindering interpretation (Allen et al., 2012), and it will thus be fruitful to find ways of reducing the dimensionality while maintaining key features. Innovative methods for visualizing findings are under development (reviewed in Margulies et al., 2013); presenting the complexity of connectivity space through bundling similar edges and using surface-based glyphs (Böttger et al., in press), as well as dynamic network visualization tools developed in other disciplines (e.g. SONIA: http://www.stanford.edu/group/sonia/) offer a glimpse into possible avenues. Finally, it will be of critical importance to move from examining variation in FC with simple descriptive measures (such as correlation) to more complex, biologically informed generative models that can allow rigorous inference of non-stationarity functional network activity from fMRI data. Continued analysis of the temporal characteristics of spontaneous brain activity with direct electrophysiological measurements, as well as further comparative studies across states, species, disease models, pharmacological manipulations, and lesions, can help to inform such models and permit a deeper understanding spontaneous activity and the dynamics thereof.

A.Appendix – FSL Atlases

Harvard-Oxford cortical and subcortical structural atlases

Probabilistic atlases covering 48 cortical and 21 subcortical structural areas (Table A-1.), derived from structural data and segmentations kindly provided by the Harvard Center for Morphometric Analysis.

T1-weighted images of 21 healthy male and 16 healthy female subjects (ages 18-50) were individually segmented by the CMA using semi-automated tools developed in-house. The T1-weighted images were affine-registered to MNI152 space using FLIRT (FSL), and the transforms then applied to the individual labels. Finally, these were combined across subjects to form population probability maps for each label (Figure A.1.).

A)

B)

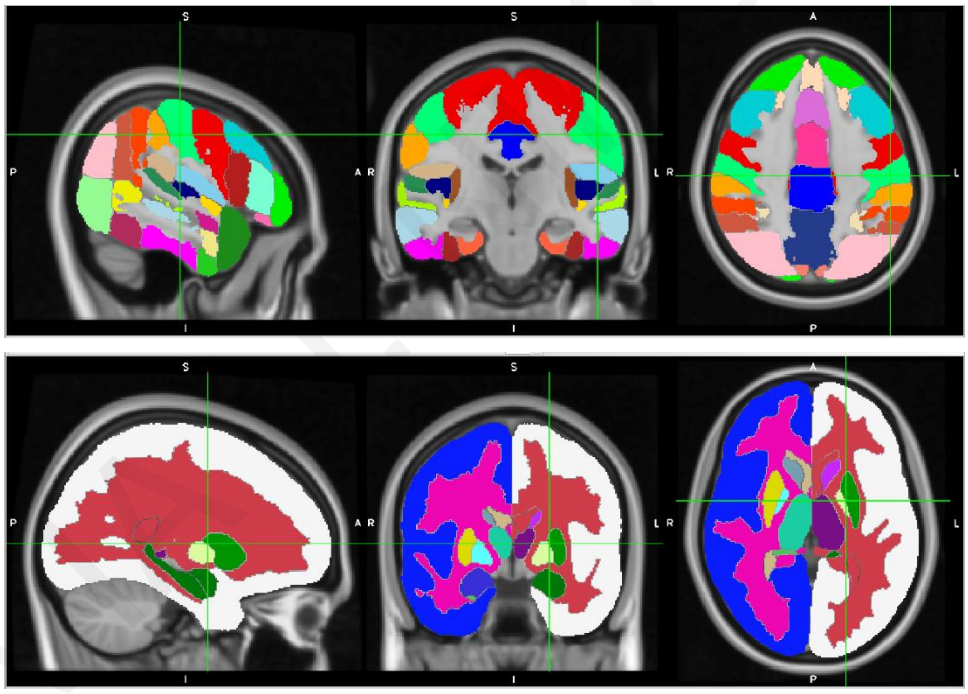

Figure A.1. Applying areas from A) Harvard-Oxford cortical and B) subcortical structural atlases.

Area / Filename	**Human Brain Position ZYX**
Cortical	
Frontal Pole	z="**35**", y="**94**", x="**48**"
Insular Cortex	z="**32**", y="**70**", x="**25**"
Superior Frontal Gyrus	z="**63**", y="**73**", x="**33**"
Middle Frontal Gyrus	z="**55**", y="**72**", x="**25**"

Inferior Frontal Gyrus, pars triangularis	z="**40**", y="**77**", x="**20**"
Inferior Frontal Gyrus, pars opercularis	z="**47**", y="**71**", x="**20**"
Precentral Gyrus	z="**68**", y="**51**", x="**44**"
Temporal Pole	z="**17**", y="**69**", x="**61**"
Superior Temporal Gyrus, anterior division	z="**32**", y="**59**", x="**73**"
Superior Temporal Gyrus, posterior division	z="**35**", y="**52**", x="**75**"
Middle Temporal Gyrus, anterior division	z="**26**", y="**59**", x="**74**"
Middle Temporal Gyrus, posterior division	z="**30**", y="**51**", x="**14**"
Middle Temporal Gyrus, temporooccipital part	z="**38**", y="**35**", x="**72**"
Inferior Temporal Gyrus, anterior division	z="**16**", y="**61**", x="**22**"
Inferior Temporal Gyrus, posterior division	z="**26**", y="**42**", x="**70**"
Inferior Temporal Gyrus, temporooccipital part	z="**29**", y="**35**", x="**70**"
Postcentral Gyrus	z="**69**", y="**42**", x="**52**"
Superior Parietal Lobule	z="**63**", y="**39**", x="**28**"
Supramarginal Gyrus, anterior division	z="**53**", y="**48**", x="**73**"
Supramarginal Gyrus, posterior division	z="**51**", y="**39**", x="**72**"
Angular Gyrus	z="**55**", y="**37**", x="**21**"
Lateral Occipital Cortex, superoir division	z="**57**", y="**28**", x="**60**"
Lateral Occipital Cortex, inferior division	z="**38**", y="**28**", x="**68**"
Intracalcarine Cortex	z="**40**", y="**23**", x="**47**"
Frontal Medial Cortex	z="**27**", y="**84**", x="**45**"
Juxtapositional Lobule Cortex	z="**63**", y="**63**", x="**45**"
Subcallosal Cortex	z="**27**", y="**74**", x="**46**"
Paracingulate Gyrus	z="**52**", y="**80**", x="**45**"
Cingulate Gyrus, anterior division	z="**57**", y="**61**", x="**45**"
Cingulate Gyrus, posterior division	z="**54**", y="**42**", x="**44**"
Precuneous Cortex	z="**55**", y="**31**", x="**45**"
Cuneal Cortex	z="**49**", y="**23**", x="**45**"
Frontal Orbital Cortex	z="**29**", y="**77**", x="**25**"
Parahippocampal Gyrus, anterior division	z="**18**", y="**62**", x="**57**"
Parahippocampal Gyrus, posterior division	z="**28**", y="**45**", x="**58**"
Lingual Gyrus	z="**33**", y="**22**", x="**41**"

Temporal Fusiform Cortex, anterior division	z="**15**", y="**61**", x="**62**"
Temporal Fusiform Cortex, posterior division	z="**24**", y="**47**", x="**64**"
Temporal Occipital Fusiform Cortex	z="**29**", y="**37**", x="**62**"
Occipital Fusiform Gyrus	z="**30**", y="**23**", x="**33**"
Frontal Operculum Cortex	z="**37**", y="**74**", x="**66**"
Central Opercular Cortex	z="**40**", y="**61**", x="**19**"
Parietal Operculum Cortex	z="**47**", y="**50**", x="**17**"
Planum Polare	z="**36**", y="**60**", x="**20**"
Heschl's Gyrus (includes H1 and H2)	z="**39**", y="**52**", x="**67**"
Planum Temporale	z="**40**", y="**53**", x="**74**"
Supracalcarine Cortex	z="**42**", y="**21**", x="**44**"
Occipital Pole	z="**34**", y="**15**", x="**37**"
Subcortical	
Left Cerebral White Matter	z="**52**", y="**37**", x="**60**"
Left Cerebral Cortex	z="**40**", y="**58**", x="**70**"
Left Lateral Ventrical	z="**41**", y="**42**", x="**56**"
Left Thalamus	z="**39**", y="**52**", x="**50**"
Left Caudate	z="**40**", y="**70**", x="**51**"
Left Putamen	z="**34**", y="**67**", x="**56**"
Left Pallidum	z="**35**", y="**62**", x="**54**"
Brain-Stem	z="**20**", y="**50**", x="**44**"
Left Hippocampus	z="**26**", y="**55**", x="**59**"
Left Amygdala	z="**25**", y="**62**", x="**57**"
Left Accumbens	z="**32**", y="**69**", x="**50**"
Right Cerebral White Matter	z="**49**", y="**38**", x="**29**"
Right Cerebral Cortex	z="**43**", y="**60**", x="**20**"
Right Lateral Ventricle	z="**44**", y="**45**", x="**35**"
Right Thalamus	z="**39**", y="**51**", x="**38**"
Right Caudate	z="**42**", y="**69**", x="**38**"
Right Putamen	z="**34**", y="**68**", x="**34**"
Right Pallidum	z="**34**", y="**62**", x="**36**"
Right Hippocampus	z="**26**", y="**56**", x="**31**"

Right Amygdala	z="**25**", y="**63**", x="**32**"
Right Accumbens	z="**32**", y="**68**", x="**40**"

Table A-1. Probabilistic atlases covering 48 cortical and 21 subcortical structural areas

Juelich Atlas

The atlas contains 52 grey matter structures and 10 white matter structures (Tables A-2.). The atlas is based on the miscroscopic and quantitative histological examination of ten human post-mortem brains. The histological volumes of these brains were 3D reconstructed and spatially normalised into the space of the MNI single subject template to create a probabilistic map of each area. For the FSL version of this atlas, these probabilistic maps were then linearly transformed into MNI152 space (Figure A.2.).

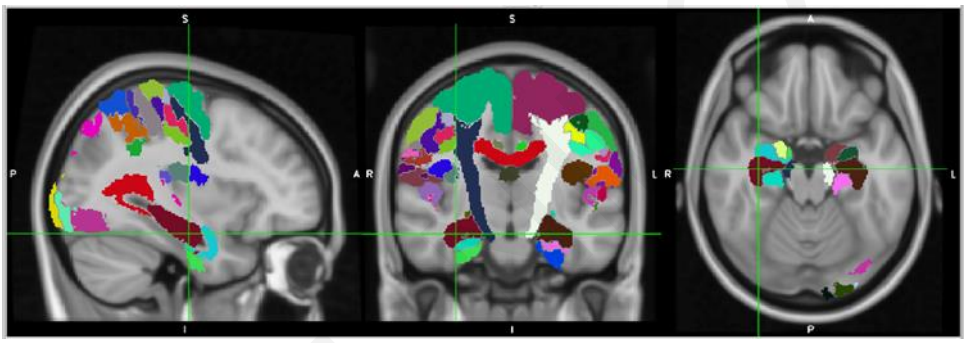

Figure A.2. Applying areas from Juelich Atlas

Area / Filename	**Human Brain Position ZYX**
Frontal Lobe	
Broca's region	
Area 44 / Broca 44	Broca's area BA44 L (z="**95**", y="**137**", x="**142**") Broca's area BA44 R (z="**87**", y="**141**", x="**36**")
Area 45 / Broca_45	GM Broca's area BA45 L (z="**85**", y="**151**", x="**142**") GM Broca's area BA45 R (z="**79**", y="**152**", x="**36**")
Agranular premotor cortex	

Area 6 / Premotor_6	GM Premotor cortex BA6 L (z="**138**", y="**112**", x="**102**") GM Premotor cortex BA6 R (z="**143**", y="**110**", x="**77**")
Primary motor cortex	
Area 4a / PMC_4a	GM Primary motor cortex BA4a L (z="**140**", y="**100**", x="**100**") GM Primary motor cortex BA4a R (z="**142**", y="**97**", x="**82**")
Area 4p / PMC_4p	GM Primary motor cortex BA4p L (z="**127**", y="**96**", x="**119**") GM Primary motor cortex BA4p R (z="**120**", y="**103**", x="**56**")
Parietal Lobe	
Somatosensory Cortex	
Area 3a / PSC_3a	GM Primary somatosensory cortex BA3a L (z="**118**", y="**99**", x="**123**") GM Primary somatosensory cortex BA3a R (z="**114**", y="**105**", x="**56**")
Area 3b / PSC_3b	GM Primary somatosensory cortex BA3b L (z="**125**", y="**99**", x="**128**") GM Primary somatosensory cortex BA3b R (z="**109**", y="**115**", x="**37**")
Area 1 / PSC_1	GM Primary somatosensory cortex BA1 L (z="**121**", y="**105**", x="**141**") GM Primary somatosensory cortex BA1 R (z="**119**", y="**109**", x="**36**")
Area 2 / PSC_2	GM Primary somatosensory cortex BA2 L (z="**118**", y="**100**", x="**139**") GM Primary somatosensory cortex BA2 R (z="**126**", y="**86**", x="**63**")
Parietal operculum / SII	

OP 1 / SII OP1	GM Secondary somatosensory cortex / Parietal operculum OP1 L (z="**91**", y="**102**", x="**138**") GM Secondary somatosensory cortex / Parietal operculum OP1 R (z="**94**", y="**99**", x="**43**")
OP 2 / SII_OP2	GM Secondary somatosensory cortex / Parietal operculum OP2 L (z="**91**", y="**103**", x="**126**") GM Secondary somatosensory cortex / Parietal operculum OP2 R (z="**90**", y="**105**", x="**54**")
OP 3 / SII_OP3	GM Secondary somatosensory cortex / Parietal operculum OP3 L (z="**89**", y="**115**", x="**132**") GM Secondary somatosensory cortex / Parietal operculum OP3 R (z="**93**", y="**112**", x="**50**")
OP 4 / SII_OP4	GM Secondary somatosensory cortex / Parietal operculum OP4 L (z="**85**", y="**117**", x="**147**") GM Secondary somatosensory cortex / Parietal operculum OP4 R (z="**85**", y="**118**", x="**28**")
Inferior parietal lobule	
Area PF / IPC_PF	GM Inferior parietal lobule PF L (z="**107**", y="**86**", x="**146**") GM Inferior parietal lobule PF R (z="**101**", y="**92**", x="**28**")
Area PFcm / IPC_PFcm	GM Inferior parietal lobule PFcm L (z="**100**", y="**84**", x="**140**") GM Inferior parietal lobule PFcm R (z="**96**", y="**93**", x="**40**")
Area PFm / IPC_PFm	GM Inferior parietal lobule PFm L (z="**106**", y="**68**", x="**141**") GM Inferior parietal lobule PFm R (z="**109**", y="**81**", x="**34**")
Area PFop / IPC_PFop	GM Inferior parietal lobule PFop L (z="**96**", y="**103**", x="**148**")

	GM Inferior parietal lobule PFop R (z="**100**", y="**108**", x="**37**")
Area PFt / IPC_PFt	GM Inferior parietal lobule PFt L (z="**108**", y="**100**", x="**145**") GM Inferior parietal lobule PFt R (z="**111**", y="**101**", x="**36**")
Area Pga / IPC_PGa	GM Inferior parietal lobule Pga L (z="**104**", y="**69**", x="**142**") GM Inferior parietal lobule Pga R (z="**104**", y="**71**", x="**37**")
Area PGp / IPC_PGp	GM Inferior parietal lobule PGp L (z="**101**", y="**54**", x="**133**") GM Inferior parietal lobule PGp R (z="**102**", y="**60**", x="**42**")
Intraparietal sulcus	
hIP1 / AIPS_IP1	GM Anterior intra-parietal sulcus hIP1 L (z="**107**", y="**75**", x="**125**") GM Anterior intra-parietal sulcus hIP1 R (z="**108**", y="**78**", x="**53**")
hIP2 / AIPS_IP2	GM Anterior intra-parietal sulcus hIP2 L (z="**109**", y="**89**", x="**135**") GM Anterior intra-parietal sulcus hIP2 R (z="**120**" y="**90**" x="**48**")
hIP3 / AIPS_IP3	GM Anterior intra-parietal sulcus hIP3 L (z="**120**", y="**69**", x="**119**") GM Anterior intra-parietal sulcus hIP3 R (z="**122**", y="**80**", x="**54**")
Superior parietal lobule	
Area 5Ci / SPL_5Ci	GM Superior parietal lobule 5Ci L (z="**116**", y="**88**", x="**105**") GM Superior parietal lobule 5Ci R (z="**117**", y="**94**", x="**79**")

Area 5L / SPL_5L	GM Superior parietal lobule 5L L (z="**139**", y="**82**", x="**108**") GM Superior parietal lobule 5L R (z="**143**", y="**76**", x="**78**")
Area 5M / SPL_5M	GM Superior parietal lobule 5M L (z="**130**", y="**84**", x="**99**") GM Superior parietal lobule 5M R (z="**132**", y="**80**", x="**83**")
Area 7A / SPL_7A	GM Superior parietal lobule 7A L (z="**135**", y="**69**", x="**111**") GM Superior parietal lobule 7A R (z="**133**", y="**68**", x="**61**")
Area 7M / SPL_7M	GM Superior parietal lobule 7M L (z="**107**", y="**51**", x="**94**") GM Superior parietal lobule 7M R (z="**115**", y="**53**", x="**86”**)
Area 7P / SPL_7P	GM Superior parietal lobule 7P L (z="**126**", y="**53**", x="**99**") GM Superior parietal lobule 7P R (z="**125**", y="**53**", x="**78**")
Area 7PC / SPL_7PC	GM Superior parietal lobule 7PC L (z="**128**", y="**78**", x="**124**") GM Superior parietal lobule 7PC R (z="**124**", y="**83**", x="**59**")
Occipital Lobe	
Visual cortex	
Area 17 / V1 / hOC1	GM Visual cortex V1 BA17 L (z="**74**", y="**30**", x="**99**") GM Visual cortex V1 BA17 R (z="**76**", y="**34**", x="**75**")
Area 18 / V2 / hOC2	GM Visual cortex V2 BA18 L (z="**66**", y="**33**", x="**98**")

	GM Visual cortex V2 BA18 R (z="**65**", y="**42**", x="**75)**
hOC3v (V3v) / hOC3v	GM Visual cortex V3V L (z="**66**", y="**43**", x="**105**") GM Visual cortex V3V R (z="**64**", y="**47**", x="**68**")
hOC4v (V4) / hOC4	GM Visual cortex V4 L (z="**61**", y="**42**", x="**117**") GM Visual cortex V4 R (z="**62**", y="**50**", x="**59**")
hOC5 (V5) / hOC5	GM Visual cortex V5 L (z="**76**", y="**52**", x="**132**") GM Visual cortex V5 R (z="**78**", y="**60**", x="**41**")
Temporal Lobe	
Auditory cortex	
Area TE 1.0 / PAC_TE10	GM Primary auditory cortex TE1.0 L (z="**79**", y="**105**", x="**137**") GM Primary auditory cortex TE1.0 R (z="**77**", y="**114**", x="**39**")
Area TE 1.1 / PAC_TE11	GM Primary auditory cortex TE1.1 L (z="**84**", y="**96**", x="**131**") GM Primary auditory cortex TE1.1 R (z="**83**", y="**100**", x="**49**")
Area TE 1.2 / PAC_TE12	GM Primary auditory cortex TE1.2 L (z="**76**", y="**113**", x="**143**") GM Primary auditory cortex TE1.2 R (z="**76**", y="**120**", x="**34**")
Hippocampus formation	
Cornu ammonis / Hippocampus_CA	GM Hippocampus cornu ammonis L (z="**53**", y="**110**", x="**119**")

	GM Hippocampus cornu ammonis R (z="**53**", y="**111**", x="**56**")
Entorhinal cortex / Hippocampus_EC	GM Hippocampus entorhinal cortex L (z="**35**", y="**121**", x="**115**") GM Hippocampus entorhinal cortex R (z="**34**", y="**125**", x="**64**")
Fascia dentata / Hippocampus_FD	GM Hippocampus dentate gyrus L (z="**53**", y="**109**", x="**119**") GM Hippocampus dentate gyrus R (z="**54**", y="**110**", x="**58**")
HATA – region / Hippocampus_HATA	GM Hippocampus hippocampal-amygdaloid transition area L (z="**50**", y="**117**", x="**107**") GM Hippocampus hippocampal-amygdaloid transition area R (z="**51**", y="**117**", x="**71**")
Subiculum / Hippocampus_SUB	GM Hippocampus subiculum L (z="**43**", y="**115**", x="**112**") GM Hippocampus subiculum R (z="**54**", y="**107**", x="**64**")
Amygdala complex	
Centro-median nucleus / Amygdala_CM	GM Amygdala_centromedial group L (z="**62**", y="**118**", x="**113**") GM Amygdala_centromedial group R (z="**63**", y="**119**", x="**64**")
Latero-basal nucleus / Amygdala_LB	GM Amygdala_laterobasal group L (z="**49**", y="**120**", x="**113**") GM Amygdala_laterobasal group R (z="**51**", y="**119**", x="**64**")
Superficial nucleus / Amygdala_SF	GM Amygdala_superficial group L (z="**54**", y="**122**", x="**109**") GM Amygdala_superficial group R (z="**61**", y="**122**", x="**67**")
White matter	

Acoustic radiation / Fiber_ar	WM Acoustic radiation R (z="**76**", y="**112**", x="**41**") WM Acoustic radiation L (z="**72**", y="**100**", x="**131**")
Callosal body / Fiber_cb	WM Callosal body (z="**87**", y="**90**", x="**89**")
Cingulum / Fiber_cing	WM Cingulum R (z="**98**", y="**84**", x="**81**") WM Cingulum L (z="**105**", y="**109**", x="**97**")
Corticospinal tract / Fiber_ct	WM Corticospinal tract R (z="**122**", y="**104**", x="**65**") WM Corticospinal tract L (z="**109**", y="**109**", x="**117**")
Fornix / Fiber_form	WM Fornix (z="**89**", y="**106**", x="**88**")
Inferior occipito-frontal fascicle / Fiber_iof	WM Inferior occipito-frontal fascicle R (z="**66**", y="**134**", x="**56**") WM Inferior occipito-frontal fascicle L (z="**64**", y="**130**", x="**121**")
Laternal geniculate body / Fiber_lgb	GM Lateral geniculate body R (z="**63**", y="**104**", x="**65**") GM Lateral geniculate body L (z="**61**", y="**103**", x="**112**")
Mamillary body / Fiber_mb	GM Mamillary body (z="**57**", y="**118**", x="**87**")
Medial geniculate body / Fiber_mgb	GM Medial geniculate body R (z="**65**", y="**100**", x="**73**") GM Medial geniculate body L (z="**64**", y="**100**", x="**106**")
Optic radiation / Fiber_or	WM Optic radiation R (z="**75**", y="**45**", x="**64**") WM Optic radiation L (z="**77**", y="**45**", x="**111**")
Superior longitudinal fascicl / Fiber_slf	WM Superior longitudinal fascicle R (z="**101**", y="**102**", x="**58**")

	WM Superior longitudinal fascicle L (z="**99**", y="**98**", x="**120**")
Superior occipito-frontal fascicle / Fiber_sof	WM Superior occipito-frontal fascicle R (z="**89**", y="**142**", x="**68**") WM Superior occipito-frontal fascicle L (z="**83**", y="**151**", x="**110**")
Uncinate fascicle / Fiber_uf	WM Uncinate fascicle R (z="**63**", y="**124**", x="**57**") WM Uncinate fascicle L (z="**62**", y="**123**", x="**121**")

Table A-2. The atlas contains 52 grey matter structures and 10 white matter structures

Scientific publications based on this thesis

Journal Publications:

Nikolaou, F., Orphanidou, C. Papakyriakou, P., Murphy, K., Wise, R.G. and G.D. Mitsis "Spontaneous Physiological Variability Modulates Dynamic Functional Connectivity in Resting-State fMRI," Philosophical Transactions of the Royal Society A 374.2067: 20150183, 2016 (I.F. 2.864).

Conference Proceedings Publications and Abstracts:

Nikolaou, F., Orphanidou, C., Murphy, K., Wise, R.G. and G.D. Mitsis "Investigation of Interaction Between Physiological Signals and fMRI Dynamic Functional Connectivity using Independent Component Analysis," 40th Ann. Intern. Conf. IEEE EMBS, Hawaii, Honolulu, July 2018 (accepted).

Nikolaou, F., Orphanidou, C., Wise, R.G. and G.D. Mitsis "Investigation of Physiological Variability Effects on fMRI Dynamic Functional Connectivity using Independent Component Analysis," ISMRM 27th Annual Meeting and Exhibition, France, Paris, June 2018 (accepted).

Nikolaou, F., Orphanidou, C., Papakyriakou, P., Murphy, K., Wise, R.G. and G.D. Mitsis "Physiological Signals Modulate Dynamic Functional Connectivity in Resting-State fMRI," 22nd Annual Meeting of the Organization for Human Brain Mapping, Geneva, Switzerland, June 2016.

Nikolaou, F., Orphanidou, C., Wise, R.G. and G.D. Mitsis "Arterial CO2 Effects Modulate Dynamic Functional Connectivity in Resting-State fMRI," 37th Ann. Intern. Conf. IEEE EMBS, pp. 1809-1812, Milano, Italy, August 2015.

Journal Publication in Preparation:

Nikolaou, F., Orphanidou, C., Murphy, K., Wise, R.G. and G.D. Mitsis "Effects of Physiological Signals and Cardiac Sympathetic and Parasympathetic Activity on DFC using ICA," (to be submitted).

References

Abou Elseoud A., Littow H., Remes J., Starck T., Nikkinen J., Nissila J., Timonen M., Tervonen O., Kiviniemi V., 2011. Group-ICA model order highlights patterns of functional brain connectivity. Frontiers in Systems Neuroscience 5,37.

Abou-Elseoud A., Starck T., Remes J., Nikkinen J., Tervonen O., Kiviniemi V., 2010. The effect of model order selection in group PICA. Human Brain Mapping 31(8),1207-1216.

Andrews-Hanna J.R., Snyder A.Z., Vincent J.L., Lustig C., Head D., Raichle M.E., Buckner R.L., 2007. Disruption of large-scale brain systems in advanced aging. Neuron 56(5),924-935.

Bandettini P.A., 2012. Twenty years of functional MRI: The science and the stories. Neuroimage 62(2),575-588.

Bandettini P.A., Wong E.C., 1997. A hypercapnia-based normalization method for improved spatial localization of human brain activation with fMRI. NMR Biomed 10,197–203.

Bandettini P.A., Wong E.C., Hinks R.S., Tikofsky R.S. and Hyde J.S., 1992. Time course EPI of human brain function during task activation. Magn. Reson. Med. 25,390–397.

Barbieri R., Matten E.C., Alabi A., Brown E.N., 2005. A point-process model of human heartbeat intervals: new definitions of heart rate and heart rate variability. Am. J. Physiol. Heart Circ. Physiol. 288,H424–H435.

Beckmann C.F. and Smith S.M., 2004. Probabilistic independent component analysis for functional magnetic resonance imaging. IEEE Transactions on Medical Imaging 23(2),137-152.

Beckmann C.F., 2012. Modelling with independent components. Neuroimage 62(2),891-901.

Beckmann C.F., DeLuca M., Devlin J.T., Smith S.M., 2005. Investigations into resting-state connectivity using independent component analysis. Philosophical Transactions of the Royal Society of London.Series B, Biological Sciences 360(1457),1001-1013.

Bernardi L., Salvucci F., Suardi R., Solda P.L., Calciati A., Perlini S., Falcone C., Ricciardi L., 1990. Evidence for an intrinsic mechanism regulating heart rate variability in the transplanted and the intact heart during submaximal dynamic exercise? Cardiovasc. Res. 24,969–981.

Berne R.M., Levy M.N., 1993. Physiology. Vol. 3. Mosby; St. Louis p. 422p. 560p. 599-602.

Berntson G.G., et al., 1997. Heart rate variability: origins, methods, and interpretive caveats. Psychophysiology 34,623–648.

Betzel R.F., Fukushima M., He Y., Zuo X.n., Sporns O., 2016. Dynamic fluctuations coincide with periods of high and low modularity in resting-state functional brain networks. NeuroImage 127(February),287–297.

Billman G.E., 2011. Heart rate variability-a historical perspective. Front. Physiol. 2,1–13.

Birn R.M., Diamond J.B., Smith M.A., Bandettini P.A., 2006. Separating respiratory-variation-related fluctuations from neuronal-activity-related fluctuations in fMRI. Neuroimage 31,1536–1548.

Birn RM., 2012. The role of physiological noise in resting-state functional connectivity. Neuroimage 62,864–870.

Biswal B., Bandettini P.A., Jesmanowicz A., Hyde J.S., 1993. Time-frequency analysis of functional EPI timecourse series. Proc., SMRM, 12th Annual Meeting; New York. p.722

Biswal B., Yetkin F.Z., Haughton V.M., Hyde J.S., 1995. Functional connectivity in the motor cortex of resting human brain using echo-planar MRI. Magnetic Resonance in Medicine : Official Journal of the Society of Magnetic Resonance in Medicine / Society of Magnetic Resonance in Medicine 34(4),537-541.

Biswal B.B., Van Kylen J., Hyde J.S., 1997. Simultaneous assessment of flow and BOLD signals in resting-state functional connectivity maps. NMR in Biomedicine 10(4-5),165-170.

Buckner R.L., Andrews-Hanna J.R., Schacter D.L., 2008. The brain's default network: Anatomy, function, and relevance to disease. Annals of the New York Academy of Sciences 1124,1-38.

Bullmore E., Sporns O., 2009. Complex brain networks: graph theoretical analysis of structural and functional systems. Nat. Rev. Neurosci. 10 (3), 186–198.

Buxton R.B., 2012. Dynamic models of BOLD contrast. Neuroimage 62,953–961.

Chang C. and Glover G.H., 2010. Time-frequency dynamics of resting-state brain connectivity measured with fMRI. Neuroimage 50,81–98.

Chang C., Liu Z., Chen M.C., Liu X., Duyn J.H., 2013. EEG correlates of time-varying BOLD functional connectivity. Neuroimage 72,227–236.

Christoff K., Irving Z.C., Fox K.C., Spreng R.N., Andrews-Hanna J.R., 2016. Mind-wandering as spontaneous thought: a dynamic framework. Nat. Rev. Neurosci., 17 (11), pp. 718-731

Clauset A., Newman M.E., Moore C., 2004. Finding community structure in very large networks. Phys. Rev. E 70 (6), 066111.

Cole D.M., Smith S.M., Beckmann C.F., 2010. Advances and pitfalls in the analysis and interpretation of resting-state FMRI data. Frontiers in Systems Neuroscience 4,8.

Cordes D., Haughton V.M., Arfanakis K., Wendt G.J., Turski P.A., Moritz C.H., Quigley M.A., Meyerand M.E., 2000. Mapping functionally related regions of brain with functional connectivity MR imaging. AJNR.American Journal of Neuroradiology 21(9),1636-1644.

Critchley H.D., Mathias C.J., Josephs O., O'Doherty J., Zanini S., Dewar B.K., Cipolotti L., Shallice T., Dolan R.J., 2003. Human cingulate cortex and autonomic control: converging neuroimaging and clinical evidence. Brain. 126,2139–2152.

Dagli M.S., Ingeholm J.E., Haxby J.V., 1999. Localization of cardiac-induced signal change in fMRI. Neuroimage 9,407–415.

Damoiseaux J.S., Rombouts S.A., Barkhof F., Scheltens P., Stam C.J., Smith S.M., Beckmann C.F., 2006. Consistent resting-state networks across healthy volunteers. Proceedings of the National Academy of Sciences of the United States of America 103(37),13848-13853.

Daubechies I., 1992. Ten lectures on wavelets. In CBMS-NSF regional conference series in applied mathematics, vol. 62. Philadelphia, PA: SIAM.

De Luca M., Beckmann C.F., De Stefano N., Matthews P.M., Smith S.M., 2006. fMRI resting state networks define distinct modes of long-distance interactions in the human brain. Neuroimage 29(4),1359-1367.

De Pasquale F., Della Penna S., Snyder A.Z., Lewis C., Mantini D., Marzetti L., Belardinelli P., Ciancetta L., Pizzella V., Romani G.L., and others, 2010. Temporal dynamics of spontaneous MEG activity in brain networks. Proceedings of the National Academy of Sciences of the United States of America 107(13),6040-6045.

Deshpande G., Sathian K., Hu X., 2010. Effect of hemodynamic variability on Granger causality analysis of fMRI. Neuroimage 52,884–896.

Di Martino A., Scheres A., Margulies D.S., Kelly A.M., Uddin L.Q., Shehzad Z., Biswal B., Walters J.R., Castellanos F.X., Milham M.P., 2008. Functional connectivity of human striatum: A resting state FMRI study. Cerebral Cortex (New York, N.Y.: 1991) 18(12),2735-2747.

Dipasquale O., Griffanti L., Clerici M., Nemni R., Baselli G., Baglio F., 2015. High-dimensional ICA analysis detects within-network functional connectivity damage of default-mode and sensory-motor networks in Alzheimer's disease. Front Hum Neurosci 9,43.

Duggento A, Bianciardi M, Passamonti L, Wald LL, Guerrisi M, Barbieri R, Toschi N. 2016 Globally conditioned Granger causality in brain–brain and brain–heart interactions: a combined heart rate variability/ultra-high-field (7 T) functional magnetic resonance imaging study. Phil. Trans. R. Soc. A 374, 20150185.

Elghozi J.L., Girard A., Laude D., 2001. Effects of drugs on the autonomic control of short-term heart rate variability. Auton. Neurosci. 90,116–121.

Elghozi J.L., Julien C., 2007. Sympathetic control of short-term heart rate variability and its pharmacological modulation. Fundam. Clin. Pharmacol 21,337–347.

Fox M.D. and Raichle M.E., 2007. Spontaneous fluctuations in brain activity observed with functional magnetic resonance imaging. Nature Reviews.Neuroscience 8(9),700-711.

Fox M.D., Snyder A.Z., Vincent J.L., Corbetta M., Van Essen D.C., Raichle M.E., 2005. The human brain is intrinsically organized into dynamic, anticorrelated functional networks.

Proceedings of the National Academy of Sciences of the United States of America 102(27),9673-9678.

Friston K.J., 2011. Functional and effective connectivity: A review. Brain Connectivity 1(1),13-36.

Friston K.J., Frith C.D., Frackowiak R.S., 1993. Principal component analysis learning algorithms: A neurobiological analysis. Proceedings.Biological Sciences / the Royal Society 254(1339),47-54.

Friston K.J., Holmes A.P., Poline J.B., Frith C.D., Frackowiak R.S., 1995. Statistical parametric maps in functional imaging: A general linear approach. Hum. Brain Mapp. 20(4),189--210.

Gianaros P.J., Van Der Veen F.M., Jennings J.R., 2004. Regional cerebral blood flow correlates with heart period and high-frequency heart period variability during working-memory tasks: implications for the cortical and subcortical regulation of cardiac autonomic activity. Psychophysiology 41,521–530.

Glover G.H., Li T.Q., Ress D., 2000. Image-based method for retrospective correction of physiological motion effects in fMRI: RETROICOR. Magn. Reson. Med. 44,162–167.

Golestani A.M. and Goodyear B.G., 2011. Regions of interest for resting-state fMRI analysis determined by inter-voxel cross-correlation. Neuroimage 56(1),246-251.

Greicius M.D., Krasnow B., Reiss A.L., Menon V., 2003. Functional connectivity in the resting brain: A network analysis of the default mode hypothesis. Proceedings of the National Academy of Sciences of the United States of America 100(1),253-258.

Gusnard D.A., Raichle M.E., Raichle M.E., 2001. Searching for a baseline: Functional imaging and the resting human brain. Nature Reviews.Neuroscience 2(10),685-694.

Hamilton P.S., Tompkins W.J., 1986. Quantitative investigation of QRS detection rules using the MIT/BIH arrhythmia database. IEEE Trans. Biomed. Eng. 33,1157–1165.

Handwerker D.A., Roopchansingh V., Gonzalez-Castillo J. and Bandettini P.A., 2012. Periodic changes in fMRI connectivity. Neuroimage 63,1712–1719.

Hemakom A., Goverdovsky V., Looney D., and Mandic D.P., 2016. Adaptive-projection intrinsically transformed multivariate empirical mode decomposition in cooperative brain–computer interface applications. Philos. Trans. R. Soc. A 374

Hommel G., 1988. A stagewise rejective multiple test procedure based on amodified bonferroni test. Biometrika 75,383–386.

Honey C.J., Sporns O., Cammoun L., Gigandet X., Thiran J.P., Meuli R. and Hagmann P., 2009. Predicting human resting-state functional connectivity from structural connectivity. Proc. Natl. Acad. Sci. U. S. A., 106(6),2035-40.

Howseman A.M. and Bowtell R.W., 1999. Functional magnetic resonance imaging: Imaging techniques and contrast mechanisms. Philosophical Transactions of the Royal Society of London.Series B, Biological Sciences 354(1387),1179-1194.

Huikuri H.V., Perkiomaki J.S., Maestri R., Pinna G.D., 2009. Clinical impact of evaluation of cardiovascular control by novel methods of heart rate dynamics. Philos. Trans. Series A. 367,1223–1238.

Hutchison R.M., Womelsdorf T., Allen E.A., Bandettini P.A., Calhoun V.D., Corbetta M., Della S., Duyn J.H., Glover G.H., Gonzalez-castillo J., Handwerker D.A., Keilholz S., Kiviniemi V., Leopold D.A., De Pasquale F., Sporns O., Walter M., and Chang C., 2013. Dynamic functional connectivity: Promise, issues, and interpretations. Neuroimage 80,360–378.

Hutchison R.M., Womelsdorf T., Gati J.S., Everling S., Menon R.S., 2013. Resting-state networks show dynamic functional connectivity in awake humans and anesthetized macaques. Hum. Brain Mapp. 34,2154–2177.

Jezzard P., LeBihan D., Cuenod D., Pannier L., Prinster A., Turner R., 1193. An investigation of the contribution of physiological noise in human functional MRI studies at 1.5 tesla and 4 tesla. Proc., SMRM, 12th Annual Meeting; New York. p. 1392

Jones D.T. et al., 2012. Non-stationarity in the ‘resting brain’s’ modular architecture. PLoS ONE 7, e39731.

Jones D.T., Vemuri P., Murphy M.C., Gunter J.L., Senjem M.L., Machulda M.M., Przybelski S.A., Gregg B.E., Kantarci K., Knopman D.S., Boeve B.F., Petersen R.C. and Jack Jr.C.R., 2012. Non-stationarity in the “resting brain's” modular architecture. PLoS One 7, e39731.

Jonsson P., Sonnby-Borgstrom M., 2003. The effects of pictures of emotional faces on tonic and phasic autonomic cardiac control in women and men. Biol. Psychol. 62,157–173.

Karahanoglu F., De Ville D. Van, 2017. Dynamics of large-scale fMRI networks: Deconstruct brain activity to build better models of brain function. Curr Opin Biomed Eng, 3, 28–36.

Kastrup A., Li T.Q., Glover G.H., Moseley M.E., 1999. Cerebral blood flow-related signal changes during breath holding. AJNR Am J Neuroradiol 20,1233–1238.

Kelley D. J.,2007. Functional Connectivity Imaging Analysis: Interhemispheric Integration in Autism. http://www.stat.wisc.edu/~mchung/teaching/MIA/projects/KelleyFC.pdf.

Kemp A.H., Quintana D.S., Gray M.A., Felmingham K.L., Brown K., Gatt J.M., 2010. Impact of depression and antidepressant treatment on heart rate variability: a review and meta-analysis. Biol. Psychiatry. 67,1067–1074.

Kim S.G. and Ogawa S., 2012. Biophysical and physiological origins of blood oxygenation level-dependent fMRI signals. Journal of Cerebral Blood Flow and Metabolism: Official Journal of the International Society of Cerebral Blood Flow and Metabolism 32(7),1188-1206.

Kiviniemi V., Vire T., Remes J., Elseoud A.A., Starck T., Tervonen O., Nikkinen J., 2011. A sliding time-window ICA reveals spatial variability of the default mode network in time. Brain Connect. 1,339–347.

Koush Y., Rosa M.J., Robineau F., Heinen K., Rieger S.W., Weiskopf N., Vuilleumier P., Van De Ville D., Scharnowski F., 2013. Connectivity-based neurofeedback: dynamic causal modeling for real-time fmri. Neuroimage, 81, pp. 422-430

Kwong K.K., Belliveau J.W., Chesler D.A., Goldberg I.E., Weisskoff R.M., Poncelet B.P., et al., 1992. Dynamic magnetic resonance imaging of human brain activity during primary sensory stimulation. Proc. Natl. Acad. Sci. U.S.A. 89,5675–5679.

Kwong K.K., Wanke I., Donahue K.M., Davis T.L., Rosen B.R., 1995. EPI imaging of global increase of brain MR signal with breath-hold preceded by breathing O2. Magn Reson Med 33,448–452.

LaConte S., Anderson J., Muley S., Ashe J., Frutiger S., Rehm K., Hansen L.K., Yacoub E., Hu X., Rottenberg D. and Strother S., 2003. The evaluation of preprocessing choices in singlevolunteer BOLD fMRI using NPAIRS performance metrics. Neuroimage 18(1),10–27.

Lane R.D., McRae K., Reiman E.M., Chen K., Ahern G.L., Thayer J.F., 2009. Neural correlates of heart rate variability during emotion. Neuroimage 44,213–222.

Li T.Q., Kastrup A., Takahashi A.M., Moseley M.E., 1999. Functional MRI of human brain during breath holding by BOLD and FAIR techniques. Neuroimage 9,243–249.

Liang P.J., Pandit J., Robbins P.A., 1996. Statistical properties of breath-to-breath variations in ventilation at constant PETCO2 and PETO2 in humans. J. Appl. Physiol. 81,2274–2286.

Licht C.M., de Geus E.J., Zitman F.G., Hoogendijk W.J., van Dyck R., Penninx B.W., 2008. Association between major depressive disorder and heart rate variability in the Netherlands Study of Depression and Anxiety (NESDA). Arch. Gen. Psychiatry. 65,1358–1367.

Looney D., Hemakom A., and Mandic D.P., 2014. Intrinsic multi-scale analysis: a multi-variate empirical mode decomposition framework. Proc. R. Soc. Math. Phys. Eng. Sci. 471,20140709.

Looney D., Li L., Rutkowski T.M., Mandic D.P., and Cichocki A., 2008. "Ocular artifacts removal from EEG using EMD," in Advances in Cognitive Neurodynamics ICCN 2007 (Dordrecht: Springer), 831–835.

Maldjian J.A., Laurienti P.J., Kraft R.A., Burdette J.H., 2003. An automated method for neuroanatomic and cytoarchitectonic atlas-based interrogation of fMRI data sets. Neuroimage 19(3),1233-1239.

Mandic D.P., Rehman N.U., Wu Z., and Huang N.E., 2013. Empirical mode decomposition-based time-frequency analysis of multivariate signals: the power of adaptive data analysis. IEEE Signal Proc. Mag. 30,74–86.

McKeown M.J., Makeig S., Brown G.G., Jung T.P., Kindermann S.S., Bell A.J., Sejnowski T.J., 1998. Analysis of fMRI data by blind separation into independent spatial components. Human Brain Mapping 6(3),160-188.

MI J.X., 2014. A novel algorithm for independent component analysis with reference and methods for its applications. Plos One 9(5), e93984.

Mitsis G.D., Iannetti G.D., Smart T.S., Tracey I., Wise R.G., 2008. Regions of interest analysis in pharmacological fMRI: how do the definition criteria influence the inferred result? Neuroimage 40,121–132.

Mitsis G.D., Poulin M.J., Robbins P.A., Marmarelis V.Z., 2004. Nonlinear modeling of the dynamic effects of arterial pressure and CO2 variations on cerebral blood flow in healthy humans. IEEE Trans. Biomed. Eng. 51,1932–1943.

Montano N., Porta A., Cogliati C., Costantino G., Tobaldini E., Casali K.R., Iellamo F., 2009. Heart rate variability explored in the frequency domain: a tool to investigate the link between heart and behavior. Neurosci. Biobehav. Rev. 33,71–80.

Mucha P.J., Richardson T., Macon K., Porter M.A., Onnela J.P., 2010. Community structure in time-dependent, multiscale, and multiplex networks. Science 328 (5980),876–878.

Murphy K., Birn R.M., Bandettini P.A., 2013. Resting-state fMRI confounds and cleanup. Neuroimage 80,349–359.

Nakada K., Yoshida D., Fukumoto M., Yoshida S., 2001. Chronological analysis of physiological T2* signal change in the cerebrum during breath holding. J Magn Reson Imaging 13,344–351.

Napadow V., Dhond R., Conti G., Makris N., Brown E.N., Barbieri R., 2008. Brain correlates of autonomic modulation: combining heart rate variability with fMRI. Neuroimage 42,169–177.

Ogawa S., Lee T.M., Kay A.R., Tank D.W., 1990. Brain magnetic resonance imaging with contrast dependent on blood oxygenation. Proceedings of the National Academy of Sciences of the United States of America 87(24),9868-9872

Ogawa S., Tank D.W., Menon R., Ellermann J.M., Kim S.G., Merkle H., et al., 1992. Intrinsic signal changes accompanying sensory stimulation: functional brain mapping with magnetic resonance imaging. Proc. Natl. Acad. Sci. U.S.A. 89,5951–5955.

Oppenheim A.V., Schafer R.W., 2009. Discrete-time signal processing, 3rd edn. Prentice-Hall Signal Processing Series. Englewood Cliffs, NJ: Prentice-Hall.

Orphanidou C., Bonnici T., Charlton P., Clifton D., Vallance D., Tarassenko L., 2015. Signal-quality indices for the electrocardiogram and photoplethysmogram: Derivation and applications to wireless monitoring. IEEE J. Biomed. Heal. Informatics 19,832–838.

Pattinson K.T.S., Mitsis G.D., Harvey A.K., Jbabdi S., Dirckx S., Mayhew S.D., Rogers R., Tracey I., Wise R.G., 2009. Determination of the human brainstem respiratory control network and its cortical connections in vivo using functional and structural imaging. Neuroimage 44,295–305.

Penttila J., Kuusela T., Scheinin H., 2005. Analysis of rapid heart rate variability in the assessment of anticholinergic drug effects in humans. Eur. J. Clin. Pharmacol. 61,559–565.

Preti M.G., Bolton T.A, Van De Ville D., 2016. The dynamic functional connectome: State-of-the-art and perspectives. Neuroimage 160,41-54.

Raichle M.E. and Snyder A.Z., 2007. A default mode of brain function: A brief history of an evolving idea. Neuroimage 37(4),1083-90; discussion 1097-9.

Raichle M.E., MacLeod A.M., Snyder A.Z., Powers W.J., Gusnard D.A., Shulman G.L., 2001. A default mode of brain function. Proceedings of the National Academy of Sciences of the United States of America 98(2),676-682.

Rogers B. P., Morgan V. L., Newton A. T., Gore J. C., 2007. Assessing functional connectivity in the human brain by fMRI. Magn. Reson. Imaging 25, 1347–135710.1016/j.mri.2007.03.007

Rostrup E., Law I., Blinkenberg M., Larsson H.B., Born A.P., Holm S., Paulson O.B., 2000. Regional differences in the CBF and BOLD responses to hypercapnia: a combined PET and fMRI study. Neuroimage 11,87–97.

Rubinov M., Sporns O., 2010. Complex network measures of brain connectivity: uses and interpretations. Neuroimage 52(3),1059–1069

Sakoglu U., Pearlson G.D., Kiehl K.A., Wang Y., Michael A. and Calhoun V.D., 2010. A method for evaluating dynamic functional network connectivity and taskmodulation: application to schizophrenia. MAGMA 23(5-6),351–366.

Smit D.J.A., Stam C.J., Posthuma D., Boomsma D.I., de Geus E.J.C., 2008. Heritability of 'small-world' networks in the brain: a graph theoretical analysis of resting-state EEG functional connectivity. Hum. Brain Mapp. 29,1368–1378.

Smith S.M. et al., 2004. Advances in functional and structural MR image analysis and implementation as FSL. Neuroimage 23(Suppl. 1), S208–S219.

Smith S.M., 2012. The future of FMRI connectivity. Neuroimage 62(2),1257-1266.

Smith S.M., Fox P.T., Miller K.L., Glahn D.C., Fox P.M., Mackay C.E., Filippini N., Watkins K.E., Toro R., Laird A.R., and others, 2009. Correspondence of the brain's functional architecture during activation and rest. Proceedings of the National Academy of Sciences of the United States of America 106(31),13040-13045.

Smith S.M., Miller K.L., Salimi-Khorshidi G., Webster M., Beckmann C.F., Nichols T.E., Ramsey J.D., Woolrich M.W., 2011. Network modelling methods for FMRI. Neuroimage 54(2),875-891.

Stillman A.E., Hu X., Jerosch-Herold M., 1995. Functional MRI of brain during breath holding at 4 T. Magn Reson Imaging 13,893–897.

Stoeckel L. et al., 2014. Optimizing real time fmri neurofeedback for therapeutic discovery and development. NeuroImage: Clin., 5, pp. 245-255

Strother S.C., Lange N., Anderson J.R., Schaper K.A., Rehm K., Hansen L.K. and Rottenberg D.A., 1997. Activation pattern reproducibility: measuring the effects of group size and data analysis models. Hum Brain Mapp 5(4),312–316.

Tagliazucchi E., vonWegner F., Morzelewski A., Brodbeck V., Laufs H., 2012b. Dynamic BOLD functional connectivity in humans and its electrophysiological correlates. Front. Hum. Neurosci. 6 (339), 1–22.

Task Force, 1996. Heart rate variability: standards of measurement, physiological interpretation and clinical use. Task Force of the European Society of Cardiology and the North American Society of Pacing and Electrophysiology. Circulation 93,1043–1065.

Taylor K.S., Seminowicz D.A., Davis K.D., 2009. Two systems of resting state connectivity between the insula and cingulate cortex. Human Brain Mapping 30(9),2731-2745.

Theiler J., 1992. Testing for nonlinearity in time series: the method of surrogate data. Physica D 58,85–77.

Van Den Heuvel M.P. and Hulshoff Pol H.E., 2010. Exploring the brain network: A review on resting-state fMRI functional connectivity. European Neuropsychopharmacology : The Journal of the European College of Neuropsychopharmacology 20(8),519-534.

Van Dijk K.R.A., Hedden T., Venkataraman A., Evans K.C., Lazar S.W., Buckner R.L., 2010. Intrinsic functional connectivity as a tool for human connectomics: theory, properties, and optimization. J. Neurophysiol. 103,297–321.

Veer I.M., Beckmann C.F., van Tol M.J., Ferrarini L., Milles J., Veltman D.J., Aleman A., van Buchem M.A., van der Wee N.J., Rombouts S.A., 2010. Whole brain resting-state analysis reveals decreased functional connectivity in major depression. Frontiers in Systems Neuroscience 4,10.3389/fnsys.2010.00041.

Vesely A., Sasano H., Volgyesi G., Somogyi R., Tesler J., Fedorko L., Grynspan J., Crawley A., Fisher J.A., Mikulis D., 2001. MRI mapping of cerebrovascular reactivity using square wave changes in end-tidal PCO2. Magn Reson Med 45,1011–1013.

Ville DE, Blu T., Unser M., 2006. Surfing the brain: an overview of wavelet-based techniques for fMRI data analysis. IEEE Engi. Med. Biol. Mag. 25,65–78.

Von Rosenberg W., Chanwimalueang T., Adjei T., Jaffer U., Goverdovsky V., Mandic D. P., 2017. Resolving ambiguities in the LF/HF Ratio: LF-HF scatter plots for the categorization of mental and physical stress from HRV. Frontiers Physiol., 8, 360.

Wallentin M., Nielsen A.H., Vuust P., Dohn A., Roepstorff A., Lund T.E., 2011. Amygdala and heart rate variability responses from listening to emotionally intense parts of a story. Neuroimage 58,963–973.

Weisskoff R.M., Baker J., Belliveau J., Davis T.L., Kwong K.K., Cohen M.S., Rosen B.R., 1993 Power spectrum analysis of functionally-weighted MR data: what's in the noise?. Proc SMRM, 12th Annual Meeting; New York. p. 7

Wise R.G., Ide K., Poulin M.J., Tracey I., 2004. Resting fluctuations in arterial carbon dioxide induce significant low frequency variations in BOLD signal. Neuroimage 21,1652–1664.

Wise R.G., Pattinson K.T., Bulte D.P., Chiarelli P.A., Mayhew S.D., Balanos G.M., O'Connor D.F., Pragnell T.R., Robbins P.A., Tracey I., Jezzard P., 2007. Dynamic forcing of end-tidal carbon dioxide and oxygen applied to functional magnetic resonance imaging. J Cereb Blood Flow Metab 27,1521–1532.

Wu G.-R., Liao W., Stramaglia S., Ding J.-R., Chen H., Marinazzo D., 2013. A blind deconvolution approach to recover effective connectivity brain networks from resting state fMRI data. Med. Image Anal. 17,365–374.

Xiong J., Parsons L.M., Gao J.H., Fox P.T., 1999. Interregional connectivity to primary motor cortex revealed using MRI resting state images. Human Brain Mapping 8(2-3),151-156.

Xu Z.H. and Chan A.K. ,2002. Encoding with frames in MRI and analysis of the signal-tonoise ratio. IEEE Transactions on Medical Imaging 21(4): 332-342.

Zalesky A., Fornito A., Cocchi L., Gollo L.L., Breakspear M., 2014. Time-resolved resting-state brain networks. Proc. Natl. Acad. Sci. 111 (July (28)), 10341–10346.